IMPERIAL COLLEGE LONDON

Faculty of Engineering

Department of Chemical Engineering

Optimisation of high-efficiency combined heat and power systems for distributed generation

---

Maria Anna Chatzopoulou

Supervised by:

Professor Christos N. Markides

A thesis submitted for the degree of

Doctor of Philosophy

December 2018

Statement of Originality

I hereby certify that, to the best of my knowledge, the content of this thesis is original and the result of my own work. All of the assistance I received and the sources I used have been properly acknowledged.

Maria Anna Chatzopoulou

December, 2018

Copyright Declaration

List of Publications

To date these are the publications that have been presented to the public domain in relation to the works herein.

Journal Publications

- Chatzopoulou MA, Simpson M, Sapin P, Markides CN. Off-design optimisation of organic Rankine cycle with piston expander for medium-scale combined heat and power applications. Appl Energy 2019;238:1211–36. doi:https://doi.org/10.1016/j.apenergy.2018.12.086.
- Chatzopoulou MA, Lecompte S, Paepe M De, Markides CN. ORC engines off-design optimisation with different heat exchangers and volumetric expanders in waste heat recovery applications. Appl Energy 2019; Under review.
- Chatzopoulou MA, Markides CN. Thermodynamic optimisation of a high-electrical efficiency integrated internal combustion engine – Organic Rankine cycle combined heat and power system. Appl Energy 2018;226:1229–51. doi:10.1016/j.apenergy.2018.06.022.
- Simpson M, Chatzopoulou MA, Oyewunmi OA, Markides CN. Technoeconomic analysis of internal combustion engine – organic Rankine cycle cogeneration systems in energy-intensive buildings. Appl Energy 2019; Under review.
- Ramos A, Chatzopoulou MA, Freeman J, Markides CN. Optimisation of a high-efficiency solar-driven organic Rankine cycle for applications in the built environment. Appl Energy 2018;228:755–65. doi:10.1016/j.apenergy.2018.06.059.
- White MT, Oyewunmi OA, Chatzopoulou MA, Pantaleo AM, Haslam AJ, Markides CN. Computer-aided working-fluid design, thermodynamic optimisation and thermoeconomic assessment of ORC systems for waste-heat recovery. Energy 2018;161:1181–98. doi:10.1016/j.energy.2018.07.098.
- Ramos A, Chatzopoulou MA, Guarracino I, Freeman J, Markides CN. Hybrid photovoltaic-thermal solar systems for combined heating, cooling and power provision in the urban environment. Energy Convers Manag 2017;150. doi:10.1016/j.enconman.2017.03.024.

Peer Reviewed Conference Publications

- Chatzopoulou MA, Lecompte S, De Paepe M, Markides CN. Off-design operation of ORC engines with different heat exchanger architectures in waste heat recovery applications. Energy Procedia 2019;158:2348–53. doi:10.1016/j.egypro.2019.01.282
- Simpson MC, Chatzopoulou MA, Oyewunmi OA, Markides CN. Technoeconomic analysis of internal combustion engine – organic Rankine cycle cogeneration systems in energy-intensive buildings. Energy Procedia 2019;158:2354–9. doi:10.1016/j.egypro.2019.01.283.
- Lecompte S, Chatzopoulou MA, Markides CN, De Paepe M. Off-design comparison of subcritical and partial evaporating ORCs in quasi-steady state annual simulations. Energy Procedia 2019;158:2064–9. doi:10.1016/j.egypro.2019.01.477.
- Chatzopoulou MA, Markides CN. Thermodynamic assessment of organic Rankine cycle systems during off-design operation in combined heat and power (CHP) Applications. Proceeding 3rd Therm Fluids Eng Conf 2018:39–50. doi:10.1615/tfec2018.aes.021587.
- Chatzopoulou MA, Sapin P, Markides CN. Optimisation of off-design internal combustion- organic Rankine engine combined cycles. 31st Int. Conf. Effic. Cost, Optim. Simul. Environ. Impact Energy Syst., Guimarães: ECOS 2018; 2018.
- Chatzopoulou MA, Markides CN. Advancements in organic Rankine cycle system optimisation for combined heat and power applications: Components sizing and thermoeconomic considerations. Proc. 30th Int. Conf. Effic. Cost, Optimisation, Simul. Environ. Impact Energy Syst., San Diego; 2017.
- Chatzopoulou MA, Acha S, Oyewunmi OA, Markides CN. Thermodynamic and economic evaluation of trigeneration systems in energy-intensive buildings. Proc. 13th Int. Conf. Heat Transf. Fluid Mech. Thermodyn., Portoroz, Slovenia; 2017.
- Ramos A, Chatzopoulou MA, Freeman J, Markides CN. Optimisation of a high-efficiency solar-driven organic Rankine cycle for applications in the built environment. Proc. 30th Int. Conf. Effic. Cost, Optimisation, Simul. Environ. Impact Energy Syst., San Diego; 2017.
- Oyewunmi OA, White MT, Chatzopoulou MA, Haslam AJ, Markides CN. Integrated computer-aided working-fluid design and power system optimisation: Beyond thermodynamic modelling. 30th Int Conf Effic Cost, Optim Simul Environ Impact Energy Syst ECOS 2017; 2017.

- Chatzopoulou MA, Markides CN. Modelling of advanced combined heat and power systems. Proc. 2nd Therm. Fluids Eng. Conf. ASTFE 2017, Las Vegas, USA: ASTFE; 2017.
- White MT, Oyewunmi OA, Chatzopoulou MA, Pantaleo AM, Haslam AJ, Markides CN. Integrated computer-aided working-fluid design and thermoeconomic ORC system optimisation. Energy Procedia 2017;129:152–9. doi:10.1016/j.egypro.2017.09.095.
- Pantaleo AM, Rotolo G, Simpson M, De Palma P, Amirante R, Oyewunmi OA, Chatzopoulou MA, Markides CN. Thermo-economic optimization of small scale ORC systems for heat recovery from natural gas internal combustion engines for stationary power generation. 4th Annu. Engine ORC Consort. Work. Automot. Satationary Engine Ind., 2017.
- Chatzopoulou M-A, Fisk D, Keirstead J, Markides CN. Informing low carbon HVAC systems modelling and design, using a global sensitivity analysis framework. ASME 2016 10th Int. Conf. Energy Sustain. ES 2016, collocated with ASME 2016 Power Conf. ASME 2016 14th Int. Conf. Fuel Cell Sci. Eng. Technol., vol. 1, 2016. doi:10.1115/ES2016-59593.
- Chatzopoulou MA, Keirstead J, Fisk D, Markides CN. Characterising the impact of HVAC design variables on buildings energy performance, using a Global Sensitivity Analysis Framework. Proc. CLIMA 2016 Conf., Aalborg, Denmark: Federation of European Heating, Ventilation and Air Conditioning Associations (REHVA); 2016. doi: http://vbn.aau.dk/en/publications/clima-2016--proceedings-of-the-12th-rehva-world-congress(f66ed00a-82ec-4f39-a4e9-f943ef3b44ee).html

"To know how to appreciate in each case, at their true value, the consideration of convenience and economy which may present themselves; to know how to discern the more important of those which are only accessories to balance them properly against each other, in order to attain the best results by the simplest means: such should be the leading characteristics of the man called to direct, to co-operate towards one useful end, of whatsoever sort it may be."

- Sadi Carnot, Physicist (1826)

Abstract

Distributed combined heat and power (CHP) systems have the potential to cover a significant amount of the global energy requirements for power, and heating. Small-to-medium scale CHP systems, in the built environment and in the industry (up to a few MWs), are typically driven by internal combustion engines (ICE). In CHP-ICE systems, more than 55% of the energy input is transferred as heat in the exhaust-gas stream and the jacket water cooling circuit. Unless these thermal outputs are utilised, the energy will be released to the atmosphere as waste heat, deteriorating the system's efficiency. Organic Rankine cycle (ORC) engines are a promising heat-to-power technology, for converting waste heat into power. Therefore, coupling ORC engines as bottoming cycles to CHP-ICEs can maximise overall system efficiency, and reduce energy costs. In this thesis, the design of ICE-ORC CHP systems is investigated from thermodynamic, operating and economic perspectives, aiming to fully unlock the potential of such advanced high-efficiency cogeneration systems.

An integrated ICE-ORC CHP optimisation tool is developed, which, unlike previous studies, captures the performance trade-offs between the two interacting engines, to optimise the combined system performance. A dynamic ICE model is developed and validated, along with a steady-state model of subcritical recuperative ORC engines. Multiple working fluids are investigated, along with naturally aspirated and turbocharged ICEs. By optimising the combined ICE-ORC CHP system simultaneously: i) the total power output increases by up to 30%, in comparison to the conventional approach where the two engines are optimised separately; ii) the electrical efficiency increases by up to 21%, in comparison to the stand-alone ICE; and iii) in the integrated system the ICE operation is adjusted to promote the ORC power output, which generates up to 15% of the total power, improving fuel efficiency. When focusing on maximising power output only, this comes at the cost of higher fuel consumption. In contrast, when optimising the integrated ICE-ORC CHP system for specific fuel consumption (SFC), the fuel consumption decreases by up to 17%. These findings prove that by taking a holistic approach in the design of ICE-ORC CHP systems, considering the combined system interactions, these can generate more power, with lower fuel consumption and costs.

ORC engines in ICE-ORC CHP systems will experience variable heat-source conditions (temperature and mass flow are), while the ICE load fluctuates. To maximise the running hours of ORC engines, and improve their economic proposition, the system should maintain high efficiency, not only at the design point, but also at off-design operation. An off-design optimisation tool is therefore developed to generate optimised off-design operation maps. This work differs from previous studies in that the tool considers explicitly the time-varying operational characteristics and interactions of the ORC engine components in the integrated system. Double-pipe (DPHEX) and plate-frame heat exchanger (PHEX) models are used for sizing the ORC evaporator and condenser, and piston and screw expander models for sizing the expander. The ORC system is first sized for full-load ICE operation (design point). Then, ICE part-load (PL) conditions are obtained and new ORC operating points are optimised. Results reveal that the ORC

engine power output is underestimated by up to 17%, when the off-design operational characteristics of the components are not considered. The piston expander efficiency increases by up to 16% at PL operation, while the ORC thermal efficiency increases by up to 7% at off-design operation. Optimised ORC engines with screw expanders operate always with two expansion stages. Although the latter generate slightly more power at their design point than when using piston machines, pistons perform better at off-design conditions. ORC engines with PHEXs generate 5-12% more power than DPHEX designs, while having *U*-values almost double that of DPHEXs. Although, heat transfer coefficients decrease by 25-30% at off-design, the HEX effectiveness increases, by up to 15%. By considering the time-varying characteristics of the ORC components, as the ICE PL reduces, the optimised ORC engine power output decreases at a lower rate: at ICE PL of 60%, the optimised ORC engine with fluids, such as R1233zd, operates at 77% of its nominal capacity (with piston expanders).

An ORC thermoeconomic optimisation tool is then developed. Unlike other studies where the component types are predefined, the tool scans alternative components' typologies, sizes, and configurations, to obtain the best-performing design. New cost correlations are presented to assist with predicting ORC costs. ORC engines optimised for maximum power output have the highest SICs, falling in the range of 1,000-7,500 GBP/kW for piston expanders, and 1,500-5,500 GBP/kW for screw expanders, due to high HEX areas, and high volumetric flow rates. In contrast, when minimising SIC, power output reduces by 15-50%, but the cost also reduces by up to 35%. In the optimised designs, the evaporator is selected to be a PHEX, the condenser is a DPHEX, whilst ORC engines with screw machines operate with two-stage expansion. Multi-objective optimisation reveals optimal ORC systems with a range of power outputs between 70-100 kW, for which increasing power by 33%, results in an increase of SIC of less than 10%. This indicates a promising range of capacities for next-generation ORC engines. ORC engines optimised for high power output result in high net present value (NPV), but also high discounted payback period (DPP). In contrast, engines optimised for low SIC achieve DPPs of 2.8-6 years, making them an attractive investment. Overall, these findings can be used by ICE and ORC engine manufacturers, and integrators, to inform component design decisions, and by ORC plant operators to maximise their system performance, under variable operating conditions.

Acknowledgements

I would like to thank my supervisor Professor Christos N. Markides, for the faith he has shown in me and for the support and expertise he has provided over the last four years. A very special gratitude for the Imperial College London President's PhD Scholarship Scheme, and for the EU Climate-KIC PhD Added Programme for supporting me and funding this research.

Special thanks to Professor Chris Cheeseman, who was the one that contacted me to inform me about the PhD scholarships available, and all his support in preparing my research proposal submission.

I would like to thank the members of the Clean Energy Processes (CEP) Laboratory - James, Victor, Niyi, Christoph, Asma, Ilaria, Niccolo, Ajay, Ali, Maria, Mike, Dauda, Ahmad, Kai, Adreas and Ray - who were there not only to offer support, by deliberating over our problems and findings, but also happily by talking about things other than just our papers.

I would not forget Alba, Paul and Solomos and our great trip (conference) in San Diego. Alba, a heartily thank you for all your insights and support with my research, the great Spanish omelettes, and most of all, thank you for saving me in the desert and allowing me to complete my PhD work! A special thank you to Alexandros for the amazing road trips, alligator hunting, bear watching, thought-provoking conversations, and the loads of fun we have had, when attending conferences. To my beloved Martha, thank you for the fantastic time we have had, when scrolling around Atlantis and all this photo-shooting, as well as for all the tele-support, in all my ups and downs, for the past couple of years.

My loving Lotus team – Marina, Tiemen, Boy and Sander – thank you for the great work, and fun we have had, when building our start-up! I would not forget the long working nights in Paris, Wroclaw and Valencia, and the great tapas places, we have visited together. It has been a great pleasure meeting you, working with you, learning all about building a business and most of all, thank you, for creating memories that I would cherish forever!

I would like to express my sincerest thanks to Cundall, and, in particular, my deepest gratitude to Malcolm for his support, enthusiasm, understanding and valuable insights, since the very beginning of my PhD research. It has been a pleasure meeting you.

I am thankful to and fortunate to have met and get constant support, and encouragement from Catia, Christina, Alexandra, Maria and Celia, who have made these past four years unforgettable. A big thank you to my loving flatmate, Apostolia, for her support and help in challenging periods, and all these fun

nights and great parties, during the past four years. I am also grateful to Katerina, Vaggelis, George, Nicolas, and George for making London a great place to be, from my day one in the UK.

Then there are my childhood friends, who although many kilometres away, they have been always there to support me in difficult periods over the past four years, to celebrate big wins, and most of all have fun every time we have been together. Thank you, Cleopatra, Rebecca, Michael, Tina, Sofia and Amalia – thirty years and we are still counting!

I am very fortunate to have met George, who has been there for me with his constant support, understanding, encouragement, and most of all positiveness throughout the write up of this thesis. Thank you for standing by me in all the ups and downs, for our amazing trips and all the fun we have had.

I would like to express my greatest gratitude to my parents, Roula and Vasilis, for their boundless love, patience, and support for the past thirty years. You were always there to remind me during my moments of doubt that with perseverance and courage, I could overcome the toughest of odds and achieve great heights.

This PhD thesis is dedicated to my beloved grandparents, my ‘yiayia’ Anna and my ‘pappous’ Ioannis, for all their unbounded love, continuous guidance, and encouragement, since I can remember myself. Always keen to know what I was doing and how I was proceeding, although it is likely that they have never grasped what it was all about!

Maria Anna Chatzopoulou

December 2018

“Let us be grateful to people who make us happy; they are the charming gardeners who make our souls blossom” – Martin Proust, Novelist

Table of Contents

List of Figures

List of Tables

Nomenclature

Abbreviations

BDC	Bottom dead centre
BMEP	Break mean effective power
CAPEX	Capital expenditure
CHP	Combined heat and power
CS	Carbon steel
DCF	Discounted cash flows
DPHEX	Double pipe heat exchanger
DPP	Discounted payback period
DSH	Desuperheater
EV	Exhaust valve
FMEP	Friction mean effective power
FOB	Free of board cost
GHG	Greenhouse gases
GT	Gas turbines
GWP	Global warming potential
HEX	Heat exchanger
HTC	Heat transfer coefficient
ICE	Internal combustion engine
IV	Intake valve
KPI	Key performance indicator
LMDT	Logarithmic mean temperature difference
MGT	Micro gas turbines
NPV	Net present value
ODE	Ordinary differential equations
ODP	Ozone depletion potential
ORC	Organic Rankine cycle
O&M	Operation and maintenance costs
PH	Preheater
PHEX	Plate heat exchanger
PL	Part-load
PR	Pressure ratio
RPM	Revolutions per minute
SH	Superheater
SS	Stainless steel

TC	Total cost
TDC	Top dead centre
VR	Volume ratio

Symbols

A	Area	(m^2)
AFR	Air-to-fuel ratio	(-)
b	Cylinder bore diameter	(-)
B_{chis}	Chisholm parameter	(-)
c	Post-expansion correction factor	(-)
c^*	Off-design correction factor	(-)
c_{p}	Specific heat capacity	(J/kg·K)
$\vec{C}$	Constraints vector	(-)
C_{D}	Discharge coefficient	(-)
C_p^0	Purchase cost	(GBP)
D	Tube diameter	(m)
D_{h}	Hydraulic diameter (piston)	(m)
D_{v}	Valve diameter	(m)
ex	Specific exergy	(J/kg)
f	Friction factor	(-)
$\vec{F}$	Objective function	(-)
F	Overall cost correction factor	(-)
F_{BM}	Bare module cost factor	(-)
F_{D}	Cost correction factor for type of motor	(-)
F_{FC}	Forced convection multiplier	(-)
F_{m}	Cost correction factor for materials	(-)
F_{p}	Cost correction factor for pressure	(-)
$flag$	Indicator of type of heat exchanger	(-)
G	Mass velocity	($kg/s{\cdot}m^2$)
h	Specific enthalpy	(J/kg·K)
h_{g}	Average heat transfer coefficient	($W/m^2{\cdot}K$)
h_{lg}	Specific enthalpy of vaporisation	(J/kg·K)
i	Interest rate	(%)
k	Mass fraction	(kg/kg,-)
l	Connecting rod (con-rod) length	(m)
l_{s}	Piston stroke length	(m)

L	Length	(m)
L_v	Valve lift	(m)
LHV	Lower heating value	(J/kg)
M	Molar mass	(kg/kmol)
m	Mass	(kg)
$\dot{m}$	Mass flow rate	(kg/s)
N	Rotational speed	(1/s)
Nu	Nusselt number	(-)
P	Pressure	(Pa)
P_r	Critical pressure ratio	(-)
PP	Pinch Point	(K)
Pr	Prandtl number	(-)
PR	Pressure ratio	(-)
$\dot{q}$	Heat flux density	(W/m^2)
$\dot{q}_w$	Gas-to-wall heat flux density	(W/m^2)
$\dot{Q}$	Heat transfer rate/thermal load	(W)
$\dot{Q}_{jw}$	Jacket water thermal load	(W)
$\dot{Q}_{loss}$	Losses	(W)
$\dot{Q}_w$	Thermal losses through the wall	(W)
r	Volume ratio	(-)
R	Gas constant	(J/kg·K)
Re	Reynolds number	(-)
s	Specific entropy	(J/ kg·K)
S_f	Suppression factor	(-)
SFC	Specific fuel consumption	(W/W, -)
SFC_{abs}	Absolute specific fuel consumption	(kg/kWh)
SHD	Superheating degree	(-)
t	Time	(s)
T_g	Instantaneous cylinder gas temperature	(K)
u	Velocity	(m/s)
U	Overall heat transfer coefficient	(W/m^2 ·K)
U_p	Piston velocity	(m/s)
v	Kinematic viscosity	(m^2/s)
V	Volume	(m^3)
$\dot{W}$	Power	(W)
W	Plate width	(m)
x	Quality	(-)

$\dot{X}$	Exergy rate	(W)
$\vec{X}$	Optimiser decision variables vector	(-)
X_{tt}	Martinelli parameter	(-)
Y_{chis}	Chisholm parameter	(-)
Z	Component attribute for costing	(Variable)
z	Corrugation depth	(m)

Greek symbols

α	Local heat transfer coefficient	(W/m^{2} ·K)
β	Corrugations angle	(rad)
γ	Ratio of heat capacities	(-)
Δ	Difference	(-)
ε	Effectiveness	(-)
η	Efficiency	(-)
ϑ	Crankshaft angle	(°)
λ	Thermal conductivity	(W/m·K)
μ	Dynamic viscosity	(Pa s)
ρ	Density	(kg/m^{3})
σ_{Boltz}	Stefan-Boltzmann constant	(W/m^{2}·K^{4})
φ_{chis}	Chisholm parameter	(-)
ω	Rotational speed	(rad/s)

Subscripts

Boltz	Stefan-Boltzmann
c	Condensing two-phase zone
chd	Chocked flow
comb	Combustion
comp	Compressor
cond	Condenser
crit	Critical
cw	Condenser/cooling water
cyl	Cylinder
d	Duration
dest	Destruction
dis	Displacement
dn	Downstream

drp	Drop
dsh	Desuperheater
DP	Double pipe heat exchanger
ef	Effective
el	Electrical
elg	Electric generator
eq	Equivalent
ev	Evaporating (two-phase) zone
evap	Evaporator
ex	Exhaust gases
exp	Expansion
f	Fuel
FC	Forced convection
fz	Foster and Zuber
g	Gas part of two-phase flow
G	Gas
gap	Piston ring gap
h	Preheater
hs	Heat source
hyd	Hydraulic
ign	Ignition
in	Input/inlet
int	Cylinder intake
intr	Intercooler
is	Isentropic
jw	Jacket water
l	Liquid part of two-phase flow
L	Liquid
lim	Limit
loss	Losses
m	Motoring
max	Maximum
mech	Mechanical
min	Minimum
n	Project life time
NB	Nucleate boiling
net	Net

nchd	Non-chocked flow
o	Initial conditions
off	Valve close
on	Valve open
out	Output/outlet
p	Plate/passage
PH	Plate heat exchanger
pist	Piston
R	Valve restriction
rec	Recuperator
sat	Saturation
sec	Section
sh	Superheater
th	Thermodynamic
turb	Turbocharger
up	Upstream
v	Vapour
V	Valve
w	Wall
wf	Working fluid
z	Axial direction

Superscripts

ac	Acceleration pressure drop
DP	Double pipe heat exchanger
fr	Frictional pressure drop
PH	Plate heat exchanger
‘	Off-design operation value
$\rightarrow$	Vector

Chapter 1

Introduction

"To waste, to destroy our natural resources, to skin and exhaust the land instead of using it so as to increase its usefulness, will result in undermining in the days of our children the very prosperity which we ought by right to hand down to them amplified and developed."

- Theodore Roosevelt, former President of the United States

1.1 Context

The worldwide dependency on energy has been steadily increasing over the past few decades [1]. Over the previous century, the vast amount of power generation and worldwide energy use was based on the combustion of fossil fuels. Originally coal was the primary energy source, and oil followed, while recently the natural gas contribution to the world energy mix has been rapidly increasing, along with renewable sources of energy, towards cleaner energy generation [2]. An inevitable consequence of combustion has been the release of the so-called greenhouse gases, and mainly of carbon dioxide (CO_2), into the atmosphere. There is a consensus in the scientific community that the over-release of greenhouse gases emissions into the atmosphere, over the past century, is responsible for the average surface global temperature rise by almost 1 °C in comparison to the pre-industrial era [3]. International agreements aim to mitigate global warming and climate change, by setting ambitious targets for reducing energy consumption and greenhouse gases emissions, and promoting sustainable energy systems. The Paris Agreement (2015) [4] has been signed by 193 countries, and has been ratified by 184 Parties (as of the end of November 2018 [5]). The Agreement, aims to maintain (amongst others) the global temperature rise in this century to below 2 °C, from the pre-industrial era, by limiting the levels of anthropogenic emissions, while ensuring that: i) climate change mitigation and adaptation measures are in place; and ii) economic growth and development are sustained.

Although significant progress has been made worldwide, with launching new energy efficiency policies, the global energy demand continues to grow, nevertheless at a lower rate than the previous decades. The global energy use is predicted to continue rising by 30% (in comparison to the 2016 energy demand levels) by 2040, reaching 17,000 Mtoe of primary energy [2]. The global population is expected to grow by approximately 20% by 2040, expanding from 7.4 billion (end of 2016) to more than 9 billion [6], while urbanisation is also anticipated to grow, with projections indicating that a city of the size of Shanghai, will be added to the world's urban population every four months, over the same period. Finally, demand for electricity is one of the key drivers for the increasing overall energy demand, corresponding to 40% of the worldwide rise in final energy consumption, in the next two decades [6].

The increase of energy consumption and emissions, along with the fuels price instability are the main reasons behind the efforts devoted to reduce energy demand and utilise efficiently alternative energy sources. Engineers, consultants and scientists are in search of: a) means of demand reduction; b) strategies to ensure the supply's security; c) technologies with enhanced energy efficiency; and d) renewable sources of energy to replace the dependency on fossil fuels [7]. Two main pathways have been identified as a means of tackling climate change, and reducing our impact on the environment: i) increase the penetration of renewable energy sources in the global energy mix, by harvesting solar, wind, biomass, geothermal or other renewable forms of energy; and ii) to improve the efficiency of conventional or new energy conversion technologies, to ensure that the systems recover the maximum technically feasible energy content, from any available source, thus covering the same demand with less energy consumption. Enhancing the efficiency of energy systems is vital for taking the stresses off the supply side, with the International Energy Agency (IEA) [6] reporting that without improving energy efficiency, the projected rise in final energy demand would be more than double. However, there still remains a significant proportion of the worldwide energy (>50%) [1,8] that is being wasted as heat into the atmosphere, both in the industry and the wider building sector. This highlights that designing novel highly-efficient energy systems, or enhancing the performance of the state-of-the art technologies is of paramount importance, to allow us to achieve the ambitious decarbonisation targets.

1.1.1 Cogeneration and poly-generation

In the light of the efforts devoted towards reducing global energy consumption and emissions, distributed combined heat and power (CHP) generation has been gaining growing interest, due to the higher overall efficiency of the system, in comparison to the separate provision of these vectors. In Fig. 1 a simplified schematic of the energy flows in a CHP system is presented. The key difference to the traditional provision of heat and power is that these vectors are generated from a single system (i.e. with the same energy/fuel input), while covering the same demand. This minimises the system energy losses, thus reducing the overall fuel consumption and carbon emissions. Other benefits of the distributed CHP systems include their proximity to the demand, which reduces distribution losses, and the opportunity to connect to renewable energy sources, such as solar collectors etc. In cases where the heat output of the CHP system is used to drive the so-called thermally driven cooling technologies, or the electricity generated is utilised by technologies, such as heat pumps, to provide cooling, the system is called 'tri-generation'. A more generalised term is also commonly used, namely a 'poly-generation' system. Poly-generation systems offer similar benefits to that of a CHP system.

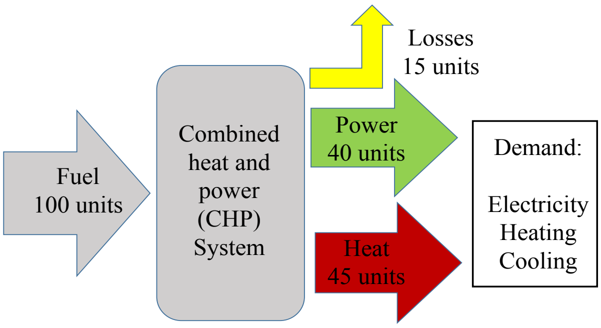

Fig. 1: Simplified energy flows schematic in a cogeneration system. The efficiency values indicated, refer to a CHP system driven by internal combustion engine, with typical electrical efficiency of 40% [9].

Bianchi et al. [10] compared the electrical efficiency of well-established prime movers for CHP applications, including internal combustion engines (ICEs), gas turbines (GT) and micro gas turbines (MGT), over a range of power outputs. In their findings, ICEs achieve electrical efficiencies of 30%-45% for power outputs from 10 kW to 10 MWs, outperforming the GT and MGT technologies. Therefore, small-medium scale CHP systems are typically driven by ICEs (CHP-ICE) coupled with a generator for electricity production. In such systems, more than 55% of the fuel energy is rejected as heat to the cooling jacket water circuit of the engine and the exhaust gas stream. Unless the available thermal output is used for heating (or other processes), it is released to the atmosphere as waste heat, reducing the system efficiency. Depending on the application, the demand for heat may vary during the year: in the building sector, where demand for heat is dependent on the weather conditions, the utilisation of the thermal output of the CHP-ICE in periods of warm weather is of key importance, because it can negatively affect the system efficiency. Additionally, in electricity intensive buildings, such as supermarkets, where the CHP-ICE units sizing is mainly driven by the demand for electricity, the thermal output of the CHP-ICE may well exceed the heating load onsite, having an adverse effect on the overall system efficiency.

Alternatively, heat-engine technologies can be used to recover the thermal surplus, and generate additional power. Various candidate technologies are available, such as Kalina cycles [11], organic Rankine cycle (ORC) engines [12] or technologies at earlier development stages, such as thermoacoustic (TAE) generators [13] or thermofluidic oscilators [14]. Markides [15] compared the efficiency of various heat-engines over a range of heat-source conditions (Fig. 2) and reports that ORC engines can achieve thermal efficiencies of 8-25% with heat-source temperature of approximately 80-400 °C. Moving beyond this temperature range, steam Rankine cycle and Stirling engines become the dominant technologies.

ORC engines are a promising candidate for utilising heat to generate additional power in CHP applications, because they are comprised of technologically mature components, and they are relatively simple in operation, with low maintenance requirements. ORC systems are suitable for distributed generation, in a range of capacities, while they are versatile, able to operate with a range of renewable heat sources, such as geothermal or solar energy, as well as waste heat [16,17]. The coupling of ORC engines, as bottoming cycles to CHP-ICE to recover heat, results in an increase of the system's power-to-heat ratio (the ratio of the demand for electricity, over the demand for heat onsite), matching the demand side power-to-heat ratio to that of the supply. Consequently, the ICE-ORC CHP system operation can be decoupled from the heating demand of the building, maximising its efficiency and energy savings, in periods when traditionally the CHP-ICE heat output would be wasted.

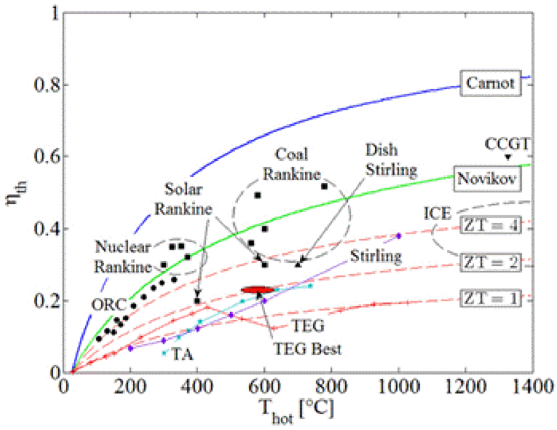

Fig. 2: Comparison of thermodynamic heat-engines for power generation, over a range of different heat-source temperatures, with a fixed heat-sink temperature of 25 °C [15]. The blue line represents the Carnot efficiency (maximum thermodynamic limit), the green line represents the Novikov efficiency (as obtained from endoreversible analysis), and the red dashed lines represent the theoretical efficiency of thermoelectric generators (TEG) with different thermoelectric figure-of-merits (ZT = 1,2,4).

1.1.2 Organic Rankine cycle systems

The development of organic Rankine cycle (ORC) systems spreads over two centuries, from the early 19th century when the first ORC engines were developed, to becoming a niche market to-date in the 21st century. In the early 19th century, major developments and innovation were performed in the steam reciprocating engines. The ORC engines were developed to recover heat from the condenser of steam cycles, which due to inadequate sealing technology, could not maintain vacuum conditions, resulting in high condensation temperatures and power loss. Organic fluids with lower evaporation temperature were then suggested for recovering the waste heat. However, improvements in the design of steam engines, along with the emergence of steam turbines, curtailed further developments in cycles with non-aqueous/organic fluids [18]. In the 20th century, the University of Naples were the first to deploy organic fluids in turbines, reviving the concept of ORC engines. The National Physical Laboratory of Israel followed, while the Italian activity in the field of ORCs started in the 1970s at the Technical University of Milano [19]. These efforts have lead to the foundation of Ormat [20] and Turboden [21], who are the biggest players in the ORC market to-date operating 65% and 13% of the worldwide installed capacity.

ORC systems are comprised of four key components: i) the evaporator heat exchanger, where heat is added to the cycle; ii) the expander device, where work in generated; iii) the condenser heat exchanger, where heat is rejected to the cooling circuit; and iv) the pump that maintains the circulation of the working fluid within the engine (Fig. 3). The simple ORC architecture illustrated in Fig. 3 can be adapted and optimised, depending on the operating conditions, and the application specific requirements. Alternative cycle architectures have been examined in the literature (recuperative, supercritical, transcritical cycles, partial evaporation, etc.) along with alternative fluids (pure compounds or mixtures), with various heat sources, covering low to high grade renewable or waste heat.

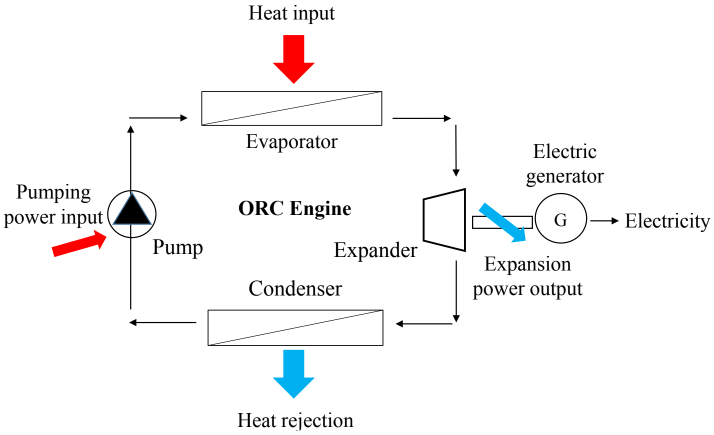

Fig. 3: Simplified typical non-recuperative organic Rankine cycle engine schematic.

Several studies can be found in the literature investigating the ORC thermodynamic performance, aiming to identify the optimum thermodynamic operating points or working fluids of the cycle, for different applications, including, among others, solar driven ORCs, geothermal plants and waste heat recovery. A common characteristic of these efforts is that they assume fixed heat-source conditions entering the ORC engine, when optimising the system performance. However, ORC engines in real installations will experience a time-varying heat-source stream. In the particular case of combined heat and power (CHP) systems, where ORC engines operate as bottoming cycles to internal combustion engines (ICEs), recovering heat from the exhaust gases, while the CHP-ICE moves to part-load operation, the ORC engine will experience a time-varying heat-source stream, in terms of temperature and mass flow rate. To maximise the ORC engine running hours, the ORC system should operate with high efficiency not only at the design conditions, but also during off-design operation. Adding to this, in ICE-ORC CHP systems, the two engines interact within the integrated system. Thus, there are performance trade-offs to be considered when optimising the complete system. These aspects require the development of integrated tools, where the interactions of the various system components are captured, in order to obtain the new adjusted optimum operating points of the system, at design and off-design conditions.

While thermodynamic optimisation and technical feasibility are at the core of the development of ORC systems, critical factor for their wider deployment is their capital expenditure (CAPEX), and operating and maintenance (O&M) costs. There is only limited literature publicly available on actual ORC system costs. In the absence of actual project cost data, to obtain credible estimates of the ORC investment cost, the correct sizing and costing of the main ORC system components is of paramount importance. These estimates form the basis of the cost calculations to be undertaken, when evaluating the financial viability of ORC systems' deployment, performing the so-called thermoeconomic evaluation. Finally, not a single ORC system design is the best performing across all applications or heat sources. Nevertheless, the numerous types of system components available, i.e. heat exchangers, expander devices, and pumps, or candidate working fluids, make the design solutions space very broad. Therefore, optimisation tools are required, where the type of components, size, geometry and cost are optimised, along with the thermodynamic performance of the system.

1.2 Aim and objectives

Despite the potential of organic Rankine cycle (ORC) engines in achieving high-efficiency combined heat and power (CHP) systems, there are still significant challenges to be addressed, to facilitate their wider adoption in the market, and in particular in high-temperature applications, such as the coupling with internal combustion engines (ICEs). In this context, the aim of this thesis is to develop modelling and analysis for the systematic optimisation of advanced ICE-ORC CHP systems from an integrated perspective, considering not only the thermodynamic design, but also the operating and cost aspects of these systems. To achieve the main goal of this research, the following objectives have been defined:

- To develop an integrated optimisation tool of ICE-ORC CHP systems capable of capturing the performance trade-offs between the two engines, and identify the designs that optimise the complete system performance;
- To maximise the efficiency of ORC systems by evaluating the performance of: i) alternative heat exchanger typologies and identify cost-effective designs that achieve high heat transfer coefficients, with low pressure drop, which are also capable of operating at high temperature/pressure levels, without deteriorating their performance; and ii) alternative expander machines for medium-scale power generation, suitable for operating at high pressure ratios and relatively low working fluid flow rates with high isentropic efficiency;
- To predict and optimise the off-design operation of ORC engines, under real variable heat-source conditions. Overcoming the latter challenge will allow the ORC engines to adjust their operation at off-design conditions, maximising the system running hours, and thus improving their financial viability and penetration to the market;

- To identify working fluids suitable for the temperature and pressure conditions experienced in an ICE-ORC recovering heat from high-temperature exhaust gases, while they have good thermodynamic properties, low global warming potential, are safe, abundant and cost-effective;
- To develop a systematic ORC engine design optimisation framework, which will be able to screen alternative components type, size and configurations, capturing the technical, but also cost aspects of ORC engines design.

1.3 Thesis structure

There is great potential in reducing energy consumption and emissions, by deploying distributed combined heat and power generation (CHP) systems, with organic Rankine cycle (ORC) engines. In spite of the benefits of adopting ORC engines as bottoming cycles to internal combustion engines (ICEs), there still remain a number of challenges that have to be addressed to promote their wider penetration in the market: i) integrated optimisation tools of ICE-ORC CHP systems are required, capable of capturing the performance trade-offs between the two engines, to obtain designs that optimise the complete system performance; ii) having means to predict and optimise the off-design operation of the system is critical for maximising the ORC engine running hours, and improve its financial proposition; and iii) considering the cost aspects of the system when designing ORC engines for CHP applications, is of paramount importance, to promote the wider adoption of this technology. These tools will assist with identifying optimised designs, not only from a thermodynamic perspective, but also considering the operating and financial aspects of the system.

This research aims to be a contribution in tackling these challenges by adopting a multi-angle approach towards the design of high-efficiency ICE-ORC CHP systems. To achieve this, the thesis has been structured as follows: Chapter 2 provides the background on CHP systems design with ORC engines. The various system components and candidate working fluids are discussed. The previous efforts on off-design optimisation of ORC engines are reviewed. The challenges in obtaining credible cost estimates of the various ORC engine configurations are also presented.

In Chapter 3, the modelling methodology deployed throughout this thesis is presented, along with the assumptions, and limitations of each modelling approach. First, the dynamic ICE model developed is presented, followed by the ORC engine steady-state thermodynamic model. The second law analysis for both systems investigated follows. Next, the heat exchangers and expanders models are presented. The importance of selecting suitable working fluids for high-temperature applications is then highlighted. A discussion on the economic analysis and financial profitability indicators used to assess the ORC systems follows.

In Chapter 4, the integrated ICE-ORC CHP optimisation tool developed in this PhD is presented. This work goes beyond other efforts in the literature in that the ICE and ORC interactions, and performance trade-offs are captured, within an integrated optimisation framework. This holistic approach allows us to identify, among other, the optimum ICE valve timing, lift and ignition timing, along with, among other, the optimum ORC operating conditions and working fluids, so that together the two engines have the optimum power output or the minimum specific fuel consumption. The tool is applied on two ICE-ORC CHP systems with i) natural aspirated, and ii) turbocharged ICEs, at different scales. The results of the optimised complete power output and minimum specific fuel consumption are presented. A comparison is then performed between the proposed integrated optimisation approach, and the conventional approach, where the two engines are treated independently.

In Chapter 5, the ORC engine off-design optimisation tool developed in this PhD is presented. Unlike other efforts in the literature, where the actual time-varying characteristics of the components are not considered, the proposed off-design optimisation tool explicitly captures the time-varying performance of the main ORC components in defining operation at part-load. The tool considers closely the interactions and performance trade-offs between the ORC engine key components, to obtain the new adjusted off-design operating points, and generates off-design performance maps. The CHP-ICE part-load conditions are obtained first, and used as input to the off-design ORC model. The off-design optimisation results for ORC engines with piston and screw expanders are then presented, considering different heat exchanger architectures. A comparison is also performed between: i) assuming fixed expander performance at off-design conditions; and ii) considering the complete evaporator and expander performance interactions.

In Chapter 6, the systematic ORC engine components selection, sizing and costing framework developed in this PhD is presented. This work differs from previous efforts, in that the heat exchanger typology, expansion stages, and components' sizing, are simultaneously optimised with the complete ORC system design for maximum power output or/and minimum specific investment cost, instead of forming a designer's predefined input. This allows the simultaneous selection of the best performing system configuration and size, given the application specific constraints, since the optimiser screens alternative components typologies, configurations and sizes to identify the best-performing design. Cost functions developed in this work are presented, and compared to other cost correlations in the literature. The single-objective and multi-objective optimisation results for ORC engines with different expander and heat exchanger typologies are then discussed. Insights on the design of ORC engines, with respect to different project key performance indicators are offered.

The thesis is concluded with a summary of the major findings and outcomes, and recommendations for future work in Chapter 7.

Chapter 2

Background

"Over the next decade, we must prepare for the future. The 2020s will require a change of gear. Technologies that are being demonstrated or deployed on a small scale now will need to move towards mass deployment."

- The Carbon Plan: Delivering our low carbon future 2011

2.1 Combined heat and power systems

There has been a growing interest in improving energy efficiency in recent years, aiming to reduce fossil-fuel consumption and our impact on the environment. In the EU, ambitious decarbonisation targets have been set, aiming to reduce the greenhouse gas emissions to 85-95% of the 1990 levels, by 2050 [22]. The greatest potential for decarbonisation has been identified in the power generation and distribution sector, while also in the building sector and the industry [23]. The latter would be achieved via decarbonising the heating and cooling provision, through the use of clean electricity or renewable sources of energy, whilst more efficient energy technologies are expected to be installed in the industry.

In this context, the distributed combined generation of heat and power from a single system (i.e. with a single energy input) has been receiving particular attention, due to the advantages these systems offer over the centralised generation and separate provision of these two vectors [15,24,25]. The benefits of distributed combined heat and power (CHP) systems include: i) lower distribution losses, since they are installed closer to the demand; ii) higher overall system efficiency than systems that generate heat and power separately, because the former can use low-medium grade waste heat to improve their thermodynamic efficiency, resulting in reduced primary energy consumption, less carbon emissions and lower operational costs; iii) they can be coupled with renewable sources of energy on-site to improve further the system efficiency and reduce emissions. CHP systems can achieve overall efficiencies that exceed 90% [9,26]. However, key for maximising their efficiency is the effective utilisation of both electric and thermal outputs.

In small-medium scale distributed power generation applications (at scales ranging from a few kWs to a couple of MWs), natural gas internal combustion engines (ICE) are widely used (CHP-ICE), due to their maturity, good performance at various loading conditions, reliability and low maintenance requiremets [27]. Nevertheless, more than 55% of the fuel energy is rejected as heat in the exhaust-gas stream and the cooling water circuit of the engine (jacket water circuit). By selecting an appropriate energy conversion technology, the thermal output of the engine (which would otherwise be wasted to the atmosphere) can be used to; i) cover the heating or cooling demand of buildings; or ii) provide heat input to industrial processes; or iii) generate additional power, via a heat-to-power conversion technology, maximising the overall CHP-ICE efficiency, and reducing the overall system emissions.

Organic Rankine cycle (ORC) technology is a promising heat-to-power energy conversion technology, suitable for recovering heat at temperatures of 400-500 °C, and at scales from the order of kWs to tens of MWs [15,28]. ORC operates using the traditional steam Rankine cycle for power generation, but organic compounds are used as working fluids instead of steam. Organic fluids have lower evaporation temperatures than water at the same pressure, and are capable of operating across higher pressure ratios (PRs) across the same temperatures differences. This allows ORC engines to generate power efficiently at lower heat source temperatures, than those available in large-scale fossil-fuel power plants, making them a highly suitable technology for the recovery and conversion of waste heat in distributed generation applications [29].

In Fig. 4, typical *T-s* diagrams of alternative ORCs are presented. A subcritical non-recuperative ORC system is presented in Fig. 4a; a subcritical recuperative system in Fig. 4b; a subcritical system with mixtures in Fig. 4c; and a partial evaporation system in Fig. 4d. Other ORC architectures are also available in the literature, covering transcritical cycles [30,31], and supercritical cycles [32,33].

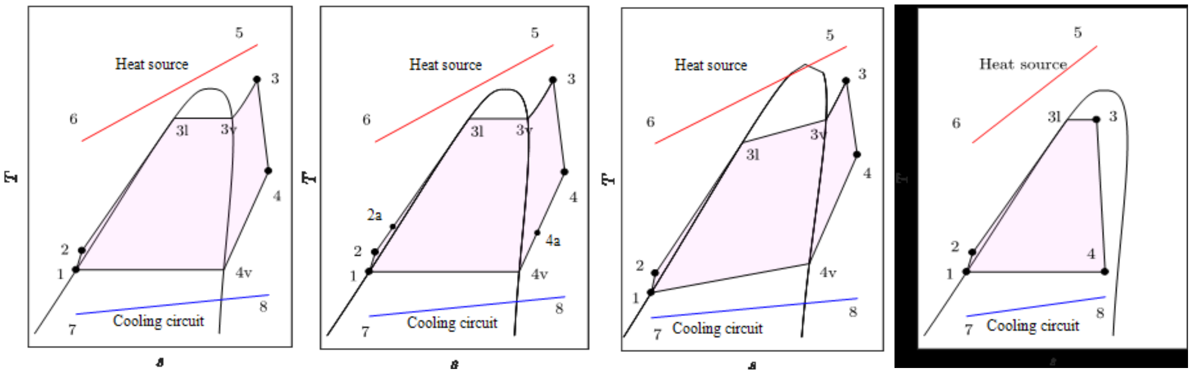

(a) (b) (c) (d)

Fig. 4: Simplified schematic *T-s* diagrams of ORC for: a) subcritical non-recuperative cycle, b) subcritical recuperative cycle, c) subcritical non-recuperative cycle with mixtures, and c) partial evaporation cycle.

In Fig. 5 the schematic of a bottoming ORC engine recovering heat from the exhaust gases of a CHP-ICE is illustrated. Several studies can be found in the literature investigating the ORC thermodynamic performance, while recovering waste heat from ICEs. Song et al. [34] examined ORC engines recovering heat from the exhaust-gas stream of an ICE. In their work, they report an increase of 6% on the combined system electrical efficiency compared to the ICE standalone operation. However, the authors assumed fixed operation of the ICE, in isolation of the ORC engine, and optimised only the ORC engine design. Similarly, Zhang et al. [35] optimised the design of a bottoming ORC engine, without accounting for the impact of the bottoming ORC engine, on the ICE operation. In their work, the ORC engines achieved thermal efficiency of 13.5-17%. Yu et al. [36] investigated the coupling of ORC engines to ICE, at different ICE part-load (PL) condition, and reported an increase of the combined system electrical efficiency of 5-6% in comparison to the standalone ICE. Similarly to the previous studies, the impact of the ORC engine on the ICE operation was not considered.

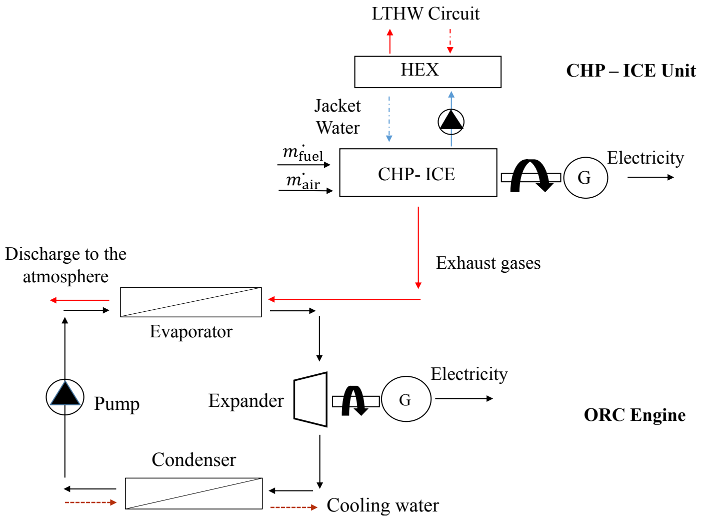

Fig. 5: Simplified schematic of an integrated ICE-ORC CHP system, with a bottoming ORC engine, recovering heat from the exhaust gases of an ICE.

However, in real ICE-ORC CHP applications, the operation of the ICE affects not only its own performance but also the condition of the exhaust gases that exit the engine (in terms of temperature, pressure and mass flow rate). The exhaust-gas stream conditions, in turn, influence the size and operation of the bottoming ORC engine that recovers heat from the ICE, while the introduction of the heat recovery heat exchanger (i.e. the ORC evaporator) will also affect the operation of the ICE. Therefore, the overall performance of integrated ICE-ORC CHP systems can only be optimised, by accounting for the interactions and performance trade-offs between the ICE and the ORC engines, as part of a single system design and operation.

Within the available literature on ICEs waste heat recovery with ORC engines, only limited efforts have adopted an integrated optimisation approach, where the interactions of the ORC and ICE engines are considered. Zhao et al. [37] investigated the control strategy of an ICE-ORC system under varying ICE load conditions. However, the authors assumed fixed ICE valve operation and size, along with fixed ignition timing. These parameters were used as an input to their model, instead of being part of the output of the optimisation procedure, which would maximise the complete ICE-ORC CHP performance. Yue et al. [38] investigated the performance of a bottoming ORC to an ICE, considering the impact of the ORC engine on the ICE operation, an issue which is often neglected in the literature. However, the ICE model developed was not dynamic, and the authors did not optimise the operation of the ORC engine together with the ICE. The operating pressures in both the evaporator and the condenser of the ORC engine were assumed fixed, along with a fixed working fluid. Xu et al. [39] studied the operation of an ORC engine in vehicle applications, while recovering heat from the ICE exhaust gases. The focus of this work was the response of the ICE-ORC system to the vehicle speed changes. Although the ICE-ORC system was treated as one complete system, owing to the nature of this application, the ICE operation was dictated by the vehicle operation (driving cycle). This application is different to the stationary CHP systems, where the ICE operating conditions can be adjusted/optimised by the manufacturer or the plant operator, to either maximise power generation or minimise fuel consumption.

These findings highlight that there is a lack of studies in the literature that consider the ORC thermodynamic cycle design, simultaneously with the ICE operating point, to yield the highest power output or fuel efficiency of the complete system. By not accounting for the interactions of the two engines can lead to sub-optimal CHP systems, since the two engines are not specifically designed to operate together as an integrated system, to give the best performance.

2.2 Organic Rankine cycle engine design

2.2.1 Heat exchanger

The design of the heat exchangers (HEXs) of ORC systems is of paramount importance, since they are responsible for 30-70% of the engine cost, while the evaporator HEX in particular is responsible for the highest percentage of exergy destruction within the engine [40]. However, there are trade-offs to consider when designing HEXs. Maximising the thermodynamic performance of the unit (maximum effectiveness) and achieving higher performance, have adverse effects on the size and the cost of the HEX, which may increase significantly. Therefore the selection of the correct HEX type and size is of paramount importance.

There is a variety of HEXs studied in the ORC literature, depending on the operating conditions and the size of the plant. Shell-and-tube HEXs are most commonly used in large-scale plants for industrial processes, because they can operate in a wide range of temperatures and pressures. They are flexible in terms of the materials used, and there are many industry standards and guidelines available for the design of such systems [41]. Shell-and-tube HEXs can be found in the ORC field in high capacity or power plant level systems, such as in geothermal and solar power plants, but also in large scale biomass combustion and waste heat recovery applications [42]. There is a number of different architectures of shell-and-tube HEXs, with the most commonly used being: i) the fixed tube plate; ii) U-tube type; and iii) the floating head. The fixed tube plate type is the simplest in construction, however they require additional expansion bellows to withstand large temperature differences and pressures. The U-type cost is at a similar level to that of the fixed tube type, while they offer the advantages of easier cleaning and operation at high temperatures. However, the bundle construction does not provide a pure counter flow heat exchange, resulting in lower heat exchanger effectiveness. The floating head type is used when the working mediums operate at extreme pressure and temperature regimes, nevertheless the latter HEXs are more expensive than the former architectures [43].

Double-pipe heat exchangers (DPHEX) key advantage is that they provide a pure counter-flow heat transfer regime, which increases the heat exchanger effectiveness for given flow conditions, while they can operate with a great variety of working fluids. They are simple in construction, suitable for high pressure applications and have a lower cost per m^2 of heat transfer area than other HEX typologies [43]. These features make them strong candidates for ORC engine applications, where high pressures in the system increase power output and improve their economic proposition. Their main drawback is the high heat transfer area requirements per kW of heat transferred, especially when these are compared to plate-frame designs (PHEXs). DPHEXs can be finned to enhance their heat transfer rate, but the construction cost per m^2 increases.

PHEXs are available in a wide range of designs, and materials depending on the application. The plates are corrugated to improve rigidity and heat transfer, but at the expense of higher pressure drop. The variety in plate corrugation patterns allows the PHEX design to be versatile and adjustable to a range of different operating conditions, and performance requirements. There are two main corrugation patterns: i) intermating corrugations that run across the plate at right angles; and ii) chevron corrugations, which are inclined at an angle φ to the direction of flow, while several groups of parallel chevrons can be provided, each at different angle. In Fig. 6, an example of a chevron type plate is presented.

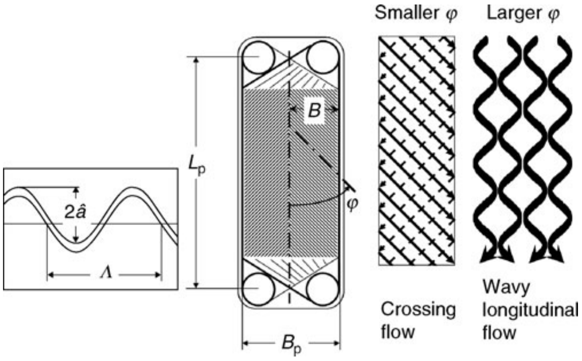

Fig. 6: Chevron-type plate, with inclination angle (φ) and the two-flow patterns illustrated. Figure reproduced from Ref. [44].

One of the main advantages of PHEXs is that they are more compact than shell-and-tube HEXs for the same duty, having only half or up to a third of the space requirements (volume) per kW of heat transferred of the latter [41,43]. The plates design and the narrow passages developed result in high *U*-values, enhancing the heat transfer rate. Their compactness makes them a good candidate HEX design for ORC engines, where space availability inside the unit may be of a premium. The key disadvantage of gasketed PHEXs is limitations in operating temperature and pressure levels, which will affect the integrity of the seals (of typical pressed plate fabrication). Welded PHEXs, made of galvanised steel or stainless steel can be used for higher duties, to withstand high pressure and temperature levels, resulting however in higher costs, in terms of GBP/m^2 of heat transfer area.

Looking at the ORC literature, Refs. [45,46] investigated the use of DPHEXs for low-temperature ORC engines in geothermal applications, from a thermoeconomic perspective. Ramos et al. [47] evaluated the use of DPHEX designs in low and high temperature solar driven ORC engines. The performance of PHEXs in the ORC engine evaporator and condenser units has been investigated in Refs. [17,48–50], while Ref. [8] used PHEX in the evaporator, and tube-and-fin design for the condenser. Walraven et al. [51] compared the performance of PHEXs to shell-and-tube configuration, for low temperature ORCs and reported that the former outperform the latter. Daccord [52] evaluated the use of PHEXs for the evaporator of an ORC engine and of tube-and-fin for the condenser, in automotive waste heat recovery applications. Finally, Zhang et al. [53] performed a thermoeconomic evaluation of low temperature ORCs, investigating alternative HEXs configurations, covering PHEXs, shell-and-tube and finned-tube designs. Results indicated that using finned-tube HEX and shell-and-tube have lower electricity production cost (EPC) than the other configurations (EPC is defined as the ratio of the capital recovery factor multiplied by the ORC engine investment cost, over the energy generated.)

Many efforts are also available in the literature aiming to identify the heat transfer coefficient (HTC) correlations that can reliably predict the performance of HEXs. Garcia et al. [54] compared alternative Nusselt number correlations for predicting the evaporation and condensing phenomena in tubes, while in Ref. [55] a similar comparison for predicting the two-phase flow heat transfer phenomena in PHEXs is presented. Finally, other efforts in the literature focused on proposing new HTC correlations specific to the new low global warming potential (GWP) and low ozone depletion potential (ODP) working fluids, such as R1234yf and R1234ze with a particular focus on PHEXs designs [55,56].

2.2.2 Expander

The expander is a key component of the ORC engines, impacting the system efficiency and cost. Depending on the application, the power output of the system, the pressure/volume ratio (VR) of the cycle, and the working fluid selected, the most suitable type of expander may vary significantly. Expanders can be classified into two major categories: velocity type devices, such as axial or radial turbines; and volumetric type devices, such as screw, reciprocating piston and scroll expanders (Fig. 7). Turbomachinery is typically used for power outputs exceeding 100 kW up to a few MWs, whilst volumetric expanders are selected for power outputs below 100 kW [42]. Generally, in the ORC field, at capacities < 100 kW volumetric machines are mainly deployed, due to the low working fluid flow rate, high expansion ratios, the expanders' low rotational speed, and their tolerance to two-phase expansion of the working fluid [57].

Expanders is one of the most well investigated component in the ORC literature, with a variety of technologies being examined. Looking at the scientific literature, the most well documented types of expander machines in ORC applications are the scroll type and the turbine machines, followed by screw and rotary expanders [58]. On the contrary, there is only limited literature on the use of reciprocating piston expanders, especially in stationary applications. Looking at the industry, turbine expanders can be found in many medium-large scale commercial ORC engines, such as those manufactured by Turboden [21], Triogen [59], Cryostar [60], and Ormat [20], while ORC engines with screw expanders are commercially available by Electratherm [61] and BEP Europe [62].

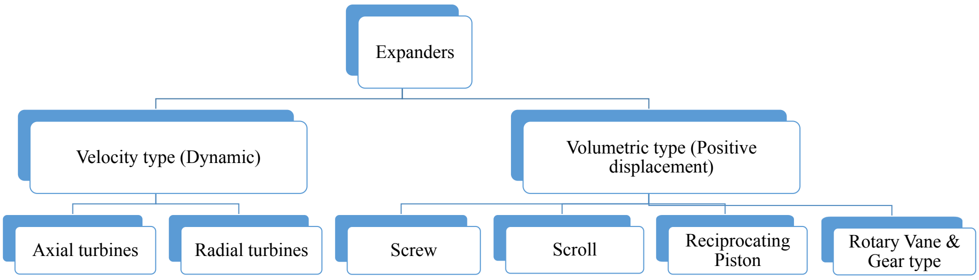

Fig. 7: Overview of expander type classification in ORC engines.

2.2.2.1 Velocity type machines

Because of the differences in thermophysical properties of steam and organic fluids, turbine expanders used in ORC applications have some specific design characteristics: i) organic fluids have higher molar masses, resulting in lower sound velocities, so the turbines design should ensure that no supersonic flow occurs downstream of the nozzles, to reduce additional shock wave losses [63]; ii) the positive slope of the saturated vapour curve, ensures that the working fluid exits the turbine while still in the dry vapour zone, reducing the blades cavitation risk; iii) in relatively low power outputs (<100 kW) turbines size reduces significantly, but their rotational speeds increase exponentially [64], therefore, magnetic bearings and a fast generator coupled with the turbine are required to correct the current frequency [65]; and iv) some of the candidate organic fluids are flammable, or toxic, or expensive, requiring extra attention on minimising leakages to the environment.

There are two major categories of turbines, namely axial type and radial type. The former are normally used for systems with high mass flow rates but low PRs, whereas the latter are suitable for application with low mass flow rates and high PRs. A key advantage of radial turbines is that they are easier to manufacture than the axial ones and they can operate under variable conditions, while maintaining high efficiency. This is achieved via the use of variable inlet guide vanes or variable rotor speed. Example of comparing those two strategies in a ORC engine at off-design operation can be found in Ref. [66]. The isentropic efficiency of radial turbines reported in the literature based on experimental studies, varies between 48-80%. When power output exceeds 500 kW, axial turbines are the most common choice in the ORC field. Such ORC engines have been developed and commercialised by Ormat [20] and Turboden [21]. For smaller sizes, the efficiency of axial turbines decreases significantly, because of the small blades, or the requirements for partial admission. Therefore, radial turbines are deployed in smaller scales, with some units produced by Atlas Copco [67] and GE Calnetix [68].

2.2.2.2 Volumetric machines

A detailed classification of the various volumetric expansion machines is presented in Fig. 8, based on the type of motion of the rotors [69].

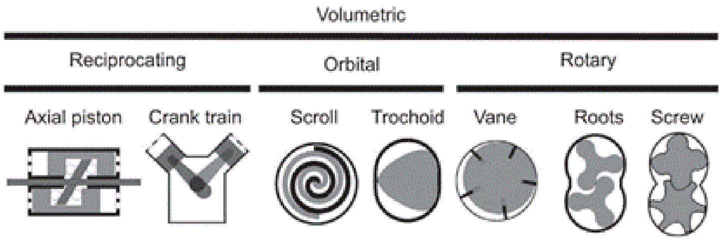

Fig. 8: Volumetric expanders' classification. Reproduced from Ref. [69].

Scroll expanders

Scroll expanders are a mature technology originating from the air-conditioning industry and the vapour compressor machines, and, thus, they can benefit from economies of scale. They do not suffer from the cavitation problems of turbines when operating with two-phase flows, they are reliable, due to the low number of moving parts, and have low maintenance requirements. One of the key drawbacks of this technology is their low VRs and as a result their low efficiency at high VR/PRs. This attribute restricts the maximum ORC operating pressure levels, and thus power output, in particular for fluids that have high critical temperature/pressure [42]. Adding to this, scroll machines cannot operate at high temperatures, because this results in high thermal expansion, increasing their leakage losses [69]. The greatest challenge when converting scroll compressors into expanders is the development of an efficient bearing lubrication system of suitable mating spiral components, and removing the check valves from the compressor casing [64].

Scroll compressors, in the heating ventilation and air-conditioning (HVAC) industry, have typical built-in VRs between 1.5 to 3.5, while scroll expanders have built-in VRs up to 5, achieving isentropic efficiency in the range of 35-80% [57,64]. The majority of scroll expanders currently used in the ORC industry are modified scroll compressors originating from: i) the HVAC industry; or ii) from automotive semi-hermetic compressors; or iii) open-drive automotive air-conditioning (A/C) scroll compressors; or iv) open-drive scroll air compressors. Air Squared [70] have developed a number of semi-hermetic scroll expanders for low grade heat recovery, at 1 kW, 5 kW and 10 kW.

Reciprocating piston expanders

The design of reciprocating piston expanders for ORC engines, originates from a range of industries, including the automotive, and energy one. In Fig. 9, a schematic diagram of the basic principle of operation of a simple piston expander is presented. Reciprocating piston expanders require careful timing of the inlet and exhaust valves operation. They can also suffer from significant friction losses, due to the relatively large number of moving parts. However, they present a number of advantages over other available volumetric expansion machines, including: i) large built-in VRs (values up to 15) at relatively small flow rates; ii) high operating pressures and temperatures; iii) ability to operate efficiently at various off-design operating points and rotational speeds; iv) their manufacturing maturity; and v) they can tolerate wet expansion conditions [69,71]. Also, by optimising the valve timing the expander performance can be further improved.

Despite their advantages, by reviewing the literature, it is revealed that there are only limited studies that have investigated the use of piston expanders in ORC engines, with those being mainly limited to waste heat recovery from ICEs on road-vehicle applications. Shonda et al. [72] performed experimental and semi-empirical modelling of piston expanders in ORC engines for passenger-vehicle applications, and reported isentropic efficiency of up to 70% (excluding mechanical losses) and volumetric efficiency of up to 60%. Daccord [52] investigated the application of ORC engines with swash-plate piston expanders for heavy commercial vehicles applications. The experimental investigation indicated that the expander reached 70% isentropic efficiency and 60% effective isentropic efficiency (including mechanical losses on the shaft), for operating PRs between 13 and 22. These results are in line with those reported in the literature about high performance of piston expanders at high PRs. Clemente et al. [73] also compared the operation of piston expanders to scroll machines. Results indicated that for large PRs the former outperform the latter. Dumont et al. [74] compared experimentally the performance of piston, scroll and screw expanders across a range of PRs. In their results, for PRs between 2 and 6, the scroll machines achieved effective isentropic efficiencies of up to 76-80%, while the screw machines achieved up to 55%. For PRs higher than 7, piston expanders achieved effective isentropic efficiencies of up to 55%, while the efficiency of scroll machines deteriorated up to 30%. Finally, Oudkerk et al. [71] experimentally tested a swashplate reciprocating-piston expander and showed that its isentropic efficiency can reach 74%.

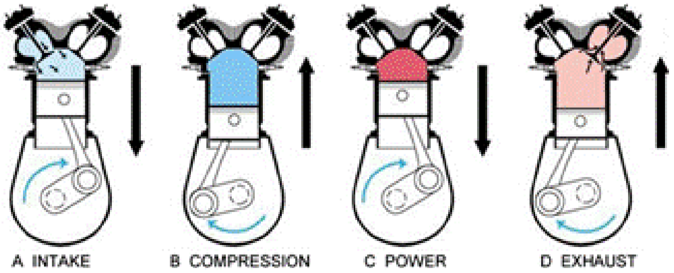

Fig. 9: Schematic diagram of a reciprocating piston expander operating principle. Reproduced from Ref. [75].

Screw expanders

Typically, screw expanders are reversed screw compressors and capable of dry gas or wet expansion (subject to specific design considerations). Unlike turbines, smaller size screw expanders for low power output do not suffer from significant efficiency reduction, with twin-screw expanders being able to operate with isentropic efficiency close to 90% [57] (excluding mechanical losses). Although screw expanders for low power output (<10 kW) are not available on the market, there is increasing availability of alternative screw expander machines for higher power outputs (30-60 kW), with a strong focus on ORC applications [57]. There are two companies offering screw expanders on the market, Heliex Power [76] for heat recovery from high pressure steam and Electratherm [61] for small-medium scale ORC waste heat recovery applications (30-110 kW).

Screw expanders have high durability, are low noise and low vibration units and have compact configuration [77]. They are suitable for a range of working fluids, such as high pressure gas, superheated or saturated steam, two-phase flows and hot liquids. The key advantages of screw expanders over turbomachinery include: i) lower rotational speeds, easing the coupling with electric generators; ii) lower manufacturing cost; iii) they offer the possibility to adjust the machine VR, to maximise the system efficiency at off-design operation; and iv) they can handle wet expansion conditions, which allows the consideration of cycles, such as trilateral ORC technically feasible [65]. However, the main disadvantage of screw expanders is their small internal VR which usually ranges between 3 and 7 [69], values which are a way lower than those generally adopted in commercial ORC engines, while these are also lower than those achievable by other volumetric expanders, such as piston expander devices.

Screw expanders have been experimentally tested for ORC engines recovering heat from a vehicle ICE, with finned-tube evaporator and R245fa [77]. In Ref. [77] the screw expander nominal design point was selected based on the highest expansion ratio of the screw expander, with 0.65 isentropic efficiency, and the ORC pressure level was then assumed fixed. A single screw expander was designed and tested by Biao et al. [78]. The maximum isentropic efficiency obtained was 85% and the shaft effective efficiency was approximately 0.55, for expansion ratios of 7-9. The built in VR was 4.86. Ref. [79] tested a screw expander for R245fa and SES36 and recorded isentropic efficiencies of up to 65% for expansion ratio of 9-10 and filling factor at approximately 1.

Finally, a comparison of the various expander machines available for ORC applications is presented in Table 1.

2.2.3 Pump

The most commonly used pump technologies in ORC systems are: i) reciprocating; ii) rotary; and iii) centrifugal devices [58]. For low PRs and flow rates, the rotary type is commonly used, while for medium to high mass flow rates and high PRs the centrifugal units dominate. Reciprocating pumps are the most versatile being able to operate in a wide range of PRs, even for low mass flow rates (Fig. 10). In terms of pump efficiency, for power requirements exceeding 1 kW, the centrifugal pumps can operate with efficiency of up to 70%, while the reciprocating pumps achieve significantly lower efficiencies of approximately 40% for a wide range of pump power.

Table 1: Comparison of expander devices for ORC applications.

Expander type	Capacity range (kW_{el})	Pressure ratio	Cost	Advantages	Disadvantages
Turbines	100 kW to few MWs	Medium - High	High	1. High efficiency 2. ORC turbines are more compact than those for steam 3. Radial type are suitable for high pressure ratios low mass flow rates 4. Axial type have high efficiency for large scale power generation	1. Low efficiency at small capacities and off-design operation 2. Axial turbines efficient at low pressure ratios only 3. Turbines' rotational speed increases exponentially with the power output reduction 4. Tight manufacturing tolerances
Scroll	1-10 kW	Low	Low	1. High efficiency at low volume / pressure ratios 2. Compact and low vibration 3. Lightweight 4. Mature technology 5. Handling two-phase flows	1. Low volume / pressure ratios 2. Significant lubrication requirements 3. Cannot tolerate high temperatures, due to thermal expansion issues 4. Under / over expansion losses, especially when deviating from design point 5. Complex geometry
Screw	20-30 kW	Low-Medium	Medium	1. High efficiency at design and off-design operation 2. Handling of two-phase flows 3.Compact and low vibration	1. Low volume/pressure ratios 2. Significant lubrication requirements 3. Challenging manufacturing process 4. Efficiency deterioration when deviating from built-in volume ratio and design pressure ratios
Reciprocating piston	10-150 kW	Medium-High	Medium	1. High efficiency at high pressure/volume ratios 2. High efficiency at design and off-design operation 3. Mature versatile technology 4. High operating temperature / pressure 5. Handling of two-phase flows	1. Requires optimisation of the valve timing 2. Losses due to moving parts 3. Heavy - weight

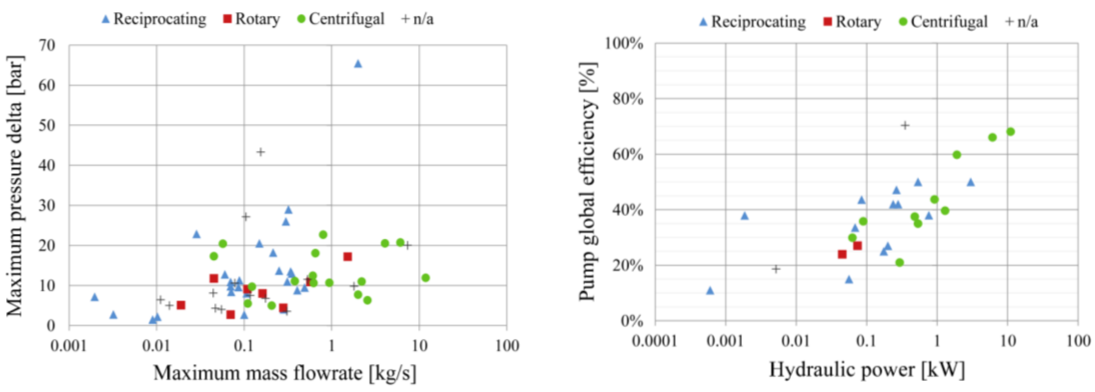

(a) (b)

Fig. 10: ORC pumps performance maps: a) operating mass flow rates and head, and b) pump efficiency [58].

2.2.4 Working fluid

The selection of suitable working fluids for ORC engines has significant impact on the efficiency, selection, design and sizing of the system individual components, and on the economics of the plant. Based on increasing concerns over global warming, certain fluids such as chlorofluorocarbons (CFCs) and hydrofluorocarbons (HFCs) have been already phased out, or are set to be phased out over the next decade. According to the Montreal Protocol [80], the use of substances with high ODP such as CFCs, has been banned since 2010. These substances include well established refrigerants in the HVAC industry, such as R11, R12, R13, R113, R114 and R115. Additionally, the use of Hydro-chlorofluorocarbons (HCFCs) will be banned by 2020, due to their high ODP, mainly because of their chlorine content [81]. This family of compounds includes refrigerants such as R21, R22, R123, R124, R141b and R142.

The Kyoto Protocol [82] and subsequent regulations around the globe, such as the F-gas regulation in the EU [83], restrict the use of compounds, which apart from high ODP have also high GWP. The new F-gas Regulation 2015 [83] has replaced the former F-gas Regulation issued in 2006 and is enforced from the 1st of January 2015 [84]. In line with the F-gas Regulation, the EU has committed to cutting the F-gas emissions by two-thirds, in comparison to the 2014 levels, by 2030. The regulations include restrictions and phase-down of the use of hydrofluorocarbons (HFCs), perfluorocarbons (PFCs) and sulphur hexafluoride (SF6), with HFCs being identified as the most relevant F-gases from a climate perspective. Some of the HFCs covered include, among others, R23, R32, R134, R134a, R143a, R152a, R245ca, R245fa and R365mfc. In this context, the industry has been developing the so-called hydrofluoroolefins (HFO), which are replacement working fluids with low ODP and GWP values. Example HFO fluids are R1234yf and R1233zd. The F-gas Regulation applies to HVAC equipment, but it has been also extended to cover ORC engines. Therefore, technical solutions which are not constrained by such regulations are required to maximise the market penetration of the ORC technology.

There is extensive literature on the identification of the best performing working fluids for ORC engines in different applications. Ramos et al. [47,85] and Freeman et al. [86] evaluated the performance of a number of refrigerants and hydrocarbons for solar-driven ORC applications, including fluids with low GWP. In their work, refrigerants such as R245ca, and R245fa, as well as new HFOs (e.g. R1233zd) generated the highest power output, while butane proved to be a good candidate hydrocarbon fluid for ORC engines, driven by high temperature concentrating solar collectors. Aljundi et al. [87] studied the performance of hydrocarbons and refrigerants, for a range of heat-source temperatures. They reported ORC thermal efficiencies with pentane and hexane of up to 15%, for heat-source temperature 450-500 K. The performance of mixtures of hydrocarbons and refrigerants against pure fluids, for low grade heat recovery, was investigated by Refs. [45,88], amongst others [89,90]. In the context of ORC engines coupled to ICEs, Yang et al. [91] evaluated the performance of zeotropic mixtures and reported a total system power output increase of 11%. Additional limitations exist in the ICE-ORC applications due to the high operating temperatures, which may promote the fluids' chemical decomposition, if these have not been carefully selected during the design stage. Fluids with high critical temperature/pressure are considered most suitable in these high temperature applications. In the work of Li et al. [92], working fluids such as n-heptane, toluene, cyclohexane, R123 and R113 have been investigated for ORC applications with heat-source temperatures of 500-560 K and achieved efficiencies of up to 31%, while thermal efficiencies up to 30-34% are reported in Ref. [93].

In the aforementioned studies, the candidate working fluids investigated were selected in advance, and the optimal working fluid was identified, after screening the various fluids, based on predefined criteria, such as maximum power output, or minimum cost. Alternatively, the computer-aided molecular design (CAMD) has been used in the literature to provide a holistic approach to working fluids selection. In CAMD, the potential working fluids are described by functional groups, which can be put together in different ways to form different molecules. Studies utilising the CAMD methodology can be found, among others, in Refs. [46,94,95].

The review highlights that depending on the optimisation criteria examined, the optimum working fluids vary. It is also noted that although numerous working fluids have been investigated in the ORC literature, only very few of them are actually commercially available, including R245fa, R134a, pentane, toluene and Sokatherm [63]. Additionally, while some fluid mixtures have been proposed as suitable candidates in heat recovery applications, because of the good thermal match they offer to the heat source, they are difficult in implementation and, hence, there is lack of applications and operational experience [16].

By reviewing the available literature, it can be readily concluded that it is not possible to identify a single working fluid as the universal optimal fluid. Thus, the selection of working fluids should be integrated into the design process of such systems. This should be optimised on a case-by-case basis, accounting for the specific characteristics and constraints of each application. The key features to be considered in the process of working fluid selection, as identified in the literature, include [28,29,92]:

- Good thermodynamic performance, including temperature and pressure at the critical point suitable for the application, high specific heat capacity etc.;

- Type of saturation curve: Positive or isentropic curves are preferable, to ensure expansion in the dry vapour zone; negative saturation vapour curve can lead to wet expansion phenomena deteriorating the expander efficiency, especially if turbine expanders are deployed;
- Vapour density: High density is preferred to reduce the volume flow rate in the expander and the HEX size;
- Low viscosity and high thermal conductivity, resulting in high heat transfer coefficients and low friction losses in the HEX;
- Acceptable pressure levels: the higher the evaporation pressure, the higher the installation costs, while condensing pressure higher than the atmospheric will prevent air from leaking into the system;
- Low toxicity and flammability, and good chemical stability within the ORC engine operating conditions;
- Freezing temperature to be lower than the minimum ambient to prevent freezing;
- Compatibility with construction materials (non-corrosive fluids);
- Low ODP and GWP values;
- Availability and low cost.

The optimisation exercises performed in this thesis are computationally expensive. Therefore a preselection of candidate ORC working fluids has been performed. The selection of the working fluids has been conducted considering good thermodynamic properties, but also safety and environmental performance. More details on the working fluid selected for this study are provided in Chapter 3.

2.3 Off-design operation

ORC engines in real applications will experience varying heat-source conditions (i.e. mass flow rate and temperature). A case in the point is ORC engines driven by solar collectors, geothermal fluids, and bottoming ORC engines recovering heat from the exhaust gases of various engines or boilers. Key for facilitating the wider adoption of these systems and improving their economic proposition is to maximise the engines running hours once installed. Therefore, ORC engine designs and operating strategies that optimise its performance, not only at design, but also at off-design operation are of paramount importance.

There is a plethora of ORC system design studies in the literature (such as those presented in Refs. [26,30,32,96]), where the authors aim to maximise the ORC engine performance. A common characteristic of the aforementioned studies is that they explore alternative designs under specific (fixed) heat-source conditions, aiming to obtain the optimum system design for alternative working fluid candidates. In a typical design problem, the cycle design and components selection and sizing are performed using the nominal heat-source conditions, aiming to maximise the engine power output. At this stage, the ORC engine HEXs architecture and available heat transfer area, along with the expander geometry, built-in VR etc. are fixed. When the heat-source temperature and/or mass flow rate entering the evaporator HEX vary, various operating and control parameters must be adjusted to optimise the ORC engine power output/efficiency, at every new heat-source condition, and maximise the system running hours. However, such optimisation can be computationally-expensive (especially as the number of variables increases), so performing this exercise in real-time is a challenging task. In contrast, optimum ORC engine performance maps can be generated and used, for predicting the optimum ORC engine operating points and performance. To achieve this, the development of modelling tools that account for the various components' time-varying characteristics and interactions is of paramount importance.

There is limited literature on predicting ORC off-design performance, with some studies focusing on HEX performance and others focusing on the expander. The off-design operation of a subcritical ORC engine with radial turbine, recovering heat from a steam turbine plant, was investigated by Song et al. [97]. The authors did not optimise the ORC engine for off-design operation. Instead they performed a parametric analysis to predict its performance under different heat-source conditions. In Ref. [98] the off-design operation of ORCs with axial turbines and plate-fin HEXs was evaluated, but the authors focused on the turbine control strategy. Punov et al. [99] performed thermodynamic optimisation of the ORC design at every ICE PL condition. However, the authors assumed a fixed expander and pump efficiency at off-design operation, while the components specific design and size were not considered. Nevertheless, in real applications, the ORC engine components are selected and sized for operating at the design point and they should be able to operate under varying thermal input. The off-design operation of a bottoming ORC for a marine ICE was investigated by Yang et al. [100]. For every PL condition of the ICE, a new ORC cycle was identified as the optimum. The system was then resized, instead of subjecting the ORC engine sized for 100% load, to off-design operation, and identifing the new optimum operating points, given the existing components. Similarly, Badescu et al. [101] considered an ORC engine recovering heat from an ICE, but they obtained a new optimised ORC design for every PL point. The research efforts discussed above developed steady-state ORC models. Refs. [102,103] focused on the dynamic modelling of the evaporator, considering the thermal inertia of this component under varying heat-source conditions.

Within the available literature for the off-design optimisation of ORC engines, it is revealed that very few studies have considered the actual components characteristics, as defined at the nominal design stage, to inform the ORC off-design operation. From this limited literature, where the components time-varying performance is incorporated in the model, the majority of the studies focus on turbine expanders, scroll, or single stage screw expanders. There are no studies available, on the off-design operation of piston expanders, in stationary ORC engine power generation applications. Di Battista et al. [104] sized an ORC engine based on the ICE nominal operation, using a sliding vane rotary expander, and then allowed the heat-source conditions in the evaporator to vary. The authors kept the ORC evaporation pressure constant under off-design operation and the expander rotational speed was allowed to vary, depending on the load and superheat degree of the working fluid. Guopeng et al. [36] sized the HEXs and the turbo-expander of an ORC system that recovered heat from an ICE, under the nominal engine's operating conditions. Then, by using turbine performance maps and with the HEXs size fixed, the authors performed a parametric analysis to obtain the ORC performance at off-design operation. A dynamic ORC model was developed by Mazzi et al. [105] to predict system performance under a varying load. Shell-and-tube HEXs were considered, while the turbine expander performance was obtained from the Stodola [22] equations. In Ref. [106], the authors evaluated the off-design performance of large-scale recuperative ORC engines with shell-and-tube heat exchangers and turbine expanders, while in Ref. [107] the authors evaluated the off-design performance of ORC engines with double stage evaporator, PHEXs and turbine expander. In Refs. [108,109] the performance of ORC engines with scroll expanders and plate/helical coil heat exchangers has been investigated. Refs. [79,110], investigated the off-design operation of small-scale single stage screw expanders with PHEXs. Finally, Matthew et al. [111] compared the off-design operation of an ORC engine with turbines and screw expanders. In their study the authors focused on the expander design, without analysing the ORC HEX performance. Results of this case study indicated that the turbine expander has similar performance to that of a single stage double-screw, although the efficiency of the latter deteriorates faster at off-design operation.

The control aspects of operating ORC engines under off-design conditions are also critical, for optimising the system performance onsite. There are a few studies in the literature aiming to identify the most promising control strategies, or design the actual controllers. Xu et al. [39] developed a dynamic ORC model recovering heat from a vehicle ICE, under transient engine operation. They focused on the control of the complete ICE-ORC system, under real vehicle operating conditions, using alternative control strategies. In their study, the HEXs were of tube-and-shell construction and a turbine expander map was used to predict the expander performance, under varying load conditions. Hu et al. [66] investigated the impact of varying geothermal conditions on an ORC engine, comprised of an axial turbine and plate HEXs, and considered alternative control strategies for the expander, including the variation of the evaporating pressure and superheating degree, to maximise performance during off-design operation. Xu et al. [112] investigated three operational strategies for a bottoming ORC engine to an ICE. Results indicated that the fuzzy logic control, where the operating conditions of the ORC engine were adjusted following the ICE PL, has the best performance when compared to strategies that control to fixed vapour temperature or to fixed degree of superheat. In Ref. [113], the sliding pressure control strategy in the evaporator was deemed the best performing. However, the system performance is highly dependent on the controller response and its ability to maintain the desired vapour conditions during the transient heat-source operation, while the actual design of such a controller is a challenging task.

To conclude, by reviewing the existing literature it is revealed that there is only a limited number of studies that consider the time-varying and interacting effects of the ORC engine components, when the system is subjected to off-design operation. Nevertheless, approaches that do not account for the performance trade-offs and interactions, between key system components, can lead to sub-optimal ORC engine off-design operating points and performance. Within the limited literature of integrated ORC off-design studies, the most commonly investigated ORC expander machines are turbines, screw or scrolls. Only a few studies have examined the use of reciprocating piston expanders in ORC systems at off-design operation. These are mainly limited to waste heat recovery from ICEs on road-vehicle applications [52,72,114]. Finally, shell-and-tube HEXs are very well documented, in terms of their time-varying performance, but PHEXs or DPHEXs are not studied often.

2.4 Thermoeconomic analysis

While thermodynamic optimisation and technical feasibility are at the core of the development of ORC systems, another critical factor for the wider deployment of ORC engines is their capital expenditure (CAPEX) and operating and maintenance (O&M) costs. However, there is only limited literature publicly available on actual ORC systems costs. In the absence of actual project cost data, to obtain credible estimates of the ORC investment cost, the correct selection and sizing of the main ORC system components are of paramount importance. These estimates form the basis of the cost calculations to be undertaken when evaluating the financial viability of ORC system deployment.

There is a variety of costing methods available in the literature, with the most widely used being the so-called 'module costing' technique [115,116]. However, this method originates from the chemical industry, where it was traditionally used to provide estimates for chemical plants costs. Apart from the module costing technique, cost correlations for ORC engine components have been developed in the literature, such as those presented in Refs. [8,17] which are based on typical materials costs, or by collating data from manufacturers' price lists, such as Ref. [65], while very limited studies are publicly available were the actual ORC components manufacturing, assembly and overhead costs of real installations are presented [52,117]. The lack of actual ORC engine and components cost data makes the validation of the cost estimates an onerous task.

In contrast to the prolific literature related to the thermodynamic analysis of ORCs, there is limited research on ORC components systematic sizing and costing. The most commonly examined metric is the specific investment cost (SIC) of ORC engines. Lecompte et al. [8] optimised a bottoming ORC in an ICE-ORC CHP system for minimum SIC. The authors selected a PHEX as the evaporator, a finned-tube type for the condenser, and a notional volumetric expander to predict the system performance. The SICs achieved vary from 2,400-4,250 GBP/ kW. Quoilin [17] performed single objective optimisation to investigate the SIC of small scale ORC (approximately 2.5-4 kW), for medium grade heat recovery (180 °C heat-source). They used PHEXs and a scroll expander for the ORC engine design. The SIC achieved for the optimised system was approximately 2,300-3,700 GBP/kW. Yang [118] performed a multi-objective optimisation for maximum power output and minimum SIC, for a vehicle waste heat recovery application. The evaporator was finned-tube type, the condenser was PHEX and the expander was a turbine. Their findings indicate high SICs of up to 26,900 GBP/kW. Other examples of thermoeconomic analysis for minimising SIC in geothermal applications can be found in Refs. [45,119], quoting SICs of 1,500-4,000 GBP/kW and in Ref. [47] for domestic small scale solar applications of 0.5-2 kW, reporting SICs of 3,500-7,900 GBP/kW.

In Fig. 11, SIC figures of ORC engines available in the literature are presented for capacities up to 400 kW, and different heat-source temperatures. These cost estimates have been obtained using the cost correlations discussed above, so they are not based on real ORC plant cost data (cost data have been obtained from White et al. [46] and Lemmens [117]). The SIC values range between 1,200-7,000 GBP/kW, depending on the ORC engine capacity. On the same figure, real cost data from ORC engines available on the market are presented. Source 1 refers to prices collected from ORC vendors quotations and Source 2 to the ORC engine price data presented in Ref. [120]. Based on the actual ORC engine cost data, the SIC varies between 2,000-4,000 GBP/kW with the exemption of one small scale ORC engine reaching 6,000 GBP/kW. As expected smaller sized engines have higher SIC figures, while also high temperature systems generate more power, thus reducing their SIC. However, there is a range of power output beyond which (>120 kW), increasing the ORC engine capacity further results in an increase of the engine SIC. Finally, the SIC of CHP-ICEs as prime movers for generating power are also presented in Fig. 11. For power output up to 400 kW the SIC of CHP-ICEs varies between 700-4,500 GBP/kW. By comparing the SIC of ORC engines and CHP-ICEs, it is noted that the SICs are comparable for power outputs of less than 60 kW, while at higher power outputs the SIC of the CHP-ICE is 10-50% lower than that of the ORC engines (figures quoted compare the CHP-ICE SICs, to that of the ORC engines on the market). CHP-ICEs are a well-established and mature technology, so lower SICs are expected. Nevertheless, the findings highlight that research efforts should focus on medium scale ORC engines and on identifying pathways for making these systems more economically competitive.

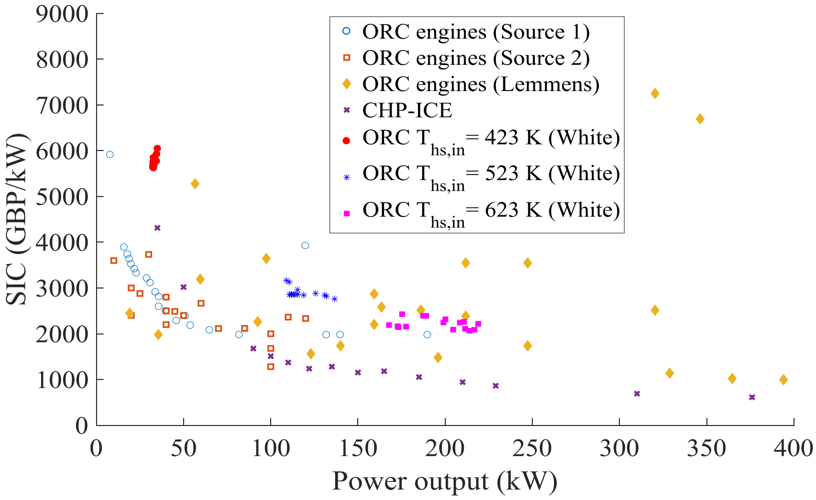

Fig. 11: ORC engine SIC figures obtained from: i) ORC studies by White et al. [46] and Lemmens [117]; ii) Source 1 refers to ORC engines vendors quotes; and iii) Source 2 refers to ORC engine costs from Ref. [120]. CHP-ICE SICs were estimated from vendors' quotes. Figures quoted reflect SICs calculated using the engine CAPEX, excluding installation costs.

Other ORC studies considered alternative economic metrics; in Ref. [119] the ORC system was optimised separately for maximum power output, minimum SIC and for a linear combination of the two, using weighting factors. The expander was a turbine and the HEXs were of shell-and-tube type. For the ORC engine CAPEX estimation, the module costing technique has been used [115]. A project profitability analysis followed the optimisation exercise, indicating that the return of investment rate ranges between 6 to 38%. A thermoeconomic analysis of ICE-ORC was also performed by Neto et al. [121]. Hydrocarbons were evaluated as candidate working fluids, while the expander machine was again a turbine and the system HEXs were of shell-and-tube construction. A parametric analysis was performed to present the impact of various ORC operating parameters on the electricity production cost (EPC) and the discounted payback period (DPP) of the ORC system. A thermoeconomic analysis of a transcritical ORC recovering heat from ICE was performed by Yu et al. [31]. PHEXs were selected, with the plates' geometry fixed, while the expander technology was a turbine. Parametric analysis was then performed to evaluate the impact of ORC operating conditions on the financial viability of the project. Tian et al. [50] finally evaluated thermoeconomically an ICE-ORC system, using PHEXs and a turbine expander for the ORC engine. The PHEX plates characteristics were fixed, while the turbine expander was modelled using fixed efficiency. The parametric analysis results indicated that EPC decreases for high evaporating pressure and net power output, reaching 0.25 GBP/kWh.

By reviewing the literature, it is concluded that the HEX and expander typologies are preselected by the designers, before proceeding to the thermoeconomic evaluation of the ORC system, instead of forming the output of the optimisation exercise. There is very limited literature on the simultaneous ORC thermoeconomic optimisation and components selection and sizing, with a couple of studies focusing on the HEX optimisation only [51,53] and others focusing on the expander design [48]. Braimakis et al. [48] presented a thermoeconomic analysis of ORC engines using PHEXs only, and compared alternative expander machines. They have optimised the system for minimum SIC (single-objective optimisation), considering turbines, screw and scroll expanders, using basic isentropic efficiency correlations to predict the expander performance. Results indicated that SIC vary from 700 GBP/kW (high temperature high capacity systems) to 13,300 GBP/kW (low temperature low capacity systems). Zhang et al. [53] performed a thermoeconomic evaluation of low temperature ORCs, investigating alternative HEXs configurations, while fixing the expander selection to turbine. They compared PHEX, shell-and-tube and finned-tube HEXs aiming to minimise the system EPC (single-objective optimisation). In their work, the PHEX plate specification was fixed, along with the tube design and size for the other HEX typologies. Results indicated that the finned-tube HEX and shell-and-tube have lower EPC than the other configurations. Walraven et al. [51,122] finally performed detail HEX sizing optimisation for shell-and-tube and PHEX constructions, allowing all HEX design parameters to vary, aiming to maximise the ORC power output. The focus was on the HEXs design without investigating the expander performance, or accounting for the economic aspects of the optimum system. Their results indicated that PHEX perform better than the shell-and-tube designs.

To conclude, the review reveals that not a single ORC system design can be identified as the optimal one; on the contrary, the most suitable HEXs and expander type vary with the application and the heat-source. Additionally, the most well documented expander type in ORC thermoeconomic studies is the turbine expander, along with the scroll machines. A few studies focus on screw expanders, with piston expanders being the least documented. Finally, it is noted that there is not a consistent costing methodology used across the board, when assessing ORC designs. The SIC figures reported in the literature can vary significantly depending on the costing method deployed. These findings highlight the need for systematic integration of component selection, sizing and costing of ORC engines for alternative applications.

2.5 Summary and conclusions

Distributed CHP systems have great potential to reduce energy consumption and emissions. ICEs are the most commonly found prime movers in CHP systems, in the built environment or in industry, and in medium-scale power generation (up to a few MWs). Key for maximising CHP-ICE efficiency is the utilisation of both the thermal and power outputs available. ORC engines are a promising candidate technology for recovering the waste heat of the exhaust-gas stream in CHP-ICE applications, maximising the overall electrical and thermal efficiency of these systems.

The modelling of ICE-ORC CHP systems is challenging, especially when trying to capture the interactions and performance trade-offs between the two engines, in order to optimise the complete system performance. Although models that consider each engine separately exist, integrated high fidelity modelling tools able to optimise the complete ICE-ORC CHP system are not properly documented. It is also revealed that ORC studies mainly focus on the design and optimisation of the engine, by using fixed heat-source conditions. In real applications, ORC engines will operate under variable heat-source conditions. To maximise the system running hours and improve its financial proposition, the ORC engine performance should be optimised not only at design, but also at off-design operation. Although off-design ORC studies exist, there is only limited number of efforts that have explicitly accounted for the time-varying characteristics of the ORC components, in defining operation at off-design conditions. The modelling studies performed to-date cover mainly ORC engines with turbine and scroll expanders, and shell-and-tube HEXs at off-design operation, with piston expanders, and PHEX/DPHEXs designs being less investigated. Capturing the cost aspects of the ORC engines design, while optimising the system thermodynamic performance is critical for improving its financial proposition. Although, many studies have performed thermoeconomic optimisation, literature lacks optimisation frameworks where the ORC thermodynamic design, components type selection, sizing and costing are performed simultaneously, screening the entire space of possible design solutions.

In the following chapters, we aim to provide means to tackle these challenges, via the development and application of suitable ICE-ORC modelling tools. Advanced ICE-ORC CHP systems are examined, from thermodynamic, operating and economic perspective, while the tools developed can be also adjusted to use other heat-source streams. In Chapter 4, the optimisation of integrated ICE-ORC CHP systems is presented. In Chapter 5, the impact of heat-source variability on the ORC engines performance is examined, for ORC engines with piston and screw expanders. The time-varying characteristics of the ORC system key components are considered, to optimise its performance at off-design operation. Optimised performance maps are generated, which can be used to optimise the operation of live installations, given the heat-source conditions onsite. Finally, in Chapter 6, the thermoeconomic aspects of ORC technology are investigated. A tool is developed that can screen various components typologies, sizes, and geometries, while also optimising the thermodynamic design of the engine, in order to identify the design that meets both the technical and financial key performance indicators of each project.

Chapter 3

Methodology

> *"Plans are of little importance, but planning is essential."*
>
> - Winston Churchill, former British Prime Minister

3.1 Introduction

In this thesis, we aim to investigate the potential of waste heat recovery from internal combustion engines (ICEs) using organic Rankine cycle (ORC) engines, in combined heat and power (CHP) stationary applications. The analysis aims to evaluate such systems, by looking into four key aspects, for their wider deployment and adoption in the market: i) thermodynamic evaluation of alternative configurations, working fluids and operating conditions; ii) components selection and sizing; iii) operational optimisation under real heat source varying conditions; and iv) financial assessment for estimating the systems' capital expenditure (CAPEX) and over-life economic performance.

In this chapter, the methodology used throughout this thesis is presented and discussed. Firstly, the ICE thermodynamic model developed in MATLAB© is presented, in Section 3.2. This is a dynamic model of spark-ignition ICEs covering both naturally aspirated and turbocharged engines, comprised of a set of ordinary differential equations (ODEs). Next, the exergy analysis of ICE is presented, for both types of engines. In Section 3.3, the ORC thermodynamic models developed in this work are presented. These cover subcritical non-recuperative and recuperative ORC engine designs. The exergy analysis of the ORC engine is also discussed. In Section 3.4, we present the working fluids selected for this study along with the key considerations related to this selection. The heat exchanger (HEX) performance modelling methodology deployed in this work is presented in Section 3.5. Two HEX typologies have been investigated, namely the double-pipe HEX (DPHEX) architecture and the plate type HEX (PHEX). The alternative Nusselt number correlations available in the literature, for predicting the heat transfer coefficients (HTCs) in the evaporator and the condenser units, have been compared, and the most well-suited have been selected and incorporated in the HEX models developed in this thesis. In Section 3.6, the expander models used in this thesis are presented, covering two types of volumetric expanders, namely piston expander and screw machines. In Section 3.7, an overview of the pump typologies available on the market is presented and the pumps selected for this work are highlighted. In Section 3.8, the methodology deployed for the ORC engines costing is presented. To obtain the ORC engine total cost, the cost of each one of its constituent component is first calculated, and then are added together to reflect the complete engine cost. The profitability analysis methodology is also presented in Section 3.8. Finally, the principles of the optimisation exercises performed in this thesis are presented in Section 3.9, covering both single-objective optimisation and multi-objective optimisation exercises.

3.2 Internal combustion engine modelling

3.2.1 Thermodynamic modelling

The CHP system examined in this work is driven by a four-stroke reciprocating ICE, which operates with the Otto cycle (spark-ignition engine) and is designed for stationary CHP applications, featuring the necessary heat recovery equipment. The operation and performance of the CHP-ICE is obtained using a set of ODEs that describe the key processes taking place inside the engine cylinders. The full set of equations is given in Eqs. 1-21, while the assumptions used for the thermodynamic modelling of the ICE are listed below:

- Every cylinder of the ICE is modelled as an open system/control volume, with the fresh air-fuel mixture charge (intake) and the combustion products (exhaust gases) crossing the system boundaries;
- The heat addition to the intake charge of the engine from combustion, is modelled using the Wiebe function that predicts the heat release rate [123];
- The heat losses through the walls of the ICE cylinders to the jacket water circuit ($\dot{Q}_{\mathrm{w}}$) are estimated using the Woschini [123,124] correlation for the phase-averaged instantaneous heat transfer coefficient, while the heat losses due to radiation are also included in the model, via the use of the correlation proposed by Annand, as presented is Ref. [125];
- The standard relations for compressible gas flows through nozzles [123] are used to calculate the mass flow rate through the intake and exhaust valves of the ICE;
- For the turbocharged engines, the compressor and turbine performance is modelled using fixed isentropic efficiency.

The equation of conservation of energy for an open control volume, including the heat losses due to convection, conduction and radiation, can be written as follows:

$$\frac{\mathrm{d}P}{\mathrm{d}\vartheta}=\frac{\gamma-1}{V}\left(Q_{\mathrm{comb}}\frac{\mathrm{d}x_{\mathrm{b}}}{\mathrm{d}\vartheta}-\frac{\mathrm{d}Q_{\mathrm{w}}}{\mathrm{d}\vartheta}\right)-\gamma\frac{P}{V}\frac{\mathrm{d}V}{\mathrm{d}\vartheta}+\frac{\gamma-1}{V}\frac{\pi}{180\omega}\left(\dot{m}_{\mathrm{int}}h_{\mathrm{int}}-\dot{m}_{\mathrm{ex}}h_{\mathrm{cyl}}\right)\,, \tag{1}$$

where the rate of change of pressure P in the cylinder with angle ϑ is a function of: i) the heat added to the cycle during combustion ($Q_{\mathrm{comb}}\mathrm{d}x_{\mathrm{b}}/\mathrm{d}\vartheta$); ii) the heat transfer losses through the cylinder wall ($\mathrm{d}Q_{\mathrm{w}}/\mathrm{d}\vartheta$); iii) the positive displacement work generated by the gases inside the cylinder, due to piston movement ($P\mathrm{d}V/\mathrm{d}\vartheta$); and iv) enthalpy flow into and out of the control volume (h_{int}, h_{cyl}), associated with the mass flow rate of the new intake charge and the mass flow rate of the exhaust gases ($\dot{m}_{\mathrm{int}}$, $\dot{m}_{\mathrm{ex}}$) crossing the system boundaries. The change of the cylinder volume in a cycle with angle ϑ ($\mathrm{d}V/\mathrm{d}\vartheta$) is calculated as a function of the compression ratio (r) of the engine, the displacement volume (V_{dis}), and the instantaneous stroke ($y(\vartheta)$):

$$y(\vartheta) = \alpha + l - [(l^2 - \alpha^2 \sin(\vartheta)^2)^{0.5} + \alpha\cos(\vartheta)] \,, \tag{2}$$

$$V(\vartheta) = \frac{V_{\mathrm{dis}}}{r-1} + \frac{3.14 b^2 y(\vartheta)}{4} \text{, and } \frac{\mathrm{d}V}{\mathrm{d}\vartheta} = \frac{V_{\mathrm{dis}}}{2}\sin(\vartheta)[1 + \cos(\vartheta)(a^2 - \sin(\vartheta)^2)^{-0.5}] \,. \tag{3,4}$$

With reference to the right-hand side (RHS) terms of Eq. 1, the heat input to the cycle due to combustion (Q_{comb}) is calculated by multiplying the lower heating value (*LHV*) of the fuel by its mass flow rate to the engine:

$$Q_{\mathrm{comb}} = m_{\mathrm{fuel}} LHV \,, \tag{5}$$

while the heat release rate during combustion with angle ϑ of the crankshaft's rotation is calculated using the Wiebe correlation, which requires as input the ignition angle (ϑ_{ign}) and the duration of the combustion process (ϑ_d):

$$\frac{\mathrm{d}x_{\mathrm{b}}}{\mathrm{d}\vartheta} = \frac{n\alpha}{\vartheta_d}\left[1 - (1 - \exp\left(-\alpha\left(\frac{\vartheta-\vartheta_{\mathrm{ign}}}{\vartheta_d}\right)^n\right)\right]\left(\frac{\vartheta-\vartheta_{\mathrm{ign}}}{\vartheta_d}\right)^{n-1} \,, \tag{6}$$

Where α = 5 and n = 3, based on typical values available in the literature [123].

The term $\mathrm{d}Q_{\mathrm{w}}/\mathrm{d}\vartheta$ represents the heat losses through the cylinder wall, and corresponds to the summation of heat transfer losses due to convection/conduction and radiation:

$$\frac{\mathrm{d}Q_{\mathrm{w}}}{\mathrm{d}\vartheta} = \frac{h_{\mathrm{g}}(\vartheta)A_{\mathrm{w}}(\vartheta)(T_{\mathrm{g}}(\vartheta) - T_{\mathrm{w}})}{N} + \frac{\beta\sigma_{\mathrm{Boltz}}A_{\mathrm{w}}(\vartheta)\left(T_{\mathrm{g}}(\vartheta)^4 - T_{\mathrm{w}}{}^4\right)}{N} \,, \tag{7}$$

$$A_{\mathrm{w}}(\vartheta) = \pi b y(\vartheta) + \frac{\pi}{2} b^2 \,. \tag{8}$$

In Eq. 7, $h_{\mathrm{g}}(\vartheta)$ corresponds to the instantaneous HTC which quantifies the heat transfer between the gases inside the ICE cylinders and the wall; $A_{\mathrm{w}}(\vartheta)$ corresponds to the instantaneous area available for heat transfer while the piston is moving; $T_{\mathrm{g}}(\vartheta)$ is the instantaneous bulk temperature of the gases inside the cylinder; T_{w} is the temperature of the cylinder wall; N is the engine's rotational speed expressed in revolutions per second (rps); β is a parameter related to the radiation losses; and σ_{Boltz} is the Stephan-Boltzmann constant. The instantaneous HTC ($h_{\mathrm{g}}(\vartheta)$) is a function of: i) the average temperature inside the cylinder; ii) the average pressure inside the cylinder; iii) the crankshaft angle; and iv) the mean speed of the piston.

Two correlations are commonly found in the ICE literature for estimating the instantaneous heat transfer coefficient in reciprocating systems: i) the correlation proposed by Annand [126]; and ii) the correlation proposed by Woschni [123,124]. In this work, the correlation proposed by Woschni has been used, as provided in Ref. [125]. Based on this correlation, the heat transfer coefficient is estimated using the following equations:

$$h_{\mathrm{g}}(\vartheta) = 3.26\, P(\vartheta)^{0.8} U_{\mathrm{pist}}(\vartheta)^{-0.8} b^{-0.2} T(\vartheta)^{-0.55}\ , \tag{9}$$

$$T(\vartheta) = \frac{P(\vartheta)V(\vartheta)}{m(\vartheta)R}\ , \tag{10}$$

where $U_{\mathrm{pist}}(\vartheta)$ is the instantaneous characteristic velocity of the gases, calculated by considering the instantaneous pressure variation inside the cylinder ($P(\vartheta)$) and the mean piston speed:

$$U_{\mathrm{pist}}(\vartheta) = 2 \cdot 2.28\, N l_{\mathrm{s}} + 0.00324\, T_0 \frac{V_{\mathrm{dis}}}{V_0} \frac{P(\vartheta) - P_{\mathrm{m}}}{P_0}\ . \tag{11}$$

In Eq. 11, l_{s} is the length of the piston stroke; V_0, T_0, P_0 are the volume, temperature and pressure at the intake stroke; V_{dis} is the cylinder displacement volume; and P_{m} is the so-called ‘motored engine pressure’, which is calculated by solving the isentropic relationship $P_{\mathrm{m}} V_{\mathrm{m}}{}^{\gamma} = P_0 V_0{}^{\gamma} = \mathrm{const.}$ This expression of the gas mean characteristic velocity is applicable when the ICE valves are closed, i.e. during the compression and expansion strokes. When the valves are open, during the intake and exhaust strokes, the mean characteristic velocity of the gas is estimated using the mean piston velocity only:

$$U_{\mathrm{pist}}(\vartheta) = 2 \cdot 2.28\, N l_{\mathrm{s}}\ , \tag{12}$$

owing to the fact that the pressure variations, during the intake and exhaust strokes, are considerably lower than those observed during the compression and expansion strokes.

To calculate the mass flow rate through the valve restriction (throat), the equations for compressible gas flows through nozzles are used. The mass flow rate is calculated using Eqs. 13-15, depending on whether the flow is choked or not:

$$\dot{m}_{\mathrm{chd}} = \frac{P_0}{\sqrt{RT_0}} C_{\mathrm{D}} A_{\mathrm{V}} \sqrt{\gamma \left(\frac{2}{\gamma+1}\right)^{\frac{\gamma+1}{\gamma-1}}}\ , \text{ or } \dot{m}_{\mathrm{nchd}} = \frac{P_0}{\sqrt{RT_0}} C_{\mathrm{D}} A_{\mathrm{V}} \left(\frac{P_{\mathrm{V}}}{P_0}\right)^{\frac{1}{\gamma}} \sqrt{\frac{2\gamma}{\gamma-1}\left[1 - \left(\frac{P_{\mathrm{V}}}{P_0}\right)^{\frac{\gamma-1}{\gamma}}\right]}\ , \tag{13}$$

$$C_{\mathrm{D}} = 0.85 - 0.25 \left(\frac{P_{\mathrm{V}}}{P_0}\right)^2\ , \tag{14}$$

$$A_{\mathrm{V}} = \pi D_{\mathrm{V}} L_{\mathrm{V}}\ , \tag{15}$$

for which the critical pressure ratio at which the flow becomes choked at the valve is required:

$$\frac{P_0}{P_{\mathrm{V}}} = \left(\frac{\gamma+1}{2}\right)^{\frac{\gamma}{\gamma-1}}\ . \tag{16}$$

In the above equations, C_{D} corresponds to the flow discharge coefficient at the valve restriction, and is calculated in Eq. 14, by using the correlation proposed in Ref. [127]; A_{V} is the minimum area available to the gas as it flows through the valve (curtain area); D_{V} is the diameter of the valve; and L_{V} is the valve lift. The gas pressure, temperature, and density upstream and downstream of the valve throat are then related by [123]:

$$\frac{T_0}{T_{\mathrm{V}}} = 1 + \frac{\gamma-1}{2}M^2 \,, \tag{17}$$

$$\frac{P_0}{P_{\mathrm{V}}} = \left(\frac{T_0}{T_{\mathrm{V}}}\right)^{\frac{\gamma}{\gamma-1}} , \tag{18}$$

$$\frac{\rho_0}{\rho_{\mathrm{V}}} = \left(\frac{T_0}{T_{\mathrm{V}}}\right)^{\frac{1}{\gamma-1}} , \tag{19}$$

with P_0, T_0 and ρ_0 being the gas pressure, temperature and density upstream of the valve (the so-called stagnation conditions); P_{V}, T_{V} and ρ_{V} being the gas pressure, temperature and density downstream of the valve; and M representing the Mach number at the valve throat (the ‘restriction’). During the intake stroke, the upstream (stagnation) conditions correspond to the conditions at the intake manifold, while during the exhaust stroke, the upstream (stagnation) conditions correspond to the conditions inside the cylinder. For more details on compressible flows modelling through nozzles, the reader is referred to Refs. [123,125].

Finally, for the turbocharged engines examined in this work, the compressor power ($\dot{W}_{\mathrm{comp}}$) and the turbocharger work ($\dot{W}_{\mathrm{turb}}$) are calculated by using constant isentropic efficiencies, following the expressions:

$$\dot{W}_{\mathrm{comp}} = \frac{\dot{m}_{\mathrm{air}}(h_1 - h_0\,)}{\eta_{\mathrm{comp}}} \,, \tag{20}$$

$$\dot{W}_{\mathrm{turb}} = \dot{m}_{\mathrm{ex}}(h_{\mathrm{ex}} - h_{\mathrm{out}})\eta_{\mathrm{exp}} \,. \tag{21}$$

The set of ODEs presented in Eqs. 1-21 represents the complete ICE thermodynamic model, which was solved in MATLAB© using the non-stiff ODE solvers ode113 [128].

3.2.2 Exergy analysis

Exergy is defined as the maximum theoretical work that a system will generate if it undergoes a reversible process, from its initial state to the environmental (dead) state [129,130]. The exergy balance for a control volume of an open system, at steady-state conditions, is calculated by the following equation:

$$0 = \int_1^2 \left(1 - \frac{T_0}{T}\right) \mathrm{d}\dot{Q} - \dot{W} + \sum_{\mathrm{i}=1}^{\mathrm{n}} \dot{m}_{\mathrm{i,in}} ex_{i,\mathrm{in}} - \sum_{\mathrm{i}=1}^{\mathrm{n}} \dot{m}_{\mathrm{i,out}} ex_{\mathrm{i,out}} - \dot{X}_{\mathrm{destr}} \,. \tag{28}$$

The integral in Eq. 28, refers to the heat exchange occurring between the system and its surroundings; the second term ($\dot{W}$) represents the work generated by (or added to) the system; the third term is the summation of the exergy flows entering the system, while the fourth term represents the exergy flows leaving the system. The last term ($\dot{X}_{\mathrm{destr}}$) represents the exergy destruction occurring in every component of the system. The signs indicated in Eq. 28 are based on the convention that: i) the heat exchange is positive, when heat is added to the system; and ii) the work is positive, when it is generated by the system [131]. To calculate the exergy flows, the following assumption are considered [132–134]:

- The magnetic and nuclear forms of exergy are neglected;
- The change in kinetic and dynamic energy is negligible, therefore the kinetic and potential exergies are also considered negligible;
- The water present in the exhaust gases is in vapour phase, so the *LHV* of methane has been used for the calculations;
- The exhaust gases inside the ORC evaporator do not react and only transfer heat to the working fluids;
- The air and exhaust gases are considered ideal gases, so the ideal gas law principles are applied;
- The combustion reaction in the Otto ICE is complete, using the air-to-fuel ratio (*AFR*) presented in the manufacturers' data sheet;
- The ambient environmental conditions are used as the reference state of the system for the exergy calculations.

Using the aforementioned assumptions, the specific physical exergy of a substance is expressed as follows:

$$ex_{\mathrm{i}}{}^{\mathrm{ph}} = (h - h_0) - T_0(s - s_0)\ . \tag{29}$$

The specific chemical exergy of reference substances is defined as [129,135]:

$$ex_{\mathrm{i}}{}^{\mathrm{ch}} = RT_0 \ln\left(\frac{P_0}{P_{p,0}}\right)\ . \tag{30}$$

The total specific exergy is therefore calculated using:

$$ex_{\mathrm{i}} = ex_{\mathrm{i}}{}^{\mathrm{ph}} + ex_{\mathrm{i}}{}^{\mathrm{ch}}\ . \tag{31}$$

For mixtures, the chemical exergy is expressed as [132]:

$$ex_{\mathrm{mix}}{}^{\mathrm{ch}} = \sum_{\mathrm{i}=1}^{\mathrm{n}} k_{\mathrm{i}} \mathrm{ex}_{\mathrm{i}}{}^{\mathrm{ch}} + \mathrm{R}T_0 \sum_{\mathrm{i}=1}^{\mathrm{n}} k_{\mathrm{i}} \ln(k_{\mathrm{i}})\ . \tag{32}$$

To obtain the exergy destruction occurring within the ICE, Eq. 28 can be rearranged to:

$$\dot{X}_{\mathrm{destr,ICE}} = \dot{X}_{\mathrm{air}} + \dot{X}_{\mathrm{f}} - \dot{X}_{\mathrm{ex}} - \dot{X}_{\mathrm{work}} - \dot{X}_{\mathrm{jw}}\ , \tag{33}$$

where the term $\dot{X}_{\mathrm{air}}$ represents the exergy flow of the air intake, $\dot{X}_{\mathrm{f}}$ represents the exergy flow of the fuel, $\dot{X}_{\mathrm{ex}}$ is the exhaust-gas stream exergy flow, $\dot{X}_{\mathrm{work}}$ represents the work generated on the ICE shaft, and $\dot{X}_{\mathrm{jw}}$ is the exergy flow to the jacket water circuit of the engine. For natural aspiration engines the exergy flow of the air intake is equal to zero, since the air enters the cylinder at environmental conditions. In the case of turbocharged engines, the exergy flow of the air intake is calculated using the air temperature and pressure after the intercooler, prior entering the ICE cylinder:

$$\dot{X}_{\mathrm{air}} = \dot{m}_{\mathrm{air}}\left[\left(h_{\mathrm{air}} - h_{\mathrm{air,0}}\right) - T_0\left(s_{\mathrm{air}} - s_{air,0}\right) + c_{\mathrm{p,air}}\mathrm{R}T_0\ln\left(\frac{P_{\mathrm{air}}}{P_0}\right)\right]. \tag{34}$$

To estimate the exergy flow of the natural gas ($\dot{X}_{\mathrm{f}}$) it is assumed that this is equal to that of methane, and it is calculated using the *LHV* of methane, as follows [132]:

$$\dot{X}_{\mathrm{f}} = \dot{m}_{\mathrm{f}}ex_{\mathrm{f}}{}^{\mathrm{ch}}, \tag{35}$$

$$ex_{\mathrm{f}}{}^{\mathrm{ch}} = LHV\left(1.033 + 0.0169\frac{\mathrm{C}}{\mathrm{H}} - \frac{0.0698}{\mathrm{C}}\right). \tag{36}$$

Here, C stands for the number of carbon atoms in the fuel an H for the number of hydrogen atoms. In the case of methane C = 1 and H = 4.

The ICE shaft work is used for estimating $\dot{X}_{\mathrm{work}}$. The ICE work is obtained from the ICE-ORC CHP modelling tool developed in this thesis. The exergy flow of the exhaust-gas stream ($\dot{X}_{\mathrm{ex}}$) is calculated using both the physical and chemical exergy terms of the combustion products. All gases are assumed to be ideal, and the combustion process to be complete. The mass fractions of the various components in the mixture are obtained using the *AFR* of the engine. The physical exergy of the exhaust gases is calculated as follows:

$$\dot{X}_{\mathrm{ex}}{}^{\mathrm{ph}} = \dot{m}_{\mathrm{ex}}\left[\left(h_{\mathrm{ex}} - h_{\mathrm{ex,0}}\right) - T_0\left(s_{\mathrm{ex}} - s_{\mathrm{ex,0}}\right)\right]. \tag{37}$$

The chemical exergy of the exhaust gases mixture is estimated using:

$$\dot{X}_{\mathrm{ex}}{}^{\mathrm{ch}} = \dot{m}_{\mathrm{ex}}\left[\sum_{\mathrm{i=1}}^{\mathrm{n}} k_{\mathrm{i}}ex_{\mathrm{i}}{}^{\mathrm{ch}} + T_0\sum_{\mathrm{i=1}}^{\mathrm{n}}\mathrm{R}_{\mathrm{i}}k_{\mathrm{i}}\ln(k_{\mathrm{i}})\right], \tag{38}$$

$$\dot{X}_{\mathrm{ex}} = \dot{X}_{\mathrm{ex}}{}^{\mathrm{ph}} + \dot{X}_{\mathrm{ex}}{}^{ch}. \tag{39}$$

The jacket water circuit exergy flow ($\dot{X}_{\mathrm{jw}}$) is calculated using the physical exergy of the water stream because there is no change in the composition of the fluid:

$$\dot{X}_{\mathrm{jw}} = \dot{m}_{\mathrm{jw}}c_{\mathrm{p,air}}\left[\left(T_{\mathrm{jw,in}} - T_{\mathrm{jw,out}}\right) - T_0\ln\left(\frac{T_{\mathrm{jw},in}}{T_{\mathrm{jw,out}}}\right)\right]. \tag{40}$$

It should be noted that Eq. 33 is applicable in natural aspiration ICEs. To obtain the exergy destruction rate of turbocharged engines the exergy flow of the compressor, the intercooler heat exchanger and the turbine-expander are required. The exergy destruction rate at the compressor ($\dot{X}_{\mathrm{dest|comp}}$) is calculated using:

$$\dot{X}_{\mathrm{dest|comp}} = \dot{m}_{\mathrm{air}}\left[\left(h_{\mathrm{air,in}} - h_{\mathrm{air,out}}\right) - T_0\left(s_{\mathrm{air,in}} - s_{\mathrm{air,out}}\right)\right] + \dot{W}_{\mathrm{comp}}\ . \tag{41}$$

The exergy destruction rate at the intercooler ($\dot{X}_{\mathrm{dest|intr}}$) is calculated with:

$$\dot{X}_{\mathrm{dest|intr}} = \dot{m}_{\mathrm{air}}\left[\left(h_{\mathrm{air,in}} - h_{\mathrm{air,out}}\right) - T_0\left(s_{\mathrm{air,in}} - s_{\mathrm{air,out}}\right)\right] + \dot{m}_{\mathrm{jw}}c_{\mathrm{p,jw}}\left[\left(T_{\mathrm{jw,in}} - T_{\mathrm{jw,out}}\right) - T_0\ln\left(\frac{T_{\mathrm{jw,in}}}{T_{\mathrm{jw,out}}}\right)\right] \tag{42}$$

The exergy destruction rate of the expander ($\dot{X}_{\mathrm{dest|turb}}$) is calculated as follows:

$$\dot{X}_{\mathrm{dest|turb}} = \dot{m}_{\mathrm{ex}}\left[\left(h_{\mathrm{ex,in}} - h_{\mathrm{ex,out}}\right) - T_0\left(s_{\mathrm{ex,in}} - s_{\mathrm{ex,out}}\right)\right] - \dot{W}_{\mathrm{turb}}\ . \tag{43}$$

Finally, the exergy efficiency of the CHP-ICE is therefore estimated by dividing the engine power output over the exergy flow of the fuel:

$$\eta_{\mathrm{ICE,ex}} = \frac{\dot{W}_{\mathrm{ICE}}}{\dot{X}_{\mathrm{f}}}\ . \tag{44}$$

3.3 Organic Rankine cycle modelling

3.3.1 Thermodynamic modelling

In this thesis, subcritical ORC engines have been investigated, since they offer a good balance of power output, efficiency and costs [11] at the small-medium power scales, which are the focus of this work. The T-s diagram of a subcritical non-recuperative ORC is illustrated in Fig. 12a, while in Fig. 12 b, the T-s diagram of a subcritical recuperative ORC is also presented. On the same figures, the main ORC engine components and processes are highlighted. In Fig. 12a, Process 1-2 corresponds to the working fluid liquid pumping; Process 2-3 represents the heat addition to the cycle, from the heat carrier fluid (exhaust-gas stream); Process 3-4 represents the working-fluid vapour expansion; and Process 4-1 corresponds to the heat rejection from the ORC to the cooling water circuit. In the recuperative cycle (Fig. 12b) two additional processes occur; Process 2-2a, which represents the heat recovery of the cold liquid working fluid, from the (desuperheated) hot vapour; and Process 4-4a, which represents the heat rejection from the superheated hot vapour to the cold liquid working fluid, after the latter has exited the pump. The temperature drop of the heat carrier fluid (Process 5-6) and the cooling water temperature rise (Process 7-8), are also illustrated on the same diagrams.

A spatially lumped (quasi) steady-state thermodynamic model of the ORC engines presented in Fig. 12 was developed in MATLAB© [128], by applying the mass and energy balance equations to every component of the system. The ORC model is described by Eqs. 45-53. The assumptions considered for the ORC modelling are listed below:

- Steady-state operation of the ORC components;
- All HEXs were assumed to be of a counter-flow design, and adiabatic;
- The pressure drop on the working fluid side in the HEXs, piping etc. is negligible;

- The recuperator effectiveness was taken to be equal to ε_{rec} = 0.80, the pump isentropic efficiency was set to $\eta_{\text{pump,is}}$ = 0.65 [40], the expander isentropic efficiency to $\eta_{\text{exp,is}}$ = 0.70 [136], and the electric generator efficiency to η_{elg} = 0.95, similar to the ICE generator performance [9].

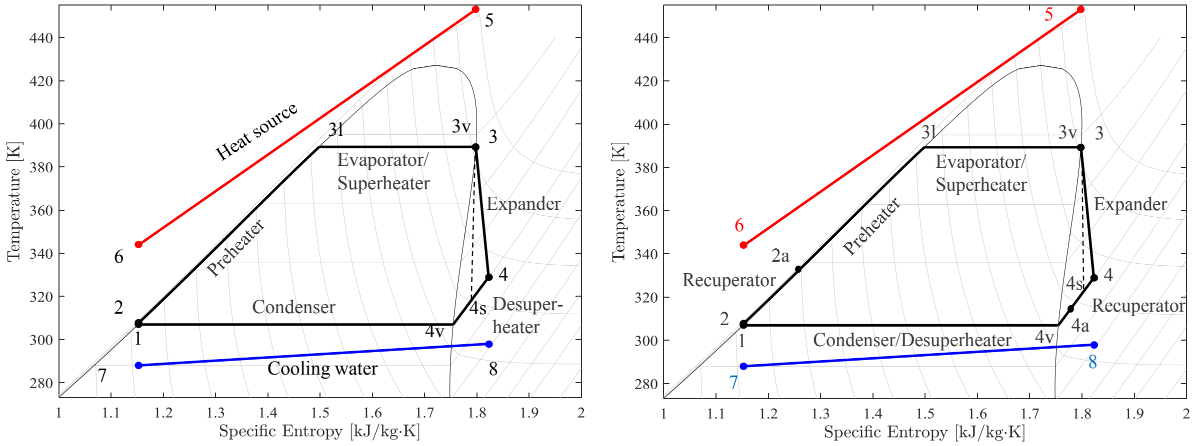

(a)

(b)

Fig. 12: Temperature (*T*) – specific entropy (*s*) diagram for: a) subcritical non-recuperative ORC, and b) subcritical recuperative ORC.

Heat flows into the cycle, in the evaporator (Process 2-3 or 2a-3). The heat input (rate) can be calculated either by using the working fluid enthalpy increase between States 2/2a and 3, or by using the heat-source stream temperature decrease between States 5 and 6, by assuming a constant c_{p} during this process:

$$\dot{Q}_{\text{evap}} = \dot{m}_{\text{wf}}(h_3 - h_2) = \dot{m}_{\text{hs}} c_{\text{p,ex}}(T_5 - T_6) \text{ (Non-recuperative ORC)} \tag{45}$$

$$\dot{Q}_{\text{evap}} = \dot{m}_{\text{wf}}(h_3 - h_{2\text{a}}) = \dot{m}_{\text{hs}} c_{\text{p,ex}}(T_5 - T_6) \text{ (Recuperative ORC)} \tag{46}$$

The normalised cycle superheating degree (*SHD*) is used to quantify the actual superheating temperature achieved in the cycle as a fraction of the maximum superheating temperature rise feasible, given the heat-source temperature and the pinch point (*PP*) temperature difference in the evaporator HEX. The definition of *SHD* is as follows:

$$SHD = \frac{T_3 - T_{3\text{v}}}{T_5 - PP_{\text{evap}} - T_{3\text{v}}} \, . \tag{47}$$

The calculation of the *SHD* requires the heat carrier fluid inlet temperature to the ORC engine (T_5), the working fluid saturation temperature during evaporation, which is also the temperature at beginning of the superheating process ($T_{3\text{v}}$), and the working fluid temperature at the exit of the evaporator HEX following superheating (T_3). In the limiting case of no superheating, *SHD* = 0, and the maximum value it can attain is *SHD* = 1.

After the evaporator, the superheated or saturated vapour enters the expander machine to generate power. For the purposes of this thesis, when the isentropic efficiency of the expander is assumed fixed, the value of η is selected to be equal to 0.7 for the nominal (design conditions) [136]. In the case where expander maps or expander efficiency correlations are used, the isentropic efficiency is predicted given the specific operating conditions. Once the expander isentropic efficiency is known the power output is estimated with:

$$\dot{W}_{\mathrm{exp}} = \dot{m}_{\mathrm{wf}}(h_3 - h_4)\eta_{\mathrm{mech}}\eta_{\mathrm{elg}} = \dot{m}_{\mathrm{wf}}(h_3 - h_{4s})\eta_{\mathrm{exp,is}}\eta_{\mathrm{mech}}\eta_{\mathrm{elg}} \,. \tag{48}$$

After the expansion process, the low-pressure superheated vapour at the expander exit flows into the desuperheater (non-recuperative ORC) or the recuperator HEX (recuperative ORC). In the latter case, the recuperator acts as a preheater, where the hot vapour heats the cold liquid working fluid after the pump:

$$\dot{Q}_{\mathrm{rec}} = \dot{m}_{\mathrm{wf}}(h_{2\mathrm{a}} - h_2) \text{ (Recuperative ORC).} \tag{49}$$

The addition of the recuperator device, reduces the load of the condenser, resulting in a smaller-sized component, while also reducing the overall heat input at the evaporator, which can act to improve the cycle thermal efficiency. However, the addition of one component to the ORC engine may have adverse effect on the cost of the system.

After the recuperator, the working fluid enters the condenser, where it rejects heat to the cooling water circuit:

$$\dot{Q}_{\mathrm{cond}} = \dot{m}_{\mathrm{wf}}(h_4 - h_1) = \dot{m}_{\mathrm{cw}}\, c_{\mathrm{p,w}}(T_8 - T_7) \text{ (Non-recuperative ORC),} \tag{50}$$

$$\dot{Q}_{\mathrm{cond}} = \dot{m}_{\mathrm{wf}}(h_{4\mathrm{a}} - h_1) = \dot{m}_{\mathrm{cw}}\, c_{\mathrm{p,w}}(T_8 - T_7) \text{ (Recuperative ORC).} \tag{51}$$

The circulation of the working fluid in the system and two pressure levels in the ORC engine are maintained by a pump, which consumes some of the generated power:

$$\dot{W}_{\mathrm{pump}} = \frac{\dot{m}_{\mathrm{wf}}\,(h_2 - h_1)}{\eta_{\mathrm{pump}}} \,. \tag{53}$$

3.3.2 Exergy analysis

The exergy destruction rate in each ORC engine component is evaluated, using the same methodology and assumption listed in Section 3.2.2. For each ORC engine component, the exergy destruction rate is calculated as follows:

$$\dot{X}_{\mathrm{dest|evap}} = \dot{m}_{\mathrm{hs}}[(h_5 - h_6) - T_0(s_5 - s_6)] + \dot{m}_{\mathrm{wf}}[(h_2 - h_3) - T_0(s_2 - s_3)] \text{ (Non-recuperative),} \tag{54}$$

$$\dot{X}_{\mathrm{dest|evap}} = \dot{m}_{\mathrm{hs}}[(h_5 - h_6) - T_0(s_5 - s_6)] + \dot{m}_{\mathrm{wf}}[(h_{2\mathrm{a}} - h_3) - T_0(s_{2\mathrm{a}} - s_3)] \text{ (Recuperative),} \tag{55}$$

$$\dot{X}_{\mathrm{dest|exp}} = \dot{m}_{\mathrm{wf}}[(h_3 - h_4) - T_0(s_3 - s_4)] + \dot{m}_{\mathrm{wf}}(h_3 - h_{4\mathrm{s}})\eta_{\mathrm{exp,is}}\eta_{\mathrm{mech}}\eta_{\mathrm{elg}} \,, \tag{56}$$

$$\dot{X}_{\mathrm{dest|rec}} = \dot{m}_{\mathrm{wf}}[(h_4 - h_{4\mathrm{a}}) - T_0(s_4 - s_{4\mathrm{a}})] + \dot{m}_{\mathrm{wf}}[\,(h_2 - h_{2\mathrm{a}}) - T_0(s_2 - s_{2\mathrm{a}})] \text{ (Recuperative),} \tag{57}$$

$$\dot{X}_{\mathrm{dest|cond}} = \dot{m}_{\mathrm{wf}}[(h_4 - h_1) - T_0(s_4 - s_1)] + \dot{m}_{\mathrm{cw}}[\,(h_7 - h_8) - T_0(s_7 - s_8)] \text{ (Non-recuperative),} \tag{58}$$

$$\dot{X}_{\text{dest|cond}} = \dot{m}_{\text{wf}}[(h_{4\text{a}} - h_1) - T_0(s_{4\text{a}} - s_1)] + \dot{m}_{\text{cw}}[\,(h_7 - h_8) - T_0(s_7 - s_8)] \text{ (Recuperative)}, \quad (59)$$

$$\dot{X}_{\text{dest|pump}} = \dot{m}_{\text{wf}}[(h_1 - h_2) - T_0(s_1 - s_2)] + \frac{\dot{m}_{\text{wf}}\,(h_2 - h_1)}{\eta_{\text{pump}}}\,. \quad (60)$$

The exergy efficiency of the ORC engine is calculated by dividing the ORC engine power output over the total exergy flow input to the system, i.e. the ICE exhaust gases exergy flow:

$$\eta_{\text{ORC,ex}} = \frac{\dot{W}_{\text{ORC}}}{\dot{X}_{\text{ex}}}\,. \quad (61)$$

Finally, for the total ICE-ORC CHP system, the exergy efficiency is estimated using the power outputs of the CHP-ICE and the ORC engine, as follows:

$$\eta_{\text{ICE}-\text{ORC,ex}} = \frac{\dot{W}_{\text{ICE}} + \dot{W}_{\text{ORC}}}{\dot{X}_f}\,. \quad (63)$$

3.4 Organic Rankine cycle working-fluid selection

Working fluid selection can strongly influence ORC engine operating conditions, performance, component size and cost. A number of working fluids have been investigated in this thesis, in order to obtain the most suitable candidate(s) for the high temperature ICE-ORC CHP applications. Due to the high computational cost of the optimisation, a pre-selection of working fluids has been performed. Apart from the good thermodynamic performance characteristics of the working fluids (high vapour density, low specific heat capacity, and high latent heat), their impact to the environment has been also gaining growing interest. This is due to the introduction of strict regulations imposing the gradual phase out of the use of refrigerants with high ozone depletion potential (ODP) and global warming potential (GWP). In the EU the so-called F-gas Regulation [84] has imposed a number of limitations to the use of refrigerants in the air-conditioning and refrigeration industry, which have recently been extended to cover power generation units, such as ORC engines. Therefore, technical solutions which are not constrained by such regulations are required to maximise the market penetration of ORC systems.

Further challenges apply in the ICE-ORC applications, when recovering heat from exhaust gases, due to the high operating temperatures of the working fluids, which may accelerate the fluids' chemical decomposition if not carefully considered at the design stage. Therefore, fluids with high critical temperatures/pressures are deemed most suitable for these applications. Vescovo and Spagnoli [93] investigated, among others, fluids such as toluene, biphenyl, diphenyl oxide, linear/alkylated hydrocarbons, and perfluoropolyether, for use at very high temperatures up to 400 °C (673 K), and reported ORC thermal efficiencies up to 30-34%. Refs. [26,30] also investigated among others, the use of R134a, R245fa, R1233zd, toluene and n-pentane for heat-source temperature of 300-400 °C (573-673 K), and obtained thermal efficiency of 16-23%. Li [92] studied fluids such as toluene, n-heptane, cyclohexane, R113 and R123 in high-temperature applications with a heat-source temperatures of 240-290 °C, obtaining ORC thermal efficiencies up to 31%. Uusitalo et al. [137] finally considered siloxanes for heat-source temperatures of up to 400 °C in a small-scale ORC experimental set-up, and achieved a thermal efficiency of approximately 16%.

Based on the above, the following refrigerants were selected for this study, as having good thermodynamic characteristics and low ODP and GWP values: R245fa, R152a, R1233zd, R1234ze, and R1234yf. R245fa is commonly used in commercial ORC engines provided by Bosch, Turboden, GE Clean start, Cryostar and Electratherm [29]. R1233zd is a very promising replacement of R123, which has shown high thermodynamic performance in previous efforts [26,138]. Similarly R1234ze and R1234yf are replacement refrigerants for R134a which is currently used in ORC units manufactured by Cryostar [30]. Apart from refrigerants, some hydrocarbons have been also investigated, including butane, pentane and hexane. It should be highlighted that hydrocarbons are listed as A3 category in the ASHRAE Classification [139], which includes fluids with low toxicity, but high flammability. Finally, toluene has been also examined, which is mostly suitable for high temperature waste heat, and it is used in ORC units manufactured by Triogen[59].

3.5 Heat exchanger design

3.5.1 Double-pipe heat exchanger

As discussed in previous sections, a key advantage of DPHEXs arises from their simple construction, form the fact that they are suitable for high pressure applications. Similarly to the PHEX designs. DPHEX can offer pure counter-flow heat transfer, while they can also be finned, but this increases their construction cost. Their key drawback is the high space requirements per kW of heat transferred, especially in comparison to PHEXs. In the following sections, the Nusselt number correlations used for predicting the HTCs in DPHEX are presented.

3.5.1.1 Evaporator

Key for predicting the HEX performance is the estimation of the HTCs achieved in the various unit sections, which also influence the total heat transfer area requirements of the HEX. For the single-phase zones (the preheater and the superheater sections), as well as for the heat-source carrier fluid, the well-established Nusselt number correlation proposed by Dittus-Boelter [140] has been used (Eqs.64-70), which can be also found in other papers in the ORC literature, such as those in Refs. [8,17]. To predict the HTCs in the two-phase zone of the evaporator, many Nusselt number correlations have been proposed in the literature. These can be classified into two main types of methods for boiling inside tubes: i) the asymptotic methods, which account for both thermal mechanisms of convection and nucleate boiling; and ii) the nucleate pool-boiling methods only [29]. A comparative study between the predictions of various Nusselt number correlations and test data, has been conducted by Garcia et al. [54], for R22. The authors reported that correlations such as those proposed by Cooper [43], Gorenflo [43,44] and Steiner [44,54] have predicted the evaporation saturation temperature with only ±2 °C deviation from the experimental data. Therefore, these correlations are deemed suitable for predicting the heat transfer rate during evaporation in tubes, and can be used for the design of DPHEXs .

A further comparative analysis has been performed in this thesis, to ensure the most well-suited Nusselt number correlation is selected for the analyses that follow (results have been published in Refs. [138,141]). Alternative Nusselt number correlations for the boiling process occurring during evaporation were selected, aiming to predict the heat transfer area requirements of alternative candidate working fluids. The correlations investigated covered both nucleate boiling and asymptotic methods, namely: i) the correlations of Steiner [44,54], Dobson [43,142], and Chen and Zuber [43,143], for the asymptotic method; and ii) the correlations of Cooper [43] and Gorenflo [44] for the nucleate pool boiling. The aforementioned correlations were applied to a number of working fluids, and the results for R245fa are presented here, which is a commonly used fluid in the ORC market. Similar trends in the two-phase evaporating heat transfer area requirements have been observed for all fluids investigated and are omitted here for brevity. The comparison exercise was conducted using as heat source the exhaust-gas stream from a CHP-ICE, namely ENER-G 2500 [17] ($\dot{m}_{\mathrm{ex}} = 3.52$ kg/s). The temperature of the heat source was then varied to reflect potential heat recovery processes occurring upstream of the ORC engine evaporator HEX.

The area requirements of the two-phase evaporating zone for R245fa at different heat-source temperatures and for alternative Nusselt number correlations is presented in Fig. 13a. It should be highlighted that the evaporator HEX duty (heat input) at every heat-source point is fixed, along with the temperature and pressure regime, and the working fluid mass flow rates. Consequently, any variations in the heat transfer area requirements, for the same heat-source temperature, are attributed to the Nusselt number correlations used, and not to the cycle operating conditions. With reference to the results, for low heat-source temperatures (Fig. 13a) and low differential between the evaporation saturation temperature and the heat source (Fig. 13b), the two-phase zone evaporating heat transfer area requirements vary significantly, depending on the correlation used. Under these operating conditions, the heat transfer area requirements vary from 3.5 m^2 when nucleate boiling correlations are used, up to 6 m^2 when asymptotic correlations are used (convective heat transfer is considered). This is attributed to the fact that correlations accounting for 100% nucleate boiling result in higher HTCs, and thus lower evaporator surface area requirements, than those obtained with correlations that account for convective and nucleate boiling phenomena.

In contrast, at high heat-source temperatures, i.e. at high temperature difference between the hot fluid and the evaporation saturation temperature, the deviations among the correlations' predictions are negligible. This trend is explained as follows; at high heat-source temperatures the nucleate boiling conditions prevail, while also the mass flow rates in the system increase (for higher heat input), therefore all correlations result in similar HTCs, and heat transfer area requirements. It is also noted that the heat flux (W/m^2) also increases while moving towards higher heat source temperatures, promoting more effective heat transfer, via nucleate boiling. Additionally, it is observed that for the same flow regime, the vertical tubes have better thermal performance (higher HTCs) than the horizontal designs, results in lower overall heat transfer area requirements (refer to Steiner results in Fig. 13a).

Based on these findings, it is concluded that in ORC engines operating with low heat-source temperatures, the evaporator HEX design should aim to maximise the HTCs in convection, to reduce the system size and thus its cost. On the contrary, for ORC engines operating with high heat-source conditions (temperature exceeding 300 °C [573 K]) such as those investigated in this thesis, the nucleate boiling phenomena prevail. Finally, in this thesis, the Nusselt number correlation developed by Chen and Zuber [43,143] has been used, which seems to slightly over-predict the heat transfer area requirements in comparison to other correlations, being on the conservative side of the equipment sizing. The correlation is presented in Eqs. 71-82.

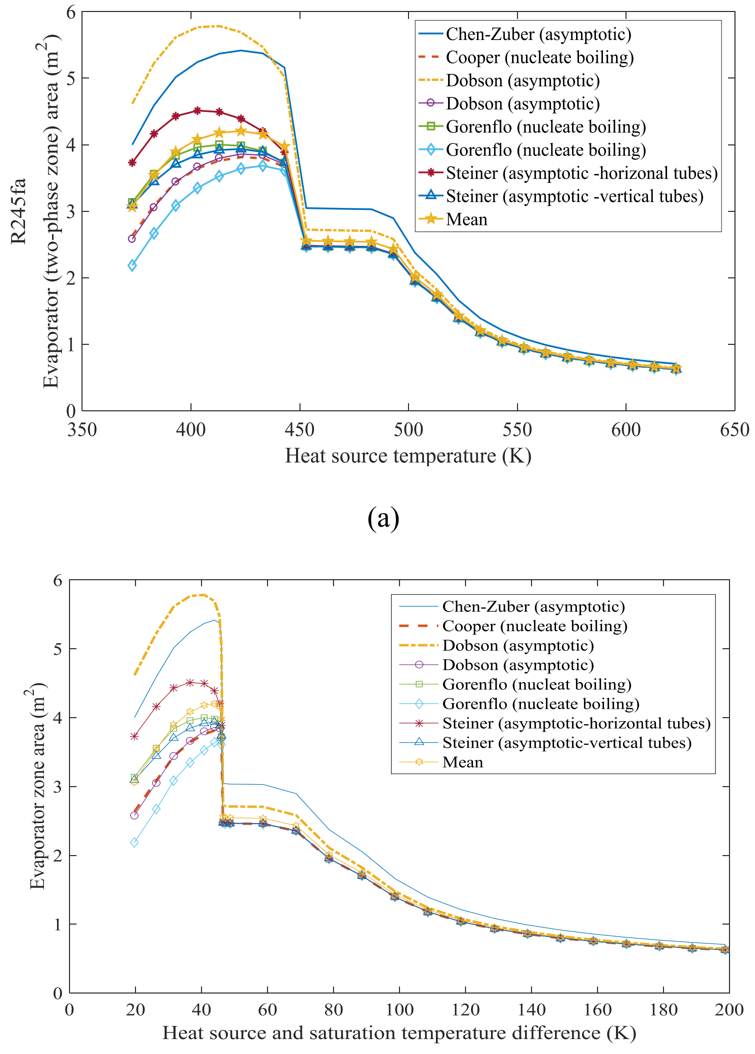

(a)

(b)

Fig. 13: Comparison between the heat transfer areas predicted from alternative Nusselt number correlations, for the evaporating two-phase zone, for a) different heat-source temperatures, and b) the difference between heat source temperature and evaporator saturation temperature.

Single-phase Nusselt number correlations

For the single-phase flow of the working fluid, the Dittus-Boelter [140] correlation was used (Eqs.64-67):

$$\alpha_{\mathrm{wf}} = Nu_{\mathrm{wf}} \frac{\lambda_{\mathrm{wf}}}{D_{\mathrm{in}}}\,, \tag{64}$$

$$Nu_{\mathrm{wf}} = 0.023\, {Re_{\mathrm{wf}}}^{0.8} {Pr_{\mathrm{wf}}}^{0.4} \text{ (heating)}\,, \tag{65}$$

$$Re_{\mathrm{wf}} = \frac{\rho_{\mathrm{wf}} u_{\mathrm{wf}} D_{\mathrm{hyd}}}{v_{\mathrm{wf}}}\,, \tag{66}$$

$$u_{\mathrm{wf}} = \frac{\dot{m}_{\mathrm{wf}}}{\rho_{\mathrm{wf}} S_{\mathrm{in}}}\,. \tag{67}$$

Similarly for the heat source (single-phase flow), the Dittus-Boelter [140] is applied (Eqs.68-70):

$$\alpha_{\mathrm{hs}} = Nu_{\mathrm{hs}} \frac{\lambda_{\mathrm{hs}}}{D_{\mathrm{out}}}\,, \tag{68}$$

$$Nu_{\mathrm{hs}} = 0.023\, {Re_{\mathrm{hs}}}^{0.8} {Pr_{\mathrm{hs}}}^{0.3} \text{ (cooling)}\,,$$

$$Re_{\mathrm{hs}} = \frac{\rho_{\mathrm{hs}} u_{\mathrm{hs}} D_{\mathrm{hyd}}}{v_{\mathrm{hs}}}\,, \tag{69}$$

$$u_{\mathrm{hs}} = \frac{\dot{m}_{\mathrm{hs}}}{\rho_{\mathrm{hs}} S_{\mathrm{out}}}\,. \tag{70}$$

Two-phase Nusselt number correlations

In the two-phase evaporation zone, for each section *i*, the quality of the working fluid is calculated, starting with saturated liquid ($x = 0$) and progressing to saturated vapour ($x = 1$). As aforementioned the asymptotic correlation proposed by Chen and Zuber [43,143] that considers both nucleate and convective boiling phenomena is then applied to every section (Eq. 71). The superposition method proposed by Chen although it has been originally developed for water, it has been also utilised in the literature in studies related to heat transfer for refrigerants, such as R134a.

$$\alpha_{\mathrm{wf}} = \alpha_{\mathrm{FC}} + \alpha_{\mathrm{NB}}\,, \tag{71}$$

with α_{wf} representing the total HTC of the two-phase flow, comprised of the forced convection HTC (α_{FC}) and the nucleate boiling HTC (α_{NB}). The forced convection coefficient (α_{FC}) is calculated using the HTC of the liquid phase of the working fluid inside the tubes, and a forced convection multiplier (F_{FC}):

$$\alpha_{\mathrm{FC}} = F_{\mathrm{FC}}\, \alpha_{\mathrm{wf,l}}\,. \tag{72}$$

The forced convection multiplier proposed by Chen [43,143] is calculated using:

$$F_{\mathrm{FC}} = 2.35 \left(\frac{1}{X_{\mathrm{tt}}} + 0.213\right)^{0.736}. \tag{73}$$

The Lockhart-Martinelli parameter (X_{tt}) is estimated using the Blasius equation for the friction factor [43]:

$$X_{\mathrm{tt}} = \left(\frac{1-x}{x}\right)^{0.875} \left(\frac{\rho_{\mathrm{wf,g}}}{\rho_{\mathrm{wf,l}}}\right)^{0.5} \left(\frac{\mu_{\mathrm{wf,l}}}{\mu_{\mathrm{wf,g}}}\right)^{0.125} . \tag{74}$$

The Reynolds number and the HTC inside the tubes for the working fluid liquid phase, flowing alone inside the channel is calculated using:

$$Re_{\mathrm{wf,l}} = \frac{\dot{m}_{\mathrm{wf}}(1-x)D_{\mathrm{hyd}}}{\mu_{\mathrm{wf,l}}} , \tag{75}$$

$$\alpha_{\mathrm{wf,l}} = 0.023\ \frac{\lambda_{\mathrm{wf,l}}}{D_{\mathrm{in}}} {Re_{\mathrm{wf,l}}}^{0.8} {Pr_{\mathrm{wf,l}}}^{1/3} . \tag{76}$$

The nucleate boiling coefficient (α_{NB}) is calculated with:

$$\alpha_{\mathrm{NB}} = S_{\mathrm{f}}\, \alpha_{\mathrm{fz}}, \tag{77}$$

where, S_{f} corresponds to the suppression factor proposed by Chen [143] and α_{fz} is the HTC proposed by Foster and Zuber for nucleate boiling, calculated as follows [43]:

$$a_{\mathrm{fz}} = \frac{0.00122\, {\Delta T_{\mathrm{sat}}}^{0.24}\, {\Delta P_{\mathrm{sat}}}^{0.75} {c_{\mathrm{p,wf,l}}}^{0.45} {\rho_{\mathrm{wf,l}}}^{0.45} {\lambda_{\mathrm{wf,l}}}^{0.45}}{{\sigma_{\mathrm{wf}}}^{0.5}\, {h_{\mathrm{lg}}}^{0.24}\, {\eta_{\mathrm{wf,l}}}^{0.29}\, {\rho_{\mathrm{wf,g}}}^{0.24}} , \tag{78}$$

$$S_{\mathrm{f}} = \frac{1}{1+2.53\times10^{-0.6} {Re_{\mathrm{wf}}}^{1.17}} , \tag{79}$$

with:

$$\Delta T_{\mathrm{sat}} = T_{\mathrm{w}} - T_{\mathrm{sat}} , \tag{80}$$

$$\Delta P_{\mathrm{sat}} = P_{\mathrm{sat}} \left\{ \exp\left[\frac{h_{\mathrm{lg}} M}{R}\left(\frac{1}{T_{\mathrm{sat}}} - \frac{1}{T_{\mathrm{w}}}\right)\right] - 1 \right\} . \tag{81}$$

The two-phase Reynolds number is then obtained from:

$$Re_{\mathrm{wf}} = {F_{\mathrm{FC}}}^{1.25}\, Re_{\mathrm{wf,l}} . \tag{82}$$

Pressure-drop correlations

Another important factor to consider when sizing the HEXs, is the pressure drop experienced by the heat-source carrier fluid and the working fluid. The pressure drop for single-phase flows was calculated, as a function of the velocity of the fluid, the diameter of the tubes, the length of the HEX, and a friction coefficient [43]:

$$Re = \frac{\rho u D}{\mu} , \tag{83}$$

$$f = 0.046\, Re^{-0.2} , \tag{84}$$

$$P_{\mathrm{drp}} = 4f \frac{L}{D} \frac{\rho u^2}{2} . \tag{85}$$

For the two-phase flow in the evaporating zone, the pressure drop calculation developed by Chisholm for two-phase flows has been used, as provided in Ref. [43]. This correlation has been compared against test data and other pressure drop correlations, and shown to slightly overestimate the pressure drop, offering some contingency in the HEX design pressure drop. The pressure drop (in Pa/m) for the two-phase flow is estimated using the following pressure gradient:

$$-\left(\frac{\mathrm{d}P}{\mathrm{d}z}\right)_{\mathrm{wf}} = -{\varphi_{\mathrm{chis}}}^2\left(\frac{\mathrm{d}P}{\mathrm{d}z}\right)_{\mathrm{L}}, \tag{86}$$

where: (87)

$${\varphi_{\mathrm{chis}}}^2 = 1 + ({Y_{\mathrm{chis}}}^2 - 1)\left[B_{\mathrm{chis}} x^{\frac{2-n}{2}}(1-x)^{\frac{2-n}{2}} + x^{2-n}\right] \text{ with } n = 0.25 \text{ [43]}, \tag{88}$$

$$Y_{\mathrm{chis}} = \sqrt{\left(\frac{\mathrm{d}P}{\mathrm{d}z}\right)_{\mathrm{G}} / \left(\frac{\mathrm{d}P}{\mathrm{d}z}\right)_{\mathrm{L}}}, \tag{89}$$

$$B_{\mathrm{chis}} = \frac{55}{{\dot{m}_{\mathrm{wf}}}^{0.5}} \text{ for } 0 < Y_{\mathrm{chis}} < 9.5, \tag{90}$$

$$B_{\mathrm{chis}} = \frac{520}{Y_{\mathrm{chis}}\,{\dot{m}_{\mathrm{wf}}}^{0.5}} \text{ for } 9.5 \le Y_{\mathrm{chis}} < 28, \tag{91}$$

$$B_{\mathrm{chis}} = \frac{15000}{{Y_{\mathrm{chis}}}^2\,{\dot{m}_{\mathrm{wf}}}^{0.5}} \text{ for } 28 \le Y_{\mathrm{chis}}. \tag{92}$$

The respective pressure gradients are estimated as follows:

$$-\left(\frac{\mathrm{d}P}{\mathrm{d}z}\right)_{\mathrm{L}} = \frac{2 f_{\mathrm{wf,L}} {\dot{m}_{\mathrm{wf}}}^2}{D_{\mathrm{hyd}} \rho_{\mathrm{wf,l}}}, \tag{93}$$

$$-\left(\frac{\mathrm{d}P}{\mathrm{d}z}\right)_{\mathrm{G}} = \frac{2 f_{\mathrm{wf,G}} {\dot{m}_{\mathrm{wf}}}^2}{D_{\mathrm{hyd}} \rho_{\mathrm{wf,g}}}. \tag{94}$$

The friction factor for the the liquid only, and the gas only flows are calculated with:

$$f_{\mathrm{wf,L}} = 0.079\, {Re_{\mathrm{wf,L}}}^{-0.25}, \tag{95}$$

$$f_{\mathrm{wf,G}} = 0.079\, {Re_{\mathrm{wf,G}}}^{-0.25}. \tag{96}$$

The Reynolds number for each flow regime is calculated as follows:

$$Re_{\mathrm{wf,L}} = \frac{\dot{m}_{\mathrm{wf}} D_{\mathrm{hyd}}}{\mu_{\mathrm{wf,l}}}, \tag{97}$$

$$Re_{\mathrm{wf,G}} = \frac{\dot{m}_{\mathrm{wf}} D_{\mathrm{hyd}}}{\mu_{\mathrm{wf,g}}}. \tag{98}$$

Finally, the *U*-value for every section of the evaporator HEX is calculated using the HTCs of the working fluid and the heat source, and then the area requirements per section are obtained using the LMDT method:

$$\frac{1}{U} = \frac{1}{\alpha_{\mathrm{hs}}} + \alpha_{\mathrm{wall}} + \frac{1}{\alpha_{\mathrm{wf}}}, \tag{99}$$

$$\mathrm{LMDT} = \frac{(T_{\mathrm{hot,i}} - T_{\mathrm{c,o}}) - (T_{\mathrm{hot,o}} - T_{\mathrm{c,i}})}{\ln\left(\frac{T_{\mathrm{hot,i}} - T_{\mathrm{c,o}}}{T_{\mathrm{hot,o}} - T_{\mathrm{c,i}}}\right)}, \tag{100}$$

$$A_i = \frac{\dot{Q}_i}{U_i \mathrm{LMDT}_i}\,. \tag{101}$$

3.5.1.2 Condenser

Single-phase Nusselt number correlations

Similarly to the evaporator HEX sizing presented in Section 3.5.1.1, for the HTC calculation of the single-phase flows in the condenser, the Nusselt number correlation presented by Dittus-Boelter [140] has been used for the working fluid and the cooling water circuit, as was previously presented in Eqs. 64-70.

Two-phase Nusselt number correlations

To obtain the HTCs in the two-phase condensing zone, there is a wide range of Nusselt number correlations available in the literature, which can be classified into those that account for: i) gravity driven condensation only; or ii) shear driven condensation only; or iii) a combination of gravity and shear driven condensation. In this thesis, alternative Nusselt number correlations for condensing phenomena have been compared, for different working fluids, to identify potential variations on the predicted heat transfer area requirements (the results of this analysis have been presented in Ref. [141]). The correlations compared include those proposed by Dobson [142], Shah [8,144] and Chaddock and Chato [43], for combined shear and gravity driven phenomena; those proposed by Hewitt [43] for gravity only condensation; and those proposed by Mikheev as presented by Hewitt [43] for shear driven condensation only. The heat transfer area requirements obtained for different heat-source temperature for every Nusselt number correlation are resented in Fig. 14, for R245fa.

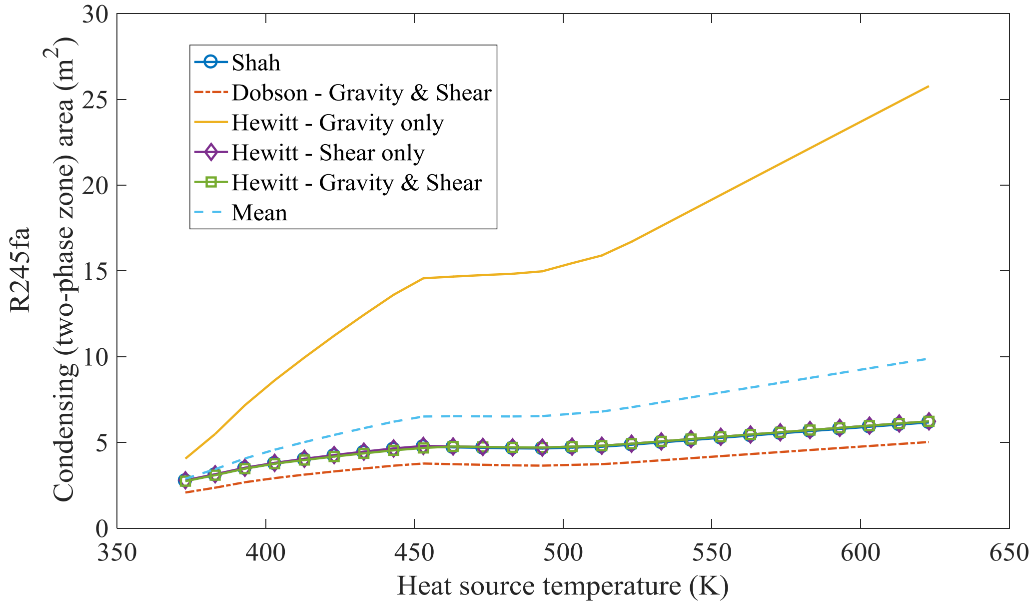

Fig. 14: Comparison between the heat transfer areas predicted by alternative Nusselt number correlations for the condenser two-phase zone, for different heat-source temperatures.

In general, it is noted that all correlations give similar results across the full range of heat-source temperature investigated, with the exemption of the gravity-only correlation, which as expected, has the highest heat transfer area requirements. All other correlations accounting for both condensing phenomena result in lower heat transfer area requirements, while the deviations within those predictions are very low. Similar results, for the condensing section were found for all working fluids investigated [141]. The correlation of Shah is on the high side of the area predictions (excluding gravity-only correlations), providing conservative estimates of the DHEX area requirements. Based on these findings the correlation of Shah [8,144] has been used to obtain the HTCs for condensation inside tubes, which is also commonly found in the literature, among others, in Refs. [8,17,53].

The HTC for the two-phase flow α_{wf} is calculated using the HTC of the liquid fluid only ($\alpha_{\mathrm{wf,L}}$) multiplied by a factor which is a function of the critical pressure ratio at the condenser (P_{r}):

$$\alpha_{\mathrm{wf}} = \alpha_{\mathrm{wf,L}}\left(0.55 + \frac{2.09}{{P_r}^{0.38}}\right), \tag{102}$$

where:

$$\alpha_{\mathrm{wf,L}} = Nu_{\mathrm{wf,L}}\frac{\lambda_{\mathrm{wf,L}}}{D_{\mathrm{in}}}, \tag{103}$$

$$Nu_{\mathrm{wf,L}} = 0.023{Re_{\mathrm{wf,L}}}^{0.8}{Pr_{\mathrm{wf,L}}}^{0.3}, \tag{104}$$

$$Re_{\mathrm{wf,L}} = \frac{\dot{m}_{\mathrm{wf}}D_{\mathrm{hyd}}}{\mu_{\mathrm{wf,L}}}, \tag{105}$$

$$P_{\mathrm{r}} = \frac{P_{\mathrm{con}}}{P_{\mathrm{crit}}}. \tag{106}$$

The condenser HEX *U*-value is finally obtained using the cooling water and working fluid HTCs, while the heat transfer are requirements are calculated using the LMDT method (Eqs. 98-101):

$$\frac{1}{U} = \frac{1}{\alpha_{\mathrm{cw}}} + \alpha_{\mathrm{wall}} + \frac{1}{\alpha_{\mathrm{wf}}}. \tag{107}$$

Pressure drop correlations

The pressure drop in the condenser HEX is calculated using the same pressure drop correlations proposed for the evaporator. For the single-phase flows of the cooling water and the desuperheating process of the working fluid Eqs. 83-85 have been used. For the condensation process of the working fluid Eqs. 86-99 have been used.

3.5.2 Plate heat exchanger

There is a great range of designs for PHEXs in the market, depending on the application and the operating conditions. The plates can be corrugated to enhance heat transfer, and improve rigidity, but at the expense of higher pressure drop. The corrugations, and the narrow paths developed for the flow, result in higher HTCs and *U*-values, increasing the heat transfer rate per m^2 of heat transfer area.

Consequently, PHEXs are suitable for applications where the physical size of the system is important. The key disadvantage of gasketed PHEXs is limitations in the operating pressure and temperature levels of the plates, which may affect the integrity of the seals (of typical pressed plate fabrication). Welded or fusion welded PHEXs, made of stainless or galvanised steel can be used instead for higher operating temperatures, while they can withstand high pressures. However, such type of construction increases the cost of the PHEXs, in terms of GBP/m^2.

3.5.2.1 Evaporator

Single-phase Nusselt number correlations

For the single-phase flows in PHEXs, the correlations proposed by Chisholm and Waniarchi [55], Martin [44] and Muley [145] are commonly used in the literature, to estimate the HTCs and thus the heat transfer area requirements. In this thesis, the correlation proposed by Chisholm and Waniarchi [55] has been used, since it is found to give conservative HTC values, when compared to the results obtained with Muley [145] and Martin [44]. These results are aligned with the findings summarised in Ref. [55]. The Chisholm and Waniarchi correlation has been also compared to experimental data by Focke [146], and was found to match the recorded values within 15-20%, for Re>1000 and β between π/3 and π/6. The Chisholm and Waniarchi [55] correlation is presented in the following equations:

$$\alpha_{\mathrm{wf}} = Nu_{\mathrm{wf}} \frac{\lambda_{\mathrm{wf}}}{D_{\mathrm{hyd}}}, \tag{108}$$

$$Nu_{\mathrm{wf}} = 0.724(6\beta/\pi)^{0.646} {Re_{\mathrm{wf}}}^{0.583} {Pr_{\mathrm{wf}}}^{1/3}, \tag{109}$$

$$Re_{\mathrm{wf}} = \frac{\rho_{\mathrm{wf}} u_{\mathrm{wf}} D_{\mathrm{hyd}}}{v_{\mathrm{wf}}}, \tag{110}$$

$$u_{\mathrm{wf}} = \frac{\dot{m}_{\mathrm{wf}}}{\rho_{\mathrm{wf}} S_{\mathrm{p}}}. \tag{111}$$

Similarly, for the heat source (single-phase flow), the Chisholm and Waniarchi correlation [55] is applied:

$$\alpha_{\mathrm{hs}} = Nu_{\mathrm{hs}} \frac{\lambda_{\mathrm{hs}}}{D_{\mathrm{hyd}}}, \tag{112}$$

$$Nu_{\mathrm{hs}} = 0.724(6\beta/\pi)^{0.646} {Re_{\mathrm{hs}}}^{0.583} {Pr_{\mathrm{hs}}}^{1/3}, \tag{113}$$

$$Re_{\mathrm{hs}} = \frac{\rho_{\mathrm{hs}} u_{\mathrm{hs}} D_{\mathrm{hyd}}}{v_{\mathrm{hs}}}, \tag{114}$$

$$u_{\mathrm{hs}} = \frac{\dot{m}_{\mathrm{hs}}}{\rho_{\mathrm{hs}} S_{\mathrm{p}}}. \tag{115}$$

Finally, the *U*-value and area requirements for every section of the evaporator are calculated using Eqs. 99-101.

Two-phase Nusselt number correlations

Alternative correlations for predicting the HTCs in the two-phase evaporating zone in PHEXs have been compared, against experimental data, in Ref. [55]. The correlations investigated included, among others, those proposed by Han [147], Hsieh [148], and Yan and Lin [149], which are commonly found in the ORC engine HEX design literature. The findings of the comparison exercise indicate that the correlation proposed by Yan and Lin [149] gives the highest HTC estimates, while the correlation of Han [147], gives conservative HTC predictions. When the same correlations were compared to experimental data, it was observed that the temperature prediction for all correlations was within ± 2°C from the recorded values. These findings indicate the suitability of those correlations for PHEX design studies. Therefore, in this thesis, the correlation developed by Han [147] has been used, to allow for some contingency in the surface area estimation of the two-phase PHEX evaporator zone.

The correlation is presented in Eqs. 116-122. The HTC in each section i is calculated using the quality x_i of the working fluid at this section as follows:

$$\alpha_{\mathrm{wf}} = c_3 \frac{\lambda_{\mathrm{wf,l}}}{D_{\mathrm{hyd}}} Re_{\mathrm{wf,eq}}{}^{\mathrm{c}_4} Bo_{\mathrm{eq}}^{0.3} Pr_{\mathrm{wf,l}}{}^{0.4}, \tag{116}$$

where:

$$Re_{\mathrm{wf,eq}} = \frac{G_{\mathrm{wf,eq}} D_{\mathrm{hyd}}}{\mu_{\mathrm{wf,l}}}, \tag{117}$$

$$G_{\mathrm{wf,eq}} = G_{\mathrm{wf,p}} \left[1 - x + x \left(\frac{\rho_{\mathrm{wf,l}}}{\rho_{\mathrm{wf,v}}}\right)^{0.5}\right], \tag{118}$$

$$Bo_{\mathrm{wf,eq}} = \frac{\dot{q}_{\mathrm{wf}}}{G_{\mathrm{wf,eq}} h_{\mathrm{lg}}}, \tag{119}$$

$$\dot{q}_{\mathrm{wf,eq}} = \frac{\dot{Q}_{\mathrm{ev}}}{A_{\mathrm{ev}}}, \tag{120}$$

$$c_3 = 2.81 \left(\frac{z}{D_{\mathrm{hyd}}}\right)^{-0.041} \beta^{-2.83}, \tag{121}$$

$$c_4 = 0.746 \left(\frac{z}{D_{\mathrm{hyd}}}\right)^{-0.082} \beta^{0.61}. \tag{122}$$

$Re_{\mathrm{wf,eq}}$ is the equivalent Reynolds number, $G_{\mathrm{wf,eq}}$ is the equivalent mass velocity, $Bo_{\mathrm{wf,eq}}$ is the equivalent boiling number, $\dot{q}_{\mathrm{wf,eq}}$ is the specific heat flux, and c_3/c_4 are coefficients related to the geometry of the PHEX.

Pressure drop correlations

The pressure drop calculation for the single-phase zones, in chevron plates with angle β, is calculated using the correlation developed by Martin [44] for both the working fluid and the heat-source, as follows:

$$P_{\mathrm{drp}}{}^{fr} = 4f_{\mathrm{p}}\frac{L_{\mathrm{p}}}{D_{\mathrm{hyd}}}\frac{G_{\mathrm{p}}{}^{2}}{2\rho}, \tag{123}$$

$$\frac{1}{\sqrt{f_{\mathrm{p}}}} = \frac{\cos\beta}{(0.18\tan\beta+0.36\sin\beta+f_0/\cos\beta)^{0.5}} + \frac{1-\cos\beta}{\sqrt{3.8f_1}}, \tag{124}$$

$$G_{\mathrm{p}} = \frac{\dot{m}}{S_{\mathrm{p}}}, \tag{125}$$

where f_{p} is the Fanning friction coefficient for one plate (one passage), and G_{p} is the mass velocity. The Fanning factor is estimated using the chevron angle β, and the Fanning coefficients (f_0/f_1) for β=0° and β=90°, respectively:

$$f_0 = \frac{64}{Re} \text{ and } f_1 = \frac{597}{Re} + 3.85, \text{ for Re} < 2{,}000\ , \tag{126}$$

$$f_0 = (1.8\log_{10}Re - 1.5)^{-2} \text{ and } f_1 = \frac{39}{Re^{0.289}}, \text{ for Re} \geq 2{,}000\ . \tag{127}$$

The pressure drop of the working fluid, while evaporating is calculated using the frictional and acceleration pressure drop terms, in one passage, in line with the correlations proposed by Han [147]. The frictional pressure drop is calculated with:

$$P_{\mathrm{drp,wf}}{}^{fr} = 4f_{\mathrm{p,wf}}\frac{L_{\mathrm{p}}}{D_{\mathrm{hyd}}}\frac{G_{\mathrm{wf,eq}}{}^{2}}{2\rho_{\mathrm{wf,l}}}, \tag{128}$$

$$f_{\mathrm{p,wf}} = c_1 Re_{\mathrm{wf,eq}}{}^{c_2}, \tag{129}$$

$$c_1 = 64{,}710\left(\frac{z}{D_{\mathrm{hyd}}}\right)^{-5.27}\left(\frac{\pi}{2}-\beta\right)^{-3.03}, \tag{130}$$

$$c_2 = -1.314\left(\frac{z}{D_{\mathrm{hyd}}}\right)^{-0.62}\left(\frac{\pi}{2}-\beta\right)^{-0.47}. \tag{131}$$

The acceleration pressure drop over one plate is estimated with:

$$P_{\mathrm{drp,wf}}{}^{ac} = \left(\frac{G_{\mathrm{wf,eq}}{}^{2}x}{\rho_{\mathrm{wf,l}}-\rho_{\mathrm{wf,out}}}\right)_{\mathrm{out}} - \left(\frac{G_{\mathrm{wf,eq}}{}^{2}x}{\rho_{\mathrm{wf,l}}-\rho_{\mathrm{wf,out}}}\right)_{\mathrm{in}}. \tag{132}$$

3.5.2.2 Condenser

Single-phase Nusselt number correlations

To obtain the HTC of the single-phase zone of the condenser (desuperheater) and of the cooling water circuit, the correlation provided by Chisholm and Waniarchi [55] has been used, as presented in Section 3.5.2.1. Similarly, the calculation of the pressure drop for the single-phase flows, in chevron plates with angle β, is calculated using the correlation developed by Martin [44], as described in Eqs. 123-127.

Two-phase Nusselt number correlations

Garcia et al. [55] compared various Nusselt number correlations that describe the two-phase condensing zone in PHEXs, against experimental data. The results indicate that the HTC values obtained from the correlation developed by Han [150] are in good agreement with the test data. Therefore, in this thesis, the correlation proposed by Han [150] has been used, to obtain the condenser two-phase section area requirements. The HTC in each section *i* is calculated using:

$$\alpha_{\mathrm{wf}} = c_7 \frac{\lambda_{\mathrm{wf,l}}}{D_{\mathrm{hyd}}} Re_{\mathrm{wf,eq}}{}^{c_8} Pr_{\mathrm{wf,l}}{}^{1/3}, \tag{133}$$

where, $Re_{\mathrm{wf,eq}}$ is the equivalent Reynolds number estimated using Eqs. 117-118. The coefficients c_7/c_8 are calculated as follows:

$$c_7 = 11.22(\frac{z}{D_{\mathrm{hyd}}})^{-2.83}\beta^{-4.5}, \tag{134}$$

$$c_8 = 0.35(\frac{z}{D_{\mathrm{hyd}}})^{0.23}\beta^{1.48}\ . \tag{135}$$

The *U*-value for every section of the condenser two-phase zone is calculated using the HTCs of the working fluid and the cooling water. Then the area requirements per section are obtained using the LMDT method.

Pressure drop correlations

The pressure drop in the two-phase condensing zone (working fluid circuit) is calculated using the correlations developed by Han [150].

$$P_{\mathrm{drp,wf}}{}^{fr} = 4 f_{\mathrm{p,wf}} \frac{L_{\mathrm{p}}}{D_{\mathrm{hyd}}} \frac{G_{\mathrm{wf,eq}}{}^{2}}{2\rho_{\mathrm{wf,l}}}\ , \tag{136}$$

$$f_{\mathrm{p,wf}} = c_5 Re_{\mathrm{wf,eq}}{}^{c_6}. \tag{137}$$

$$c_5 = 3521.1(\frac{z}{D_{\mathrm{hyd}}})^{4.17}\beta^{-7.75}, \tag{138}$$

$$c_6 = -1.024(\frac{z}{D_{\mathrm{hyd}}})^{0.0925}\beta^{-1.3}\ . \tag{139}$$

3.6 Expander design

3.6.1 Piston expander

Despite the advantages of piston expanders, by reviewing the literature of small-medium scale ORC engines, it is highlighted that there is only a limited number of studies that have investigated the use of piston expanders in detail, or considered its performance under variable operating conditions. Within this limited literature, the majority of the studies have either focused on the piston expander design in isolation of the remaining system, or have considered the deployment of piston expanders in ORC engines for automotive applications. In this thesis, the deployment of piston expanders in stationary waste heat recovery applications with ORC engines is investigated, under design and off-design operation.

To predict the piston expander efficiency when operating within an ORC system, performance maps have been used. The performance maps have been generated, using a dynamic lumped-mass model for reciprocating expander machines. The time-resolved piston expander model is presented and validated in Refs. [138,151]. The model captures three major loss mechanisms, namely: i) losses through the valves; ii) mass leakage at the piston rings; and iii) heat transfer losses between the gas and the cylinder walls (Fig. 15). The frictional losses account for 13% to 25% of the indicated power [71,152,153], and generator losses are a further 5% of the shaft power, with both applied at a post-processing stage. While there is some uncertainty in the estimation of frictional losses, for fixed-speed operation the frictional loss can be roughly approximated as constant for a given machine [154], and hence a fair comparison can be made between different operating points at on- and off-design conditions.

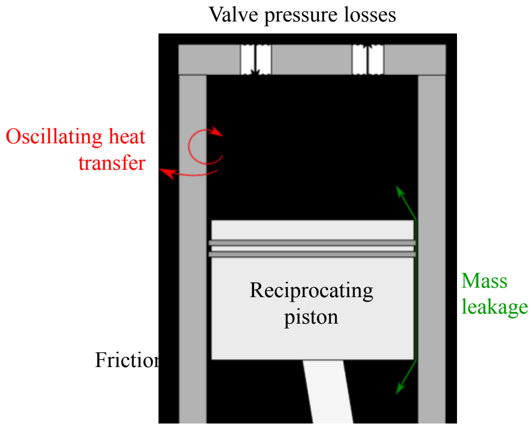

Fig. 15: Schematic diagram of reciprocating piston expander and loss mechanisms. Figure reproduced from Ref. [138].

The lumped-mass model solves dynamic mass and energy conservation equations [151]:

$$\frac{\mathrm{d}m}{\mathrm{d}t} = \dot{m}_{\mathrm{in}} - \dot{m}_{\mathrm{out}} \,, \tag{140}$$

$$\frac{\mathrm{d}}{\mathrm{d}t}(mh) = \dot{Q}_{\mathrm{w}} + V\frac{\mathrm{d}P}{\mathrm{d}t} + \sum \dot{m}_{\mathrm{in}} h_{\mathrm{in}} - \sum \dot{m}_{\mathrm{out}} h_{\mathrm{out}} \,, \tag{141}$$

with *m* representing the mass of the gas/vapour in the cylinder; $\dot{m}_{\mathrm{in}}$ and $\dot{m}_{\mathrm{out}}$ representing the intake and exhaust mass flow rates; *h* is the specific enthalpy; $\dot{Q}_{\mathrm{w}}$ is the heat transfer rate between the gases and the cylinder wall; and *P* and *V* are the (time-varying) cylinder pressure and volume.

The flows through the intake and exhaust valves are modelled using the equations for flows through nozzles (1-D modelling), which are assumed isentropic, until they reach the valve throat. A discharge coefficient is then applied to capture the real gas-flow effects [155]. The expander valves are assumed to be popper type, with the minimum area available to the flow being determined by the valve position. Leakages through the valves are neglected, and the duct flow from the intake manifold/to the exhaust manifold are considered ideal with no losses:

$$\dot{m}_{\mathrm{in/out}} = C_{\mathrm{D}}\, A_{\mathrm{R}} \sqrt{2(h_{\mathrm{up}} - h_{\mathrm{R}})} \,, \tag{142}$$

$$C_{\mathrm{D}} = 0.85 - 0.25\left(\frac{P_{\mathrm{dn}}}{P_{\mathrm{up}}}\right)^2 , \tag{143}$$

$$h_{\mathrm{R}} = h(P_{\mathrm{dn}}, S_{\mathrm{up}}) , \tag{144}$$

with A_{R} representing the minimum cross-sectional area experienced by the flow through the valve. The various quantities are measured upstream ('up'), downstream ('dn') or at the minimum area or throat ('R').

A crevice model is used to simulate the mass leakage past the piston rings [151], with the two piston rings dividing the volume between the piston and the cylinder walls into three crevices. A pressure-driven model is used to predict the mass flow rate between the crevices, with the use of a discharge coefficient as follows:

$$\frac{\mathrm{d}m_{\mathrm{crev}}}{\mathrm{d}t} = \dot{m}_{\mathrm{in,crev}} - \dot{m}_{\mathrm{out,crev}} , \tag{145}$$

$$\dot{m}_{\mathrm{in/out,crev}} = C_{\mathrm{d}}\, \rho_{\mathrm{crev}}\, A_{\mathrm{gap}} \sqrt{2(h_{\mathrm{up}} - h_{\mathrm{gap}})} , \tag{146}$$

$$h_{\mathrm{gap}} = h(P_{\mathrm{dn}}, S_{\mathrm{up}}) . \tag{147}$$

The temperature of the cylinder walls is assumed uniform and constant and is set equal to the mean gas temperature over a cycle by an iterative process. The expander is considered to be well insulated, such that there is no net heat transfer to the surroundings during steady-state operation.

The heat transfer between the gases and the cylinder wall, during the expansion and compression strokes is calculated using a complex Nusselt number correlation from Lekic and Kok [156]. The complex term of the correlation captures the heat transfer component that is out-of-phase with the bulk temperature difference between the gases and the cylinder, due to the boundary layer effects during compression and expansion. During the intake and exhaust strokes only the real part of this correlation is used, since the out-of-phase heat transfer effects are only active under pressure changes [157]:

$$\dot{q}_{\mathrm{w}} = -\frac{\lambda}{D_{\mathrm{h}}}\left[Nu_{\mathrm{r}}(T - T_{\mathrm{w}}) + \frac{1}{\omega} Nu_{\mathrm{i}} \frac{\mathrm{d}T}{\mathrm{d}t} \right] , \tag{148}$$

$$D_{\mathrm{h}} = \frac{4V}{A_{\mathrm{w}}} , \tag{149}$$

where $\dot{q}_{\mathrm{w}}$ is the heat flux rate from wall to gas, λ is the instantaneous thermal conductivity, D_{h} is the instantaneous hydraulic diameter based on cylinder volume V and surface area A_{w}, Nu_{r} and Nu_{i} are the real and imaginary Nusselt number components, and ω is the crankshaft speed in radians per second. The reader can refer to Refs. [138,151,157] for the piston expander modelling details and validation.

Finally, the isentropic efficiency of the expander $\eta_{\mathrm{exp,is}}$ is defined based on the indicated expander power $\dot{W}$ and the enthalpy change of an equivalent isentropic and adiabatic expansion process [151,157], whilst when the mechanical losses on the shaft are considered this is defined as the effective expander efficiency, as follows:

$$\eta_{\mathrm{exp,is}} = \frac{\dot{W}}{\dot{m}(h_{\mathrm{in}} - h_{\mathrm{out,s}})}, \tag{150a}$$

$$\eta_{\mathrm{exp,ef}} = \frac{\dot{W}}{\dot{m}(h_{\mathrm{in}} - h_{\mathrm{out,s}})} \eta_{\mathrm{mech}}, \tag{150b}$$

which is compatible with Eq. 48 when heat transfer is small, as confirmed for the conditions modelled here. While throughout this thesis the piston expander efficiency is mostly reported as the isentropic efficiency, the other definitions are useful for comparing the results to other studies in the literature.

3.6.2 Screw expander

As discussed in previous sections, screw expanders have high durability, operate efficiently at low-medium volume ratios (VRs) of up to 8 and pressure ratios of up to 10, are low noise, low vibration and have compact configuration [158]. In Fig. 16, a schematic diagram of typical screw machines is presented. Screw expanders typically are reversed screw compressors and are capable of dry gas or wet vapour expansion. In contrast with the piston expanders, there are a few studies in the literature that consider single-stage screw expanders in ORC engines, mainly for recovering heat from low-medium temperature heat sources [158]. In this work, the operation of screw expanders within ORC engines for high temperature waste heat recovery are investigated, at design and off-design conditions, and compared to the performance of piston expanders.

To predict the screw expander isentropic efficiency, the correlation provided by Astolfi [65] has been used. The correlation is based on available efficiency data of screw compressors on the market. The efficiency of the expander is obtained using the following equations:

$$\eta_{\mathrm{exp}} = c\left[0.9403305 + 0.0293295\ln(\dot{v}_{\mathrm{wf}}) - 0.0266398 r_{\mathrm{exp}}\right], \tag{151}$$

$$c = 1, \text{ if } r_{\mathrm{exp}} \leq 7, \tag{152}$$

$$c = 1 - 0.264 ln\left(\frac{r_{\mathrm{exp}}}{7}\right), \text{ if } r_{\mathrm{exp}} > 7, \tag{153}$$

$$c^{*} = -0.03229\left(\frac{r_{\mathrm{exp}}'}{r_{\mathrm{exp}}}\right)^{4} + 0.288\left(\frac{r_{\mathrm{exp}}'}{r_{\mathrm{exp}}}\right)^{3} - 0.8995\left(\frac{r_{\mathrm{exp}}'}{r_{\mathrm{exp}}}\right)^{2} + 1.0064\frac{r_{\mathrm{exp}}'}{r_{\mathrm{exp}}} + 0.60558, \tag{154}$$

where η_{exp} is the screw expander efficiency, $\dot{v}_{\mathrm{wf}}$ is the working fluid volume flow rate, r_{exp} is the VR of the expander at the design point, defined as the ratio of the specific volume of the working fluid at the discharge of the expander over the specific volume of the working fluid at the intake, r_{exp}' is the VR of the expander at off-design operation, c is a correction factor for sizing he screw expander depending on the VR at the design point, and c^{*} is a post-expansion correction factor, which captures the efficiency reduction of screw expander, due to off-design operation effects. Because the Astolfi [65] correlation has been developed using the efficiencies of commercial units with maximum VRs of 7, the correction factor c is applied to the expander efficiency, in the cases where the expander operates at higher VRs.

Once the expander design is fixed (i.e. built-in VR, volume flow rate and thus its isentropic efficiency), the screw off-design efficiency is obtained by applying a correction factor (c*) that captures the efficiency penalisation due to off-design operation. It is highlighted that the efficiency correlation has been presented without indicating whether this is the isentropic expander efficiency or whether it includes losses, such as power generation losses. Therefore, in this thesis further power generation losses are added to obtain the final expander efficiency, being on the conservative side of the calculations. Finally, due to the screw expander efficiency deterioration at high pressure/VRs, in the following chapters it is revealed that the optimised ORC engines with screw expanders operate with two-stage expansion, aiming to operate each machine at lower expansion ratios, and thus higher efficiencies.

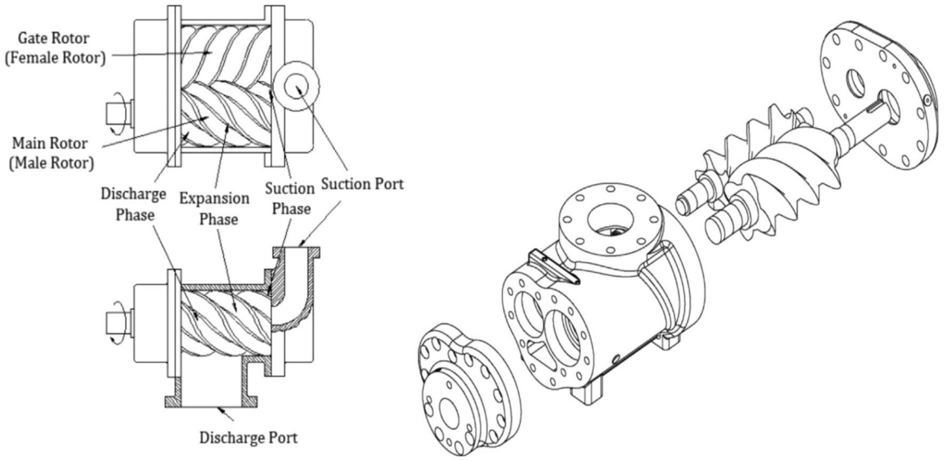

Fig. 16: Single and twin crew expanders' schematic diagram [158].

3.7 Pump selection

The input parameters for the ORC engine pump performance are the working fluid flow rate, the enthalpy at the exit of the condenser and at the inlet of the preheater, and the efficiency of the pump:

$$\dot{W}_{\text{pump}} = \frac{\dot{m}_{\text{wf}}\,(h_2 - h_1)}{\eta_{\text{pump}}}. \tag{155}$$

In line with the literature review conducted by Landelle et al. [58] the most common pump technologies used in ORC units are reciprocating machines, rotary and centrifugal. For low pressure ratios and flow rates the rotary type are commonly used, for medium to high mass flow rates and high pressure ratios the centrifugal units dominate, while the reciprocating pumps are the most versatile being able to operate in a wide range of pressure ratios, even for low mass flow rates. Therefore, in this thesis, the ORC engine pump is assumed to be a centrifugal unit. A fixed value of the pump isentropic efficiency of 0.65 was chosen, which falls within the range of values suggested in previous studies [8,17,40].

3.8 Organic Rankine cycle engine economic analysis

Following the ORC system sizing, using the methodology presented in Sections 3.5, 3.6 and 3.7, cost estimates of the ORC engine components can be obtained, using alternative cost correlations. As discussed in Chapter 2, there is a variety of costing methods available in the literature, with the most widely used being the so-called module costing technique [115,116]. Apart from the module costing technique, cost correlations for ORC engine components have been also developed by various researchers using typical materials costs, such as those presented in Refs. [8,17], or by collating data from manufacturers' price lists, such as Ref. [65], while very limited studies are publicly available were the actual ORC components manufacturing, assembly and overhead costs of real installations are presented [52,117]. The lack of actual ORC engine and components cost data makes the validation of the cost estimates an onerous task. In this thesis, we compare alternative costing methods, while presenting new cost correlations, based on vendors' price lists and real ORC engine cost data, aiming to establish cost correlations which can provide realistic cost estimates for the CAPEX of ORC engines. In this section, the module costing technique is presented, while the new correlations developed as part of this thesis are presented in Chapter 6. Finally, the various financial indexes utilised throughout this thesis to compare alternative system designs and configurations are presented.

3.8.1 Component costing

The general format of the cost correlations deployed in the module costing technique is illustrated in Eqs. 156-157, as provided by Turton [115] and Seider [116]:

$$C_p^0 = F\ 10^{(K_1+K_2\log_{10}Z+K_3\log_{10}{}^2Z)}\ [115]\,, \tag{156}$$

$$C_p^0 = F\ \exp(K_1 + K_2\ln Z + K_3\ln^2 Z + K_4\ln^3 Z + K_5\ln^4 Z)\ [116]\,, \tag{157}$$

where C_p^0 represents the component purchase cost (or the so-called free of board - FOB - cost); F represents a cost factor considering the components' manufacturing, including F_p which accounts for the cost correction based on the operating pressure of the system, and F_m which accounts for the components' material; Z corresponds to the specific component attribute based on which the costing is conducted; and K_i are the cost coefficients described in Turton [115] and Seider [116], which depend on the type of component.

To calculate the bare module cost, other cost components should be considered, including installation costs of associated piping, ductwork etc., labour cost, construction overheads etc. These cost components have been incorporated by Guthrie [116] in one factor, the so-called bare module factor (F_BM), for the most commonly used equipment in chemical plants. The aim of this work is to estimate the cost of the ORC engine itself, rather than the complete construction cost of a power generation plant, therefore the F_BM is not incorporated in the cost correlations presented below. Finally, the Lang factor of 1.18 that captures the manufacturing/construction contingencies is used as a multiplier to the total purchase cost of all the components comprising the ORC engine, to obtain the capital expenditure in line with Refs. [115,116].

The cost coefficients (F_p, $F_{m.,}$ K_i) for estimating the purchase cost of each piece of equipment, using the module costing technique, are summarised in Table 2. The cost coefficients for the HEXs are selected as follows:

- For estimating the DPHEX cost using Seider [116], F_p is set equal to 1 because the HEX pressure in the systems investigated is lower than 4,000 kPa, and F_m is 2 for stainless steel (SS) inner tube construction. This correlation is applicable to the single-phase zones of the evaporator and the condenser DPHEXs, and is valid for heat transfer areas up to 22 m^2.
- For the two-phase zone of the DPHEX, the Seider [116] correlation for forced circulation DPHEX is used. The correlation is applicable for heat transfer areas up to 900 m^2.
- For the PHEX costing, one correlation is provided by Seider [116] for SS plates, which is applicable to heat transfer areas up to 1,400 m^2.
- For estimating the DPHEX cost, using Turton [115], F_m is set to 1.8 for SS inner tube design, and F_p is set to 1, for operating pressures lower than 4,000 kPa. This correlation is applicable to the single-phase zones of the evaporator and the condenser DPHEXs, and is valid for heat transfer areas up to 10 m^2.
- For the two-phase zone of the DPHEX, the correlation of Turton [115] for forced circulation is used. This is applicable to HEX areas of up to 1,000 m^2. For carbon steel (CS) construction, the F_m corresponds to 3, while the pressure factor is calculated as follows (P in bar):

  $$F_p = 10^{\left(C_1+C_2\log_{10}P+C_3\log_{10}{}^2P\right)}, \tag{158}$$

  with C_1=0.1578, C_2=-0.2992, C_3=0.1413 for pressure in the range of 10<P<150 bar, and F_p=1 for lower pressure levels.
- For the PHEX costing, only one correlation is provided by Turton [115] with F_m being equal to 2.4 for SS plates, and F_p being equal to 1 for operating pressures below 4,000 kPa. The cost correlation is applicable to PHEX area of up to 1,000 m^2.

For the calculation of the pump cost, the correlation of Seider [116] is used, and the specific attribute required is:

$$S = \frac{\dot{v}_{wf}}{0.0631}\left(\frac{P}{0.0299}\right)^{0.5}, \tag{159}$$

where $\dot{v}_{\mathrm{wf}}$ is the volume flow rate of the working fluid in l/s, and P is the pump head in bar.

To convert the costs to today's values the Chemical Engineering Cost Index (CEPCI) has been used. For Turton [115], base year is 2001 (CEPCI_{2001}=397), and for Seider [116], is 2013 (CEPCI_{2013}=567).

All costs were converted to 2017 values, using $CEPCI_{2017}$=562.1. USD were converted to GBP using: for 2001, the conversion rate of 0.6944, and for 2013, the rate of 0.63955 [159]. At the point of writing only interim CEPCI for 2018 were available, therefore the $CEPCI_{2017}$ has been used.

Table 2: Cost coefficients used for the module costing technique, based on Refs. [115,116].

Component	***Z***	***F***	**F_p/F_m/ F_D**	**K_1**	**K_2**	**K_3**	**K_4**	**K_5**	**Ref.**
DPHEX	Area (ft^2)	1	1/2/-	7.2718	0.160	-	-	-	[116]
Preheater/ Desuperheater	Area (m^2)	1	1/1.8/-	3.3444	0.2745	-0.0472	-	-	[115]
DPHEX	Area (ft^2)	1	1/1/-	8.0369	0.6994	-0.00004	-	-	[116]
Evaporator/ Condenser (forced circulation)	Area (m^2)	1	F_p/3/-	5.0238	0.3475	0.0703	-	-	[115]
PHEX	Area (ft^2)	10,070 $(Z)^{0.42}$							[116]
Preheater/ Desuperheater	Area (m^2)	1	1/2.4/-	4.6656	-0.1557	0.1547	-	-	[115]
Reciprocating compressor	Power (Hp)	1	-/1/1	4.6762	1.23	-	-	-	[116]
	Power (kW)	3.5	-/-/1	2.2897	1.3604	-0.1027	-	-	[115]
Screw compressor	Power (HP)	1	-/1/1	8.2496	0.7243	-	-	-	[116]
	Power (kW)	2.5	-/-/1	5.0355	-1.8002	0.8253	-	-	[115]
Pump	S ($gpm\sqrt{ft_{head}}$)	1	2/1.35	12.1656	-1.1448	0.0862	-	-	[116]
Pump motor	Power (HP)	1	-/1.4	5.3992	0.16829	0.110056	0.071413	0.0063788	[116]

The module costing technique correlations do not provide cost functions for screw type or piston expanders. To estimate the cost of those expanders, the cost correlations provided for their respective counter-part compressors have been used. This is a reasonable assumption, since these volumetric machines can operate in reverse mode (expansion) with relatively simple modifications. Therefore, it is a common practice in the literature to use the volumetric compressor costs, as indicators of the volumetric expanders cost. The cost coefficients for the expanders are summarised in Table 2, and have been selected as follows:

- For the reciprocating compressors cost, when using Seider [116], F_D=1 for an electric motor driven compressor, and F_m=1 for CS construction. This correlation is valid in the range of 70-14,900 kW.
- For the screw compressors cost, when using Seider [116], F_D=1 for electric motor driven compressor, and F_m=1 for CS construction. The correlation is valid for 8-560 kW of power output.
- Turton [115] provide two general correlations; one covering axial, centrifugal and reciprocating compressors, and another one for rotary compressors. The validity range is 450 to 3,000 kW for the

former, and 18-950 kW for the latter. It is noted that the correlations are suitable for large scale (power plant level) machines, rather than small-medium scale units required in the ORC engines considered in this study. However, the correlations are included in the study, for completeness. The pressure factor is set to 1 (F_p=1) and the material factor F_m is not given. Instead, a general cost factor for CS compressors is provided, which is equal to 3.5 for reciprocating piston, and 2.5 for rotary type.

In Chapter 6, the cost predictions using the module costing technique presented here, are compared to those obtained, when using the new cost correlations developed in this work. By comparing the two approaches we aim to identify those correlations, which provide the most credible cost estimates.

3.8.2 Profitability analysis

A commonly used cost index for comparing alternative ORC system configurations is the specific investment cost (SIC), defined as the ratio of the ORC engine capital cost, over the net power output:

$$SIC = \frac{CAPEX_{\mathrm{ORC}}}{\dot{W}_{\mathrm{ORC,net}}}\,. \tag{160}$$

To quantify the impact of the different ORC engines designs on the project whole life financial viability, the discounted payback period (DPP) and the net present value (NPV) of the ORCs in an ICE-ORC CHP configuration are estimated, using the following equations:

$$DPP = \frac{Actual\ cash\ flows}{(1+i)^n}\,. \tag{161}$$

The cash flows are estimated as the savings on the electricity bill of the user on an annual basis, because of the use of the ORC engine, and by subtracting the annual operation and maintenance (O&M) costs. The user is assumed to be a large-scale commercial or industrial facility, covering supermarkets or university buildings. More details are provided in Chapter 6. The NPV of the system is estimated using:

$$NPV = -CAPEX_{\mathrm{ORC}} + \frac{Actual\ cash\ flow_1}{(1+i)^1} + \frac{Actual\ cash\ flow_2}{(1+i)^2} + \cdots + \frac{Actual\ cash\ flow_n}{(1+i)^n}\,, \tag{162}$$

with n being the project lifetime in years.

Energy prices for both electricity and gas are required to calculate the annual energy costs, and potential savings of the systems investigated. The electricity and gas prices data used in this study are based on previous work done in Refs.[160,161] and are based on the prices offered to commercial and industrial users in the UK. The gas price used is 2.4 p/kWh [24]. For the electricity prices, half-hourly price points have been used for typical weekend (WD) and weekdays (WD). In Fig. 17, the profile of electricity prices variation are presented, for typical WD and WE as forecasted for 2019.

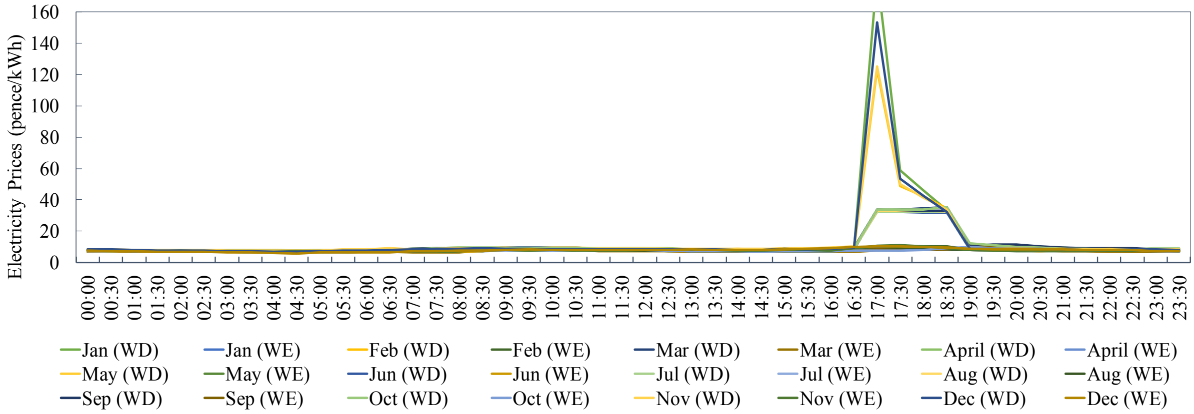

Fig. 17: Half-hourly electricity prices for typical days per month, for 2019; data obtained from Refs. [160,161].

3.9 Optimisation

In the light of demanding energy performance standards, designing sustainable energy technologies requires the consideration of multiple design parameters, and constraints (technical and financial), making the possible solutions design space very wide. To deal with these challenges, mathematical optimisation techniques can be proved very useful. Optimisation methods can be classified into Global optimisation techniques and Heuristic methods. Global optimisation techniques guarantee that the global optimum in the design space will be obtained, whereas the heuristic methods offer an efficient way of finding the optimum or getting close to it with a high probability [162]. The general structure of an optimisation algorithm is illustrated in Fig. 18.

Objective function(s) are constructed, subject to a set of constraints, relevant to the optimisation problem. For an ORC engine design, the constraints will ensure that fundamental thermodynamic principles are not violated, or that non-feasible values for the design variables are excluded from the optimisation process, followed by other constraints, related to the equipment sizing, and operating conditions. More details on the optimisation exercises objectives and constraints can be found in Chapters 4, 5 and 6 that follow. Generally, the optimisation algorithm generates new values for the decision variables, which form new input to the model, i.e. the objective function. Then, whether the constraints are satisfied is tested, and if yes, the value of the objective function is computed and saved. In the end, the vector with the optimum set of values of the decision variables that minimise/maximise the objective function(s) is obtained.

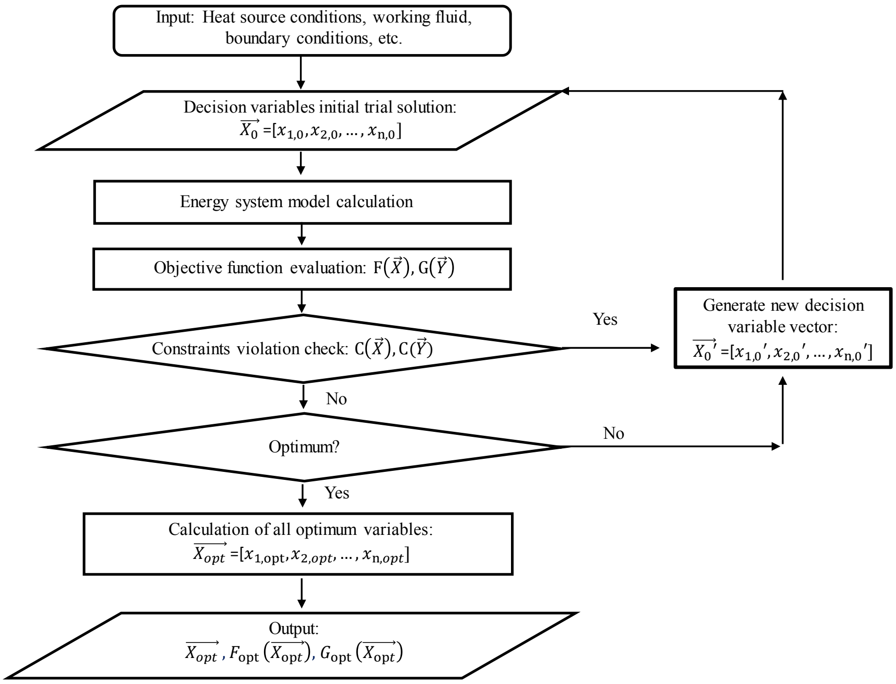

Fig. 18: Simplified schematic diagram of optimisation workflow.

3.9.1 Single-objective optimisation

In a typical single-objective optimisation problem, there is one objective function $\vec{F}(\vec{X})$, which we seek to minimise or maximise, subject to a number of constraints. Vector $\vec{X}$ contains all the decision variables, i.e. the independent variables that the optimiser is allowed to alter within a predefined and feasible range, in order to minimise or maximise the objective function $\vec{F}(\vec{X})$. In this thesis, single-objective optimisation has been deployed in Chapters, 4, 5 and 6. Three objectives have been mainly investigated (separately): i) net power output of the ORC engine, or of the ICE-ORC CHP system; ii) the specific fuel consumption (*SFC*) of the ICE-ORC CHP system; and iii) the SIC of the ORC engine. In the following chapters, the optimisation problem formulation specific to the case of interest is presented, including: i) the specific objective functions; ii) the decision variables vector; and iii) the constraints list. The models developed draw on the Refprop software package [163] for the fluid properties investigated.

The single-objective optimisation problem was solved in MATLAB© [128] using the *multistart* structure, which repeatedly runs a local solver from a number of different starting points (between 20-120), predefined by the user. In this work, the interior point algorithm *fmincon* was used as the solver to minimise the constrained nonlinear multivariable objective functions. For the maximum power output optimisation exercise, the negative value of the power output was minimised instead. The reader can refer to Ref. [164] for more details on the mathematical formulations of the optimisation algorithm.

3.9.2 Multi-objective optimisation

When designing energy systems, there is always a trade-off to consider between achieving highly energy efficient designs and minimising the cost of the system. Typically, aiming to achieve the most efficient system design from a thermodynamic perspective only, gives rise to antagonistic effects related to the cost of these designs. On the contrary, designs which may not outperform from a thermodynamic perspective, may have a more favourable economic proposition, since the marginal benefit gain in terms of power output (or efficiency) beyond this point, may come at a disproportionate high cost. In the case of particularly early-stage technologies, such as the ORC systems investigated in this thesis, the focus on improving the system economics is even higher, since to facilitate the wider adoption of novel systems in the market, they have to be competitive when compared to other conventional technologies, not only in terms of performance, but also in terms of costs. Therefore, tools that allow for the simultaneous consideration of alternative objectives of interest, or the so-called key performance indicators (KPIs) when optimising the design of energy technologies is of paramount importance.

In this context, multi-objective optimisation principles can be deployed to identify the best performing system design, while satisfying multiple objectives. In a typical multi-objective optimisation problem, there is a minimum of two objectives which we seek to satisfy, i.e. two objective functions $\vec{F}(\vec{X})$ and $\vec{G}(\vec{Y})$, which we seek to minimise or maximise, subject to a number of constraints. Vectors $\vec{X}$ and $\vec{Y}$ contain all the decision variables, i.e. the independent variables that the optimiser is allowed to alter within a predefined and feasible range, in order to minimise or maximise the objective functions. The decision variable vectors ($\vec{X}$ and $\vec{Y}$) may or may not include the same variables.

The multi-objective optimisation problem was solved in MATLAB© [128] using *gamultiobj.* The *gamultiobj* structure, uses an elitist controlled genetic algorithm, which is a variant of NSGA-II [165] to generate the Pareto front. The Pareto front is defined as the set of points in the parameter space (the space of decision variables) that have non-inferior fitness function values. Each point on the Pareto front is considered "optimal", in the sense that it is not possible to improve one of the objective functions for this point, without degrading one or more of the other objectives [90]. More details on the mathematical formulations related to *gamultiobj* can be found in Ref. [165].

In this thesis multi-objective optimisation has been deployed in Chapter 6, where we aim to optimise simultaneously two objective functions: i) the net power output of the ORC engine, which we aim to maximise; and ii) the SIC of the ORC engine which we aim to minimise. Given the Pareto front obtained, the designers or stakeholder can choose the solutions that meets the overall aims and objectives of the project. In the following chapters, the setup of the optimisation exercises performed is presented in detail, along with the relevant decision variables vectors and constraints.

3.10 Summary

The modelling methodology deployed in this thesis has been outlined in this chapter, and the key assumptions have been presented. The methods deployed cover: i) thermodynamic modelling of energy conversion technologies, using the first and second law analysis; ii) ORC engine components sizing and performance prediction, including alternative types of HEXs and expander devices; iii) financial indicators and costing techniques, for evaluating the financial viability of waste heat recovery with ORC engines in CHP applications; and iv) optimisation workflow for single and multi-objective problems with non-linear constraints. In the next chapters, the modelling methodology presented in Chapter 3 is applied on ICE-ORC CHP system optimisation studies to evaluate the technical and financial viability of such systems from thermodynamic, equipment sizing, operational and economic perspective.

Chapter 4

Integrated ICE-ORC CHP optimisation

> *"Distributed energy resources represent critical technologies and strategies through which buildings evolve from passive consumers to active partners with the grid."*
>
> - ASHRAE, Building our new energy future (2018)

4.1 Introduction

In the light of increasing energy efficiency standards, and strict greenhouse gases emission targets, combined heat and power systems (CHP) for distributed generation have been gaining growing interest, due to their higher combined system efficiency, than the separate provision of these vectors [166]. Crucial for maximising a CHP system's overall efficiency is the effective utilisation of both the power generated and of the heat rejected by the prime mover. Specifically, in the case of internal combustion engines (ICE) designed for use in CHP applications, which are at the focus of this thesis, more than 55% of the fuel energy is rejected as heat to the cooling jacket water circuit of the engine and the exhaust-gas stream.

Organic Rankine Cycle (ORC) systems are a promising candidate energy conversion technology for recovering heat from the exhaust-gas stream of ICEs to generate additional power, improving the overall system efficiency [15]. To optimise the performance of ICE-ORC CHP systems and evaluate their technical and financial viability, factors such as, alternative operating conditions, alternative working fluids, various components design and configurations, the system response to alternative heat source and demand profiles (off-design operation), etc. should be investigated to inform design decisions. By reviewing the literature on waste heat recovery from ICEs with ORC engines, for stationary CHP applications, it is revealed that the available studies have considered either: i) the design and operation of ICEs in isolation and how this affects their performance; or ii) the optimisation of ORC engines in isolation, with ICEs considered simply as a heat source to the ORC system, without considering modifications to the ICE design or operation, due to the coupling to the ORC engines and vice-versa [32,33,92,167]. This can lead to sub-optimal CHP systems, since the two engines are not specifically designed to operate together as an integrated system, to give the best performance.

The present work goes beyond previous efforts, by performing combined optimisation of an integrated CHP system that consists of interacting ICE and ORC components, both of which are modelled in detail and validated (especially the ICE which is a dynamic model), such that both ICE and ORC engines are optimised simultaneously within the combined system. This holistic approach allows us to capture key interactions and trade-offs between the ICE and ORC engines operation, such as higher backpressure on the ICE for higher heat recovery at the ORC engine, or higher exhaust-gas temperature leaving the ICE for maximising the ORC power output, and to identify a solution where the complete ICE-ORC system performance is maximised. Therefore, the analysis provides new insights into appropriate designs and operating conditions for both engines, for which the optimum performance of the combined, integrated ICE-ORC CHP system can be expected. Finally, we are able to answer questions such as: i) does the overall ICE-ORC CHP system performance improve equally for the case of small or larger ICEs coupled to ORCs; ii) is the dominant driver for the integrated ICE-ORC system performance the ICE design or the ORC design and how is this affected by the rated power of the ICE; iii) is the type of aspiration of the ICE affecting the ICE-ORC CHP performance; and iv) finally, which ORC engine designs are most well suited for integration in ICE-ORC CHP systems.

To achieve this, this chapter is structured as follows: firstly, the validation results of the ICE model developed in this thesis are presented and discussed in Section 4.2 (for the mathematical formulations of the ICE model refer to Chapter 3). Performance data from various CHP-ICEs available on the market have been used for the validation exercise, covering both naturally aspirated and turbocharged engines. Next, the integrated ICE-ORC CHP system optimisation framework formulation is presented in Section 4.3. The optimisation framework covers scenarios where the two subsystems (CHP-ICE and ORC) are optimised separately for maximum power output or minimum *SFC* and compares their performance to cases where the integrated ICE-ORC CHP system is optimised as one combined system for the same objectives. The optimisation results for ICE-ORC CHP systems driven by naturally aspiration engines are presented in Section 4.4, whilst the results for ICE-ORC CHP systems driven by turbocharged engines are presented in Section 4.5. The findings of the exergy analysis for the optimised ICE-ORC CHP systems developed in this work, are then discussed in Section 4.6. Finally, conclusions and recommendations based on this work are discussed in Section 4.7.

4.2 Internal combustion engine model validation

In Section 3.2, the dynamic model developed for an Otto ICE was presented. In this section, we use data from manufacturers' technical specification sheets for natural gas CHP-ICEs (provided by EnerG [9]), in order to validate the model. More precisely, the ICE model was validated against operating data for three stationary CHP-ICEs available on the market, namely 'CHP-160', 'CHP-230' and 'CHP-2500', covering both turbocharged and natural aspiration engines, at full and part-load (PL) conditions. In Table 3, a summary of the engines' geometric and operating characteristics is presented. Owing to lack of information on some operational and design aspects of the CHP-ICEs, some assumptions were made using data available in the literature. Specifically, the unavailable data are associated to: (i) the size of the valves, their timing and opening profile; (ii) the ignition timing and duration; (iii) the design of the ICE oil circuit; (iv) the crankshaft friction losses (FMEP); and v) the type, geometry and efficiency of the turbocharger.

Table 3: CHP-ICE specification data taken from Ref. [9].

	CHP-ICE		
Parameter	**CHP-160**	**CHP-230**	**CHP-2500**
$\dot{W}_{\text{net}}$ (kW)	150	230	2,535
N (RPM)	1,500	1,500	1,500
Number of cylinders	8	12	20
r (-)	12	12	14
V_{dis} (m^3)	0.0018	0.0018	0.0048
s (m)	0.142	0.142	0.21
b (m)	0.128	0.128	0.17
l (m)	0.22	0.22	0.326
Intake valve diameter (m)	0.43 b	0.43 b	0.43 b
Exhaust valve diameter (m)	0.35 b	0.35 b	0.35 b
AFR (-)	16.5	16.5	29.5
T_{in} (K)	298	298	298
Initial mass (kg/cyl)	0.0016	0.0016	0.0144
T_{w} (K)	298	298	298
LHV (kJ/kg)	48,074	48,074	49,152
Turbocharged (Yes/No)	No	No	Yes
η_{el} (%)	95.4	95.4	97.5

To proceed with the validation exercise the following assumption were used:

- The size of the intake and exhaust valves was estimated as a function of the cylinder diameter, in line with Ref. [123], while the valve timing and opening profile were based on information provided in Refs. [123,125];
- The ignition timing was varied between 40° and 5° before top dead centre (TDC);
- The friction losses of the ICE were selected to be 10% of the shaft work, as an average value found in the literature [153,168];

- The turbine and compressor efficiencies were selected at 70% and 75%, respectively, in line with data provided in Refs. [125,153].

The pressure and temperature profiles of the exhaust gases inside a cylinder of the turbocharged CHP-2500 ICE are presented in Fig. 19. Similar results are illustrated in Fig. 20, for the natural aspiration CHP-230 ICE. The results highlight the different operating conditions of these two types of engines; in the case of the turbocharged CHP-ICE, the temperature inside the cylinder reaches a peak of 2,200 K, whilst the temperature of the exhaust gases inside the natural-aspiration engine exceeds (only instantly) 3,000 K. The difference is attributed to the higher (lean) air-to-fuel ratio (*AFR*) used in the CHP-2500 ICE, which operates with *AFR* of 29.5, as opposed to the stoichiometric *AFR* used in the CHP-230 engine, which corresponds to *AFR* = 16.5. Looking at the pressure profile inside the cylinders, as anticipated, the peak pressure reached in the CHP-2500 ICE is 22,500 kPa, which is significantly higher than the maximum of 8,000 kPa reached in the case of CHP-230. The difference in pressure is owing to the use of the turbocharger in the CHP-2500 ICE, which results in an initial pressure inside the cylinder of 240 kPa, even prior to the commencement of the compression stroke.

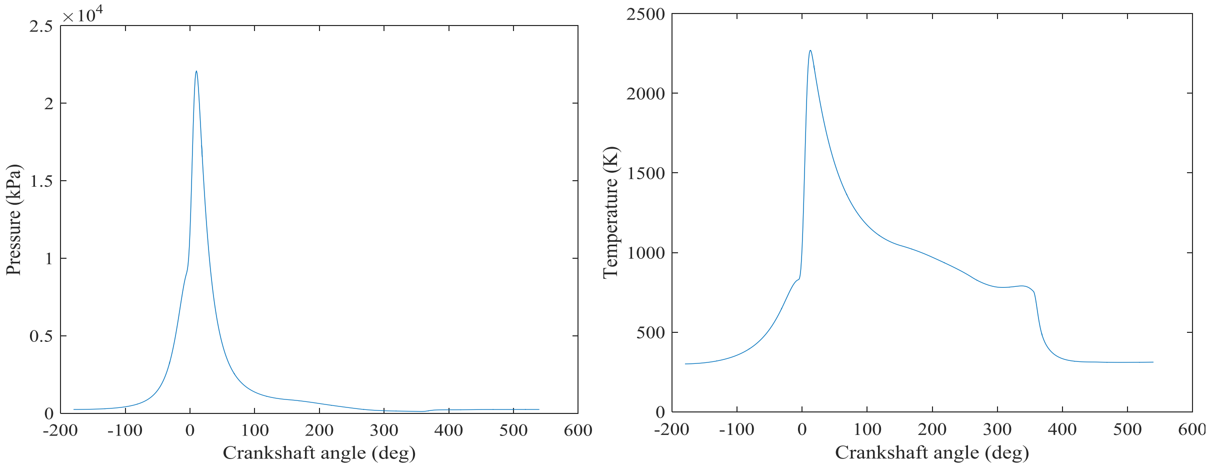

(a) (b)

Fig. 19: CHP-2500 ICE exhaust gases: a) pressure profile, and b) temperature profile inside the cylinder, at 100% load.

The CHP-ICE model predictions are summarised in Table 4, and compared against manufacturer's data, for all engines investigated. The modelling results are in good agreement with the real measured results, which are quoted by the manufacturer with a ±10% uncertainty range. Only a few discrepancies are recorded, which are attributed to the lack of information on some operating and design aspects of the engines and thus had to be assumed for the validation exercise. The highest deviation observed between the model-predicted power output results, and the figures reported by the manufacturer is equal to 4.3%, for CHP-160 operating at 100% load. This figure falls well within the ±10% uncertainty range, stated in the specification data sheets of the engine. When looking at the thermal energy content of the exhaust-gas stream as predicted by the model, this also lies within the ±10% uncertainty range reported in the engine data sheets, with the exception of CHP-230 when operating at 50% PL for which the model prediction is 16% lower than the values indicated in the engine specification.

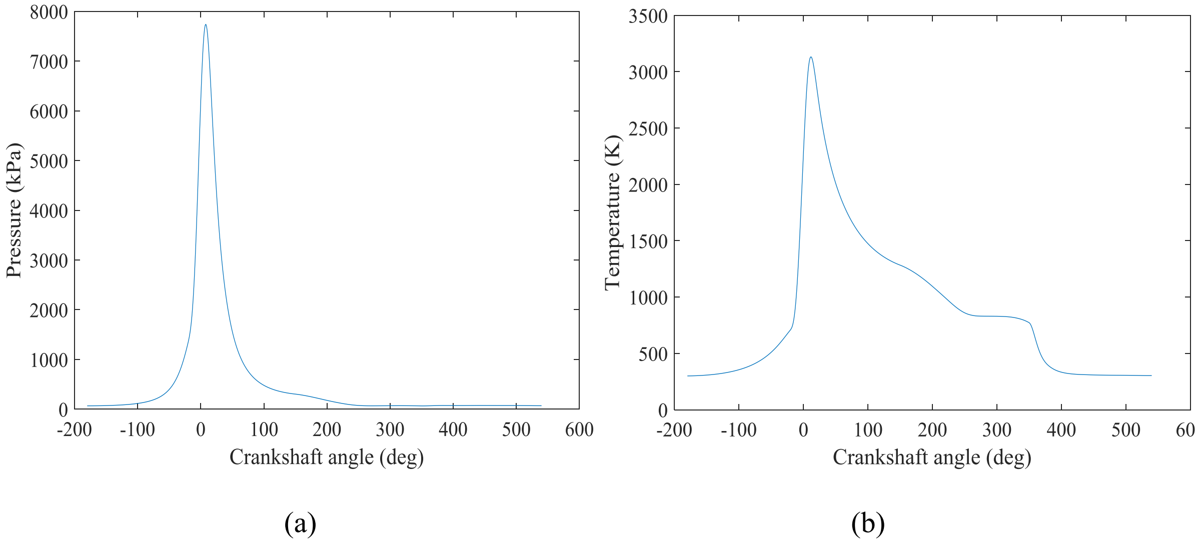

(a) (b)

Fig. 20: CHP-230 ICE exhaust gases: a) pressure profile, and b) temperature profile inside the cylinder, at 100% load.

A very good agreement is also observed between the predicted exhaust-gas stream temperature and the temperature quoted in the engine data sheets, corresponding to a ±4% deviation. The only exemption is noted for CHP-2500 when operating at 75% PL, where the temperature predicted by the model is 9.7% higher than those reported by the manufacturer. Finally, the predicted heat losses of the engine to the jacket water circuit deviate by 0.9-9% from those reported in engines data sheets, falling again within the ±10% uncertainty range of the engine sheets. Overall, the results of the validation exercise reveal that the ICE model predictions are in good agreement with the data reported by the manufacturers. Therefore, it can be used with confidence to predict the dynamic performance of CHP-ICE systems.

The validation results highlight that for both natural aspiration CHP-ICEs, while the engine load decreases from 100% to 50% the exhaust-gas stream temperature also decreases, whilst for the turbocharged engine, the opposite trend is observed; when the engine load reduces from 100% to 50%, the exhaust-gas temperature increases from 663 K up to approximately 800 K. This trend, recorded in the engines data sheets and also captured by the model, can be explained as follows; the lower expansion work generated on the engine shaft and by the turbine expander at PL, result in higher enthalpy content of the exhaust-gas stream when leaving the engine, thus increasing its temperature. On the other hand, the mass flow rate of the exhaust-gas decreases at PL conditions for all engines investigated, which is in line with the lower fuel consumption (and fixed *AFR*).

Table 4: Summary of CHP-ICE model validation results for different engines and load conditions.

		100% Load			**75% Load**			**50% Load**		
Engine	**Parameter**	**Data**	**Model**	**Deviation**	**Data**	**Model**	**Deviation**	**Data**	**Model**	**Deviation**
CHP-160	$\dot{W}_{\text{net}}$ (kW)	150	144	-4.3%	113	112	-0.6%	75	80	7.2%
	$\dot{Q}_{\text{comb}}$ (kW)	432	432	0.0%	345	345	0.0%	257	257	0.0%
	$\dot{Q}_{\text{jw}}$ incl. $\dot{Q}_{\text{w}}$ & intercooler* (kW)	155	155	0.3%	131	131	0.1%	99	106	7.8%
	$\dot{Q}_{\text{ex}}$ at 393 K (kW)	79	80	1.1%	60	58	-3.3%	43	39	-8.4%
	$\dot{Q}_{\text{loss}}$ incl. friction & oil circuit* (kW)	53.6	61.5	14.6%	34.5	37.2	7.6%	36.8	28.5	-22%
	$\dot{m}_{\text{ex}}$ (kg/s)	0.16	0.15	-3.2%	0.13	0.12	-3.8%	0.09	0.09	-4.6%
	T_{ex} (K)	867	886	2.2%	844	844	0.00%	826	795	-3.7%
	η_{th} (-)	0.55	0.54	-0.3%	0.55	0.55	-1%	0.55	0.56	1.5%
	η_{el} (-)	0.35	0.33	-5.7%	0.33	0.33	-0.6%	0.29	0.31	7.2%
CHP-230	$\dot{W}_{\text{net}}$ (kW)	229	221	-3.7%	171	171	-0.2%	114	121	6.4%
	$\dot{Q}_{\text{comb}}$ (kW)	649	649	0.0%	519	519	0.0%	386	386	0.0%
	$\dot{Q}_{\text{jw}}$ incl. $\dot{Q}_{\text{w}}$ & intercooler* (kW)	236	232	-1.7%	200	198	-0.94%	151	158	4.6%
	$\dot{Q}_{\text{ex}}$ at 393 K (kW)	120	129	7.3%	91	95.5	4.95%	66	63	-4.4%
	$\dot{Q}_{\text{loss}}$ incl. friction & oil circuit* (kW)	88.6	81.9	-7.6%	76.7	74.5	-2.95%	69.7	58	-16.7%
	$\dot{m}_{\text{ex}}$ (kg/s)	0.24	0.23	-2.8%	0.19	0.18	-4.1%	0.14	0.13	-5.1%
	T_{ex} (K)	873	900	3.1%	850	890	4.7%	838	839	0.1%
	η_{th} (-)	0.55	0.52	-5.6%	0.56	0.57	0.9%	0.56	0.58	2.8%
	η_{el} (-)	0.35	0.34	-3.7%	0.33	0.33	-0.2%	0.30	0.31	6.4%
CHP-2500	$\dot{W}_{\text{net}}$ (kW)	2,530	2,498	-1.3%	1,899	1,834	-3.4%	1,258	1,210	-3.8%
	$\dot{Q}_{\text{comb}}$ (kW)	5,748	5,748	0.0%	4,391	4,391	0.0%	3,037	3037	0.0%
	$\dot{Q}_{\text{jw}}$ incl. $\dot{Q}_{\text{w}}$ & intercooler* (kW)	1,375	1,380	0.4%	998	1,088	9.1%	668	652	-2.4%
	$\dot{Q}_{\text{ex}}$ at 393 K (kW)	1,147	1,051	-8.4%	966	991	2.6%	726	805	11%
	$\dot{Q}_{\text{loss}}$ incl. friction & oil circuit* (kW)	844	968	14.7%	429	388	-9.7%	324	316	-2.7%
	$\dot{m}_{\text{ex}}$ (kg/s)	3.60	3.51	-2.6%	2.70	2.64	-2.2%	1.83	1.78	-2.8%
	T_{ex} (K)	682	663	-2.8%	716	751	4.9%	750	823	9.7%
	η_{th} (-)	0.44	0.40	-9.5%	0.42	0.45	6.3%	0.43	0.45	4.8%
	η_{el} (-)	0.44	0.44	-1.4%	0.43	0.42	-3.4%	0.41	0.40	-3.8%

* The term $\dot{Q}_{\text{loss}}$ differs from the term $\dot{Q}_{\text{jw}}$, in that it includes all other thermal losses due to friction, exhaust-gas mass trapped inside the engine cylinder(s), tail-pipe thermal losses, etc., which are not included in the thermodynamic model.

These two observations are noted here, because they will have significant impact on the ORC engine operation under PL conditions examined later in this thesis. In the case of turbocharged engines, the higher exhaust-gas temperature at low load allows the increase on the heat-source ΔT, compensating for the reduced exhaust-gas (heat-source) mass flow rate reaching the ORC engine evaporator HEX. Nevertheless, this approach is not applicable in the case of natural aspiration engines, where the temperature and the mass flow rate of the exhaust-gases will both decrease at PL.

4.3 Integrated ICE-ORC CHP modelling tool

4.3.1 System overview

The schematic diagram of the integrated ICE-ORC CHP system investigated in this work is presented in Fig. 21, indicating the main system components. The main components of the ICE, which is a reciprocating engine designed for and aimed specifically at CHP applications, and referred to as “CHP-ICE” henceforth, are: i) the prime mover, which in this case is a four-stroke spark-ignition ICE; ii) the electric generator; iii) the jacket water (cooling water) circuit of the ICE; and iv) the exhaust-gas heat recovery module. The jacket water circuit thermal load is used for the provision of low temperature hot water (LTHW) and for space heating to a building. The thermal energy recovered from the exhaust gases in the heat recovery module of the CHP-ICE acts as the heat input to a bottoming ORC engine. The ORC engine is based on a subcritical and recuperative cycle, and consists of the following main components: i) the evaporator heat exchanger (HEX), where the heat is added to the cycle from the exhaust gases; ii) the expander, where power is generated; iii) the recuperator HEX, where the (hot) desuperheating working fluid vapour exchanges heat with the (cold) working fluid liquid leaving the pump; iv) the condenser HEX, where heat is rejected to a cooling circuit; and v) the pump, which maintains the working fluid circulation in the cycle.

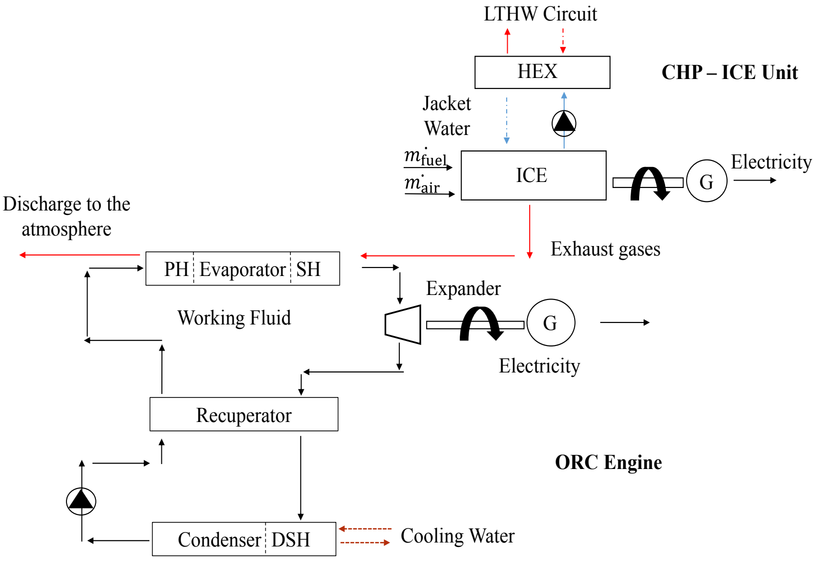

Fig. 21: Simplified ICE-ORC CHP schematic diagram, with subcritical recuperative ORC engine.

4.3.2 Optimisation problem definition

In a typical single objective optimisation problem, there is one objective function $\vec{F}(\vec{X})$, which we seek to minimise or maximise, subject to a number of constraints. Vector $\vec{X}$ contains all the decision variables, i.e. the independent variables that the optimiser is allowed to alter within a predefined and feasible range, in order to minimise or maximise the objective function $\vec{F}(\vec{X})$. In this section, two separate objective functions related to the performance of the integrated ICE-ORC CHP system have been defined and optimised. The first objective function predicts the combined net power output of the CHP-ICE ($\dot{W}_{\mathrm{ICE}}$) and ORC ($\dot{W}_{\mathrm{ORC}}$) engines, which we aim to maximise with given heat-source conditions (in this case the heat source for the ORC engine is the exhaust-gas stream), and subject to a set of operational constraints. A second objective function has been also defined, which calculates the *SFC* of the combined ICE-ORC CHP system. In this case, we seek to minimise the system's *SFC,* again subject to a set of operational constraints.

Vector $\vec{X}$ contains 14 decision variables related to the operation of the ICE and the ORC engines. The variables associated with the ICE operation are: i) combustion ignition angle (ϑ_{ign}); ii) duration of combustion (ϑ_{d}); iii) intake valve (IV) timing, i.e. crankshaft angle at which this valve will open and close ($\vartheta_{\mathrm{IV,on}}$, $\vartheta_{\mathrm{IV,off}}$); iv) exhaust valve (EV) timing, i.e. crankshaft angle at which this valve will open and close ($\vartheta_{\mathrm{EV,on}}$, $\vartheta_{\mathrm{EV,off}}$); v) IV lift height ($L_{\mathrm{v,IV}}$); vi) EV lift height ($L_{\mathrm{v,EV}}$); vii) initial pressure conditions inside the cylinder (P_0), and those related to the operation of the ORC engine are: viii) evaporating pressure (P_{evap}); ix) condensing pressure (P_{cond}); x) working fluid mass flow rate ($\dot{m}_{\mathrm{wf}}$); xi) superheating degree (*SHD)*; and xii) expander volume ratio (r_{exp}). The two objective functions are presented in Eqs. 163 and 164:

$$\underset{\vartheta_{\mathrm{ign}},\vartheta_{\mathrm{d}},\vartheta_{\mathrm{IV,on}},\vartheta_{\mathrm{IV,off}},\vartheta_{\mathrm{EV,on}},\vartheta_{\mathrm{EV,off}},L_{\mathrm{v,IV}},L_{\mathrm{v,EV}},P_0,P_{\mathrm{evap}},P_{\mathrm{cond}},\dot{m}_{\mathrm{wf}},SHD,r_{\mathrm{exp}}}{\underline{\text{maximise}}} : \ \{\dot{W}_{\mathrm{net}} = \dot{W}_{\mathrm{ICE}} + \dot{W}_{\mathrm{ORC}}\}\ , \qquad (163)$$

$$\underset{\vartheta_{\mathrm{ign}},\vartheta_{\mathrm{d}},\vartheta_{\mathrm{IV,on}},\vartheta_{\mathrm{IV,off}},\vartheta_{\mathrm{EV,on}},\vartheta_{\mathrm{EV,off}},L_{\mathrm{v,IV}},L_{\mathrm{v,EV}},P_0,P_{\mathrm{evap}},P_{\mathrm{cond}},\dot{m}_{\mathrm{wf}},SHD,r_{\mathrm{exp}}}{\underline{\text{minimise}}} : \ \left\{SFC_{\mathrm{net}} = \frac{\dot{Q}_{\mathrm{comb}}}{\dot{W}_{\mathrm{ICE}}+\dot{W}_{\mathrm{ORC}}}\right\}\ , \qquad (164)$$

which we seek to optimise subject to:

- The *PP* in any given HEX should not violate a minimum value *PP*$_{\mathrm{min}}$: $PP_{\mathrm{min}} \leq PP$;
- The pressure in the evaporator should be lower than the working fluid's critical pressure (for the subcritical ORC design considered here), and the condensation pressure should be lower than the evaporation pressure: $P_{\mathrm{cond}} < P_{\mathrm{evap}} < P_{\mathrm{crit}}$;
- The normalised *SHD* can take values between 0 and 1: $0 \leq SHD \leq 1$;
- The pressure drop experienced by the heat source (exhaust-gas stream) in the ORC engine evaporator HEX, should not exceed 50 kPa, to avoid giving rise to significant negative backpressure effects on the ICE operation. During optimisation, in every iteration the new exhaust-gas temperature, pressure

and mass flow rate are calculated, and the revised ICE power output is estimated, based on the obtained backpressure. This ORC evaporator HEX pressure drop limit is at the high end of reported values in the literature (up to 40 kPa in Refs. [104,169]);

- The exit temperature of the heat source (exhaust-gas) when leaving the evaporator HEX should not be lower than a limiting temperature to avoid the risk of reaching the gas dew-point temperature: $T_{\mathrm{lim}} \leq T_{\mathrm{hs,out}}$;
- For each ORC working fluid, the maximum temperature experienced should not exceed the maximum allowable temperature that would ensure its chemical stability, as provided in Ref. [163];
- In order for the steady-state assumption to be valid, the pressure and the mass of the air-fuel mixture inside each one of the ICE cylinders at the end of one complete cycle (720° of crankshaft rotation) should be equal to the initial mass and pressure conditions;
- The value of ϑ_{ign} should lie between -40° and -5° before TDC and that of ϑ_{d} between 20° and 40° [123];
- The height of the ICE valves lift can vary up to a maximum of ± 25% in comparison to the nominal design values, with the average lift height calculated based on Ref. [170];
- The CHP-ICE engine *AFR* is set equal to the nominal design value (refer to Table 3) to avoid issues with NO_x formation, due to the alteration of the combustion mixture composition.

4.3.3 Optimisation cases

As mentioned in previous sections, the novelty of this work is that we aim to optimise simultaneously the combined integrated ICE-ORC CHP system, instead of assuming that the exhaust-gas conditions exiting the ICE are fixed and optimising only the ORC engine design and performance. To achieve this, five cases have been investigated, to illustrate the importance of optimising the combined system performance. In Case 1 (C1), the ICE operates at its nominal design conditions, and only the ORC engine is optimised for maximum power output, while recovering heat from the exhaust-gas stream. In Case 2 (C2), the ICE is optimised for maximum power output (independently of the ORC design), and then the ORC engine is sized (optimised) using the new exhaust-gas conditions. In Case 3 (C3), the integrated complete ICE-ORC CHP system is optimised simultaneously for maximum power output. In Case 4 (C4), the ICE is optimised for minimum *SFC*, and the results are used for the subsequent sizing of the ORC engine. Finally, Case 5 (C5) considers the combined integrated ICE-ORC CHP system, which is optimised simultaneously for minimum *SFC*. All optimisation cases are examined for two ICEs: CHP-230 (natural aspiration ICE) and CHP-2500 (turbocharged ICE), as those were presented in Section 4.2. In Table 5, the specification of the sub-critical recuperative ORC engine used in the present optimisation studies is summarised.

Table 5: ORC engine operation summary of specification.

Parameter	**Value**	**Parameter**	**Value**
PP_{cond} (K)	10	$P_{\text{evap,max}}$ (kPa)	0.95 P_{crit}
PP_{evap} (K)	5	r_{exp} (-)	8-18
$T_{\text{cw,in}}$ (K)	288	ε_{rec} (-)	0.80
$T_{\text{cw,out}}$ (K)	298	T_{lim} (K)	263
$\dot{m}_{\text{hs}}$ (kg/s)	From ICE simulation	$\eta_{\text{exp,is}}$ (-)	0.70
$T_{\text{hs,in}}$ (K)	From ICE simulation	$\eta_{\text{pump,is}}$ (-)	0.65
$P_{\text{cond,min}}$ (kPa)	10	η_{elg} (-)	0.93

4.4 Integrated modelling results – I: Natural aspiration CHP-ICE

In this section, the modelling results for Cases C1-C5, for an ICE-ORC CHP system driven by a natural aspiration engine (CHP-230 ICE) are presented and discussed. First, the optimised ICE-ORC CHP systems for maximum power are presented, followed by the optimisation results when aiming to minimise the *SFC* of the system. Then, the optimised ORC engine designs obtained in each case are discussed, focusing on i) the operating pressures in the system, which impact the expander technology selection; ii) the breakdown of the heat input/rejection to/from the cycle over the various HEXs in the system, which influences the HEX selection and size.

4.4.1 CHP system performance

The optimisation results for the naturally aspirated CHP-230 ICE are presented in Fig. 22a, for each case and fluid investigated. The highest ICE power output is recorded for Case C2 (305 kW), when the system is optimised for maximum power output for the CHP-ICE only. This is followed by Case C3 with the ICE generating 303 kW, when the integrated ICE-ORC CHP system is optimised for maximum combined power. Comparing the optimised ICE power output in Case C2 (305 kW) to the nominal ICE operation Case C1 (221 kW), the former is 37% higher than the latter (refer also to Table 3 and Table 6). The significant increase observed in the ICE power output can be attributed to a few factors, related to the operating conditions of the engine. Firstly, the ignition angle of the optimised CHP-ICE is delayed at -5° before TDC, compared to the nominal Case C1 operation (-20° before TDC). This results in higher pressure inside the cylinders prior the expansion stroke, which in turn increases the displacement power on the engine shaft. Next, it is revealed that the optimised IV and EV lift heights increase by approximately 8% when compared to those provided at the ICE nominal design (Case C1). For a fixed *AFR* of the combustion, higher valve lifts allow for increased fuel flow entering the cylinders, which in turn increases the engine power output. However, this operating strategy will result to higher fuel consumption of the engine (as discussed in subsequent sections). Furthermore, in the optimised design the ICE EV opens later than in the case of the nominal design (Case C1), allowing more work to be generated on the crankshaft, while also reducing the engine blow-down losses.

In Cases C4 and C5, when the system is optimised for minimising *SFC*, the power output of the ICE decreases (in comparison to Case C2) to 299 kW when the ICE-only is optimised for minimum *SFC* (Case C4), and to 294 kW when the combined ICE-ORC CHP system is optimised for minimum *SFC* (Case C5). Although, these figures are lower than the designs obtained for maximum power output, they are still 35% and 33% higher than the nominal ICE power output of 221 kW (Case C1), as provided in Table 6. The changes in power output can be explained by comparing the operating conditions of the ICE in Cases C2 and C4. Results reveal that the valve timing and opening duration vary between these two designs. When optimising the ICE-only for maximum power output (Case C2), the IV opens earlier and closer slightly later, allowing flow rate of the fuel-air mixture into the cylinders. As aforementioned, the *AFR* in all optimisation exercises was fixed to the values recommended by the vendor, so higher mass flow rate into the cylinders is associated with higher fuel consumption. This is confirmed by looking at the fuel consumption of the engine in Table 4 and Table 6, which correspond to 0.0171 kg/s for Case C2 (power-optimised ICE) and to 0.0165 kg/s for Case C4 (minimum *SFC* optimisation). Finally, it is observed that when the ICE is optimised for maximum power output, the EV closes at a later angle. This finding is aligned with data available in the literature on high performing engines that operate with the EV open for longer period to maximise their power output [123].

The ORC engine optimum power output is presented in Fig. 22b for all cases and fluids investigated. The optimised ORC engine designs generate from a minimum power output of 15 kW to a maximum of 41 kW (almost three times higher) depending on the working fluid and case considered. The maximum power output for all candidate working fluids is recorded in Case C3, when the integrated ICE-ORC CHP system is optimised simultaneously for its combined power output. The best performing fluid is pentane (41 kW), followed by butane (39 kW), R1233zd (37 kW) and toluene and hexane (34 kW). The optimum power outputs obtained in Case C3 are higher than those obtained from the optimised ORC engines design for the nominal case (Case C1) for the same fluids, by 26%, 23%, 23%, 34% and 23%, respectively. Even the least performing fluids examined, R1234yf and R1234ze, present an improvement in their power output of 11-20%, between the nominal ORC system design and the integrated system optimisation.

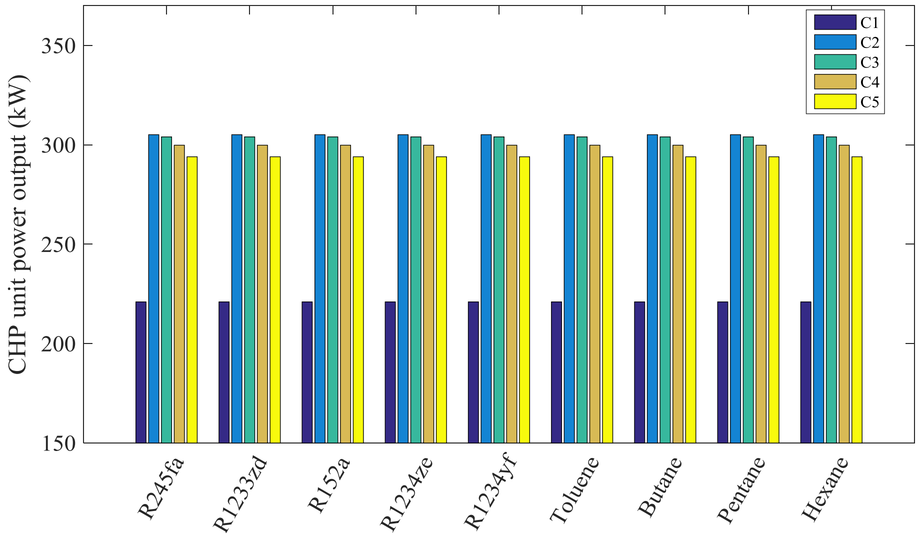

(a)

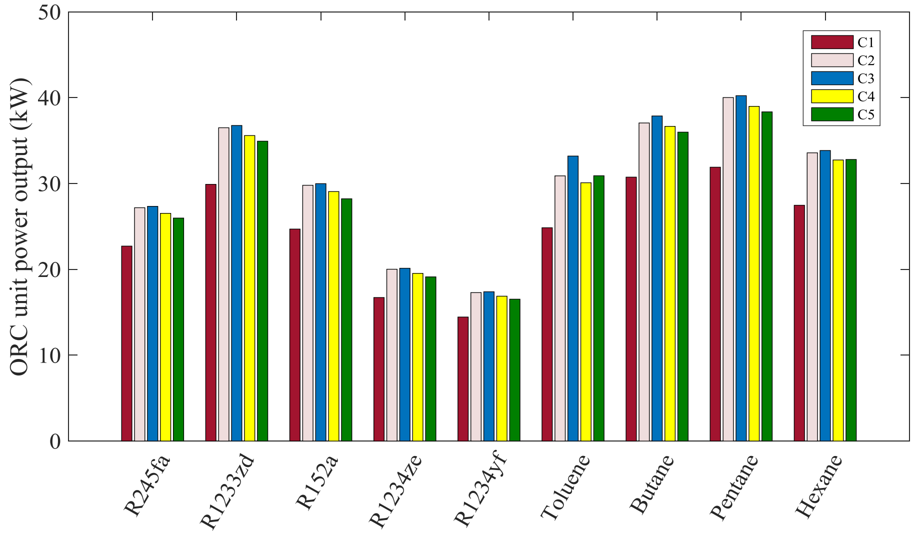

(b)

Fig. 22: Power output of: a) CHP-230 ICE, and b) optimum bottoming ORC engine (Cases C1-C5 from left to right).

The increase of the ORC engine power output (Case C3) is highly related to the ICE operating conditions. By reviewing Table 6, it is revealed that when the integrated ICE-ORC CHP system is optimised for maximum power output (Case C3), the ICE operation is adjusted so as to increase the temperature (enthalpy content) of the exhaust-gas stream exiting the ICE, and entering the ORC engine evaporator HEX. This gives rise to a slight decrease of the power output from the CHP-ICE (Case C3) in comparison to Case C2 in order to maintain the exhaust-gas temperature high, but it results in higher power output of the ORC engine within the combined system, and of the complete ICE-ORC CHP system.

Table 6: Optimum CHP-230 ICE operation results.

CHP-ICE	**Parameter**	**Cases**				
		C1 (nominal)	**C2**	**C3**	**C4**	**C5**
CHP-230	$\dot{W}_{\mathrm{ICE}}$ (kW)	221	305	303	299	294
	$\dot{Q}_{\mathrm{comb}}$ (kW)	649	840	833	821	803
	$\dot{Q}_{\mathrm{jw}}$ incl. $\dot{Q}_{\mathrm{w}}$ & intercooler (kW)	236	252	244	246	238
	$\dot{m}_{\mathrm{ex}}$ (kg/s)	0.236	0.292	0.289	0.287	0.275
	$\dot{m}_{\mathrm{f}}$ (kg/s)	0.013	0.017	0.017	0.017	0.016
	T_{ex} (K)	873	1002	1011	997	1011
	η_{th} (for exhaust gases cooled to 120 °C)	0.55	0.52	0.51	0.52	0.51
	η_{el}	0.35	0.36	0.37	0.37	0.37

The integrated optimisation approach allows us also to capture other trade-offs when coupling ORC engines as bottoming cycles to ICEs, such as the impact of the ORC evaporator HEX on the ICE backpressure. The ICE model developed in this work is a dynamic model, which is capable of predicting important operating parameters such as exhaust-gas temperature, pressure, mass flow rate, etc. Unlike other studies where such engine operating characteristics and power output are assumed fixed, in the integrated ICE-ORC CHP modelling, the exhaust-gas stream temperature and pressure, along with the ORC engine are closely monitored to do not give rise to antagonistic effects of backpressure on the ICE, reducing the power output of the system. When a HEX, here the ORC evaporator, is introduced to the ICE exhaust-gas stream, the pressure drop experienced is accounted for in the ICE model. The model re-adjusts the ICE operating conditions (valve timing, ignition angles, etc.) and recalculates the available power output on the shaft of the engine, based on the backpressure. The maximum allowable pressure drop in the evaporator is limited to 50 kPa, which is near the high end of backpressures already reported in the literature [81,104]. However, these studies consider heat recovery from vehicle ICEs, whereas the stationary engines considered in this study are designed for heat recovery, so they can tolerate additional pressure drop.

The power output breakdown between the CHP-ICE and the ORC engines for all working fluids and cases investigated is presented in Fig. 23. As anticipated, the CHP-ICE power output dominates the total power generation of the complete system, with the ORC engine power output corresponding to 6-13% of the total, depending on the working fluid and the case. Results reveal that although the power output in Cases C2 and C3 is similar, the contribution of the ORC engine to the power generation of the system increases, when the combined integrated ICE-ORC CHP system (Case C3) is optimised for maximum power output. More precisely, for ORC engines with fluids such as butane and toluene, in Case C2 their power output corresponds to 9% and 10% respectively, of the total system power generation, whilst in Case C3 the same fluids contribute 10% and 12% to the total power generation (increase of 10%-20%). The higher ORC power output within the complete system is associated with lower fuel consumption of the ICE-ORC CHP, while generating the same power output, as summarised in Table 6. Finally, the best performing optimised integrated ICE-ORC CHP system generates 345 kW of power (Fig. 23c) with pentane, which is 36% higher than the power generation in the nominal case (Case C1) with the same working fluid (253 kW). Overall, the optimised complete ICE-ORC CHP systems outperform the designs for nominal conditions (Case C1) generating 31-36% more power output.

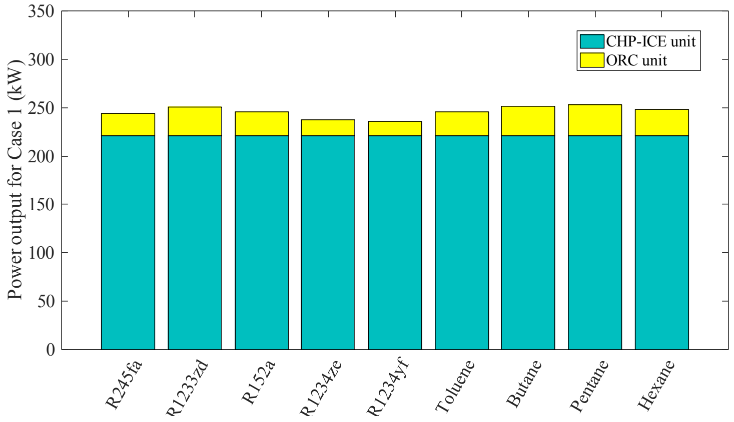

(a)

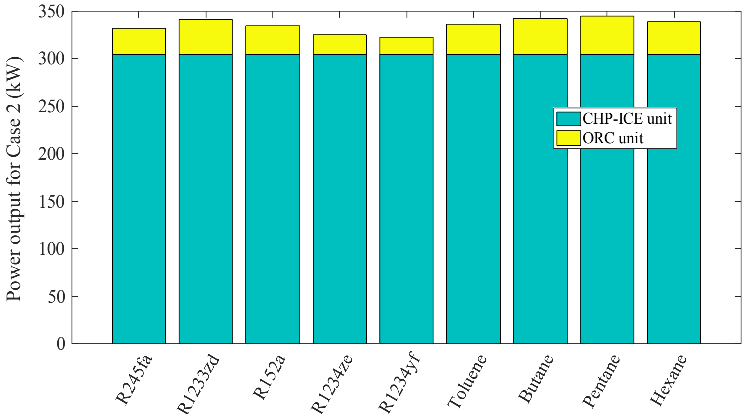

(b)

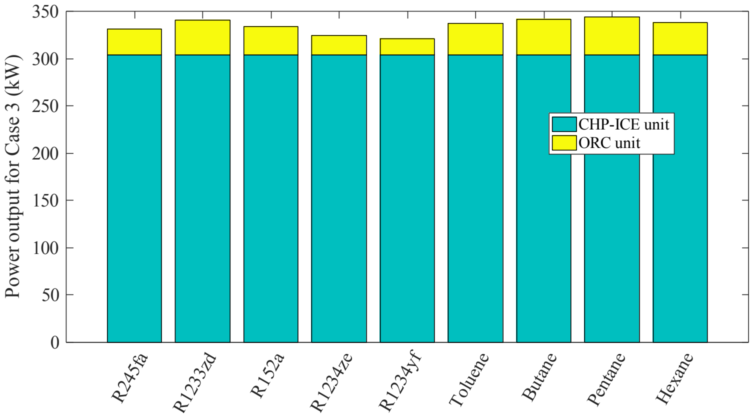

(c)

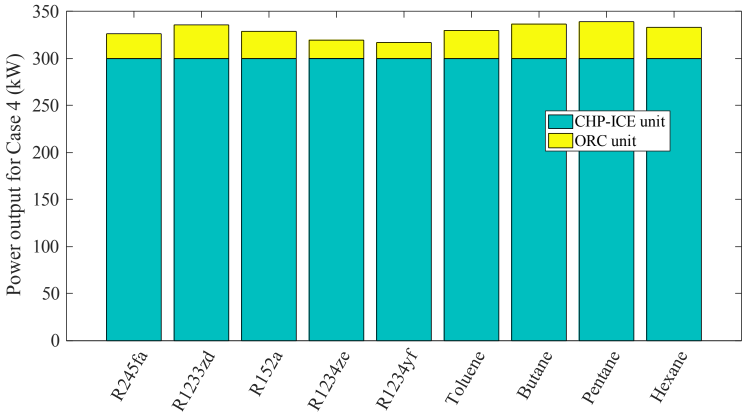

(d)

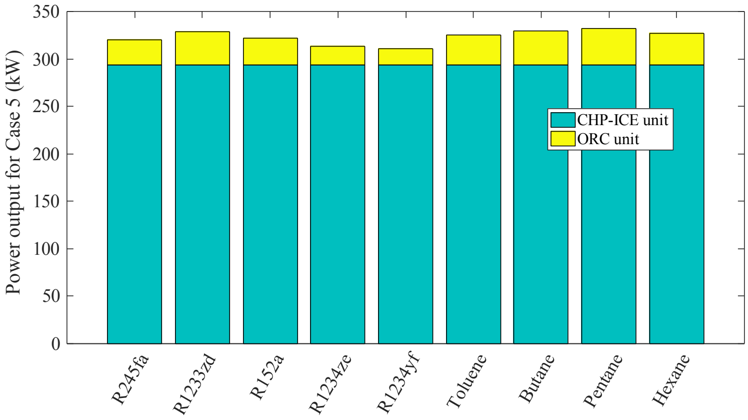

(e)

Fig. 23: Power output breakdown between the CHP-230 ICE and the bottoming ORC engine for: a) Case C1, b) Case C2, c) Case C3, d) Case C4, and e) Case C5.

The next metric investigated is the ICE-ORC CHP *SFC* for all working fluids and optimisation cases. Results reveal that when the ICE-ORC CHP system is optimised for maximum power output, this leads to system designs that consume more fuel, resulting in higher *SFC*s. The *SFC*s of the optimised ICE-ORC CHP systems are summarised in Fig. 24, for all fluids and cases investigated. The *SFC*s vary from 2.4 kW/kW (Case C3 integrated ICE-ORC CHP optimisation with pentane) up to 2.9 kW/kW (Case C1 nominal CHP-ICE only designs). The absolute SFCs (SFC_{abs}) are also illustrated in Fig. 24 and vary from 0.22 kg/ kWh_{net} in Case C1 (nominal CHP-ICE only design) to 0.175 kg/ kWh_{net} in Case C3 (with pentane). Therefore, it is revealed that *SFC*s can decrease by up to 20% with respect to the nominal case (C1) when the CHP-ICE operates at its nominal point. The addition of the ORC engine has also a profound impact on the SFC_{abs} not only when comparing different cases, but also within each case investigated, reducing these by up to 15%. It is also observed that ICE-ORC CHP systems optimised for minimum *SFC* in (Case C5) have similar *SFC*s to those achieved in Case C3, when the complete system is optimised for maximum power output. However, looking at the total fuel consumption of the two systems, the former has approximately 5% lower fuel consumption than the latter, while generating only 3% lower power output. Overall, these findings highlight that when optimising the CHP-ICE for maximum power output independently of the ORC engine design, the systems may have higher annual fuel consumption, increasing their running costs.

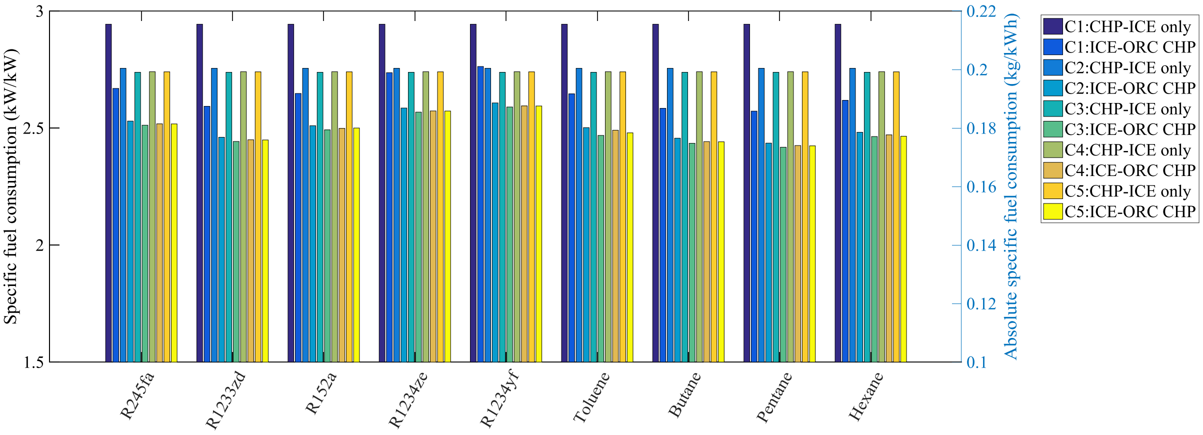

Fig. 24: *SFC* and SFC_{abs} for the different cases investigated, based on CHP-230 ICE with and without a bottoming ORC engine (Cases C1-C5 from left to right).

4.4.2 ORC engine design considerations

The optimum ORC engine design and operating set points are influenced by the optimisation objectives. The optimum ORC engines pressure ratio (PR) and working fluid flow rates, for all cases investigated are presented in Fig. 25. Results indicate that with some exceptions, for the majority of the working fluids and optimisation cases, the optimum ORC evaporating and condensing pressure levels stay almost the same. This is attributed mainly to the fact that the ORC engines investigated are subcritical, and because the heat source temperature is very high (>870 K), even when the CHP-ICE operates at nominal design conditions, the evaporating pressure is maximised even at the nominal case, and the subcritical constraint is active. Most PRs fall within the range of 7-25, while the working fluids mass flow rate varies strongly between the cases investigated, impacting the power outputs observed is previous sections. It is noted that the *PR*s for toluene only are quite high (up to ~45-55), especially in Cases C3 and C5 in which the integrated ICE-ORC CHP system is optimised. This has significant implications on the design and selection of the expander machines for this application.

Additionally, it is revealed that optimised ORC engines with fluids such as pentane, toluene, hexane and R1233zd operate with higher *PR*s (25-55), whilst their mass flow rates in the cycle are low, varying between 0.4-0.6 kg/s. On the contrary, most of the refrigerants investigated (R245fa, R152a, R1234yf, and R1234ze) present the opposite trend, i.e. lower *PR*s with higher mass flow rates in the cycle. This finding can be explained as follows; for every fluid the optimiser chooses to maximise the cycle power output, by first increasing the PR over the expander (i.e. the pressure difference between the evaporator and the condenser), without violating the constraints that the ORC engine should be subcritical. When these constraints are active, the next lever for increasing power output, is the increase of the working fluids mass flow rate. Since the cooling water circuit operating temperature is fixed (288-298 K), the condensation temperature is restricted by the water temperature and the condenser HEX *PP* (PP_{cond} = 10 K). For fluids, such as R152a, R1234ze, and R1234yf the saturation temperature is in the range of 308 K, at pressures of 6-9 bars, whilst pentane and hexane have similar saturation temperature at 1.4 and 0.5 bar, respectively. The differences in condensation pressure for similar condensing temperature, drive the differences in PRs amongst the various ORCs.

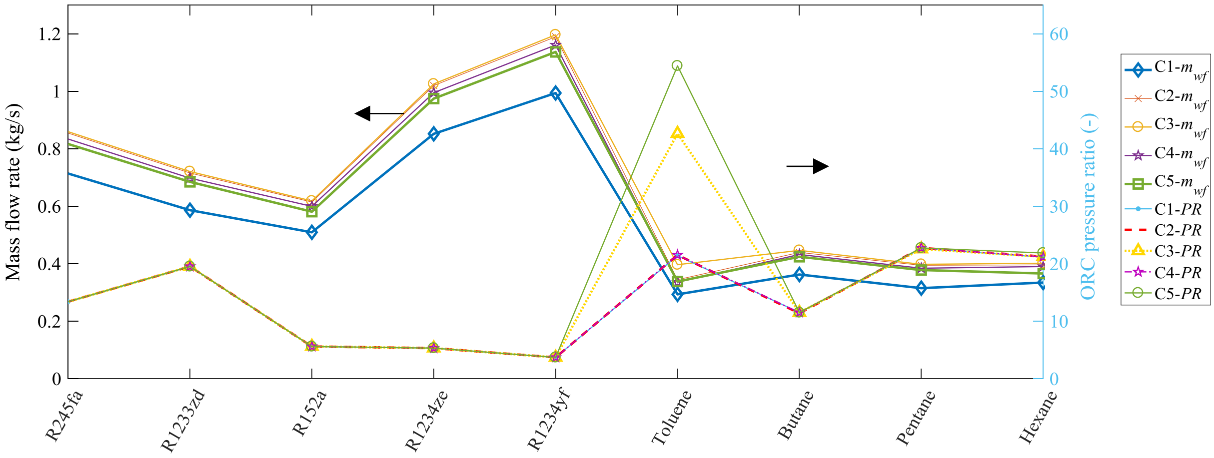

Fig. 25: Optimum ORC engine working fluid flow rate and pressure ratio for the CHP-230 ICE.

The heat input to the various ORC engine HEXs is illustrated in Fig. 26. Dry fluids, such as pentane, butane, toluene, hexane, R1233zd, and R1245fa, have little preheater load, because most of the preheating is performed in the recuperator HEX. This is owing to the high superheating degree of those fluids after the expander. The positive slope of the saturated vapour line results in these fluids being highly superheated when exiting the expander, offering great opportunity for recovering heat in the recuperator to preheat the high pressure cold liquid fluid after the pump. This is also illustrated in Fig. 26, where for these fluids approximately 70% of the heat rejection is performed in the recuperator and the desuperheater. In contrast isentropic fluids, such as R1234ze and R1234yf have important preheater load (Fig. 26.), while more that 50% of the heat rejection of the same fluids is performed in the two-phase condensing zone (Fig. 27). These findings have implications on the HEX architecture, design and costing, so as to maximise the ORC engine performance.

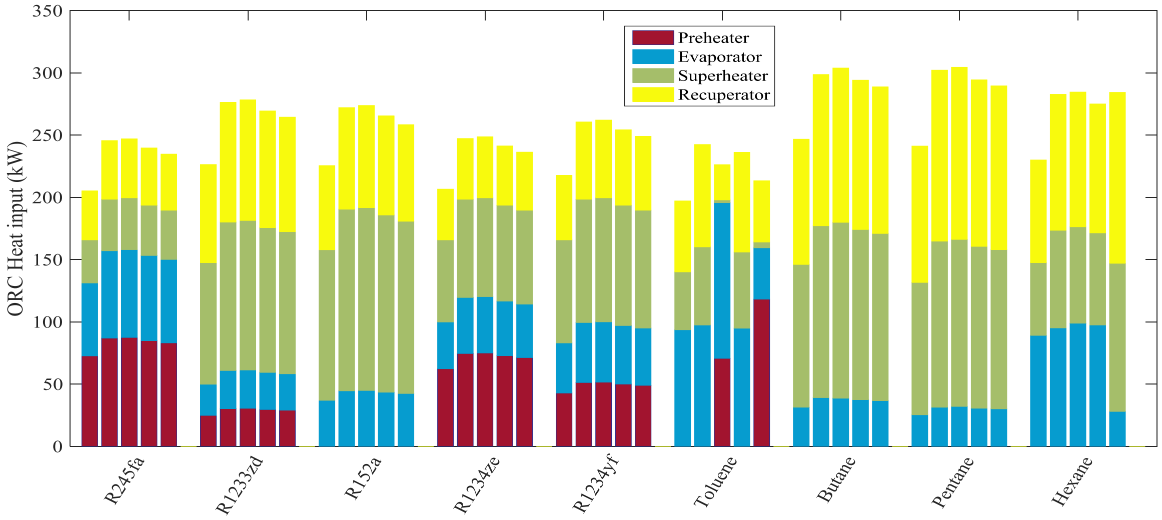

Fig. 26: ORC engine heat input load breakdown over the various HEX components for all working fluids and for all investigated cases (Cases C1-C5 from left to right, CHP-230 ICE).

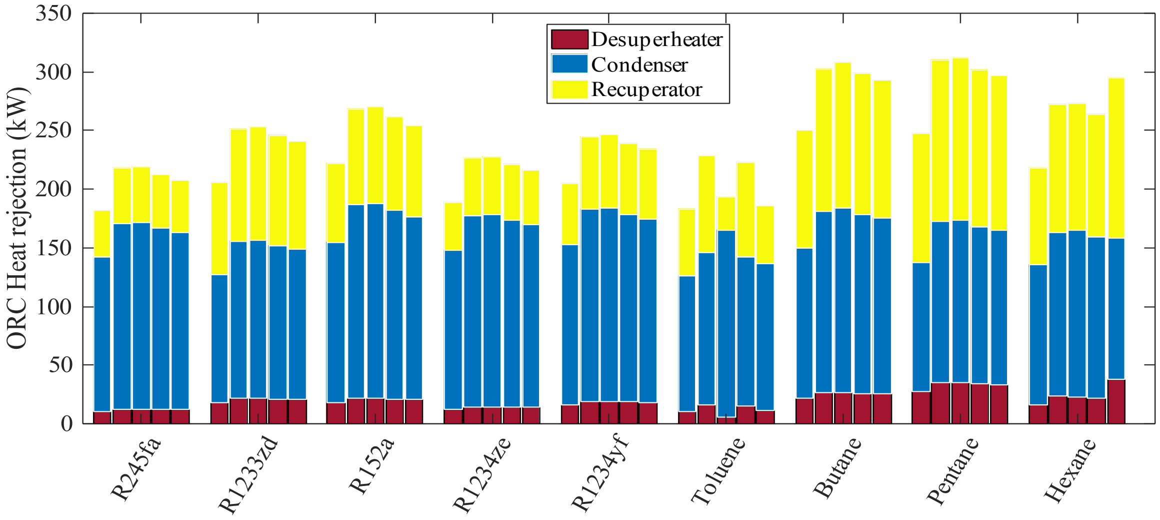

Fig. 27: ORC engine heat rejection load breakdown over the various HEX components for all working fluids and for all investigated cases (Cases C1-C5 from left to right, CHP-230 ICE).

The highest heat input to the ORC is generally recorded for the engines with the highest power output. Pentane (best performing fluid) has the highest heat input of 320 kW followed by butane with 310 kW (numbers quoted refer to Case C3 results). R1233zd has slightly lower heat input than hexane, although the former generates more power than latter. This is attributed to the higher cycle thermal efficiency of R1233zd in comparison to hexane. In Fig. 28, the ORC engine thermal efficiencies for all fluids and cases investigated are summarised. Pentane has the highest thermal efficiency (25%), followed by butane (22%), R1233zd (20.5%), hexane (19.5%) and toluene (17.5%). R1233zd operates with higher efficiency than hexane, therefore requires less heat input to the ORC evaporator HEX, in order to generate similar level of power output. Finally, a comparison of the ORC engines thermal efficiencies reveals only little variations across the various cases, with the exemption of Case C5, where the ORC engine efficiency is slightly higher.

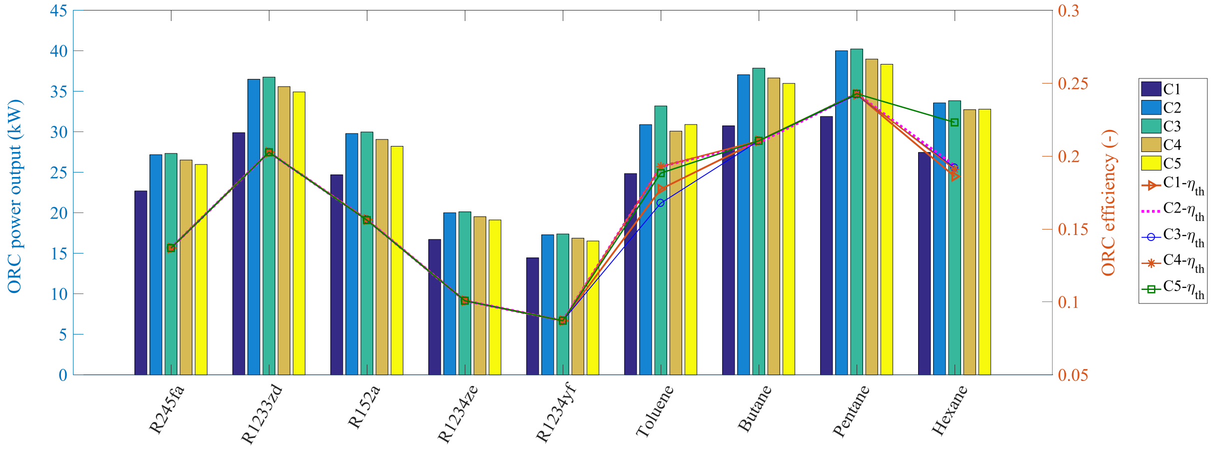

Fig. 28: ORC engine power output, and thermal efficiency for all cases with CHP-230 ICE (Cases C1-C5 from left to right).

4.5 Integrated modelling results – II: Turbocharged CHP-ICE

In this section, the modelling results for Cases C1-C5 for a turbocharged ICE-ORC CHP (CHP-2500 ICE) are presented and discussed. As with the analysis performed for the natural aspiration driven ICE-ORC CHP system (Section 4.4), firstly the system designs obtained when optimising for maximum power output are discussed, followed by the systems optimised for minimum *SFC*. Next, the implications of the various optimisation cases/objectives, on the ORC engine design are presented, focusing on the selection of expander machines and HEXs suitable for each case investigated.

4.5.1 CHP system level performance

The turbocharged CHP-2500 ICE power output, for every working fluid and case investigated is presented in Fig. 29a. Similarly to the trend observed for the natural aspiration CHP-230 ICE, the maximum power output of the ICE alone is obtained in Case C2, when the CHP-ICE is optimised for maximum power output. The highest power output corresponds to 2,540 kW, which is 42 kW higher than the nominal case (increase by approximately 2%). The exhaust-gas stream temperature when exiting the engine in Case C2 is 661 K, which is similar to the temperature obtained at nominal design operation (663 K), while the fuel consumption increases slightly (refer to Table 7). The electrical efficiency of the engine reaches 44% indicating a more efficient operation for Case C2, as opposed to the nominal operating conditions. A closer examination of the ICE operating conditions in Case C2, reveals that the EV stays open for longer than in Case C1, which is in agreement with data available in the literature for high performing engines. Furthermore, for both the IV and EV the lift height is approximately 8% larger than in the nominal design (Case C1), decreasing the blow-down losses of the ICE. In contrast, when the ICE-ORC CHP is optimised for minimum *SFC* (Cases C4 and C5), the power output of the ICE reduces by ~10% relative to Case C1. Nevertheless, such designs are associated with significant reduction in the fuel consumption of the system, by up to 14%, and higher combined system efficiency. Furthermore, looking at the exhaust-gas stream temperature exiting the turbocharged engine, this is 660-668 K for the optimum designs for maximum power output, but reaches 680 K in the designs optimised for minimum *SFC* (Table 7). This is related to the higher contribution of the ORC engine to the total power output in the designs for minimum *SFC*, as it will be discussed in subsequent sections.

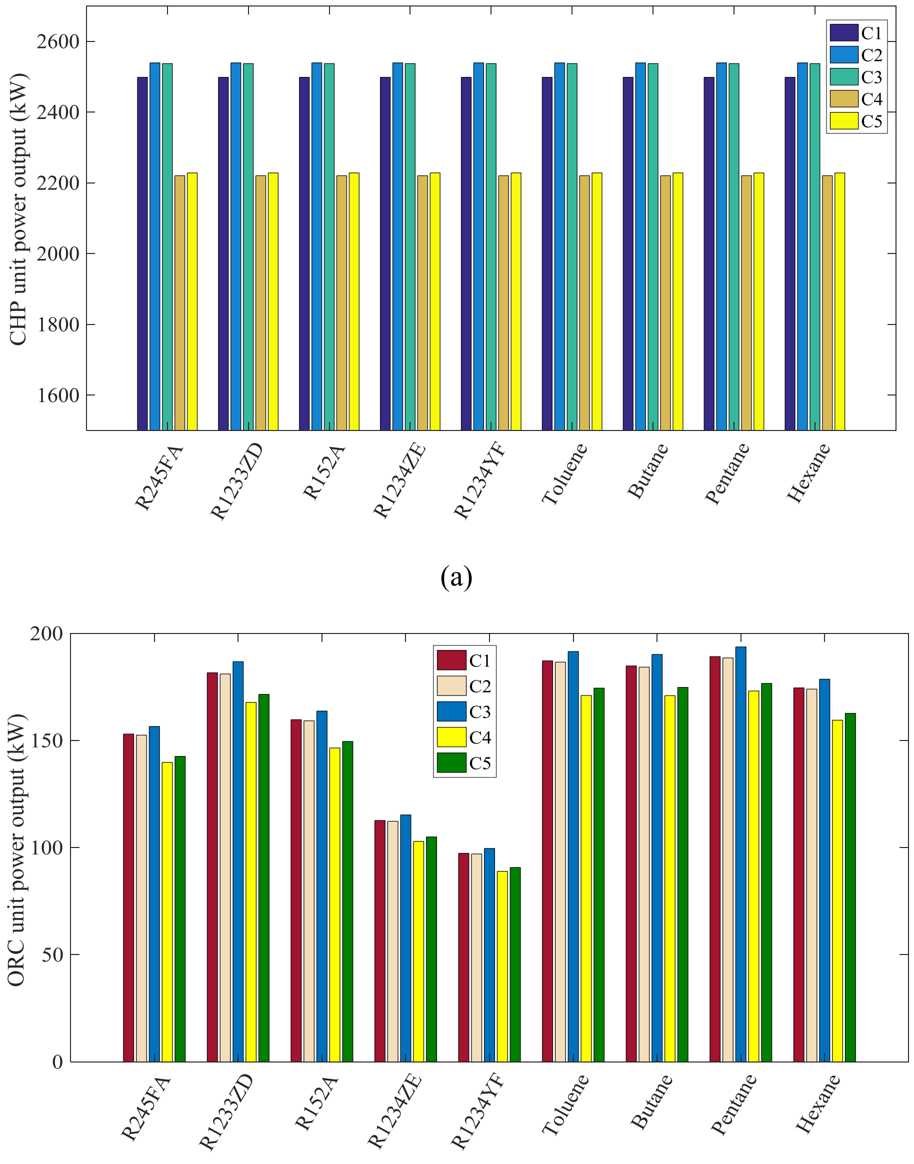

(a)

(b)

Fig. 29: Power output of: a) CHP-2500 ICE, and b) optimum bottoming ORC engine (Cases C1-C5 from left to right).

The optimum power output of the ORC engines, for all fluids and cases investigated is presented in Fig. 29b. When the ORC engine is optimised using the CHP-ICE nominal operating conditions (661 K exhaust-gas stream temperature), the highest power output recorded is 187 kW with pentane, 186 kW with toluene, 184 kW with butane, 181 kW with R1233zd, 174 kW with hexane and 152 kW with R245fa. In Case C2, when the CHP-ICE alone is optimised for maximum power output, the exhaust-gas stream temperature and mass flow rate are very similar to that of the nominal design operation (Table 7), thus the ORC engine design is similar to Case C1. The maximum power output is obtained in Case C3, when the integrated ICE-ORC CHP system is optimised for maximum power output. This finding is aligned with the results recorded for the natural aspiration engines. The best performing fluid in Case C3 is pentane generating 195 kW, followed by toluene with 192 kW, butane with 191 kW, and R1233zd with 187 kW. These power outputs are approximately 4-7% higher than those obtained in the nominal design scenario (Case C1).

Table 7: Optimum CHP-2500 ICE operation results.

		Cases				
CHP-ICE	**Parameter**	**C1 (nominal)**	**C2**	**C3**	**C4**	**C5**
CHP-2500	$\dot{W}_{\mathrm{ICE}}$ (kW)	2,498	2,540	2,537	2,220	2,230
	$\dot{Q}_{\mathrm{comb}}$ (kW)	5,748	5,787	5,778	5,038	5,087
	$\dot{Q}_{\mathrm{jw}}$ incl. $\dot{Q}_{\mathrm{w}}$ & intercooler (kW)	1,380	1,381	1,147	1,234	1,230
	$\dot{m}_{\mathrm{ex}}$ (kg/s)	3.51	3.50	3.52	3.06	3.09
	$\dot{m}_{\mathrm{f}}$ (kg/s)	0.117	0.118	0.118	0.103	0.104
	T_{ex} (K)	663	661	668	676	680
	η_{th} (for exhaust gases cooled to 120 °C)	0.40	0.40	0.37	0.42	0.42
	η_{el}	0.43	0.44	0.44	0.44	0.44

The total generated power breakdown between the CHP-2500 ICE and ORC engines for the various cases and fluids is presented in Fig. 30. The highest power output of the complete ICE-ORC CHP system is recorded in Case C3 with pentane or toluene and is equal to 2,732 kW (Fig. 30c). This represents an increase of 2.5% in comparison to the nominal case results (Case C1). As anticipated, the CHP-ICE power output dominates the system generation, with the ORC engine being responsible for 4-8% of the overall power output. The highest proportion of power generated by the ORC engine within the complete system is observed when the ICE-ORC CHP is optimised for minimum *SFC*. In generally, the ORC engine contribution to the total power generation is lower than that obtained for the natural aspiration engine CHP-230, due to: i) the lower exhaust-gas temperature of the CHP-2500 ICE; and ii) the inherent higher electrical efficiency of the large-scale ICE in comparison to the medium size engine, which favours the electricity generation from the CHP-ICE.

Despite the different ORC engine contribution to the total power generated, between the two CHP-ICE engines, the same trend applies in that, although Cases C2 and C3 have similar power outputs, the fraction of power generated by the ORC engine increases in Case C3, when the integrated ICE-ORC CHP system is optimised for maximum power output. It is noted that the ORC engine with toluene in Case C2, is responsible for 6.5% of the total generated power, whereas in Case C3 the same engine is responsible for 7.5%. Importantly, the increase of the proportional ORC power output is associated with a reduction of the total fuel consumption relative to Case C2, as shown in Table 7. As discussed for CHP-230 ICE, these differences can have significant operational, lifetime and maintenance implications, since ORC engines are generally associated with lower maintenance than ICEs.

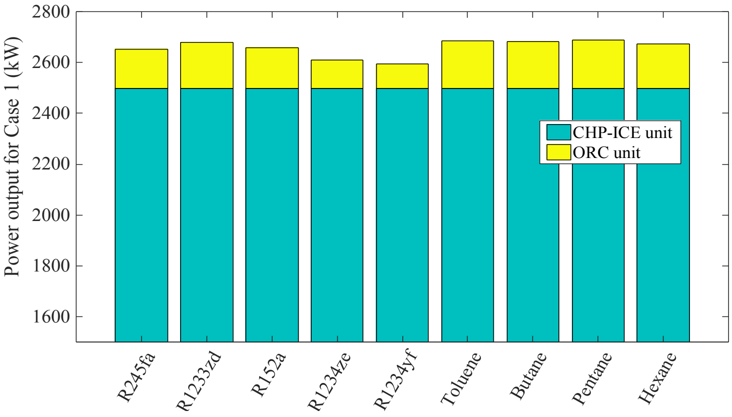

(a)

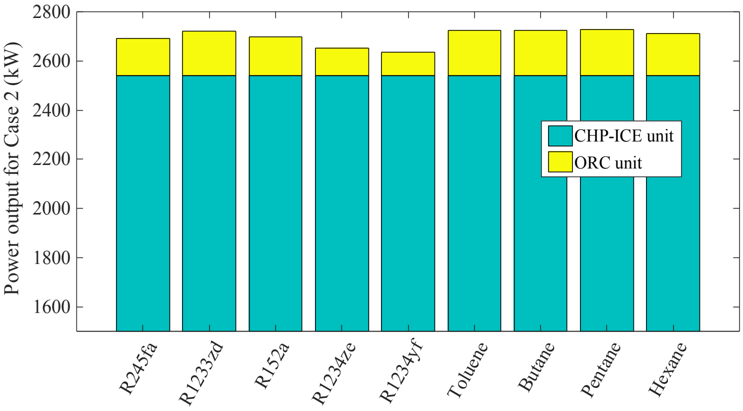

(b)

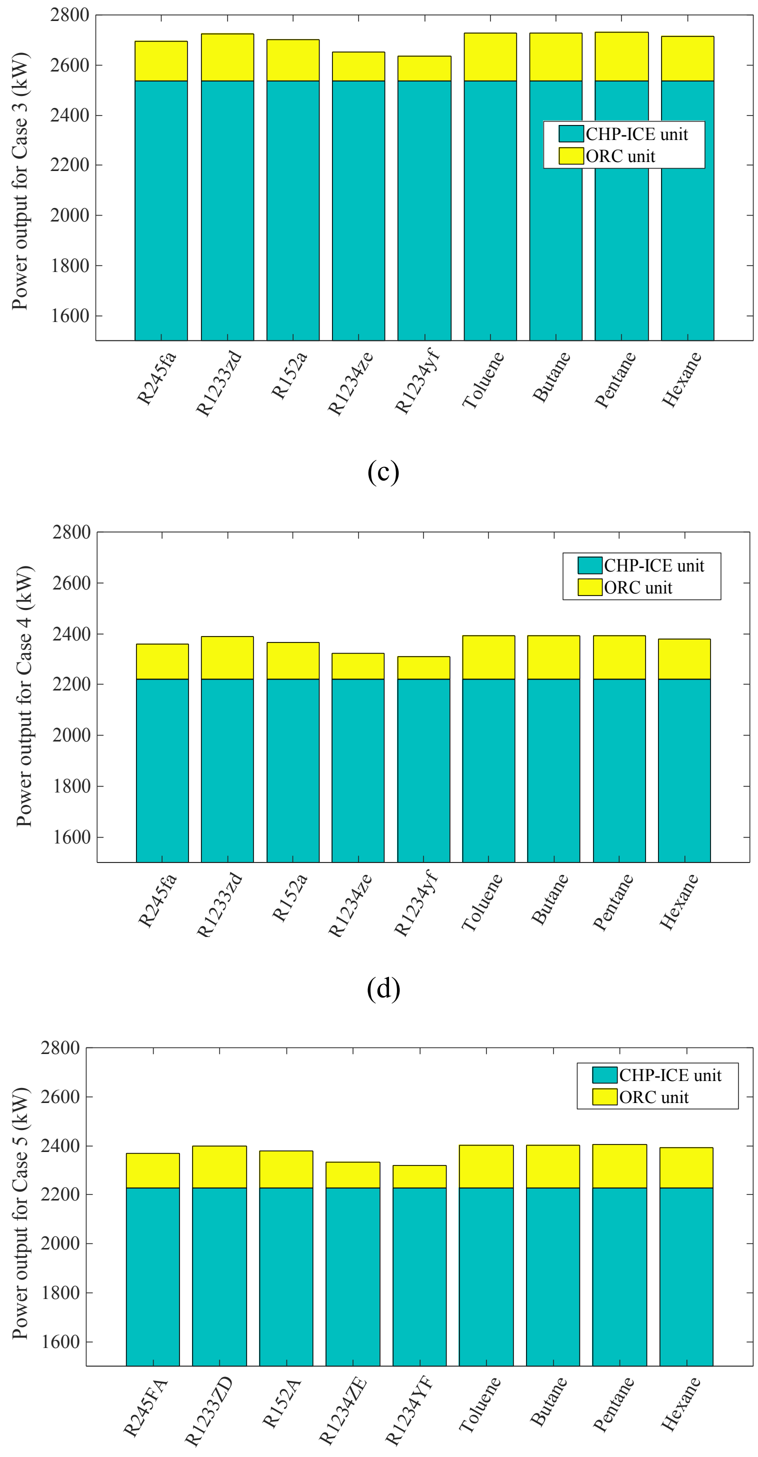

(c)

(d)

(e)

Fig. 30: Power output breakdown between the CHP-2500 ICE and the bottoming ORC engine for: a) Case C1, b) Case C2, c) Case C3, d) Case C4, and e) Case C5.

In Fig. 31, the *SFC* results are presented, for all fluids and cases investigated. The lowest *SFC*s are recorded for toluene and pentane in Cases C4 and C5, corresponding to 2.1 kW/kW. This value is approximately 8% lower than the nominal Case C1 for the CHP-ICE alone. The absolute SFC_{abs} follow a similar trend; the ICE-ORC CHP with pentane consumes 0.155 kg/kWh (Case C5), which is 4.5% lower that the integrated

ICE-ORC CHP in Case C1 for the same fluid, and 8% lower than the stand-alone ICE, when operating at nominal conditions (Fig. 31). Additionally, the values of the *SFC* (or SFC_{abs}) when optimising for minimum *SFC* are similar to those obtained in Case C3, when the complete system is optimised for maximum power output, but the former are associated with significantly lower fuel consumption, while also the power output breakdown differs by promoting the ORC engine power generation. The results highlight that there is a trade-off to be considered whereby optimising for maximum power output the system has higher fuel consumption. These findings can be utilised by the stakeholders, to evaluate the financial viability of alternative system configurations, with different associated upfront and operational costs.

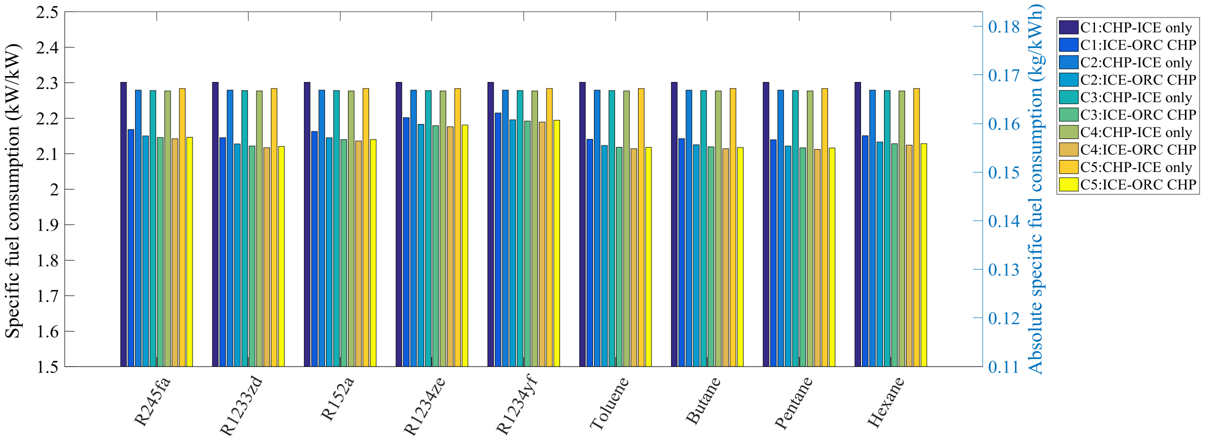

Fig. 31: *SFC* and SFC_{abs} for the different cases investigated based on CHP-2500 ICE, with and without a bottoming ORC engine (Cases C1-C5 from left to right).

4.5.2 ORC engine design considerations

As discussed earlier, a key difference in the operating conditions of ORC engines coupled with turbocharged engines or natural aspiration ones, is the exhaust-gas stream temperature entering the ORC engine evaporator, which ranges between 660 and 680 K for the former (turbocharged engines) and corresponds to approximately 1,000 K for the latter (natural aspiration engines). This is reflected in the ORC engine power output, operating set points, and efficiency. More precisely, in Fig. 32, the ORC engine *PR*s and working fluid flow rates are presented. The optimised ORC engines recovering heat from the exhaust-gas stream of the turbocharged engine operate with lower PRs of 5 to 34 (PR is 44 only for toluene), as opposed to the PRs of 7 to 55 obtained for the natural aspiration CHP-ICE (Section 4.4). This finding indicates that transcritical ORC engines may be suitable for high temperature applications. However, the additional cost of these systems might risk the overall viability of the project and need to be carefully considered. Similarly to the findings for CHP-230 ICE, fluids with high *P*Rs operate with lower mass flow rates, and vice versa. Comparing the PRs between the different cases investigated, for all cases the optimum PRs per fluid are similar, indicating the constraints for the minimium/maximum pressure levels or pinch point are active. Consequently, the power output of the ORC engine can improve further by increasing the working fluid mass flow rate in the system, or the *SHD*.

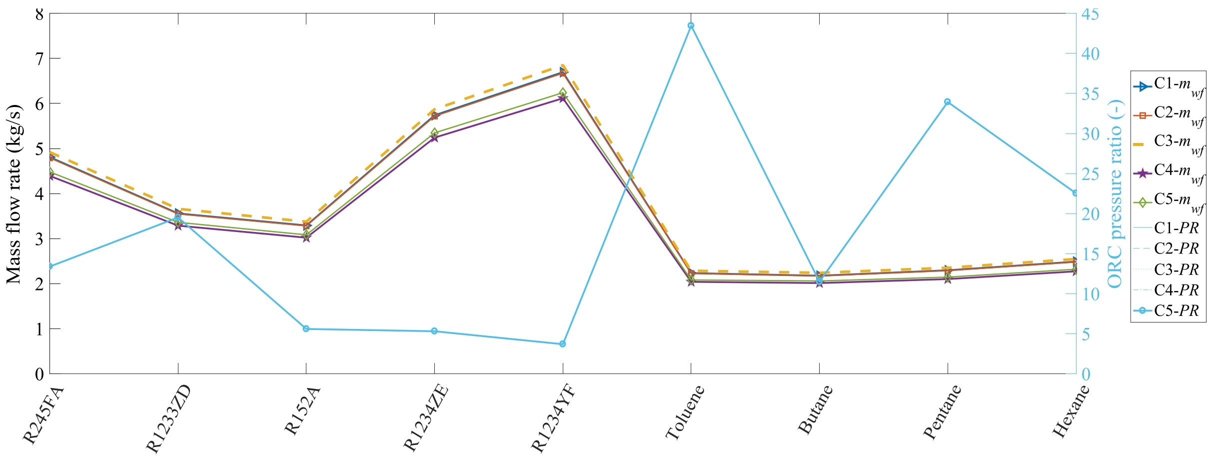

Fig. 32: Optimum ORC engine working fluid flow rate and pressure ratio for the CHP-2500 ICE.

The ORC engine heat input and heat rejection loads are presented in Fig. 33 and Fig. 34, providing also the load breakdown between the various HEXs of the system. When the ORC operates with high *SHD*, the recuperator load increases, because the working fluid exiting the expander is still highly superheated. A case in the point is fluids such as butane, R1233zd, and R152a which have approximately 53% of the heat input delivered in the superheater, and 30% in the recuperator (Fig. 33). Consequently, for the same fluids more than 50% of the heat rejection occurs in the recuperator and the superheater (Fig. 34).

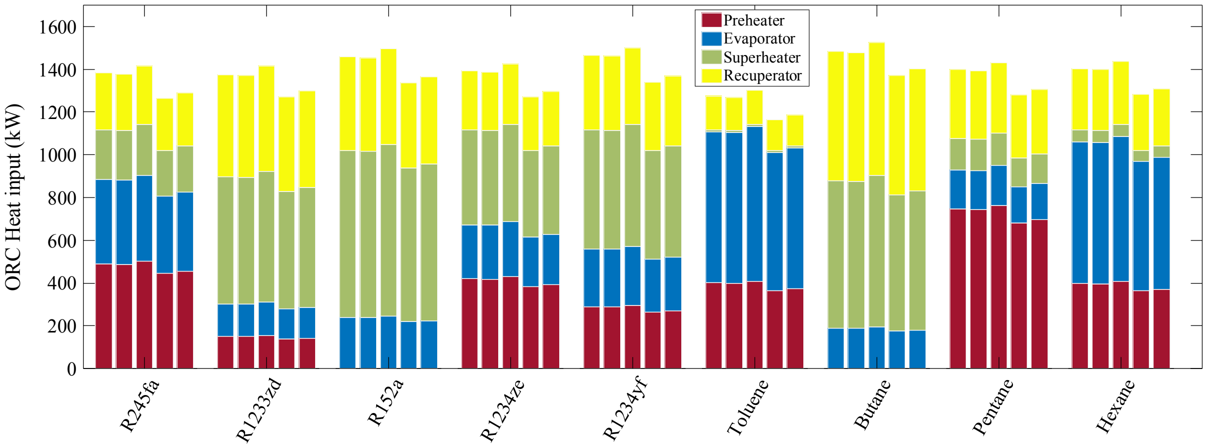

Fig. 33: ORC engine heat input load breakdown over the various HEX components for all working fluids and for all investigated cases (Cases C1-C5 from left to right, CHP-2500 ICE).

In contrast, fluids with low *SHD* (e.g. pentane and toluene), have low heat rejection to the recuperator and desuperheater. This is attributed to the differences in evaporation saturation temperatures between these fluids; for the latter, the saturation temperature in the evaporator is 467 K (pentane) and 445 K (toluene), which are higher than those for R152a (384 K) or butane (422 K), allowing higher superheating, without violating the evaporator *PP*. Therefore, depending on the fluid and the optimisation objective, more focus should be given on the recuperator, or the superheater design, to ensure good heat transfer. This however, may impact the cost of the ORC engines. These aspects will be discussed in subsequent chapters, where the ORC engines design will be assessed from a thermoeconomic perspective.

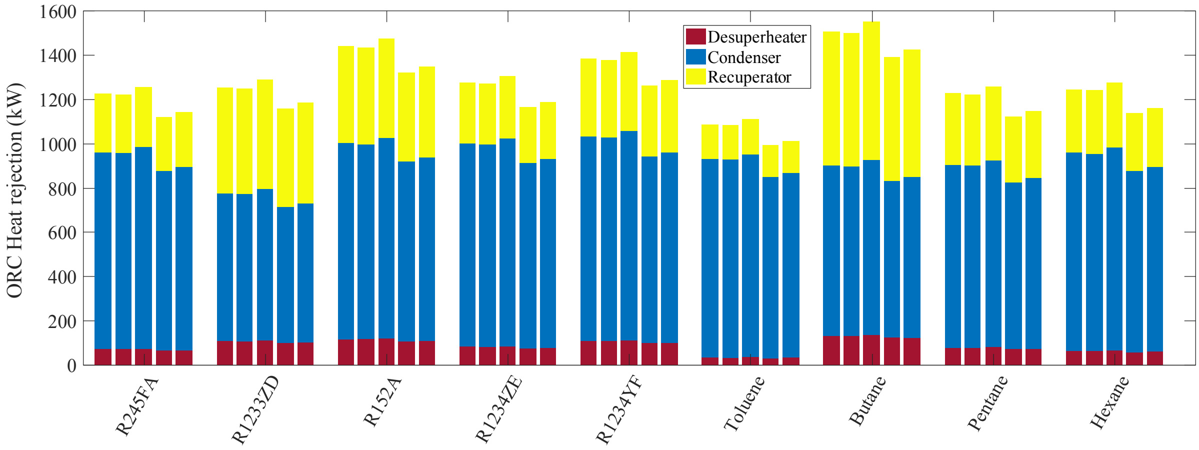

Fig. 34: ORC engine heat rejection load breakdown over the various HEX components for all working fluids and for all investigated cases (Cases C1-C5 from left to right, CHP-2500 ICE).

The ORC engine thermal efficiencies are presented in Fig. 35. The highest thermal efficiency is obtained with butane (21%), followed by R1233zd (20.3%), pentane (18%), toluene (17%) and hexane (16%). It is highlighted that the ORC efficiency figures obtained for the turbocharged CHP-2500 ICE are lower than those recorded with the naturally aspirated CHP-230 ICE, mainly owing to the higher exhaust-gas stream temperature of the latter. It is also noted that the best performing fluid in terms of thermal efficiency (butane) does not coincide with the fluids with the highest power output (pentane or toluene), indicating that the former may be able to utilise less available heat while generating equivalent amount of power. Finally, by comparing the best performing fluids for ORC engines coupled to CHP-230 ICE and CHP-2500 ICE, it is indicated that the same four working fluids outperform, namely pentane, butane, R1233zd and toluene, with the order of magnitude in terms of power output, dependent on the optimisation case investigated.

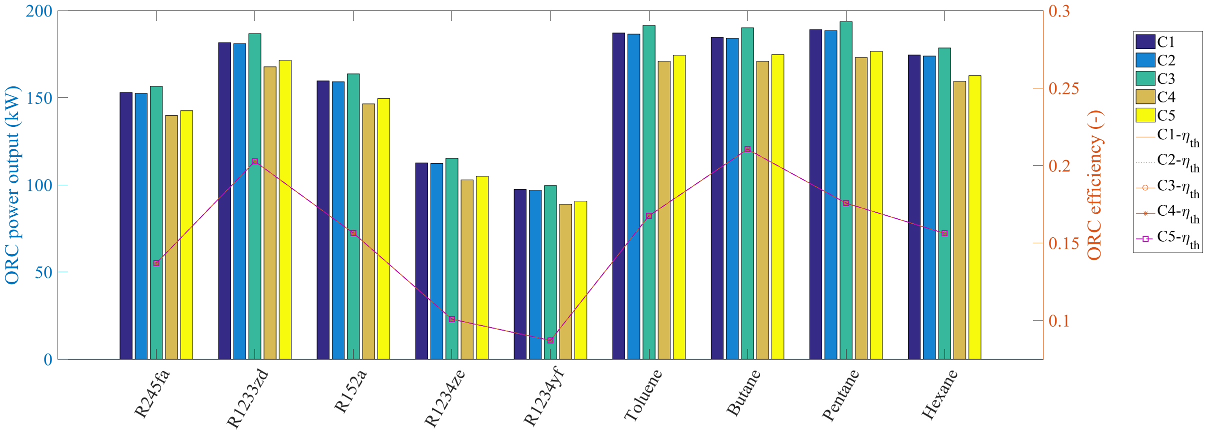

Fig. 35: ORC engine power output, and thermal efficiency for all cases with CHP-2500 ICE (Cases C1-C5 left to right).

4.6 Integrated modelling results – III: Exergy analysis

The exergy destruction rate in the integrated ICE-ORC CHP system is presented in Fig. 36, for CHP-230, for all working fluids and cases investigated. On the same figure, the ORC engine exergy efficiency and the combined integrated ICE-ORC CHP system exergy efficiency are illustrated. When the power output of the ICE-ORC CHP system increases, the exergy destruction rate also increases (in absolute terms). Nevertheless, results highlight that the exergy efficiency of the optimised ICE-ORC CHP systems also increases, indicating that we utilise better the available exergy of the fuel. These findings are aligned with the results reports in Section 4.4, where the electric efficiency of the ICE in the optimised systems increases, in comparison to the baseline case (Case C1). The ORC engine thermal efficiency also increases when the integrated ICE-ORC CHP system is optimised. The maximum combined system exergy efficiency is observed in Case C5, corresponding to 47%, 46% and 45% for pentane, butane and R1233zd, respectively.

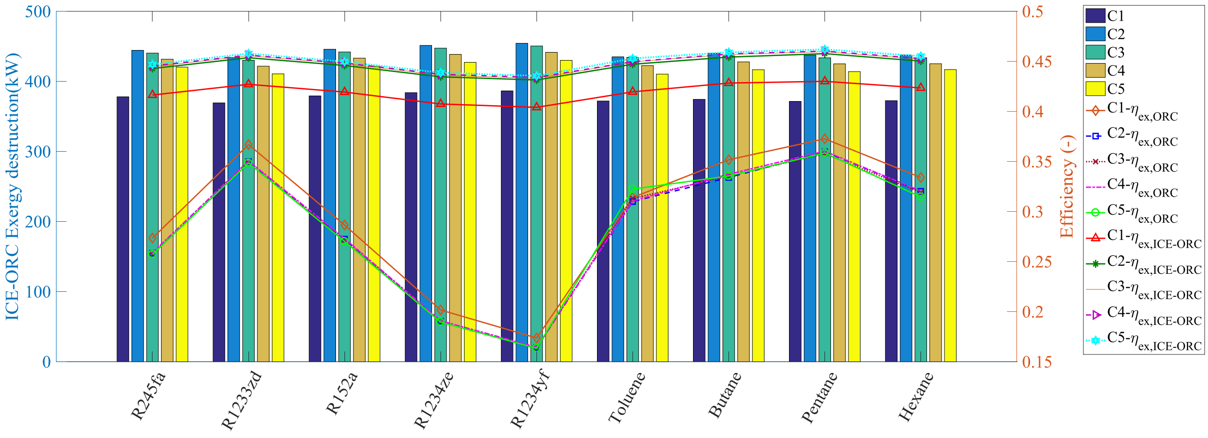

Fig. 36: ICE-ORC CHP exergy destruction, and exergy efficiency for CHP-230 ICE and all investigated cases (Cases C1-C5 left to right).

Looking at the findings for CHP-2500, the exergy efficiency of the integrated complete system also increases while moving from Case C1 to Case C5 (Fig. 37). It is noted that the integrated system exergy efficiency of CHP-2500 exceeds 50%, reaching 54%, which is higher than the figures recorded for CHP-230. Results also highlight that the absolute exergy destruction rate for this engine decreases, when the system is optimised for minimum SFC, similarly to the results obtained for CHP-230. This finding suggests that maximising the power output of the engine does not always mean that the utilisation of the available useful work is also maximised.

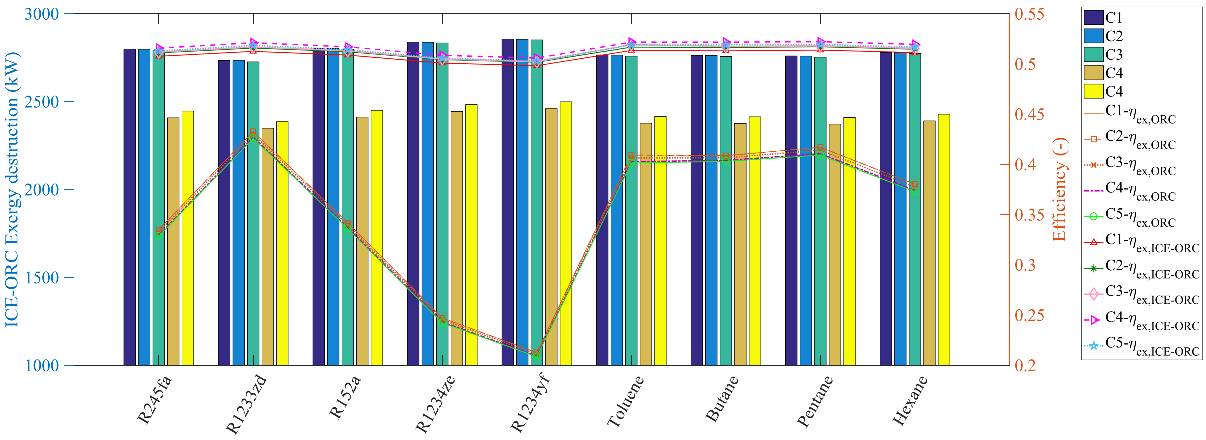

Fig. 37: ICE-ORC CHP exergy destruction, and exergy efficiency for CHP-2500 ICE and all investigated cases (Cases C1-C5 left to right).

Results also reveal a strong correlation between the absolute exergy destruction rate recorded and the ICE power output, for both CHP-ICEs investigated. The exergy destruction rate (in absolute terms) follows the ICE power output, in that when the latter increases or decreases, the exergy destruction rate (in absolute terms) also increases or decreases accordingly. This finding is explained by looking at the exergy destruction rate breakdown amongst the various components of the ICE-ORC CHP system, in Fig. 38 and Fig. 39. The exergy destruction breakdown reported is based on pentane and R1233zd, and is representative of the findings for all working fluids investigated. As anticipated, the majority of the exergy losses occur as an inevitable consequence of the combustion process in the ICE. Depending on the case and the fluid investigated, the contribution of the ICE to the total exergy destruction varies between 83% and 91%.

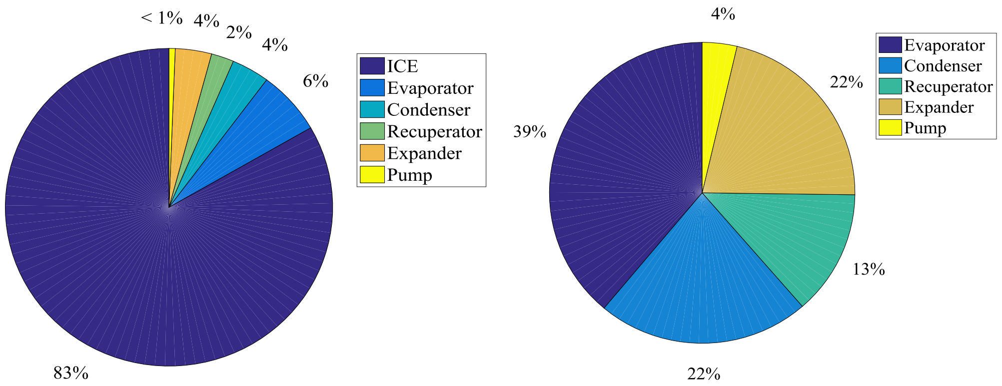

(a)
(b)

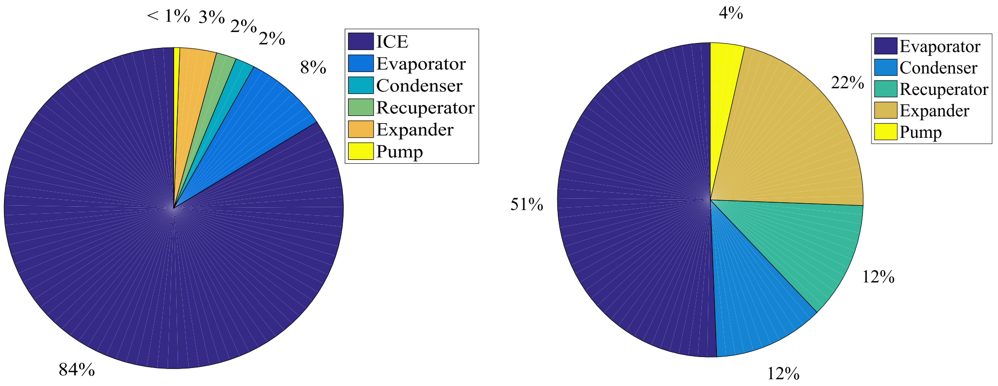

(c) (d)

Fig. 38: Exergy destruction rate breakdown: a) integrated ICE-ORC CHP system with pentane, b) ORC engine with pentane, c) integrated ICE-ORC CHP system with R1233zd, d) ORC engine with R1233zd, for CHP-230 ICE. The results presented here refer to Case C3, but are representative of all investigated cases (Cases C1-C5).

The ORC engine is therefore responsible for 9-13% of the total exergy destruction rate in the ICE-ORC CHP system. By examining the exergy destruction breakdown within the ORC engine components only (Fig. 38b,d and Fig. 39b,d) for the case of pentane, the evaporator HEX contributes between 37% and 39% to the total exergy destruction, followed by the expander with 22-35%, the condenser unit with 16-22%, the recuperator with 6-13%, and the pump with approximately 4-6%. When R1233zd is used as the ORC engine working fluid, the contribution of the evaporator to the total exergy destruction is higher than that recorded for pentane, corresponding to 51%. The latter finding is attributed to the larger temperature difference between the fluids entering and exiting the evaporator of the R1233zd ORC engine, especially when coupled to the CHP-230 engine. The cycles investigated are all subcritical therefore the highest evaporating temperature in the system is restricted by the maximum cycle pressure or the HEX pinch point. Since the exhaust gases of the CHP-230 ICE are at 1,000 K, there is a higher temperature difference between the working fluid evaporation temperature and the heat source. Adding to this, pentane can reach higher temperatures than R1233zd, before reaching the point where chemical decomposition phenomena of the fluid start occurring, therefore it offers a better temperature match to the heat source than R1233zd. The results presented in Fig. 38 and Fig. 39 are representative of the findings for the other working fluids investigated. A potential means of reducing the exergy destruction in the evaporator HEX would be the use of supercritical or subcritical cycles, to allow a better temperature match between the heat-source temperature and the working fluid. However, as aforementioned there are other cost and operating aspects to be evaluated when considering such ORC architectures.

To conclude, the findings highlight the importance of the evaporator HEX design and geometry. Designs should aim to maximise the HEX effectiveness, while reducing the backpressure effects on the exhaust-gas stream side. The ORC evaporator design and off-design operation is further investigated in Chapters

5 and 6, focusing on the optimal ORC engine components designs and off-design performance prediction. Finally, results reveal that the expander machine is the second biggest source of irreversibility in the ORC engines (findings aligned with other studies in the literature such as Ref. [92]), therefore careful selection of the correct type and design of the expanders is of paramount importance. In Chapters 5 and 6 that follow, we aim to identify the best performing expander machine and designs for ORC engines, from an operational perspective (design and off-design operation) and from an economic perspective (ORC engine specific investment cost - SIC).

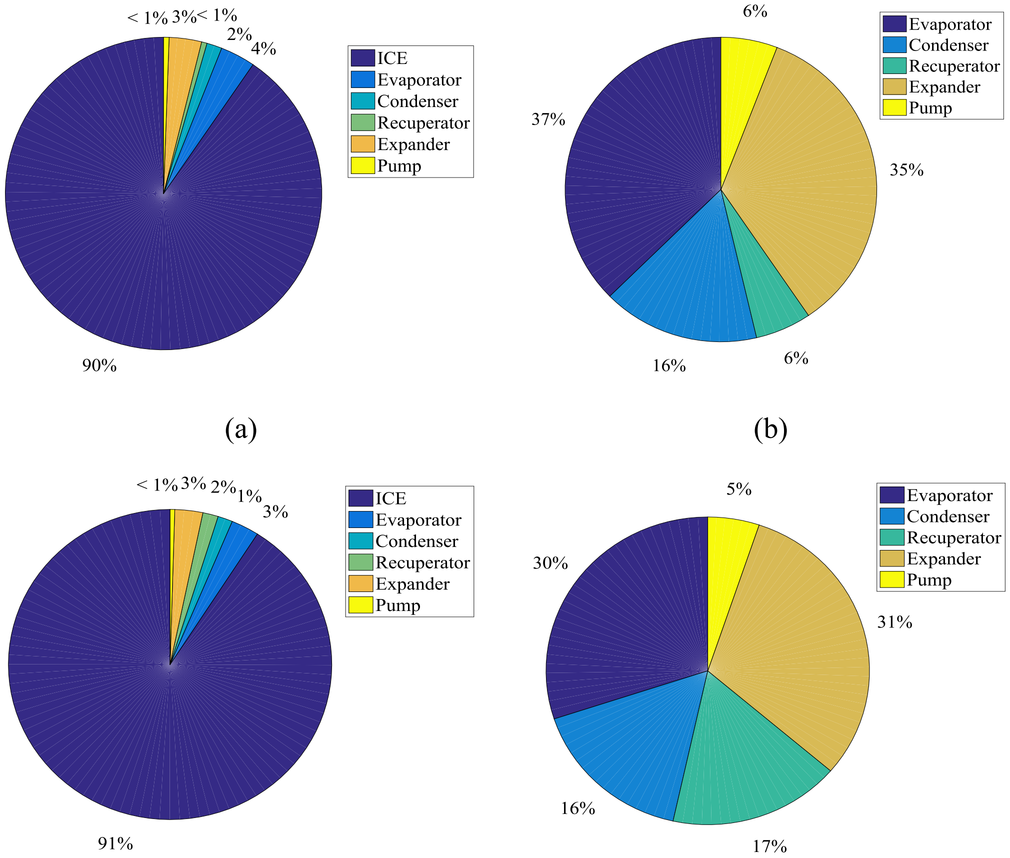

(a) (b)

(c) (d)

Fig. 39: Exergy destruction rate breakdown: a) integrated ICE-ORC CHP system with pentane, b) ORC engine with pentane, c) integrated ICE-ORC CHP system with R1233zd, d) ORC engine with R1233zd, for CHP-2500 ICE. Results are representative of all investigated cases (Cases C1-C5).

4.7 Summary and conclusions

An integrated ICE-ORC CHP whole-system optimisation framework has been developed for high-performance, advanced stationary cogeneration systems. This work differs from earlier efforts in that it accounts explicitly for the design parameters and operational conditions of both the ICE and ORC engines to optimise overall system performance, by capturing trade-offs between optimum ICE and ORC design and operation. In particular, we can identify, amongst other, the optimum ICE valve timing, lift and ignition timing, along with, amongst other, the optimum ORC working fluid and flow rate, evaporation and condensation pressures, superheating degree, so that together the two engines have the maximum total power output, or minimum total *SFC*. The framework includes a validated ICE model (covering naturally aspirated and turbocharged engines) and a steady-state subcritical recuperative ORC engine.

Findings reveal that the proposed optimised integrated ICE-ORC CHP system (Case C3) can achieve up to 30% higher power output than a nominal (Case C1) ICE design, with the ORC engine contributing between 4-15% of the total generated power, depending on the case and fluid. It is noted that the whole-system power output percentage improvement is higher for the CHP-230 ICE than for the CHP-2500 ICE, highlighting that heat recovery from medium scale CHP-ICEs may be more promising. The contribution of the ORC engine to the total power generation is higher in the case of the smaller ICE, improving the system fuel efficiency. Importantly, there are also operational, lifetime and maintenance implications that arise from these differences, since ORC engines are generally associated with lower maintenance requirements than ICEs.

Looking at the integrated ICE-ORC CHP efficiency (Case C3), this increases by up to 21% in comparison to the stand-alone CHP-ICE, and by 11% when compared to the nominal Case C1. The ICE efficiency also increases by up to 7.5% (Case C5), in comparison to the nominal ICE operation. The importance of accounting for the complete ICE-ORC CHP system optimisation is further highlighted, when comparing these figures to other studies available in the literature. Wang et al. [171] reported a maximum 6% efficiency improvement for ICEs within ICE-ORC CHP systems, whilst other studies reported even a decrease of the ICE efficiency by 2-3% [38]. Additionally, other studies investigating heat recovery from ICEs with ORC reported efficiency improvements of up to 8%, for the combined system [34,37,38].

When optimising for maximum power output of the ICE only (Case C2), the optimised operating conditions result in lower exhaust-gas temperatures exiting the ICE, which in turn maximise the power generation on the ICE shaft. On the contrary, when optimising for maximum power output the integrated ICE-ORC CHP system (Case C3), the exhaust-gas stream leaving the ICE is at higher temperature and pressure, to promote the power generation by the ORC engine; but this comes at the cost of slightly lower power output from the ICE (when compared to Case C2). This highlights the trade-off between achieving high heat recovery at the ORC engine, for lower power generation on the ICE side. The importance of the design of the ORC evaporator is also indicated, which should be sized to impose minimal pressure drop on the exhaust-gas stream to reduce the rise of antagonistic effects that deteriorate the ICE performance. It is also recorded that optimisation for maximising power results in higher fuel consumption, in comparison to the nominal ICE design (Case C1). Therefore, higher power output comes at the cost of higher fuel consumption. In contrast, when the system is optimised for minimum fuel consumption, this reduces by up to 17%, also allowing for an important reduction on the annual operating costs of the system.

Findings reveal that the type of aspiration of the ICE affects the exhaust-gas temperature entering the ORC evaporator, and thus the design and efficiency of the latter. Assuming the same expander machine efficiency, ORC engines coupled to CHP-230 ICE (natural aspiration) have higher thermal efficiency, because of the heat-source temperature reaching 1,000 K. The best performing ORC engine with pentane operates with 25% thermal efficiency, whilst for the same fluid the efficiency drops to 20% when coupled to CHP-2500 ICE (turbocharged engine), where the exhaust-gas temperature after the turbine does not exceed 700 K. The higher temperature difference observed in the ORC evaporator designed for CHP-230 ICE also results in lower heat transfer area requirements from the HEX. In turn, the pressure drop experienced in this smaller HEX by both the exhaust-gas and the working-fluid streams will be lower. The HEX will also be less expensive, reducing the ORC engine capital cost.

The ORC PRs observed between the two engines also differ. In the CHP-230 ICE case (high temperature exhaust gases), the PR ranges between 7 and 55, whilst in the case of the CHP-2500 ICE it does not exceed 44. The difference in PRs indicate the need for further developments towards suitable expander technologies for this application, while also suggesting that multi-stage machines may prove to be a suitable solution for the very high PR cases. In terms of working fluid selection, this study provides strong evidence that new hydrofluoroolefins such as R1233zd, are very promising for such high-temperature ORC applications, while being non-toxic, having a low flammability in comparison to hydrocarbons, and a low GWP. So, these fluids should be considered by the ORC vendors in the design of next generation ORC engines.

To conclude, when designing ORC engines as a bottoming cycle for stationary CHP applications, the impact of the optimised ICE design, operation and performance on the overall design is very important, also affecting the ORC engine design and power output. This study has proven that these systems should be addressed in an integrated manner. The novelty and where this work goes beyond previous efforts can be summarised as follows: i) this is a fully-integrated ICE-ORC CHP system tool that can simultaneously optimise the design and operating conditions of the ICE and the ORC engines, instead of assuming that the ICE operates independently from the ORC engine; ii) it considers closely the overall power and thermal performance trade-offs of the combined system; iii) it provides insights for the design of ICEs for stationary cogeneration applications, which can be used by ICE manufacturers when considering projects where the ICE will operate in conjunction with a bottoming ORC engine; and iv) it provides insights for the design of ORC engines, specifically for these applications where they are to be coupled to ICEs. Integrator companies, who buy the engines from the ICE and ORC vendors, to install and commission them on-site, are good candidates for adopting the complete ICE-ORC CHP optimisation approach presented in this thesis, since they have access to both engines. An alternative approach is to engage the ICE and ORC engine vendors, at the early design stages of an ICE-ORC CHP project. In doing so, both vendors will work together with the design team, to optimise the complete ICE-ORC CHP system performance, based on the specific requirements of the project.

Finally, the key areas identified as requiring further research for the integration of ORC engines in waste heat recovery CHP systems include:

- The design of the evaporator HEX to be able to withstand high operating temperature and pressure, while also having high effectiveness;
- The evaporator HEX design should minimise the backpressure effects on the CHP-ICE;
- The high PRs observed in the ORC engine require suitable expander selections, able to maintain high efficiency at such operating conditions;
- Suitable working fluids for high temperature application which are also environmentally benign are required.

In the next chapters, we focus on the ORC engine components performance optimisation that would yield the highest ORC engines efficiency improvement, as identified from the above analysis, i.e. i) the design of the ORC engine evaporator to maximise the HEX effectiveness, while reducing the backpressure effects on the exhaust-gas stream side; and ii) on the expander selection and operation, to identify the most well-suited technology for ICE-ORC CHP systems.

Chapter 5

Organic Rankine cycle off-design performance

> *"Energy efficiency is the one energy resource that every country possesses in abundance and is the quickest and least costly way of addressing energy security, environmental and economic challenges."*
>
> -International Energy Agency, World Energy Outlook 2016

5.1 Introduction

Organic Rankine cycle (ORC) engines is a promising candidate technology for recovering waste (or renewable) heat to generate power. In real applications, such as the coupling with solar collectors, geothermal energy, or the waste heat recovery from internal combustion engines in combined heat and power systems (CHP-ICE) examined in this thesis, the ORC systems will operate under variable heat-source conditions, in terms of temperature and mass flow rate. Therefore, to facilitate the wider adoption of these systems, apart from optimising the system thermodynamic performance at the nominal design point, special attention should be also paid on the optimisation of its performance at off-design conditions.

The ORC engine efficiency depends on: i) the ability of the evaporator heat exchanger (HEX) to extract heat from the heat source and transfer it to the working fluid; and ii) the efficient operation of the expander device, under varying pressure levels and mass flow rates. It is noted, in relation to (i), that the cooling water flow rate at the condenser can be readily adjusted to absorb a variable heat-rejection load at off-design operation by a variable-speed pump, which lends greater controllability to this component and shifts the focus to the evaporator. Studies in the ORC off-design literature have considered either: i) the optimisation of ORC designs for given heat-source conditions, and a new ORC configuration was obtained for every new heat-source condition (e.g. in an ICE-ORC CHP, for every part-load (PL) point operation of the ICE), instead of subjecting the nominal design ORC engine into off-design operation [101]; or ii) the ORC engine design for nominal conditions was subjected to off-design operation assuming that the components' performance will stay constant and equal to that at the design point [99,100]; or iii) particular focus has been given only on one ORC engine component under off-design operation, normally on the expander [74] or the evaporator [102,103] , but in isolation from each other. The aforementioned approaches can lead to sub-optimal ORC engine off-design operating points and performance predictions, since the interactions of the key ORC engine components (i.e. expander and evaporator) are not captured in an integrated manner.

From the limited literature on ORC engines operating at off-design conditions, where the components time-varying performance is incorporated in the complete engine model, the majority of the studies focus on turbine expanders, or single-stage screw expanders, with limited literature available on piston expanders off-design operation. Song et al. [97] evaluated the off-design performance of an ORC engine with radial-inflow turbine and plate heat exchangers (PHEXs), while recovering heat from a steam-turbine plant. However, the authors did not perform an off-design performance optimisation, but instead a simple parametric analysis has been conducted. ORC engines with axial turbines and plate-and-fin HEXs have been investigated in Ref. [98], focusing mainly on the off-design control strategies of the turbine. Pili et al. [106] evaluated the off-design performance of an ORC engine with turbine expanders and PHEXs, in waste heat applications, while Guopeng et al. [36] performed an off-design performance analysis of an ORC engine recovering heat from the exhaust-gas stream of an ICE. The turbo-expander and the PHEXs were designed for the rated ICE capacity, and then the system was subjected to off-design operation, accounting for the expander and HEX time-varying performance. Single-stage single screw expanders at off-design operation have been evaluated by Ziviani et al. [79] for small scale low temperature ORCs. Particular focus was given on the control strategy of the screw expander to maximise power output or efficiency, while the same authors in Ref. [172] have presented an ORC engine framework, including a notional volumetric expander and PHEXs, for performing off-design analysis. Finally, Refs. [77,111] have also investigated the off-design operation of ORC engines using single-stage screw expanders. In their study the authors focused on the expander design, without analysing the ORC HEX performance.

The literature review reveals that in contrast with the turbine and single-stage screw expanders, the design and off-design performance of piston expanders in ORC engines for stationary power generation is very limitedly documented. The aim of this work is to develop an off-design optimisation tool, which evaluates the performance of ORC engines with piston expanders, and alternative HEX architectures under varying heat-source conditions, while accounting explicitly for the time-varying characteristics of both the HEXs and expander of the ORC system. The tool identifies the new optimum operating points of the ORC system and generates off-design performance maps for the complete system, as well as for its constituent components. The tool developed can be also coupled with other expander devices models (of various levels of fidelity), to compare the off-design performance of alternative system configurations. To illustrate these capabilities, in this thesis the framework has been also utilised to predict the ORC engine off-design performance with two-stage screw expanders and compare this to designs with piston expanders.

This chapter is structured as follows: firstly, the subcritical non-recuperative ORC model considered is described, followed by a presentation of the HEX and expander sizing methodology for the nominal sizing and the off-design operation in Section 5.2. The optimisation problem for both the nominal (design) and off-design performance exercises is then explained in Section 5.3. The results for optimised ORC systems delivering maximum power output, while recovering heat from the exhaust gases of a CHP-ICE at 100% load are discussed in Section 5.4. The HEXs, and expanders are designed to deliver the nominal duty, as obtained from the maximum power optimisation analysis (Section 5.4). Next, with the components design fixed, the ORC engine operation is optimised for maximum power output, under different CHP-ICE part-load (PL) conditions. Alternative off-design modelling approaches are compared, and off-design operation maps are constructed for ORC engines with piston expanders (Section 5.5). The framework developed is then used to optimise the ORC engine off-design performance with screw expanders, and results are compared to the performance of ORC engines with piston expanders (Section 5.6). Finally, conclusions are drawn based on these findings (Section 5.7).

5.2 Organic Rankine cycle engine off-design modelling

The ICE-ORC CHP system considered in this study is comprised of a subcritical non-recuperative ORC engine, which recovers waste heat from the exhaust-gas stream of a CHP-ICE (Fig. 40). The ORC modelling equations have been previously presented in Section 3.3.

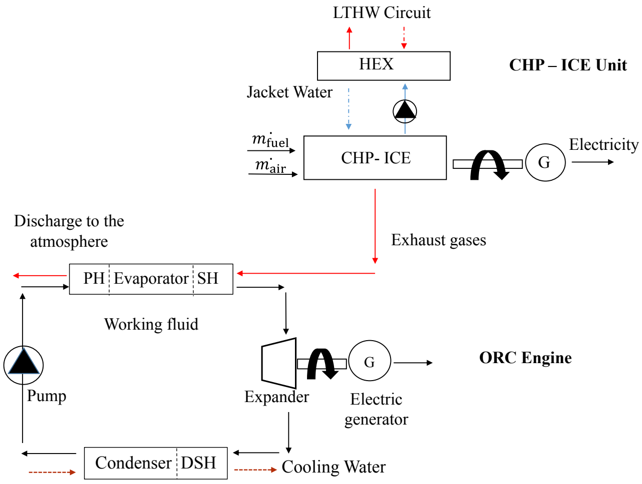

Fig. 40: Simplified ICE-ORC CHP system schematic, with non-recuperative ORC engine.

5.2.1 Heat exchanger off-design modelling

In this study, two HEX architectures have been compared for their off-design performance, namely double pipe HEXs (DPHEX) and plate type (PHEX). DPHEX have been selected because they provide a counter-flow heat transfer regime, increasing the HEX effectiveness for given flow conditions [43]. The optimised ORC cycles obtained in this thesis operate close to the critical pressure level of the working fluids, due to the high exhaust-gas temperature leaving the ICE-CHP. At high operating pressures, there is little enthalpy of vaporisation available, resulting in the majority of the heat transfer occurring in the preheater (single-phase) zone or in the recuperator (if a recuperative system is considered). To maximise the HEX effectiveness in the single-phase zones, achieving a "pure" counter-flow regime is of paramount importance. A case in the point is Fig. 33, which illustrates the heat transfer breakdown between the single and two-phase zones, within the evaporator HEX. On the condenser side, there is a higher percentage of heat transfer occurring in the two-phase condensing zone, however, due to the high degree of superheat of the working fluids, there is also an important amount of heat rejection occurring in the single-phase zone in the desuperheater or in the recuperator. Therefore, maximising the heat transfer in the single-phase zone of the condenser HEX, via achieving a counter-flow regime is also important. Fig. 34 illustrates a representative break-down of the heat rejection load within the condenser HEX. However, DPHEXs have higher area requirements per kW of heat transferred (kW/m^2) especially when compared to PHEXs. PHEXs main advantage is their compactness, due to the high HTCs achieved. However, potentially higher pressure drops may be observed in the PHEX, while also the materials selection should be such to ensure the unit can operate at high pressure/temperature regimes. The modelling approach used for the HEX nominal sizing and optimisation, and for the off-design optimisation is presented in Fig. 41.

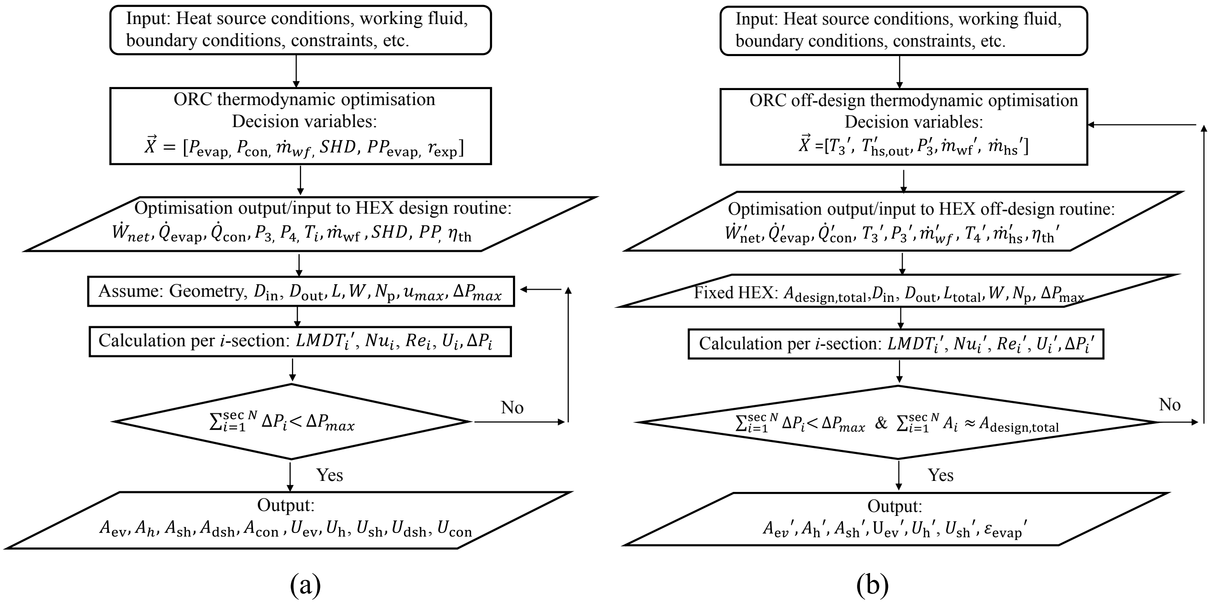

Fig. 41: Heat exchanger design routine for: a) nominal sizing, and b) off-design operation.

In the ORC design stage (Fig. 41a), the optimum thermodynamic cycle for every working fluid is first identified, using the exhaust gases leaving the CHP-ICE, while operating at 100% load. For detail description of the ORC operating variables presented in Fig.41, the reader is referred to the Nomenclature section. The optimum design cycle points defined in the ORC thermodynamic optimisation stage (refer to Section 5.4) are then used to size the various components. For the sizing exercise, the HEX area requirements, geometry, etc. are defined, aiming to maintain a maximum pressure drop across the HEX. For the evaporator HEX in particular, the heat-source side pressure drop (in this case the exhaust gases) is restricted to a few kPa (10-60 kPa) at the peak 100% mass flow rate, to avoid giving rise to significant negative backpressure effects on the ICE operation. It is noted that although backpressure phenomena can be severe is ICE for vehicles, in stationary CHP-ICE units, the ICEs are designed for waste heat recovery so an additional pressure drop is anticipated in the heat recovery component. The sizing is achieved by discretising the HEX in space into *N*-sections, and by calculating for each section *i* the corresponding local heat transfer coefficient (HTC) ‘α_i’, based on the working fluids mass flow rate, quality, temperature and pressure. The logarithmic mean temperature difference (LMDT) method is then used to obtain the area requirements for each section (A_i).

During the off-design operation, the temperature and the mass flow rate of the heat source will vary, following the CHP-ICE PL. During this stage the moving boundaries method is used to predict the HEX performance. In this modelling approach (Fig. 41b), there are no specific predefined zones in the HEX, instead the HEX is spatially split into i-segments (Fig. 42), and the quality of the working fluid is calculated in every segment, by assuming equal heat input per segment. Eq. 10 describes how heat is added to the working fluid, while this flows from segment “i-*1*” to segment “i” and then segment “i+*1*” (Fig. 42). More precisely, the working fluid enters segment “i”, with the specific enthalpy of segment “i-*1”*, absorbs heat “Q_i” (for the evaporator or rejects heat in the condenser) and its enthalpy rises (evaporator) / decreases (condenser) by $\Delta h(i)_{\mathrm{wf}}$:

$$\dot{Q}(i)_{\mathrm{wf}} = \dot{m}_{\mathrm{wf}}(h(i-1)_{\mathrm{wf}} + \Delta h(i)_{\mathrm{wf}}) \ . \tag{10}$$

This approach is suitable for off-design performance evaluation, since the changes in the temperatures and mass flow rates of the fluids affect the location of the transition points of the working fluid from liquid to vapour phase, and vice versa. The total HEX area available is fixed from the design step. By estimating the new HTC, the optimiser predicts the revised HEX performance at each section, and thus the amount of heat that the system can actually recover under the new operating conditions. For the condenser, it is assumed that the water flow rate can vary to accommodate the new heat rejection rate during off-design operation. The calculation of the HTCs for estimating the heat transfer area of the DPHEX and PHEX, during sizing and off-design operation has been presented in Chapter 3.

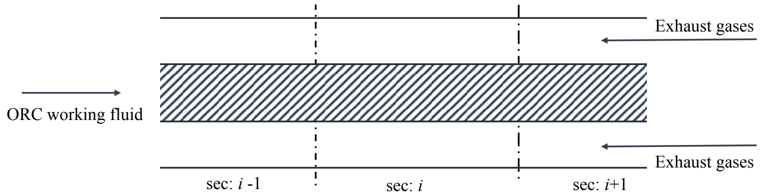

Fig. 42: Schematic diagram of typical heat exchanger sections segmentation for HTC calculation.

5.2.2 Expander off-design modelling

As discussed in previous section, piston expanders have great potential in power generation with ORC engines, due their ability to operate at high pressure ratios (PR) and relatively small volume flow rates, while maintaining good performance both at design and off-design operation. The modelling approach for predicting the off-design performance of the expander devices is presented in Fig. 43. During off-design operation the design and size of the expander is fixed, but the exhaust-gas flow rate and temperature vary, following the CHP-ICE PL. The ORC engine operating points should therefore be adjusted, to operate with the new heat-source conditions.

The piston expander off-design operation optimisation is presented in Fig. 43a. The optimiser selects some new operating points, in terms of evaporating pressure, degree of superheat, working fluid mass flow rate, etc. and solves the energy and mass balance equations. The new operating points are used as an input to the piston expander maps and the new isentropic efficiency of the expander, along with the real mass flow rate achieved are obtained. The optimisation continues until the figures obtained from the expander model (and the HEX models discussed in Section 5.2.1) converge with those of the thermodynamic energy and mass balance equations. Similarly, performance correlations for a screw expander have been used to predict the expander performance at off-design operation (Fig. 43b), and were compared to the piston expander results. The new operating points are used as input to the screw expander model, the off-design losses are calculated and the new isentropic efficiency and actual power output are obtained. Finally, for the pump off-design operation a fixed conservative efficiency has been assumed equal to 65% [40].

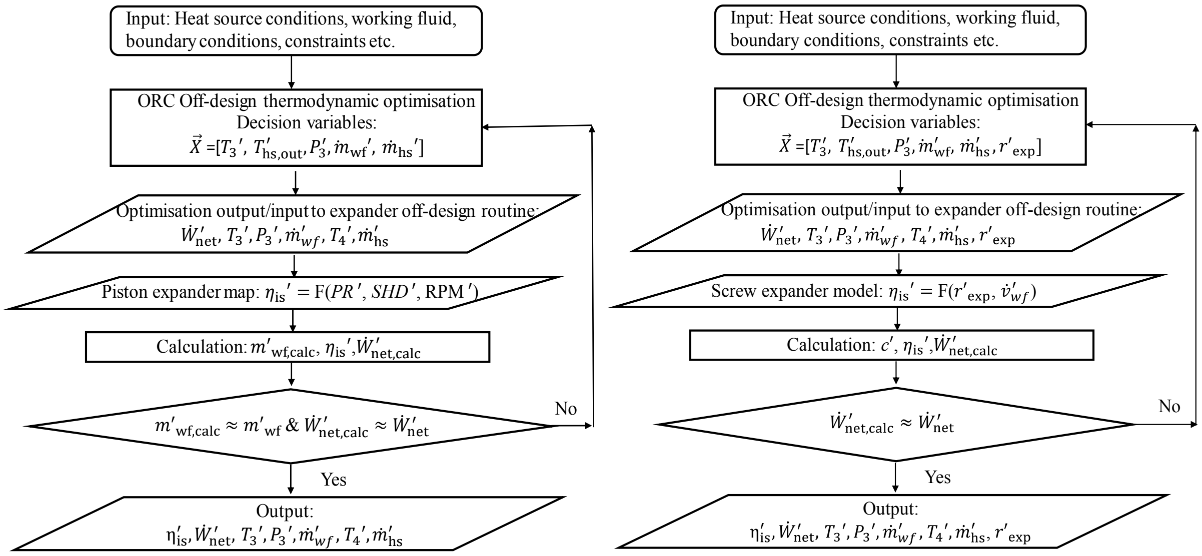

(a) (b)

Fig. 43: Off-design expander routine for: a) piston expander, and b) screw expander.

5.3 Off-design operation optimisation

In this section, single-objective optimisation has been used, aiming to maximise the net ORC power output, during both the nominal ($\dot{W}_{net}$) and the off-design ($\dot{W}_{net}'$) optimisation. While the objective function is the same for both exercises, the set of decision variables and constraints differ. The optimisation problem was solved in MATLAB© [128] using the *multistart* structure, which repeatedly runs a local solver (*fmincon*) from a number of different starting points, predefined by the user. The reader can refer to Chapter 3 for more details on the optimisation algorithms deployed in this work.

5.3.1 Nominal design optimisation

The optimisation function for the nominal system design is presented in Eq. 163. At this stage, the heat-source mass flow rate and temperature correspond to the CHP-ICE operating at 100% PL. The decision variable vector ($\vec{X}$) for the nominal operation consists of: i) the pressures in the evaporator and condenser (P_{evap}, P_{cond} [Pa]); ii) the mass flow rate of the working fluid ($\dot{m}_{\mathrm{wf}}$ [kg/s]); iii) the superheating degree (*SHD*) normalised over the maximum feasible, given the heat-source inlet temperature; iv) the pinch point of the evaporator (PP_{evap} [K]); and v) the volume ratio (r_{exp}) of the expander. For the screw nominal sizing, due to the low volumetric ratios achievable (5-7) [65], the optimiser has the option to select between single and two-stage expansion. The decision variables vector ($\vec{X}$) includes the same variables as per the piston expander sizing, with the exemption of the last variable (r_{exp}), which is replaced, by the variable (x_{exp}), which dictates the number of expansion stages.

$$\text{Maximise: } \frac{\{\dot{W}_{\mathrm{net}}\}}{\vec{X}=[P_{\mathrm{evap}},\, P_{\mathrm{cond}},\, \dot{\mathrm{m}}_{\mathrm{wf}},\, SHD,\, PP_{\mathrm{evap}},\, r_{\mathrm{exp}}]} \tag{163}$$

$$\text{Subject to: } P_{\mathrm{cond}} < P_{\mathrm{evap}} < P_{\mathrm{crit}} \tag{164}$$

$$0 \leq SHD \leq 1 \tag{165}$$

$$T_3 \leq T_{\mathrm{wf,max}} \tag{166}$$

$$PP_{\mathrm{min}} \leq PP \tag{167}$$

$$x_{\mathrm{wf},3\rightarrow4} = 1 \tag{168}$$

$$T_{4\mathrm{v}} \leq T_4 \tag{169}$$

$$T_{\mathrm{lim}} \leq T_{\mathrm{hs,out}} \tag{170}$$

The constraints ensure that the optimum thermodynamic cycle is technically feasible. The pressure at the evaporator should be lower than the working fluid's critical pressure, for the subcritical cycle assumption to be valid, and the condenser pressure must be lower than the evaporator pressure, to make the cycle feasible (Eq. 164). The normalised *SHD* over the maximum possible should vary between 0-1 (Eq. 165). For every working fluid, the temperature at the evaporator exit should not exceed the maximum allowable temperature that would ensure its chemical stability, as suggested in Ref. [163] (Eq. 166). Other constraints ensure that there are no pinch point violations across the HEXs (Eq. 167), or exclude ORC designs with two-phase expansion (Eq. 168-169). The heat-source fluid temperature when leaving the evaporator HEX is constrained by the dew point of the exhaust gases, to avoid condensation. For exhaust gases from a natural gas ICE, the typical dew point temperature can vary between 60 °C and 35 °C (333-308 K), depending on the concentration of oxygen [139,173]. Therefore, in this study 80 °C (353 K) was selected as the minimum allowable temperature for the exhaust-gas stream, well above the reported dew point levels. For the completion of the thermodynamic optimisation a notional isentropic efficiency for the expander equal to 0.7 is used, a figure very often reported in the ORC literature. The optimum cycle points obtained with this assumption are then used for the design of a piston expander capable of operating with isentropic efficiency of 0.7 at its design point. Additional mechanical and electric generator losses are applied as a post-processing factor to obtain the final efficiency, as discussed in Chapter 3. A similar approach is deployed for the screw expander performance. For the pumping process, a centrifugal variable speed pump with an assumed fixed efficiency of 0.65 has been used [40], as discussed in Chapter 3.

5.3.2 Off-design optimisation: Variable heat-exchanger and expander performance

Following completion of the nominal thermodynamic optimisation stage, the ORC engine optimum cycle points are used for the selection and sizing of the major system components. After this stage, the ORC engine components design and size are fixed. In the off-design optimisation, the new exhaust-gas mass flow rate and temperature, leaving the CHP-ICE are used as an input to the ORC optimisation. The HEX area available is known, along with the tube sizes, or the plates' width, corrugation etc. For the piston expander, the geometry is known, along with the number of cylinders, and isentropic efficiency maps are obtained for a range of PR, superheat and RPM. For the screw expander, the design point efficiency, volume ratio (VR) and flow rate are also known. For the pumping process, a centrifugal variable-speed pump is selected with relatively flat curve, which can maintain a constant pressure head across a range of flows. This property is important, because for the off-design operation, the pressure head of the system may be maintained at high levels to maximise the power output, while the flow rates/temperatures vary. For the pump off-design operation, a fixed efficiency of 0.65 [40] is used. The pressure level at the condenser is also fixed and equal to the nominal design operation. This is a reasonable assumption, since the cooling water flow and return temperature are fixed, while it is assumed that the cooling water mass flow rate can be adjusted to absorb the varying heat rejection load of the system at off-design operation. With the widespread use of variable-speed pumps in the building services sector, due to the energy savings they offer, this assumption reflects a real building installation. In this context, this work mainly focuses on the investigation of the evaporator HEX performance, under varying boundary conditions. These specifications form the input to the off-design optimiser, to ensure that the new optimum operating points are feasible, given the design and operational limitations of the components.

To perform the off-design optimisation, the decision variables vector ($\overrightarrow{X'}$) includes: i) the working fluid and heat-source temperature at the evaporator exit ($T_3', T_{\mathrm{hs,out}}'$ [K]); ii) the working fluid evaporation pressure (P_3' [Pa]); and iii) the working fluid and heat-source mass flow rate ($\dot{m}_{\mathrm{wf}}', \dot{m}_{\mathrm{hs}}'$ [kg/s]). The off-design objective function is presented in Eq. 171. Apart from the constraints considering the thermodynamic feasibility of the cycle (listed in Eqs. 164-170), additional constraints are required in this exercise, to ensure that the selected components are capable of delivering the new duties at the new operating points, as some combinations of the decision variables produce infeasible cycles. The additional constraints are summarised below:

$$\text{Maximise: } \frac{\{\dot{W}_{\mathrm{net}}{'}\}}{\overrightarrow{X'}=[T_3', T_{\mathrm{hs,out}}', P_3', \dot{m}_{\mathrm{wf}}', \dot{m}_{\mathrm{hs}}']} \tag{171}$$

$$\text{Subject to: } \frac{\mathrm{abs}(\dot{m}_{\mathrm{wf,th}}-\dot{m}_{\mathrm{wf,exp}})}{\dot{m}_{\mathrm{wf,exp}}} \leq 0.05 \tag{172}$$

$$\frac{\mathrm{abs}(A_{\mathrm{evap}}-A_{\mathrm{evap}}{'})}{A_{\mathrm{evap}}} \leq 0.05 \tag{173}$$

$$T_{4\mathrm{v}} \leq T_4{'} \tag{174}$$

$$x_{\mathrm{wf},3\rightarrow4}{'} = 1 \tag{175}$$

The mass flow rate of the working fluid delivered by the expander, for the new operating pressure and *SHD,* must be equal to the mass flow rate obtained from the simple energy and mass balance equations with the new temperature and pressure conditions (Eq. 172) with a contingency of ±5%. The heat transfer area required to deliver the new heat input at every PL, given the new temperature and flow regimes, should be equal to that available in the HEXs (Eq. 173) with a contingency of ±5%. The new temperature of the working fluid at the exit of the expander should be above the fixed condenser saturation temperature (Eq. 174). The new working fluid operating points should not fall within the two-phase region during expansion (Eq. 175). The piston expander RPM has been kept fixed and equal to the nominal design settings, to ensure compatibility with the electrical generator connected to the expander. Finally, for the screw expander off-design optimisation, the same principles apply, with the difference that in the decision variables vector ($\overrightarrow{X'}$) the variable $\dot{m}_{\mathrm{wf}}'$ is replaced by x'_{exp}, which defines the new breakdown of PRs between the expansion stages. The objective function is presented below:

$$\text{Maximise: } \frac{\{\dot{W}_{\mathrm{net}}{'}\}}{\overrightarrow{X'}=[T_3', T_{\mathrm{hs,out}}', P_3', \dot{m}_{\mathrm{hs}}', x_{\mathrm{exp}}{'}]} \tag{176}$$

5.3.3 Off-design optimisation: Variable heat-exchanger performance and fixed expander isentropic efficiency

Finally, the results of the complete time-varying optimisation presented in Section 5.3.2, are compared to a simplified off-design optimisation exercise where the (piston) expander efficiency is assumed fixed across all PL conditions. In this exercise, the evaporator pressure is also assumed fixed and equal to that during nominal (design) operation, aiming to maintain the design PR in the cycle. The condensation pressure is fixed as previously. In this case, the decision variables vector $\vec{X}'$ includes: i) the working fluid and heat-source temperature at the evaporator exit ($T_3', T_{\mathrm{hs,out}}'$ [K]); and ii) the working fluid and the heat-source mass flow rates ($\dot{m}_{\mathrm{wf}}{'}, \dot{m}_{\mathrm{hs}}{'}$ [kg/s]). The objective function is again the maximisation of the net power output of the ORC engine for every CHP-ICE PL point, while the set of constraints includes both the thermodynamic constraints listed in Section 5.3.1, and the components' operational constraints listed in Eqs. 173-175.

5.4 System optimisation and sizing results – I: Nominal operation

5.4.1 ORC power output optimisation

The operating characteristics of the ENER-G [9] CHP-ICE 1520 kW at PL are summarised in Table 8. The data points for 100% and 75% were taken directly from manufacturers' data sheets. The other points have been generated by the CHP-ICE thermodynamic model developed and validated in this thesis (refer to Chapter 4). With regards to the numbers, it is noted that while the load of the CHP-ICE engine is decreasing, the exhaust-gas mass flow rate also reduces, whilst the temperature increases. This is attributed to the operation of the turbo-charger of the engine. This feature will impact the ORC off-design optimisation, because the influence of the lower mass flow rate can be partially off-set by the higher heat-source temperature. The ORC engine nominal design optimisation (Section 5.4.1) and sizing (Section 5.4.2-5.4.3) are first performed assuming the CHP-ICE engine is loaded at 100% (nominal engine capacity). A summary of the ORC specification for the nominal system thermodynamic optimisation is presented in Table 9.

Table 8: CHP-ICE 1520 part-load operating conditions.

CHP-ICE 1520 PL	**Exhaust-gas mass flow rate $\dot{m}_{\text{hs}}$ (kg/s) (Heat source)**	**Exhaust-gas temperature T_{hs} (K) (Heat source)**
100%	2.16	682
90%	1.91	717
80%	1.70	720
75%	1.64	720
60%	1.29	727

Table 9: Summary of the ORC engine specification for the thermodynamic optimisation at nominal CHP-ICE operation.

Parameter	**Value**	**Parameter**	**Value**
PP_{cond} (K)	10	$P_{\text{evap,max}}$ (kPa)	0.95 P_{crit}
PP_{evap} (K)	5-30	$r_{\text{exp}}/x_{\text{exp}}$ (-)	8-18 / 0-1
$T_{\text{cw,in}}$-$T_{\text{cw,out}}$ (K)	288-298	T_{lim} (K) (for heat source)	353
$\dot{m}_{\text{hs}}$ (kg/s)	From CHP-ICE	$\eta_{\text{exp,is}}$ (-)	0.70
$T_{\text{hs,in}}$ (K)	From CHP-ICE	$\eta_{\text{pump,is}}$ (-)	0.65
$P_{\text{con,min}}$ (kPa)	30	η_{elg} (-)	0.95

The optimum power output of the ORC engine for all fluids investigated is presented in Fig. 44, along with the ORC thermal efficiency (η_{th}) achieved for CHP-ICE 100% load. Optimised ORC engines with screw expanders (Fig. 44b) generate slightly more power than the piston designs (Fig. 44a). However this is achieved by using two-stage expansion (two screw expanders in series). Due to the lower VRs of the screw machines the optimiser selects two-stage expansion to maximise the overall PR of the ORC engine. In contrast, piston expanders can operate with PRs of up to 30, so there is no requirement for two-stage expansion. The impact of these differences on the ORC engine cost are captured in the thermoeconomic analysis that follows in Chapter 6.

For ORC engines with piston expanders (Fig. 44a), the best-performing hydrocarbon is pentane with 88 kW, followed by toluene (83 kW), and hexane (78 kW). The best-performing refrigerant is R1233zd (85 kW), followed by R245fa (78 kW). For the majority of the working fluids, the optimiser aims to maximise the PR across the expander first until the maximum pressure constraint for a subcritical cycle is active, prior to increasing the *SHD*, or the working fluid mass flow rate. Therefore, most cycles operate very close to the fluid's critical pressure. However, the value of the PR over the expander varies between fluids, with the high-performing fluids having also the highest PR. This is explained as follows: for fluids such as R1234yf, R152a and R1234ze, the condensation pressure possible for the given heat sink temperature is higher (600-800 kPa) than that of fluids like R1233zd and pentane (90-156 kPa). This results in lower PR for the former fluids over the expander, and explains the low power output of the ORC engine for the same fluids.

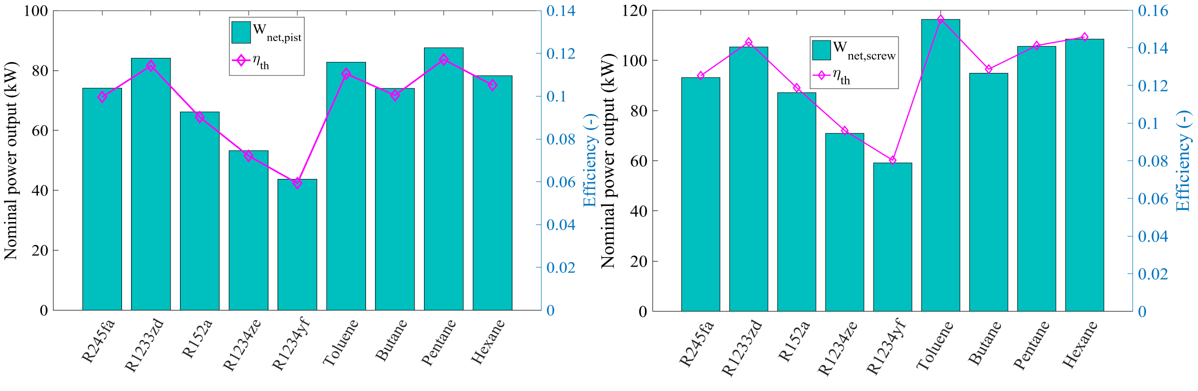

(a) (b)

Fig. 44: ORC engine optimum power output, and thermal efficiency, for nominal CHP-ICE operation (100%), with: a) piston expander, and b) screw expander.

The best performing hydrocarbon for ORC engines with screw expanders (Fig. 44b) is toluene (115 kW), followed by hexane (110 kW) and pentane (107 kW). The best performing refrigerant is R1233zd (108 kW) followed by R245fa (92 kW). Although the absolute power output figures may vary slightly from those achieved with piston expanders, the trend in the best performing fluids is similar. The thermal efficiency of the optimum cycles is also presented in Fig. 44, for all working fluids investigated. As expected, the best performing fluids in terms of power output, also have the highest thermal efficiency corresponding to 12%, 11.5%, 11%, and 10.4%, for pentane, R1233zd, toluene and hexane, respectively (ORC with piston expanders). A similar trend is observed for the thermal efficiency of ORC engines with two-stage screw expanders; the thermal efficiencies correspond to 15.5%, 15%, 14%, 14%, 12.5%, for toluene, hexane, pentane, R1233zd, and R245fa, respectively. The efficiency findings have been compared to other studies which used R245fa, the most a widely-studied working fluid in the ORC literature. In this work, the optimised ORC thermal efficiency with R245fa ranges between 10-12% (at the design point), whilst in Ref. [100], the authors report thermal efficiency of 10.5%-12.5%, Ref. [50] report efficiencies of 11.5-12.5%, and Ref. [174] thermal efficiency of 10.2%. These findings support the validity of the present model, since the present results are well aligned with those reported in the literature.

5.4.2 Nominal heat exchanger design and sizing

The next step in the ORC sizing problem is to size the HEXs of the system to deliver the nominal duty. The optimum thermodynamic cycle points obtained will be used for the ORC HEX sizing, following the methodology presented in Chapter 3. As discussed, the HEXs selected for this study are DPHEXs and PHEXs. The heat transfer area requirements of the evaporator HEX for ORC engines with piston expanders are shown in Fig. 45 and with screw expanders in Fig. 46. When DPHEX is used, for most of the working fluids, the total area requirements do not exceed 200 m^2, with the exception of toluene, which requires almost 500 m^2 of heat transfer area in ORC engines with piston expanders and 600 m^2 in ORC engines with screw expanders. This significant difference in area requirements is mainly attributed to the logarithmic mean temperature difference (LMDT) across the HEX for toluene, and the other candidate working fluids (Fig. 45a and Fig. 46a). The optimal cycle with toluene has the lowest evaporator pinch point among the fluids investigated, resulting in the lowest LMDT, especially in the preheating zone. For the same HEX section, while the other working fluids operate with a LMDT of 60-90 K, toluene operates with 16 K, which dramatically increases the heat transfer area (Fig. 45c,d). For all working fluids the lowest LMDT is observed in the preheating section, followed by the evaporating two-phase zone, and the superheater. This finding is explained by the high heat-source temperature when entering the evaporator, which results in a high temperature gradient over the superheater and the two-phase evaporating zone.

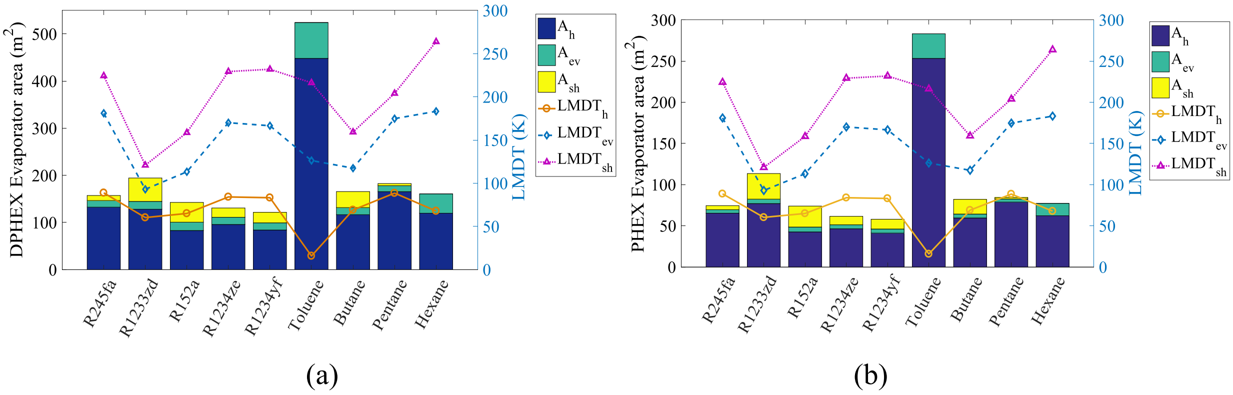

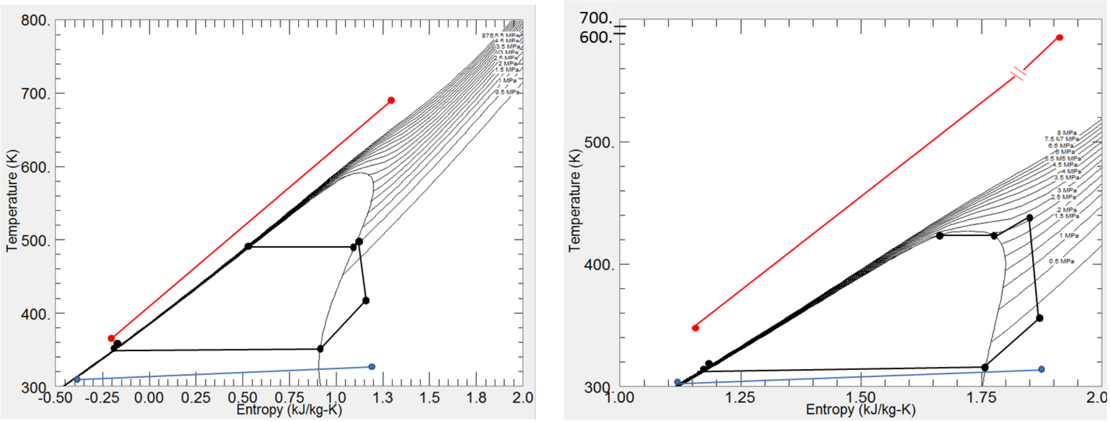

(c) (d)

Fig. 45: Evaporator heat transfer area breakdown and LMDT for nominal sized ORC with piston expander and a) DPHEX, b) PHEX designs (CHP 100%); ORC operating cycle with c) toluene and d) R1233zd .

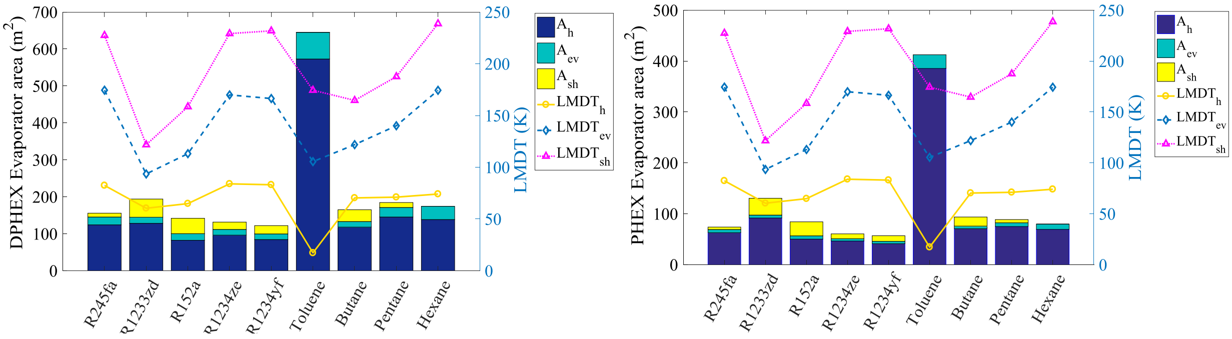

(a) (b)

Fig. 46: Evaporator heat transfer area breakdown and LMDT for nominal sized ORC with screw expander and a) DPHEX, and b) PHEX designs (CHP 100%).

The PHEX heat transfer area requirements are also presented in Fig. 45b for ORC engines with piston expanders and in Fig. 46a with screw devices. It is highlighted that for all fluids investigated, the PHEX areas are up to 50% lower than those with DPHEX, ranging between 50-270 m^2 (with the exception of toluene in the screw expander design).The findings are in line with the data reported in the literature about the compactness of PHEX designs. Additionally, the relative magnitude of area requirements between the various working fluids is similar to that recorded in the DPHEX designs. Results also highlight that overall the optimised ORC engines with screw designs require slightly higher heat transfer area than those with piston expander, indicating that the higher power output of the former ORC engines, comes at the cost of larger (and thus more expensive) system components.

In terms of the HEX area breakdown, this is similar for both the PHEX and DPHEX designs, since the LMDT trends are the same. The preheating section dominates the HEX design (Fig. 45 for DPHEXs and Fig. 46 for PHEXs). This is owing to the evaporator operating pressure which is close to the critical conditions for every fluid. This increases significantly the preheating section heat load, while the evaporator two-phase zone load drops. Also, it is observed that fluids with low evaporation saturation temperature - such as R1233zd, R152a and butane - operate with higher *SHD*, which results in higher superheater area. In contrast, fluids such as pentane and toluene have high saturation temperature at the evaporator pressure, 470 K and 480 K, respectively, so they do not require any superheating. In subsequent sections, the impact of off-design operation on the breakdown of the evaporator HEX areas will be discussed. Finally, it is noted that fluids with similar power outputs (such as pentane and toluene) may have significantly different HEX size requirements. This highlights that apart from the thermodynamic optimisation the system cost aspects should be considered in the design phase. The analysis of the costs of ORC systems is presented in Chapter 6 that follows.

The area breakdown of the condenser HEX is presented in Fig. 47, for ORC engines with piston expanders, and in Fig. 48, with screw devices. It is noted that the condenser area requirements are significantly lower than the respective ones for the evaporator, for both engines and HEX architectures. This is a result of: i) the temperature gradient between the working fluid and the cooling water circuit, which operates at 288-298 K (15-25 °C); ii) the better HTC achieved when there are liquid flows versus gas flows; and iii) the high fraction of the heat rejection being performed in the two-phase zone, which is characterised by higher *U*-values.

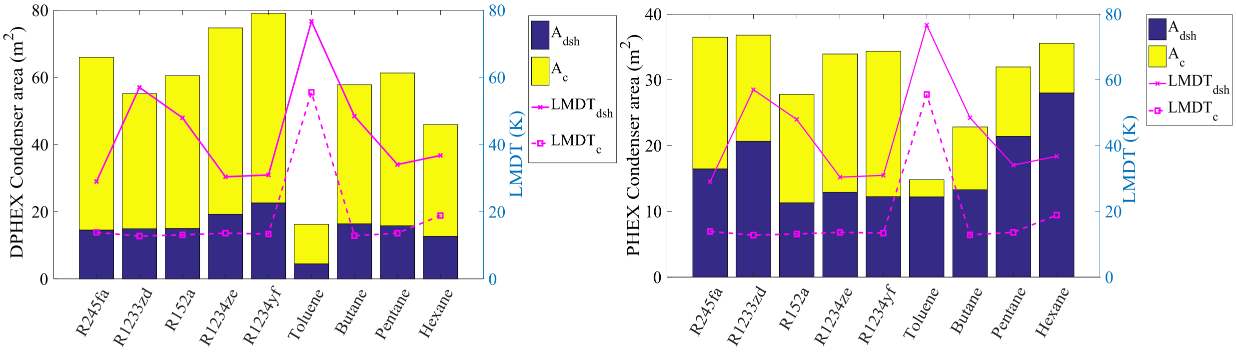

(a) (b)

Fig. 47: Condenser heat transfer area breakdown and LMDT for nominal sized ORC with piston expander and: a) DPHEX, and b) PHEX designs (CHP 100%).

Contrary to the evaporator HEX design, where the available enthalpy of vaporisation in the two-phase zone is low, due to the high operating pressure of the cycle, in the condenser (low pressure) there is high latent heat available during phase change, which results in a large fraction of the heat rejection taking place in the two phase zone with, high HTCs. It can also be seen that toluene has the minimum area requirements among the fluids investigated, for the condenser. This is explained by the condensing saturation temperature of toluene, 345 K, compared to 300-305 K for the other fluids. The higher temperature difference across the HEX for toluene results in lower area requirements for a similar heat rejection load.

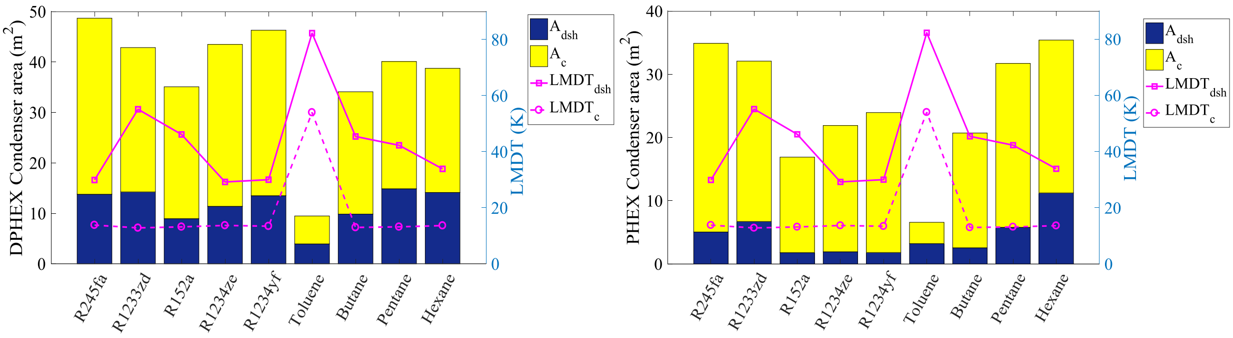

(a) (b)

Fig. 48: Condenser heat transfer area breakdown and LMDT for nominal sized ORC with screw expander and a) DPHEX, and: b) PHEX designs (CHP 100%).

5.4.3 Nominal expander design and sizing

The best-performing fluids identified during the thermodynamic optimisation are almost identical for both ORC engine designs (with piston or screw expanders), namely R1233zd, R245fa, toluene and pentane. For the aforementioned fluids, a piston expander has been designed and sized to meet the nominal operating conditions of each fluid. The expander modelling methodology is based on Refs. [138,151] and has been introduced in Chapter 3. For the nominal sizing exercise, the optimum points identified in the ORC thermodynamic optimisation are used, with an initial assumed expander isentropic efficiency of 0.70. The mass flow rate of working fluid, superheat temperature, and PR, in the expander design exercise are summarised in Table 10.

A number of possible expander designs are generated, using Latin hypercube sampling, and simulated at the initial operating conditions, to identify the most promising candidates. Among these designs, the following design parameters are allowed to vary: the cylinder bore, stroke length, clearance height, valve diameters and opening durations. The candidate design is selected to jointly maximise isentropic efficiency and power density, where power density is defined as the output power per unit cylinder volume. A degree of engineering judgement is required to balance isentropic efficiency and power density, to avoid a high efficiency but very large expander, or the converse. A thermoeconomic analysis assessing the trade-offs between achieving high isentropic efficiency, but at the cost of a larger and more expensive expander would enable an objective approach, when selecting the piston expander design. However, such assessment is beyond the scope of the present work, and would be considered a future addition to the framework presented here.

Table 10: Nominal operating points from initial optimisation.

	R1233zd	R245fa	Pentane	Toluene
Evaporator pressure (bar)	33.93	34.54	32.01	6.56
Condenser pressure (bar)	1.57	1.95	0.90	0.32
Mass flow rate (kg/s)	1.88	2.68	1.26	1.38
Superheat temperature (K)	15	15	5	5

Table 11: Expander design parameters. Intake and exhaust valves open at TDC and BDC respectively.

	R1233zd	R245fa	Pentane	Toluene
Number of cylinders	2	4	4	6
Bore (mm)	254	124	201	206
Stroke length (mm)	359	187	279	411
Clearance height (mm)	29	17	20	44
End of intake (degrees after TDC)	22.5	41.9	21.2	46.3
End of exhaust (degrees after TDC)	256.1	325.6	249.2	304.8

Once the expander design is fixed, the expander simulation is run for a range of PRs, superheating degrees, mass flow rates and rotating speeds (RPM). This produces operating-performance maps for a set of possible PL conditions. In Fig. 49 the expander maps for R1233zd, R245fa, toluene and pentane are presented, for a fixed rotational speed. These maps are then input to the ORC off-design optimisation framework, to predict the expander performance under varying operating conditions.

With reference to the piston expander maps in Fig. 49, the peak isentropic efficiencies are achieved at low mass flow rates, also corresponding to low PRs. This is attributed to the intake-valve losses, which are a significant contributor to the overall expander losses for reciprocating-piston machines, and these losses are less severe for low PRs. On the other hand, achieving high power output, calls for high PRs and mass flow rates, with a corresponding reduction in efficiency. These trade-offs are going to be captured during the off-design optimisation, when the new optimum ORC operating points that maximise the power output of the engine should be identified. It is noted that the isentropic efficiency figures presented in Fig. 49, exclude the mechanical losses on the shaft or the electrical losses of the generator. As discussed in Section 3.6.1, considering the mechanical losses ($\eta_{\mathrm{mech}} = 85\%$), the piston expander effective efficiency varies between 0.45-0.77, figures which are well-aligned with those reported in other studies in the literature, such as those reported in Refs. [71,175].

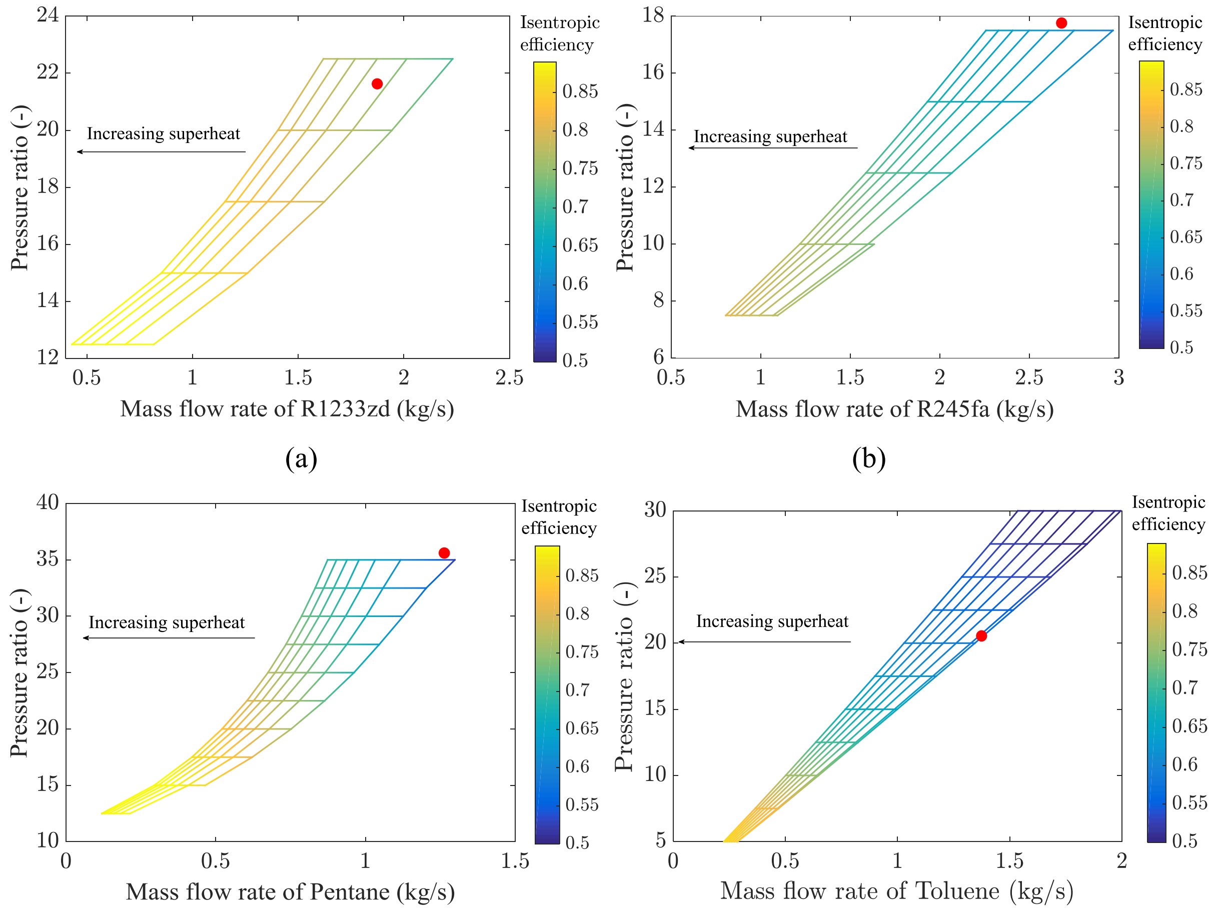

(a) (b)

(c) (d)

Fig. 49: Piston expander performance map for: a) R1233zd, b) R245fa, c) pentane, and d) toluene. Lighter colours represent higher isentropic efficiency. Oblique lines join points at constant superheat temperature, with maximum superheat at the left of each plot. Maps are shown for 500 RPM for toluene and 1500 RPM for the other fluids, based on full-cycle optimisation. The circle indicates the nominal design point, with a fixed isentropic efficiency of 0.70.

To predict the off-design performance of the screw expander, and compare it to the performance of piston devices, the screw expander efficiency correlation developed in Ref. [65] has been used, as presented in Chapter 3. This is a low fidelity efficiency correlation, which, however, is based on real screw machines performance, and is one of the very few references that provide correction factors for off-design operation. In Fig. 50, the screw expander efficiency at the nominal design point is illustrated, for ORC engines optimised for maximum power output, at 100% CHP-ICE PL. All optimum cycles have a two-stage expansion, aiming to keep the VR of the expanders between 4 and 6. It is noted that the fluids with the highest power output do not have the highest screw expander efficiency ($\eta_{\mathrm{exp,is}}$). Although more power is generated from fluids such as R1233zd or toluene ($\eta_{\mathrm{exp,is}}$ = 0.71-0.79), the expander efficiency is best for fluids such as R1234yf and R1234ze ($\eta_{\mathrm{exp,is}}$ = 0.8-0.83). These findings highlight that cycles with the former fluids can tolerate lower specification on the expander design, while still generating more power at the design point.

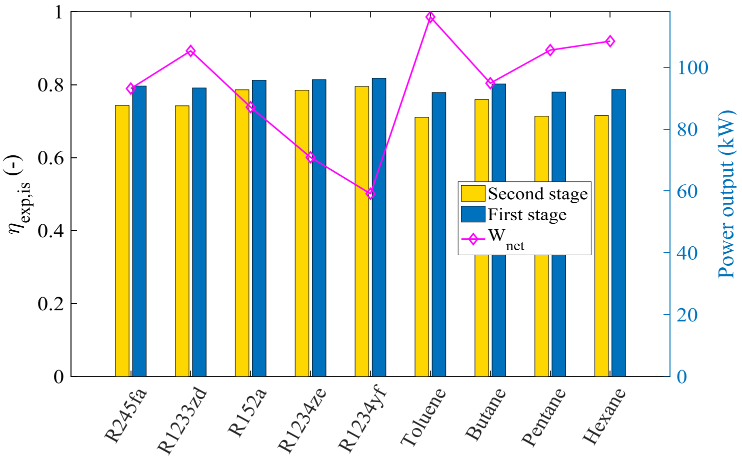

Fig. 50: Screw expander nominal (design) operation performance.

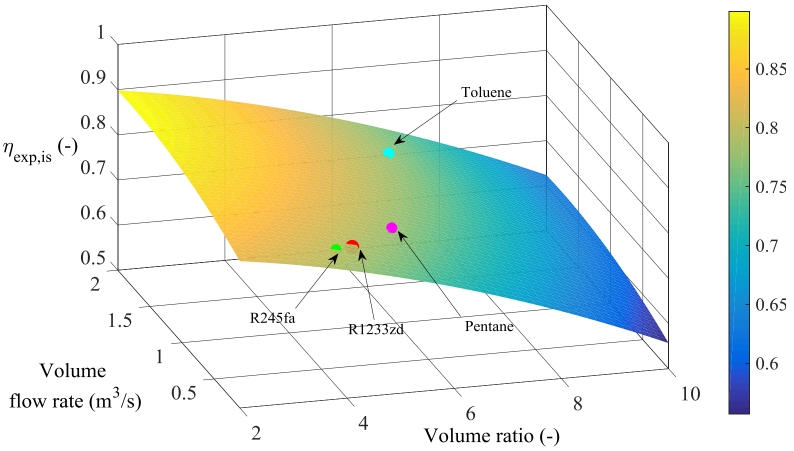

Fig. 51: Screw expander isentropic efficiency map, and optimum operating points for nominal ORC sizing, for the best performing fluids: R245fa, R1233zd, pentane, and toluene. Highlighted points correspond to the operating conditions of the second stage expander.

In Fig. 51, the screw expander performance map is presented along with the optimum operating points, for the best performing fluids. It is noted that for high VRs the screw expander efficiency deteriorates significantly, therefore the optimum operating points lie on the small to medium VR range. Furthermore, the screw expander efficiency is more sensitive to changes in VR than volume flow rates. For fixed volume flow rate, while the VR increases from 2 to 10, the isentropic efficiency reduces by 35%, whilst for fixed VR increasing the volume flow rate increases only slightly the isentropic efficiency. This finding is aligned with other studies in the literature which report that for a given size screw expander (i.e. given design VR and volume flow rate), the efficiency is mostly affected by variations in the VR of the device [79]. Comparing the isentropic efficiencies of screw expanders to those presented in the piston expander maps, these are slightly higher than those obtained for piston although the former operate at lower PRs than the latter. However, the screw devices performance has been estimated using a generalised correlation, while the piston efficiency has been calculated specifically for the fluids investigated and using a validated lump thermodynamic model. Finally, the performance maps generated in this section will be used in subsequent sections to optimise the ORC off-design power output for varying heat-source conditions.

5.5 System optimisation and sizing results – II: Off-design operation with piston expander

5.5.1 Combined ICE-ORC CHP system optimisation

After the nominal ORC system optimisation and sizing, the major component geometries, and performance maps are fixed, and are used as an input to the ORC off-design optimisation tool. The exhaust-gas flow rate and temperature are varied according to the values in Table 8, for the CHP-ICE PL from 100% down to 60%. For every new PL point, the operation of the ORC system is optimised to adjust to the new conditions. First, a reference case is obtained with the piston expander isentropic efficiency fixed at 0.70 (nominal design) for all PR conditions. In this case the PR of the ORC is kept fixed, while the working fluid mass flow rate and superheating are allowed to vary, along with the mass flow rate of heat-source fluid and its temperature, at the exit of the evaporator. Then, for the best performing fluids discussed in Section 5.4, the full piston expander variable performance maps are incorporated into the off-design optimisation and the results are compared to the reference case with fixed isentropic efficiency. The optimiser in the second case is allowed to adjust not only the mass flow rate/temperature of the working fluid, but also the evaporation pressure. The new expander isentropic efficiency is then estimated using performance maps, while the expander rotational speed is fixed at 1500 RPM, to ensure smooth coupling with the electric generator. The mass flow rate and temperature of the heat-source fluid leaving the evaporator are also allowed to vary.

5.5.1.1 Fixed expander performance

The optimum ORC power output is presented in Fig. 52 for all CHP-ICE PL points, with the expander isentropic efficiency being fixed to the nominal design (0.7). In line with the results, the best performing fluids during nominal operation, are those that also outperform during the off-design operation, for both HEX architectures. For all optimum cycles, the optimiser utilises the full heat-source mass flow rate available, while it also aims to maximise the working fluid temperature when leaving the evaporator (high *SHD*) to the minimum value between: i) the peak temperature the fluid can operate without the risk of chemical degradation; and ii) the maximum allowable by the *PP* constraints. It is noted that the ORC power output follows the CHP-ICE PL trend, but the ORC PL level is always higher than the respective one of the CHP-ICE. A case in the point is R1233zd, where for 90% CHP-ICE PL, the ORC engine operates with 97% PL, for 80% CHP-ICE PL, the ORC operates with 87% PL, and at 75% CHP-ICE PL the ORC engine operates at 82%. This is attributed mainly to the evaporator HEX performance; the exhaust-gas temperature at PL is higher than the nominal conditions, so the temperature gradient across the HEX increases making the heat transfer more effective over the same heat transfer area. Additionally, the power output achieved with PHEX architectures during off-design operation is slightly higher than that achieved when DPHEX architecture is used. This is attributed to the higher PHEX effectiveness. The details of the DHEX and PHEX performance are discussed in Section 5.5.2.

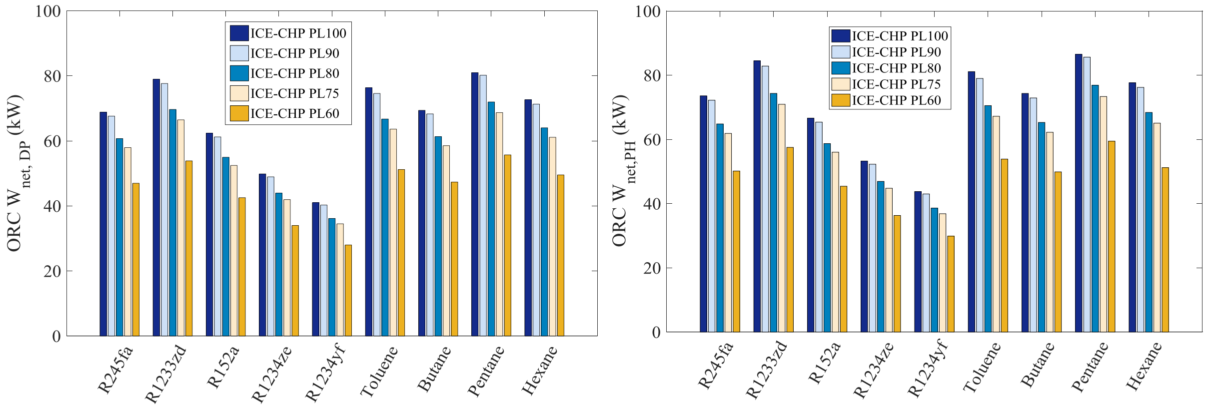

(a) (b)

Fig. 52: ORC optimum power output at off-design operation with piston expander, for CHP-ICE part-load 100%-60% (left to right), assuming fixed expander efficiency and: a) DPHEXs and b) PHEXs.

5.5.1.2 Variable expander performance

For the findings summarised in Fig. 52, the expander isentropic efficiency has been kept fixed among all the fluids and conditions investigated. In this section, the variable performance maps of the piston expander are incorporated in the off-design tool. The revised ORC power output is illustrated in Fig. 53. First, it is highlighted than when the piston expander is sized for nominal conditions, for fluids such as R245fa and toluene, the isentropic efficiency achieved is slightly lower than the initial assumption of 0.70, corresponding to 0.60-0.66 (Fig. 55). This affects the ORC engine power output at nominal conditions, which is slightly lower than the optimum power output achieved by the same fluids in the thermodynamic optimisation (Section 5.5.1.1). This reveals that because the thermodynamic optimisation does not account for the component-specific physical and performance limitations, it may lead to designs which are technically challenging.

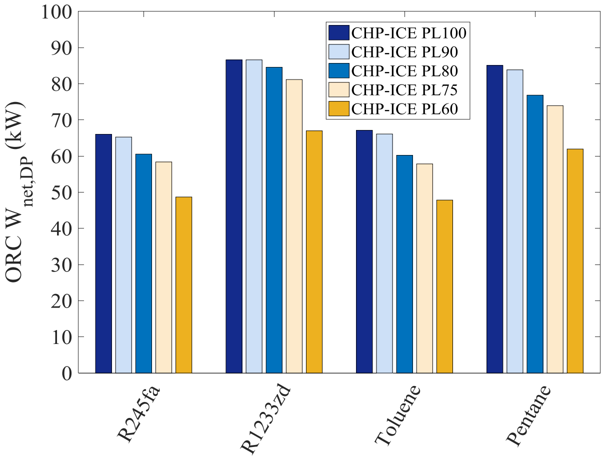

(a)

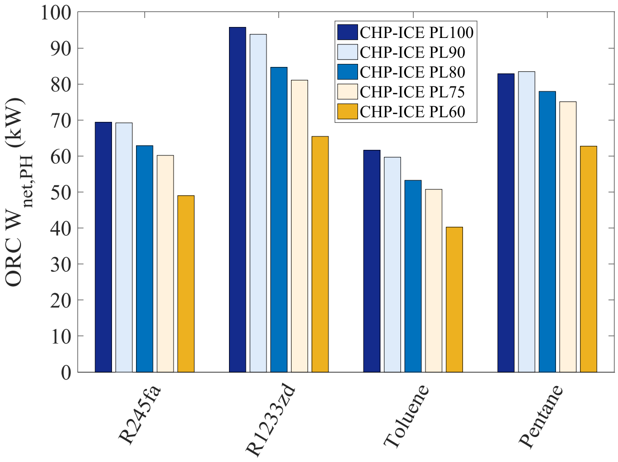

(b)

Fig. 53: ORC optimum power output at off-design operation with piston expander, for CHP-ICE part-load 100%-60% (left to right), with variable expander performance and: a) DPHEX, and b) DPHEX.

By comparing the power output of the ORC engines in the case of fixed expander efficiency and in the case of varied performance, the former approach underestimates the power output by up to 17% for CHP-ICE PL 60%. It is also noted that ORC engines with R1233zd and R245fa and PHEXs generate 4-10% more power than those achieved with DPHEX designs, with the same fluids. The opposite trend is observed with toluene, for which the power output of the engine with DPHEX is higher than in the case with PHEXs by approximately 6%. ORC engines with pentane have very similar performance with both HEX architectures. These findings are closely associated with the new operating points and mass flow rates in the system, along with the piston expander efficiency achieved in each design, as discussed in subsequent sections.

Furthermore, while the CHP-ICE load decreases, the ORC power output also reduces, but with lower rate than in the case of the assumed fixed expander isentropic efficiency. For R1233zd with DPHEXs, at 90% CHP-ICE PL, the ORC engine operates almost at 100% load, for 80% CHP-ICE PL, the ORC operates with 97% PL, and at 60% CHP-ICE PL, the ORC engine still operates at 77%. These findings are explained by looking at the optimum PR of the ORC engines at off-design operation (Fig. 54) and at the respective isentropic efficiency of the piston expander (Fig. 55). While the ORC engine operates at off-design conditions the new optimised piston expander isentropic efficiency improves for all fluids, and both HEX architectures, by 6-16%, exceeding 0.82 for fluids, such as R1233zd. The expander isentropic efficiency improvement at off-design conditions results in higher ORC engine power output, than in the case when the expander isentropic efficiency was assumed fixed.

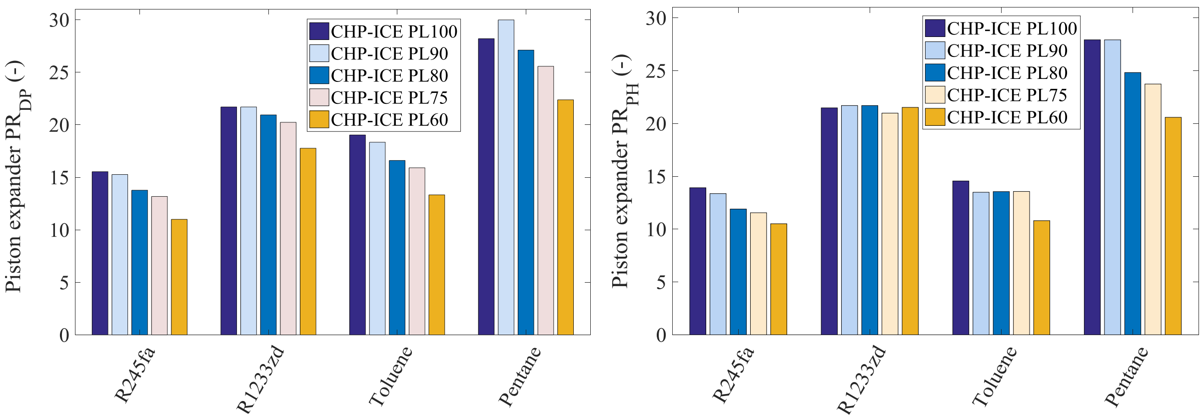

(a) (b)

Fig. 54: ORC optimum pressure ratio (PR) at off-design operation, for CHP-ICE part-load 100%-60% (left to right) with variable expander performance, and: a) DPHEX and b) PHEX.

This initially counterintuitive trend can be understood by looking at the new PR of the ORC for all fluids (Fig. 54). While the CHP-ICE load reduces, the optimum PR over the expander also decreases, i.e. even though the temperature of the exhaust-gas increases at PL, the optimum ORC evaporating pressure decreases. This trend is in contrast with the thermodynamic analysis, where the optimum evaporator pressure level was always the one resulting in the highest PR over the expander. In real piston expander machines, operating points with lower PR and lower working fluid mass flow rate can reach higher isentropic efficiency. This is why the optimiser chooses to reduce the evaporating pressure, and increases the *SHD*, instead of maximising the evaporating pressure. Finally, comparing the isentropic efficiencies achieved with PHEX and DPHEX designs (Fig. 55), it is noted that piston expanders in ORC engines with R245fa and DPHEXs have lower isentropic efficiency than in the case of engines with PHEXs, while in the case of R1233zd the expander efficiency is higher in the case of the PHEX design for PL100% to 75%, but the opposite trend is observed at low PL 60%. Toluene performs better with DPHEXs than in the case of PHEXs designs, while pentane has very similar performance with PHEXs or DPHEXs designs. These findings highlight than depending on the working fluid selection, the most efficient system architecture may vary.

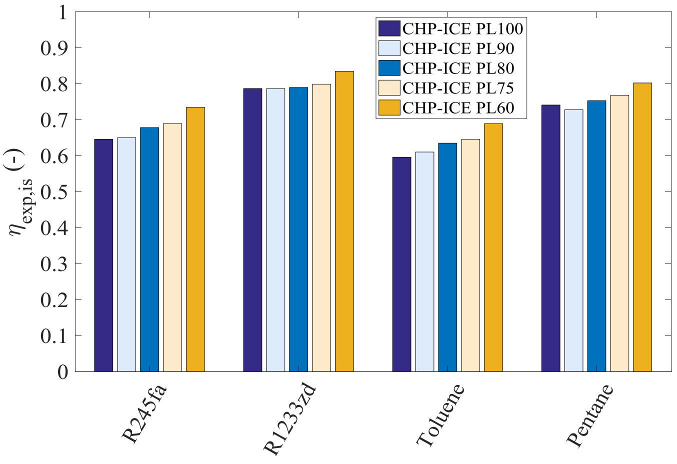

(a)

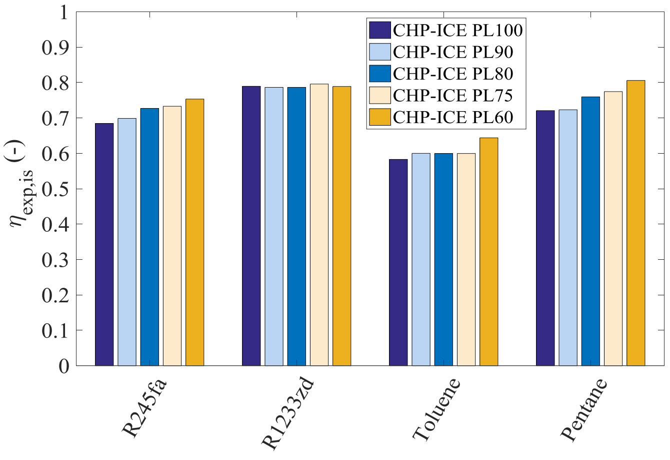

(b)

Fig. 55: ORC piston expander optimum isentropic efficiency at off-design operation, for CHP-ICE part-load 100%-60% (left to right), with: a) DPHEX and b) PHEX.

Further to the expander performance analysis, the results of the moving boundaries HEX modelling are illustrated in Fig. 56 for off-design operation with DPHEX, and in Fig. 57 for PHEX designs. As the CHP-ICE PL reduces, the heat-source temperature increases, which allows the optimiser to increase the *SHD* of the working fluid exiting the evaporator HEX, either to the maximum degree allowable by the HEX pinch point or to its respective maximum that prevents degradation. This trend is recorded for all fluids investigated. Owing to the higher-grade heat input to the cycle, most working fluids will have already reached the new saturation evaporating temperature, before they reach the end of the preheating section, as this was defined in the nominal HEX sizing. At the end of the preheating section the fluids are already in the two-phase zone, while they will enter the superheated stage before the end of the evaporating zone (as this was defined in the design stage).

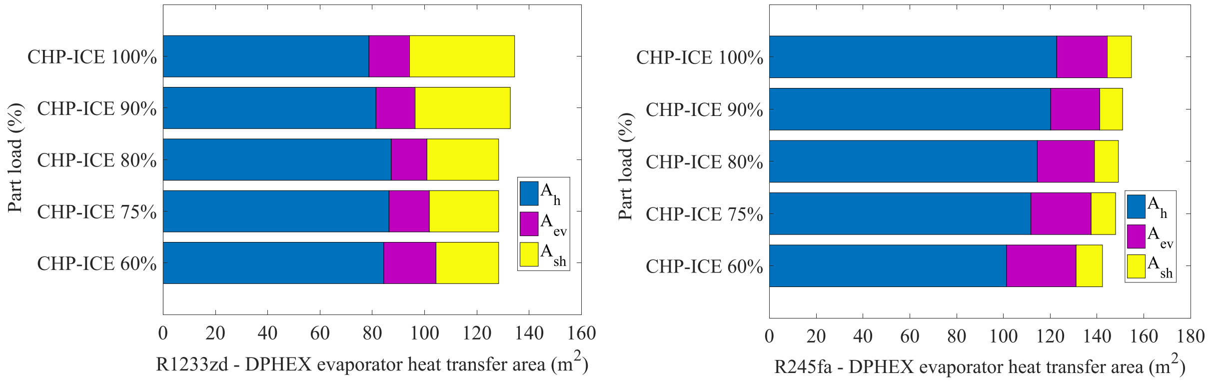

(a) (b)

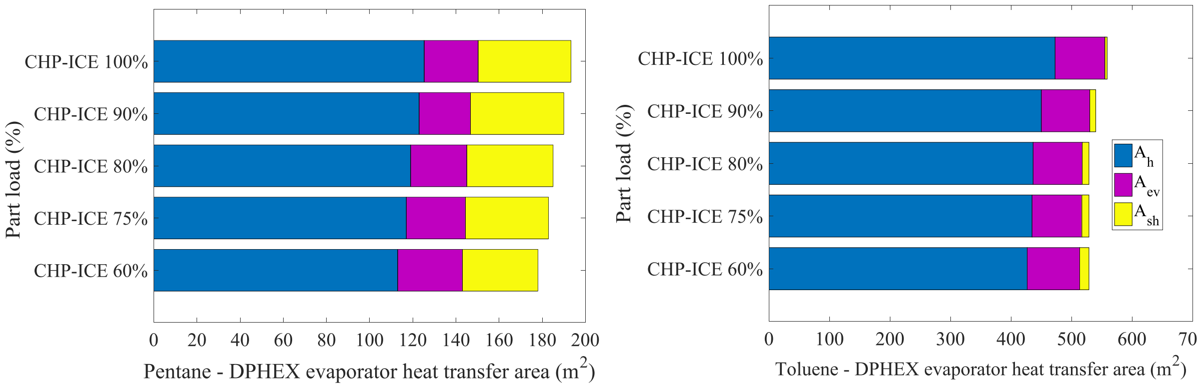

(c) (d)

Fig. 56: DPHEX evaporator heat transfer area boundaries (moving boundaries) at off-design operation for: a) R1233zd, b) R245fa, c) pentane, and d) toluene, for CHP-ICE part-load 100%-60% with variable expander performance.

As aforementioned, the off-design evaporator pressure is lower than the nominal one, leading to a larger fraction of the heat recovery be taking place in the two-phase zone. This is illustrated in the area requirements of the two-phase section for every fluid in Fig. 55 (for DPHEX) and Fig. 56 (for PHEX), where, while moving from CHP-ICE 100% to 60% PL, the two-phase zone area increases. It is noted that heat transfer in the two-phase zone is associated with higher HTCs (as will be discussed in subsequent sections), which increases the HEX effectiveness when recovering heat. Finally, it is observed that in the case of R1233zd with DPHEX design, when the complete optimisation is performed, including the HEXs and the expander time-varying performance models, at CHP-ICE 100% PL operation, the heater section area requirements are lower than that in lower loads. In this particular case, the operating points that maximise simultaneously the HEX effectiveness and expander efficiency, correspond to high LMDT over the heater section, reducing the heat transfer area requirements.

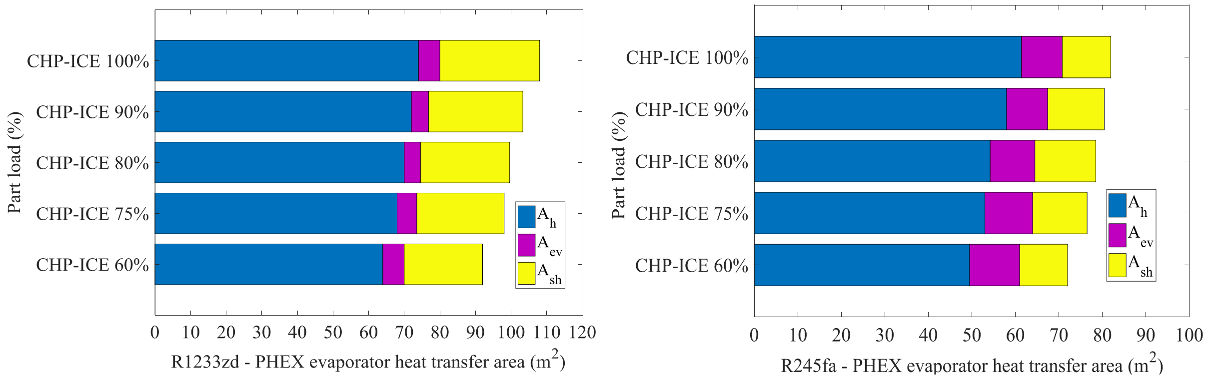

(a) (b)

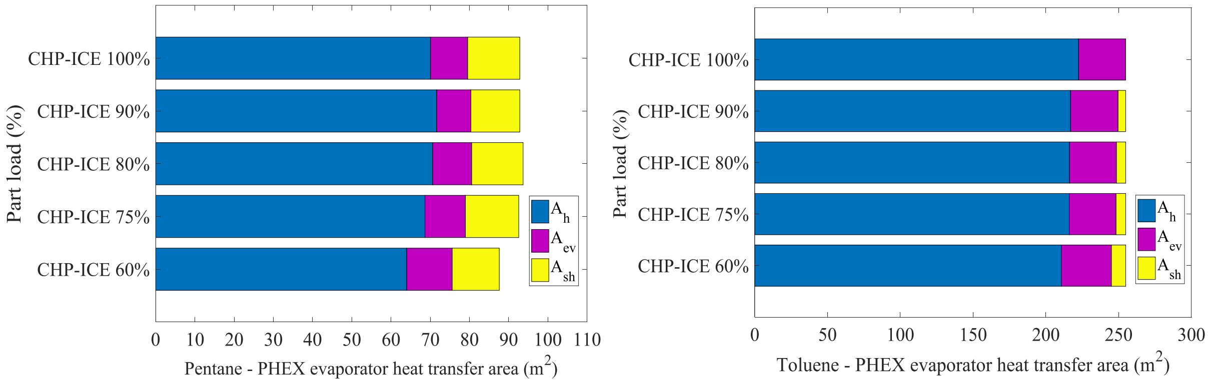

(c) (d)

Fig. 57: PHEX evaporator heat transfer area boundaries (moving boundaries) at off-design operation for: a) R1233zd, b) R245fa, c) pentane, and d) toluene, for CHP-ICE part-load 100%-60% with variable expander performance.

5.5.2 ORC off-design performance maps

5.5.2.1 Evaporator performance maps

In the previous section, the ORC engine operation at specific CHP-ICE PL points has been investigated. Here, performance maps of the evaporator HEX are generated, using the full spectrum of possible exhaust-gas temperature and flow rates leaving the CHP-ICE. In Fig. 58, the overall heat transfer coefficient (*U*) maps of the evaporator HEX are presented for R1233zd, for both HEX architectures and design approaches presented in Section 5.5.1. The results are representative of the trends observed for the other working fluids. While the CHP-ICE PL reduces, the *U*-value also decreases for both the DPHEX and PHEX designs, and for fixed or variable expander efficiency. For fixed heat-source temperature, the *U*-value reduces by up to 30%, while the mass flow rate of heat carrier fluid decreases from 2.16 kg/s (CHP-ICE nominal conditions), down to 1.29 kg/s (CHP-ICE 60% PL). The same trend is observed for all HEX sections, and in both design approaches. This is mainly attributed to the changes of the Reynolds number, which is affected by the decrease in the flow rates of both the heat source and the working fluid. The Reynolds number on the working fluid side ranges between 10^5 to 10^6, whilst on the exhaust gas side is within the 10^5. In contrast, for constant mass flow rate of the heat source, while the temperature increases, the *U*-value increases only moderately, since it is only affected by the potential transition from convective boiling to nucleate boiling conditions. More precisely, the HTC for nucleate boiling is between 70-75% of the total HTC on the working fluid side.

Looking at the relative magnitude of the *U*-values at the different HEX sections, the evaporator section has the highest heat transfer rate due to phase change. In the two-phase section, the nucleate-boiling phenomena prevail at higher wall surface temperatures, so the *U*-value is always higher than the respective one in the preheating zone, while it is comparable to the one in the superheating section. Comparing the *U*-values of the DPHEX to those of PHEX, it is highlighted that the latter are up to three times higher than the former. These findings are in line with the HEX sizing results presented in Section 5.4, where the DPHEX area requirements are almost double than those of the PHEX designs. Finally, it is observed that when the PR over the expander was fixed (Fig. 58a,c), the *U*-value is underestimated relative to that with dynamic expander modelling (Fig. 58b,d). This is mainly a consequence of the change in the operating pressure of the evaporator, which reduces at off-design operation. This results in a larger fraction of the heat transfer taking place in the two-phase zone, where the HTCs are higher, increasing the overall *U*-value of the HEX.

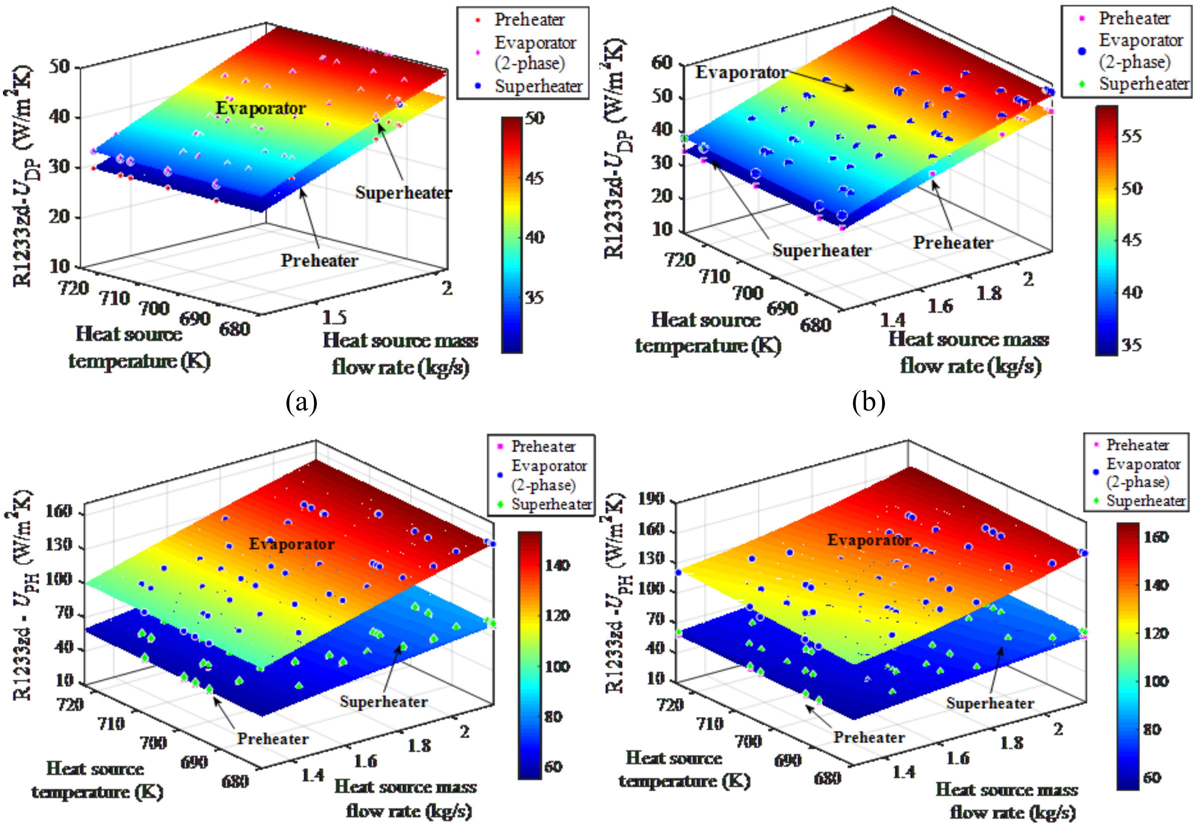

(a)

(b)

(c)

(d)

Fig. 58: Evaporator heat transfer coefficient performance map for DPHEX with: a) fixed expander efficiency, and b) variable expander efficiency; and for PHEX with: c) fixed expander efficiency, and d) variable expander efficiency, for R1233zd at off-design operation.

The HEX *U*-value variation for all fluids, at off-design operation, with the expander dynamic performance incorporated, is illustrated in Fig. 59 (DPHEX) and Fig. 60 (PHEX). The *U*-value performance is similar among all fluids investigated, and in both HEX architectures. What is changing is the absolute values of *U* achieved. It is noted that R1233zd, and pentane have higher *U*-values than R245fa and toluene, in both HEX designs. This is explained by the different mass flow rate and temperature regimes within each cycle. In DPHEX designs, pentane (Fig. 59c) operates with the highest *U*-values across all sections, varying between 42-60 W/m^2 K, in the evaporator and the superheating sections, and 38-53 W/m^2 K in the preheating zone. The *U*-values for toluene (Fig. 59d) are similar to those for R245fa (Fig. 59b). The superheater and the evaporator in the DPHEX consistently have the highest *U*-value for all PL conditions, ranging between 36-53 W/m^2 K, followed by the preheating section with 32-48 W/m^2 K. It is noted that the *U*-values obtained in this work are in agreement with data reported in the literature that DPHEX designs with gas on one side achieve U-values between 10-60 W/m^{2}K [44] .

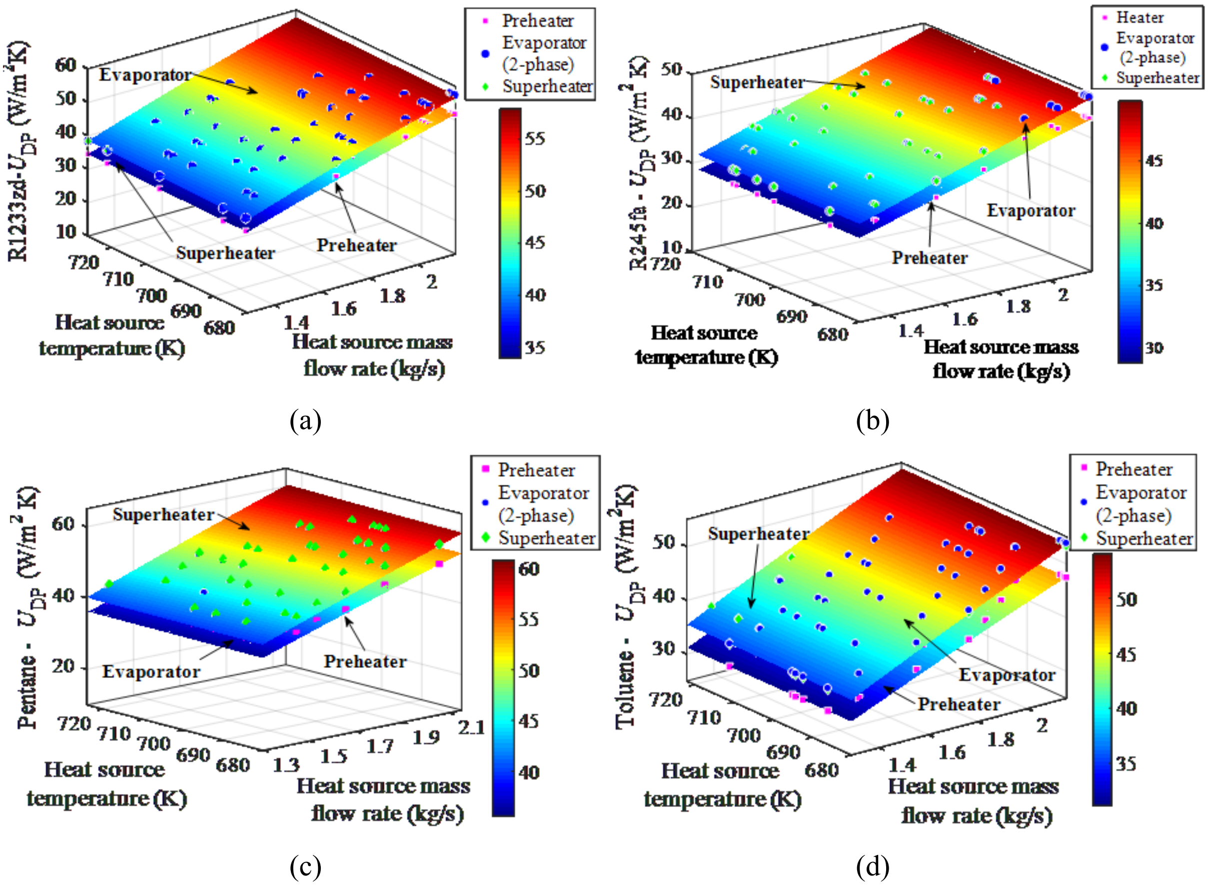

(a) (b)

(c) (d)

Fig. 59: DPHEX evaporator overall heat transfer coefficient map at off-design operation, with variable piston expander efficiency for: a) R1233zd, b) R245fa, c) pentane, and d) toluene.

In PHEX designs (Fig. 60), R1233zd has the highest U-values, varying between 120-160 W/m^2 K in the evaporating zone, and between 60-85 W/m^2 K in the preheater and superheater section. The other fluids operate with U-values of 110-140 W/m^2 K in the evaporating zone, and 55-80 W/m^2 K in the preheater/superheater sections. The low U-values recorded are attributed the high thermal resistance on the exhaust-gas side. More precisely, the HTC achieved on the gas side (for DPHEXs) ranges between 0.05-0.1 kW/m^{2}K, whilst on the working fluid side the HTC varies between 1-1.6 kW/m^2 K in the single-phase zones, and between 15-21 kW/m^{2}K in the two-phase evaporating zone. It is noted that the U-values of the DPHEX in the two-phase zone are not significantly higher than those achieved in the superheater/preheater sections. In contrast, in the PHEX design the U-values in the two-phase zone are significantly higher than those in the other sections. In the DPHEX case, because the tube sizes are the same for the full length of the HEX, we need to ensure that the working fluid velocity is low enough when it is in the liquid/two-phase states, so we do not create high pressure drops, when the working fluid is in superheated state (i.e. low densities, resulting in high velocities for the same mass flow rate and cross section area). Also, the exhaust-gas side pressure drop should stay within the maximum pressure drop range, to avoid significant backpressure effects on the CHP-ICE. Therefore, the exhaust-gas stream velocity cannot increase significantly neither, to enhance heat transfer. Alternatively, tube bundles can be used, where the flow splits into multiple tubes, resulting a better control of the flow rates, and pressure drop. to This challenge is not as profound in the PHEX design because the flow can split into a number of different plates/passages. So, the flow rates of both streams are better controlled, while also the number of passages may vary between the preheater/evaporator section, and the superheater section, to ensure the best flow breakdown and heat transfer rate. This is the reason why higher HTCs are obtained in the PHEX design, for all HEX sections. Finally, as with DPHEX designs, the *U*-value drops with the reduction of the heat-source mass flow rate, although the heat-source temperature increases, but in the PHEX design the *U*-value reduction at off-design operation does not exceed 25%.

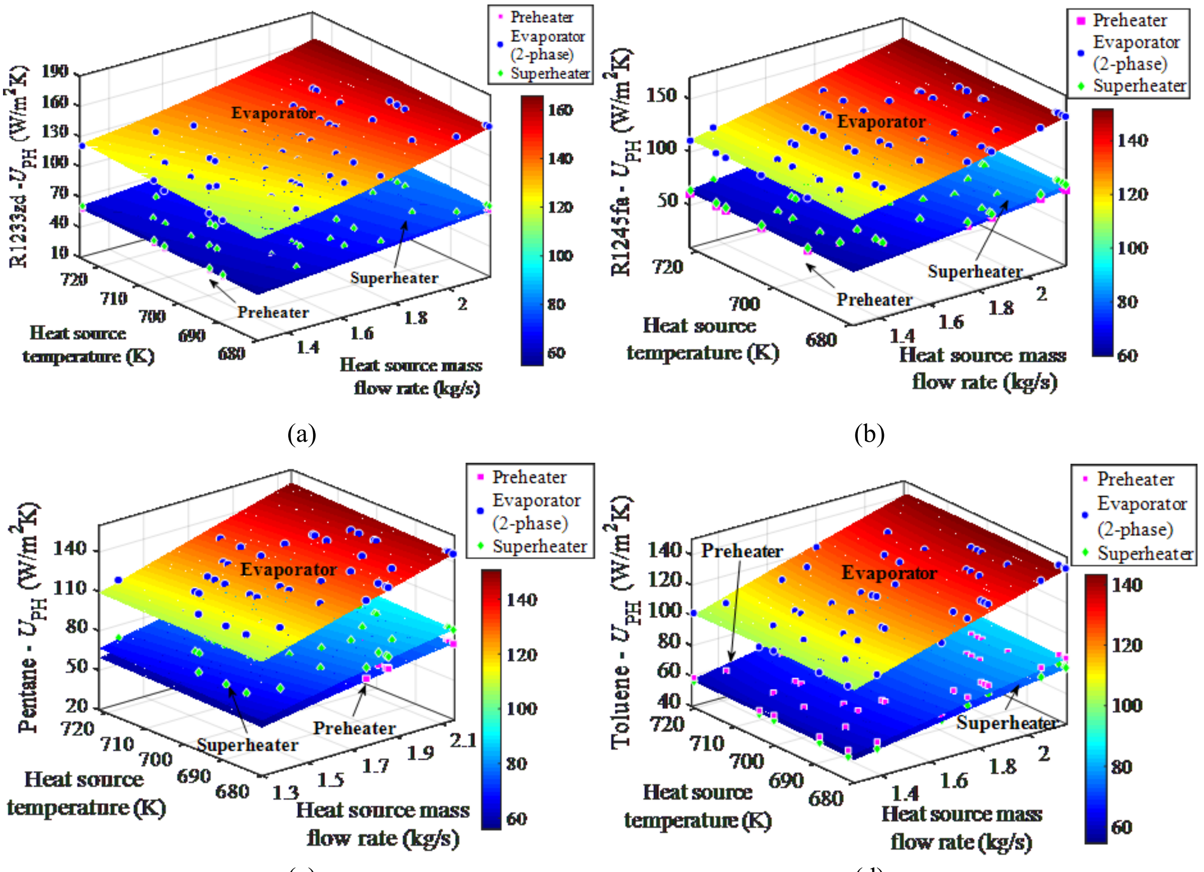

(a) (b)

(c) (d)

Fig. 60: PHEX evaporator overall heat transfer coefficient map at off-design operation, with variable piston expander efficiency for: a) R1233zd, b) R245fa, c) pentane, and d) toluene.

The comparison of HEX effectiveness (ε) for R1233zd, between the two design approaches, is presented in Fig. 61, while the results of the dynamic expander performance are presented in Fig. 62, for DPHEXs, and in Fig. 63, for PHEXs. Effectiveness (ε) is defined as the ratio of the actual heat transfer achieved in the HEX over the maximum one, if there was an infinitely long HEX, where the outlet temperature of the cold fluid, was equal to the inlet temperature of the hot fluid. Although the *U*-value drops with PL and one may expect the effectiveness of the HEX to drop accordingly, the findings reveal that ε increases with PL. The higher effectiveness is attributed to the increase of the LMDT in the HEX subsections, and especially in the superheater and two-phase zone (Fig. 64 for DPHEXs and Fig. 65 for PHEXs). The higher heat-source temperature entering the evaporator at CHP-ICE PL increases the temperature difference between the two working fluids, increasing the heat transfer taking place over the same heat transfer area.

When comparing the effectiveness results of the two approaches, in Fig. 61a,c (fixed expander isentropic efficiency) while the ICE PL reduces, the effectiveness in the superheater increases by 10%, in the preheater by 5%, whilst the effectiveness of the evaporator two-phase zone stays almost constant. In Fig. 61b,d (variable expander isentropic efficiency), the preheater effectiveness behaves similarly to that in Fig. 61a,c, but the increase of the evaporator effectiveness, while the ICE PL reduces, is higher, almost increasing by up to 50% (for DPHEX). This is explained by the lower evaporator pressure in the system at off-design operation, which results in lower evaporator temperature and larger fraction of heat transfer occurring in the two-phase zone with better HTCs, and with higher temperature gradient across the HEX. The superheater effectiveness is either similar or lower in Fig. 61b,d, owing to the lower superheat and temperature of the working fluid, dictated by the piston expander optimum operating point.

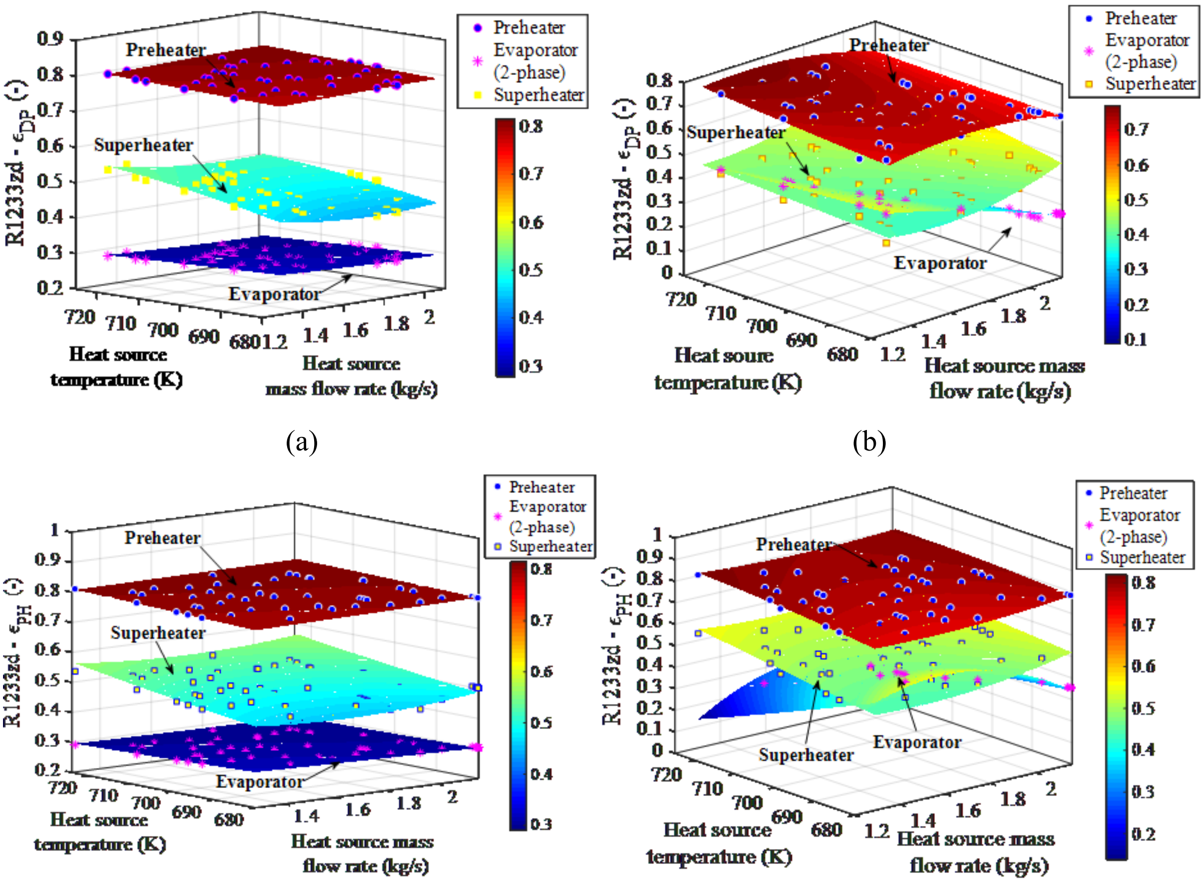

(a)

(b)

(c)

(d)

Fig. 61: Evaporator effectiveness map for DPHEX with: a) fixed expander efficiency, and b) variable expander efficiency; and for PHEX with: c) fixed expander efficiency, and d) variable expander efficiency, for R1233zd at off-design operation.

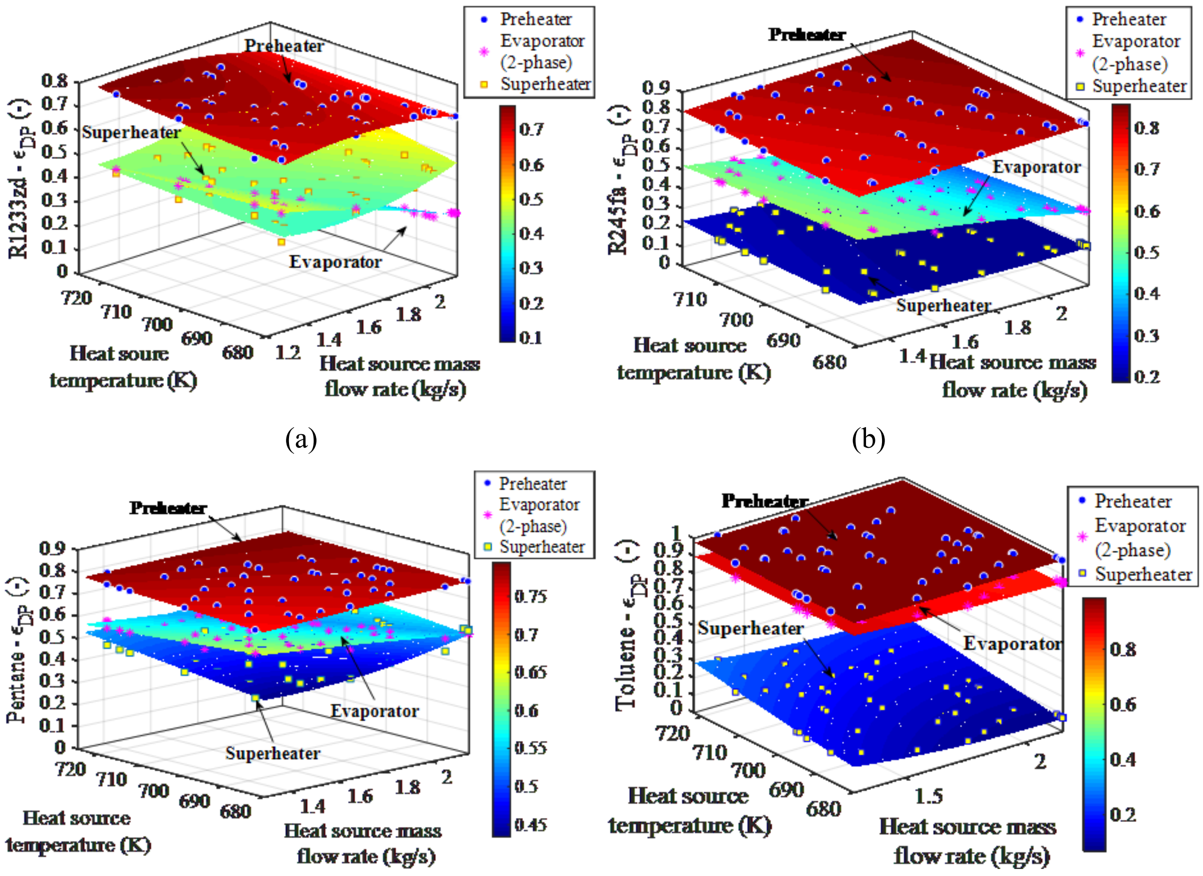

(a) (b)

(c) (d)

Fig. 62: DPHEX evaporator effectiveness map at off-design operation with variable piston expander efficiency for: a) R1233zd, b) R245fa, c) pentane, and d) toluene.

For both HEX architectures, the preheating zone has the highest effectiveness, because the minimum pinch point is observed in this area (Fig. 62 for DPHEXs and Fig. 63 for PHEXs). Toluene in particular presents the highest effectiveness, which is aligned with the high evaporator area requirements obtained at nominal design (Section 5.4) and the very low evaporator pinch point of the optimum ORC cycle. Nevertheless, the high HEX effectiveness comes at the cost of a larger and more expensive HEX. The cost aspects of the ORC systems, should also be considered in the design process and are further investigated in Chapter 6.

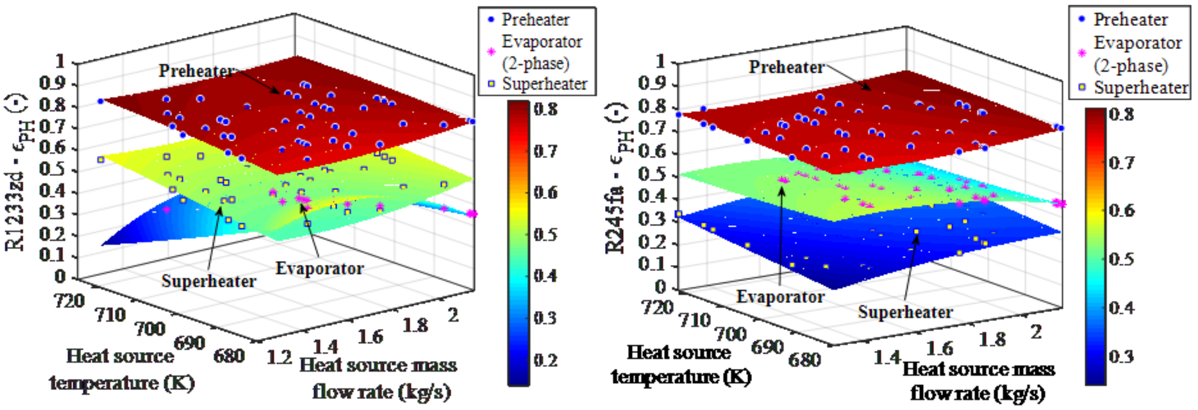

(a) (b)

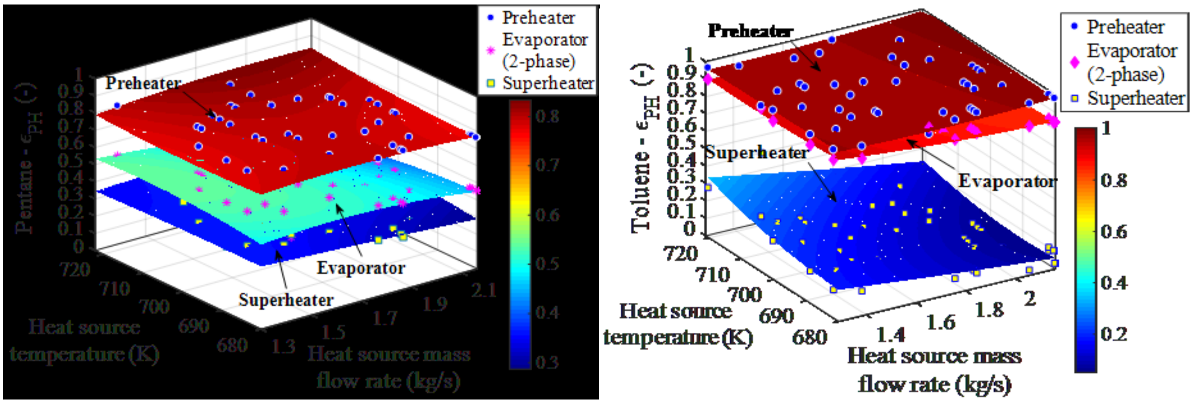

(c)

(d)

Fig. 63: PHEX evaporator effectiveness map at off-design operation with variable piston expander efficiency for: a) R1233zd, b) R245fa, c) pentane, and d) toluene.

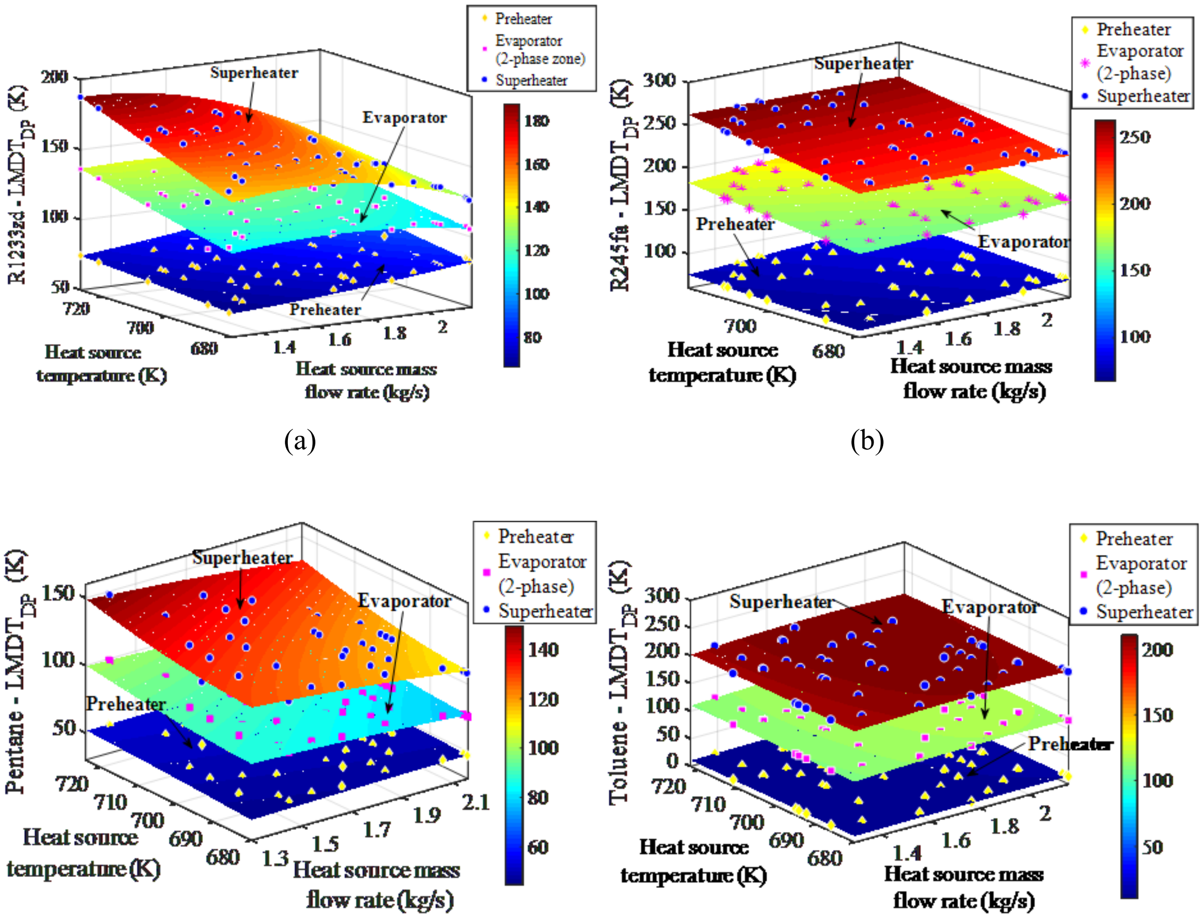

(a)

(b)

(c)

(d)

Fig. 64: DPHEX evaporator temperature gradient map at off-design operation with piston expander for: a) R1233zd, b) R245fa, c) pentane, and d) toluene.

The lowest effectiveness is recorded in the superheater zone. This is attributed to the high temperature difference between the working fluid and the heat source as illustrated in Fig. 64 for DPHEXs and in Fig. 65 for PHEXs. While the CHP-ICE PL reduces, the heat-source thermal content is available at higher temperature, but this cannot be fully utilised by the ORC engines, because the working fluid temperature cannot increase any further. The limiting factors may be: i) the maximum allowable working fluid temperature before decomposition phenomena occur; or ii) the expander performance that may dictate lower pressure levels and superheating degree for maximising the power output. A case in the point is fluids such as R245fa (Fig. 62b, and Fig. 63b) which operates with an effectiveness of 0.19-0.22 (DPHEX) or 0.2-0.28 (PHEX) in the superheater section, because the system cannot increase the temperature any further than 440 K, which is the maximum limit for R245fa to avoid chemical instability issues. In contrast, pentane (Fig. 62c and Fig. 63c) operates with superheater effectiveness of 0.45-0.55 (DPHEX) and 0.35-0.45 (PHEX), because its maximum allowable temperature is 600 K. In the case of toluene, although its maximum temperature is 700 K, the optimiser chooses a low evaporator pressure level (and temperature) to maximise the expander efficiency. Therefore, toluene's superheater effectiveness (Fig. 18d) is also low in the region of 0.15-0.25. Finally, the evaporator effectiveness is higher than that of the superheater. A better matching is achieved between the evaporating temperature and the heat-source temperature in the two-phase zone, increasing the HEX effectiveness, while higher *U*-values are also observed in the two-phase zone.

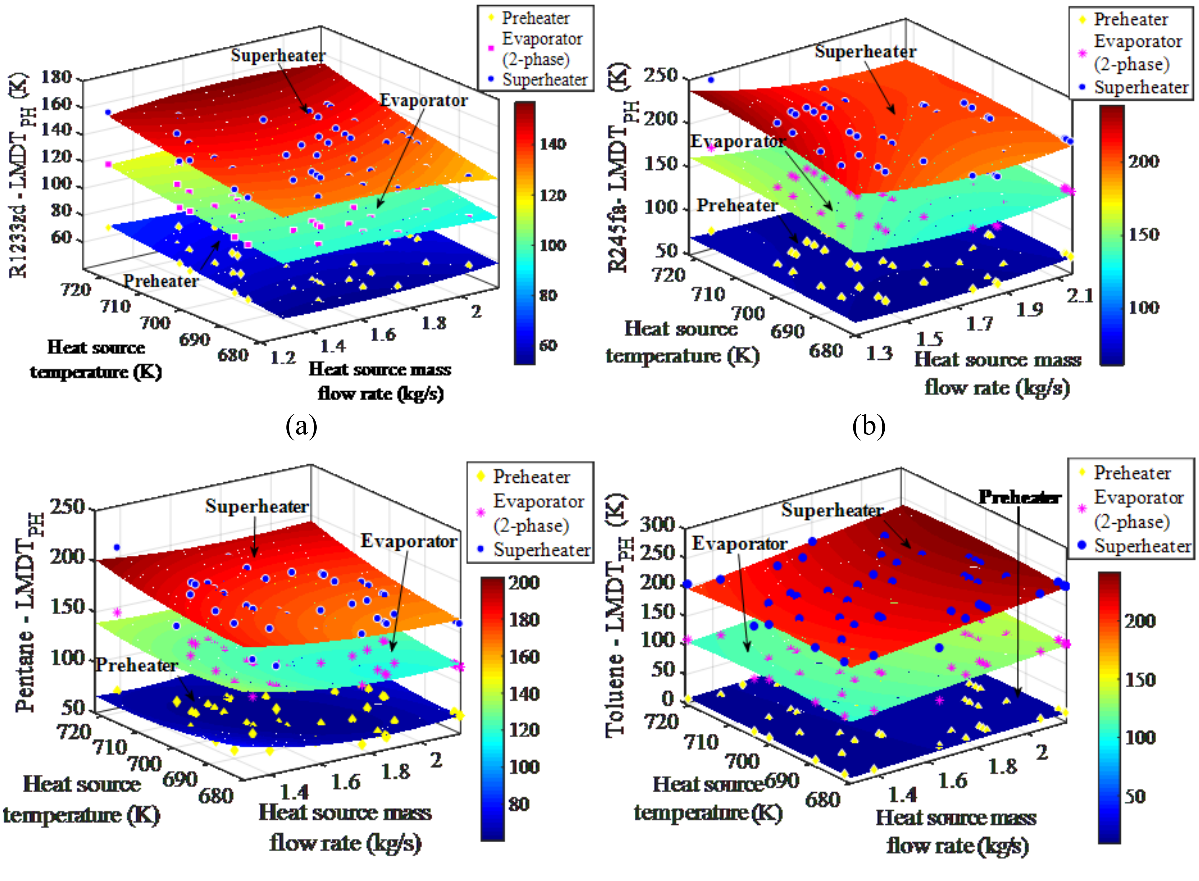

(a)

(b)

(c)

(d)

Fig. 65: PHEX evaporator temperature gradient map at off-design operation with piston expander for: a) R1233zd, b) R245fa, c) pentane, and d) toluene.

5.5.2.2 Power output performance maps

Using time-varying modelling for the evaporator HEX (given the specific HEX design), the actual HEX performance and heat recovered by the ORC engine is obtained. The optimum power output of the ORC engine at off-design operation in estimated by: i) assuming fixed piston expander efficiency across all load conditions; and ii) incorporating piston expander performance maps in the optimisation to predict the new expander efficiency at every operating point. In Fig. 66, the ORC power output map is illustrated for both approaches, and two HEX architectures, for R1233zd (findings are representative of all fluids investigated). In Fig. 67, the power output of all fluids investigated using the time-varying expander and HEX analysis are then presented.

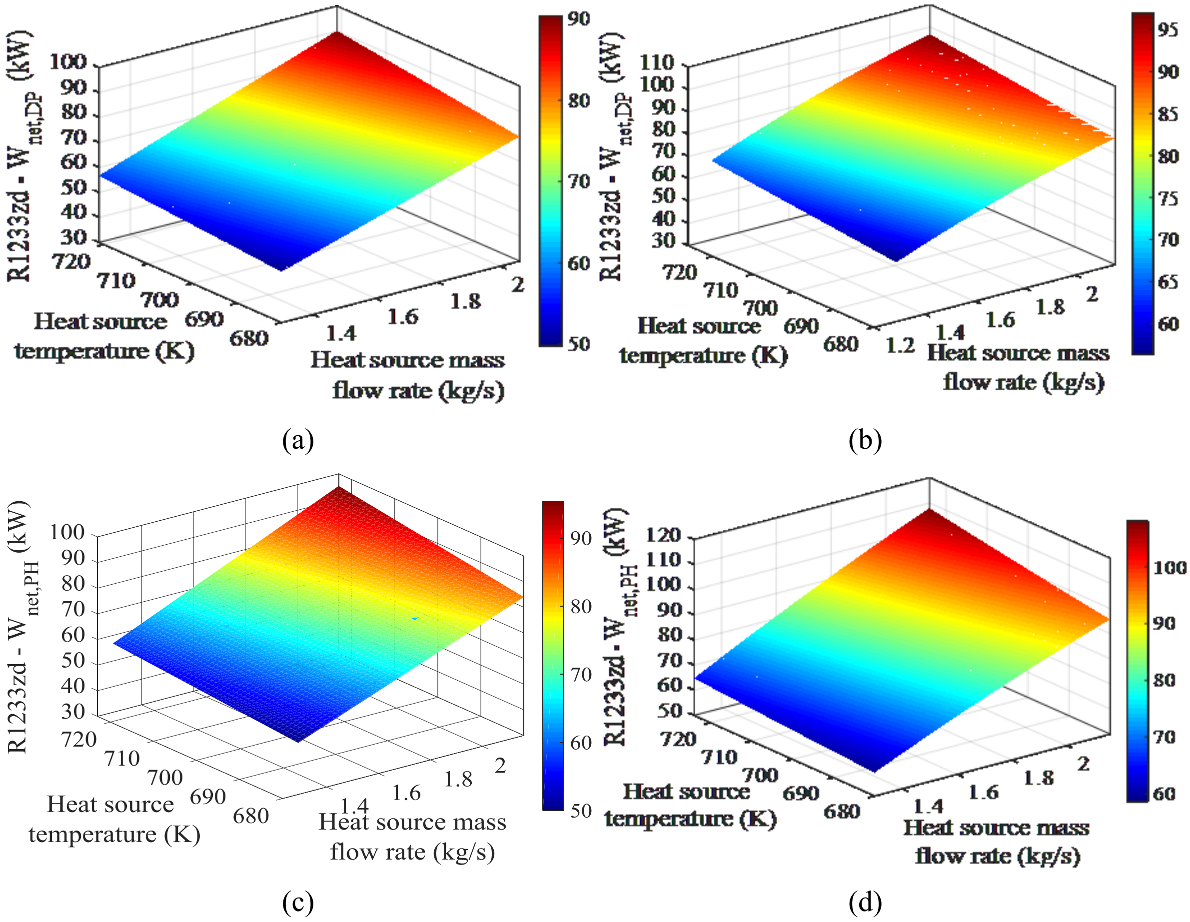

Fig. 66: Optimum ORC power output performance map for R1233zd at off-design operation, with DPHEX: a) fixed piston expander efficiency and, b) variable piston expander efficiency; and PHEX: c) fixed piston expander efficiency and, d) variable piston expander efficiency.

When the isentropic efficiency of the expander is fixed, the power output of the ORC is underestimated by up to 17% (Fig. 66), particularly for low CHP-ICE PL. As the CHP-ICE power output decreases, so does the ORC power output, but at a lower rate. This is owing to the improvement of the efficiency of the evaporator HEX, and the piston expander at lower mass flow rates and PRs (see also Section 5.5.1 and 5.5.2.1). As expected, the highest power output is recorded for high mass flow rate and high temperature on the heat-source side. The power output ranges from 90 kW down to 55 kW for fixed expander efficiency and DPHEX (Fig. 66a), and from 95 kW to 65 kW for PHEX (Fig. 66c). For variable expander efficiency with DPHEX, the ORC engine power output varies between 97-65 kW (Fig. 66b), and with PHEX between 110-62 kW (Fig. 66d). Additionally, fixing the heat-source temperature, but increasing the heat-source mass flow rate, increases the power output by up to 50%. In contrast, increasing the heat-source temperature, with fixed heat-source mass flow rate, increases the power output by up to 17%, within the range of conditions considered. This trend is consistent between both approaches and HEX architectures.

ORC power output maps for all fluids using the time-varying HEX and expander performance are shown in Fig. 67. In Fig. 67a, the optimised ORC engine power output map for DPHEX is presented. The best performing fluid is R1233zd, followed very closely by pentane, then R245fa and toluene. Similar trend is observed in the ORC engines with PHEXs (Fig. 67b), but the absolute values of power output are higher by 5-12%, at high PL conditions. The PHEX design allows for different number of plates and corrugation style being used in the preheater/evaporator section and the superheater, in order to maximise heat transfer, but also maintain the pressure drop of the working fluids within the maximum pressure drop limitation. This allows for slightly higher mass flow rates on the organic fluid side, which results in higher PHEX effectiveness, recovering slightly more heat from the heat source, and thus generating more power. For all fluids investigated, the power output is significantly affected by the heat-source mass flow rate drop at PL. The power output of the ORC engine reduces by approximately 30%, from 100% ICE operation down to 60% ICE PL operation. These findings are important because: i) they can be utilised by the ORC systems operators to identify the optimum design point given the heat-source conditions; and ii) they can inform decisions about the system sizing and schematic to ensure that the optimum mass flow rate and temperature reaches the ORC evaporator.

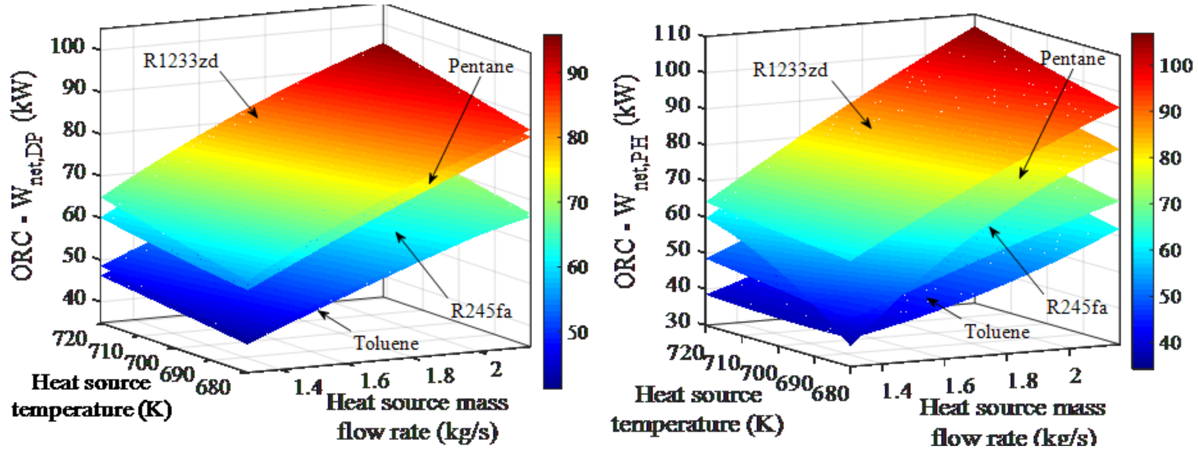

(a) (b)

Fig. 67: Optimum ORC power output performance maps at off-design operation with variable piston expander efficiency and: a) DPHEX and b) PHEX design for R1233zd, R245fa, pentane, and toluene.

5.5.2.3 Efficiency maps

The piston expander isentropic efficiency off-design maps, for fixed RPM (1500 RPM), with regards to the heat-source conditions variation are presented in Fig. 68. For all fluids investigated the piston isentropic efficiency increases at off-design conditions. Therefore, the power output reduction is lower than that in the ‘fixed efficiency’ scenario. More precisely, while the heat-source mass flow rate drops, and the temperature increases with the CHP-ICE PL, the expander efficiency in ORC engine with DPHEX (Fig. 68a) increases from 0.75 to 0.82 for R1233zd, from 0.62 to 0.74 for R245fa, from 0.73 to 0.81 for pentane and from 0.61 to 0.72 for toluene. This behaviour is explained by the working fluid optimum pressure and mass flow rate during off-design operation. In ORC engines with PHEX (Fig. 68b) it is noted that although the piston expander efficiency achieved is higher at nominal and high PL conditions, than that of the DPHEX design, the latter outperforms the former at lower PL conditions.

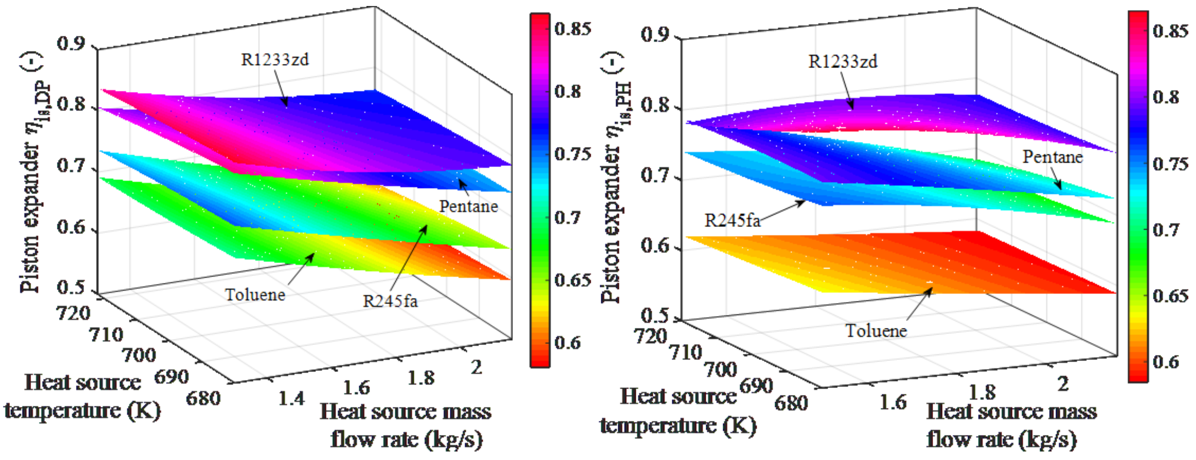

(a) (b)

Fig. 68: Piston expander isentropic efficiency maps with: a) DPHEX and b) PHEX, for R1233zd, R245fa, pentane, and toluene.

The expander performance map at off-design conditions, with respect to the inlet PR and working fluid flow rate is presented in Fig. 69 (for fixed RPM and fixed condenser pressure). The findings reveal that for all fluids investigated the optimum ORC operating points at off-design operation have lower evaporator pressure than the nominal point, and lower working fluid mass flow rate, helping to maximise the expander isentropic efficiency. When the variable performance of HEX and expander is incorporated into the analysis, the optimiser no longer seeks to maximise the cycle PR, as in the case of assumed fixed expander efficiency, but instead adjusts the evaporator pressure level to: i) increase the HEX effectiveness; and ii) operate the expander at high efficiency. Piston expanders efficiency improves at lower volume flow rates and/or PRs, because the losses through the valves improve significantly. For example, for R1233zd and pentane, where the expander isentropic efficiency increases with superheat temperature, the optimal PL cycle operates at high superheat, but decreasing PR. For R245fa and toluene, the expander efficiency is less sensitive to superheat and a lower superheat is selected as optimal, associated with lower pressure at the evaporator.

Finally, by considering the components time-varying characteristics during the off-design operation optimisation, we manage to maintain or even slightly increase the thermal efficiency of the ORC engine at off-design conditions (Fig. 70), for all fluids investigated and both HEX architectures. Nevertheless, an important challenge for the realisation of such practices is the design of real-time controllers, capable of monitoring the heat-source variations, and adjusting the ORC engine operation accordingly. Some interesting work on these aspects can be found in Refs. [79,112,113].

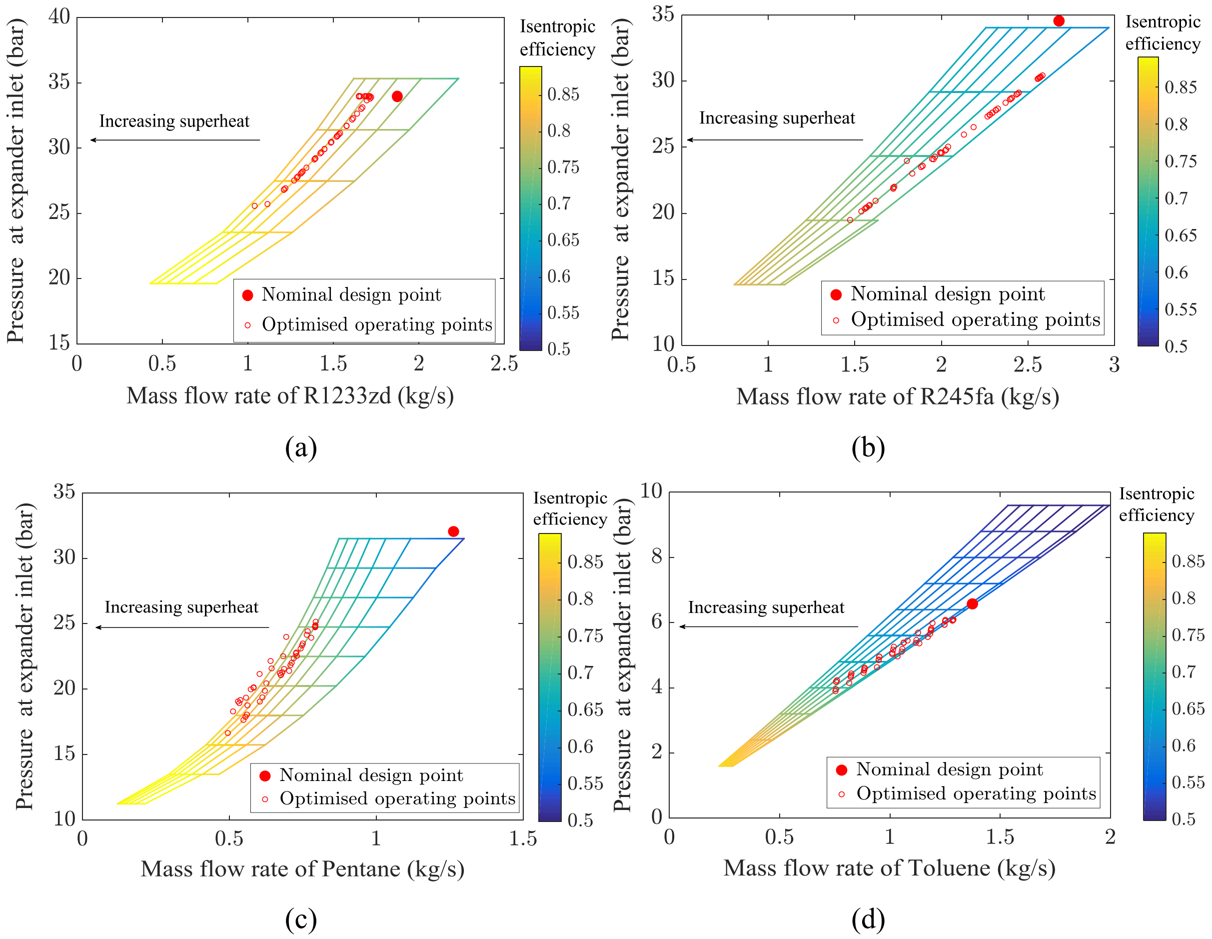

(a)

(b)

(c)

(d)

Fig. 69: Piston expander optimised operating points at off-design conditions for: a) R1233zd, b) R245fa, c) pentane, and d) toluene. The filled dot indicates the nominal design point, found using a fixed isentropic efficiency. Results presented here refer to DPHEX designs, and are representative of the PHEX designs.

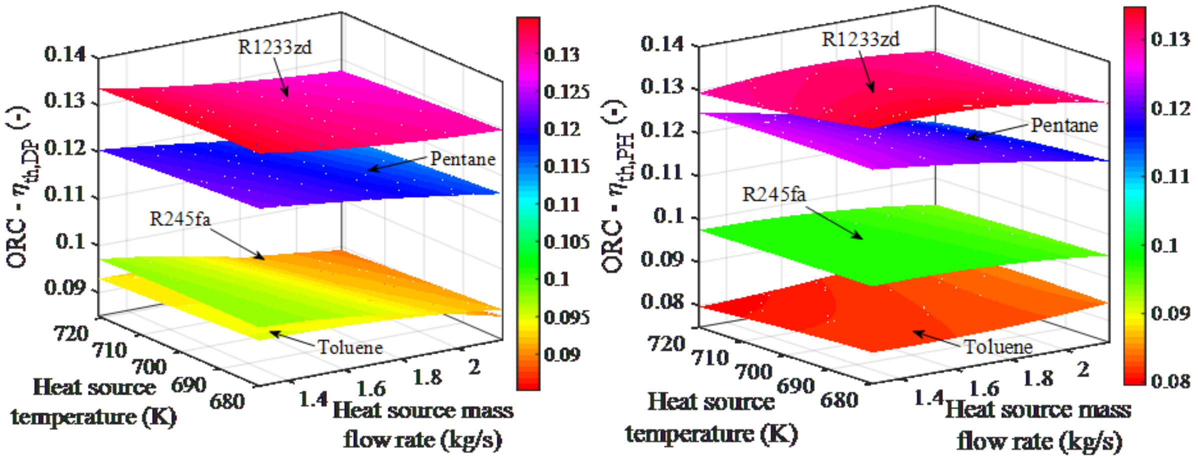

(a) (b)

Fig. 70: ORC thermal efficiency at off-design operation with variable piston expander efficiency with a) DPHEX and b) PHEX, for R1233zd, R245fa, pentane, and toluene.

5.6 System optimisation and sizing results – III: Off-design operation with screw expander

A similar off-design performance analysis for ORC engines with screw expanders has been performed, following the optimisation methodology described in Section 5.3, and using the nominal sizing results presented in Section 5.4, for optimised ORC engines with screw expanders. In the following sections the off-design performance maps for the ORC engine with screw expanders are presented, and compared to those recorded for ORC engines with piston expanders.

5.6.1 Evaporator performance maps

The *U*-values obtained in the ORC engine with screw expander are very similar to those achieved in the piston expander designs, with the former being slightly lower. This is attributed to the different operating points of the two cycles as discussed in subsequent sections. The *U*-values achieved in the ORC evaporator HEX with screw expanders are presented in Fig. 71 for toluene, which is the best performing fluid with screw expander. Similar trends have been recorded for the other fluids investigated, and the findings are presented in detail, in Appendix A.

The overall heat transfer coefficient varies between 30-50 W/m^2 K and 50-120 W/m^2 K, for DPHEX and PHEX designs, respectively. Similarly to the findings for piston expanders, the evaporator two-phase section has the highest *U*-value at all PL points, followed very closely by the superheating section. The preheating section presents the lowest *U*-value, mainly due to the higher fluid density in the HEX that leads to smaller volume flow rates, and thus velocities in the tubes/channels, decreasing the Reynolds number and the convective heat transfer rate. Additionally, in the preheater zone the temperatures of both the heat source and the working fluid are lower than those in the other HEX sections. Looking at the variation of the *U*-value with PL, the mass flow rate reduction at off-design operation has significant influence on the overall heat transfer coefficient. While the heat-source mass flow rate reduces from 2.1 kg/s to 1.29 kg/s (CHP-ICE PL 100% to 60%), the *U*-value reduces by up to 30%. In contrast, for fixed heat-source mass flow rate, the temperature increase has on only marginal impact on the *U*-value achieved.

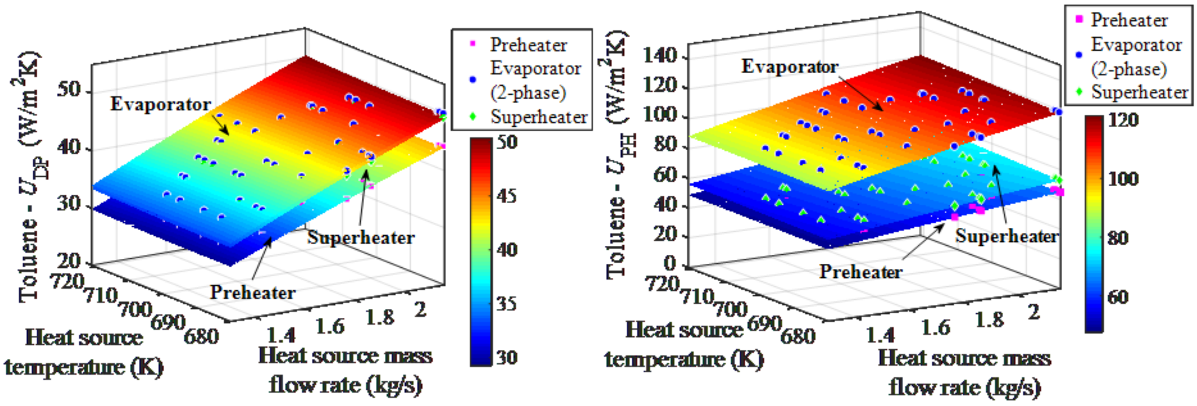

(a) (b)

Fig. 71: Evaporator overall heat transfer coefficient map at off-design operation, with variable screw expander efficiency and toluene for: a) DPHEX and b) PHEX.

The evaporator effectiveness is presented in Fig. 72. The highest effectiveness is observed in the preheating section, exceeding 0.9, where the pinch point of the evaporator HEX is also observed. The superheater section has the lowest effectiveness ranging between 0.15-0.22. The evaporator effectiveness is relatively high (0.6-0.7) for toluene, due to the operating conditions of the cycle for this fluid. Toluene can operate at higher evaporating saturation temperatures than the refrigerants investigated (while still being in the subcritical region), and thus the optimiser can increase its operating temperature, following the heat-source temperature increase at PL. This improves the temperature match of the evaporating zone, to the heat-source, maintaining a fairly constant LMDT across all PL conditions (Fig. 73). Finally, it is noted that this operating profile is different to that observed in ORC engines with piston expanders, where the optimum off-design operating points have lower evaporation temperature/pressure than the nominal point, to improve the piston efficiency.

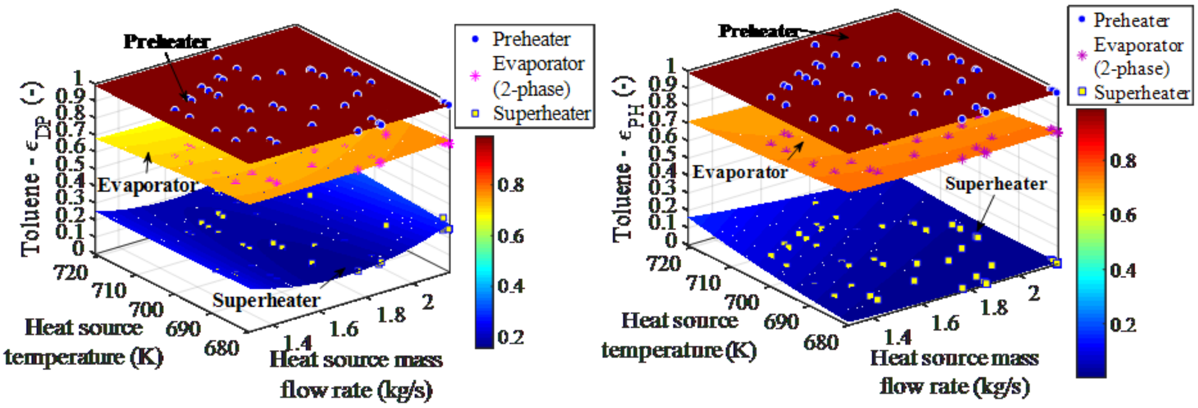

(a) (b)

Fig. 72: Evaporator effectiveness map at off-design operation with variable screw expander efficiency and toluene for: a) DPHEX, and b) PHEX.

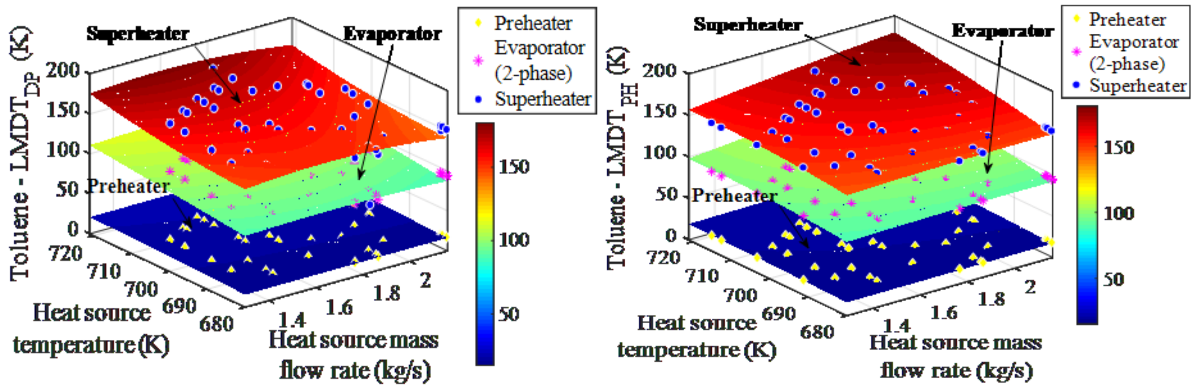

(a) (b)

Fig. 73: Evaporator temperature gradient map at off-design operation with screw expander and toluene for: a) DPHEX, and b) PHEX.

5.6.2 Power output performance maps

The optimised ORC power output with screw expanders and two HEX architectures is presented in Fig. 74. Similarly to the trend observed in ORC engines with piston expander, the power output of the ORC engine with PHEXs is higher than that achieved with DPHEXs design, at nominal conditions. In the case of ORC engines with screw expanders, the power output with PHEXs is 5-8% higher than that achieved with DPHEXs (depending on the fluid), for operating conditions close to the nominal design point. On the contrary, at low PL (e.g. CHP-ICE 60%) the power output of the two HEX architectures is comparable (Fig. 74), with the DPHEX designs performing better for fluids such as toluene. Similarly, in ORC engines with piston expander, PHEXs perform better at high PL by generating up to 11% more power output, but at lower PL the power output of the two architectures is comparable (Fig. 68).

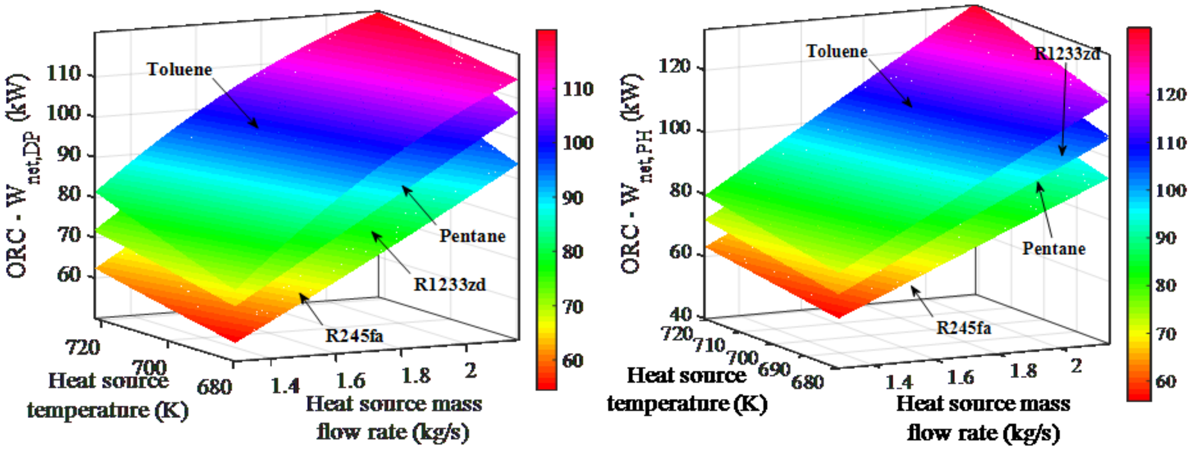

(a) (b)

Fig. 74: Optimum ORC power output performance maps at off-design operation with screw expander and: a) DPHEX and b) PHEX design, for R1233zd, R245fa, pentane, and toluene.

As discussed, ORC engines with piston expanders generate overall slightly lower power output than that of the two-stage screw expanders, by approximately 5-15%, with the exemption of toluene which generates approximately 38% lower power output (at the design point). However, by comparing the power output reduction at off-design operation of ORC engines with screw expanders, to that of piston expanders, it is noted that in the former design (screw expanders) the power output reduces with a higher rate than the latter (piston expanders), for all fluids investigated. A case in the point is pentane, for which when the ORC engine operates with piston expander, while the CHP-ICE PL decreases from 100% to 60% the power output of the ORC engines decreases from 100% to 76%, whilst with screw expander for the same fluid, the power output reduces down to 67% (Fig. 74) (figures quoted reflect DPHEX designs).

Results also reveal that although in ORC engines with piston expander the system aims to reduce the PR over the expander at low PL, to increase the piston expander efficiency, in the case of screw expanders, the PR either stays the same, or increases slightly, depending on the fluid (Fig. 75). For a given screw expander design, the impact of variable volume flow rate on the efficiency of the expander is minimal, in comparison to the impact of deviating from the machines' built-in VR [79], by changing the operating temperature and pressure levels. Therefore, in all off-design points, refrigerants operate with VRs (and PRs) very close to the design point (built-in VR), while in the case of hydrocarbons, VRs increase slightly. The hydrocarbons' VRs increase at off-design operation, because these operate at higher evaporator temperature, while the heat-source temperature increases at CHP-ICE PL. Because pentane and toluene can tolerate higher operating temperatures than refrigerants, before decomposition phenomena start occurring, the optimiser chooses to increase the temperature/pressure of these fluids when recovering heat, to increase power output, but at the cost of reducing the screw expander efficiency, as discussed in the next section.

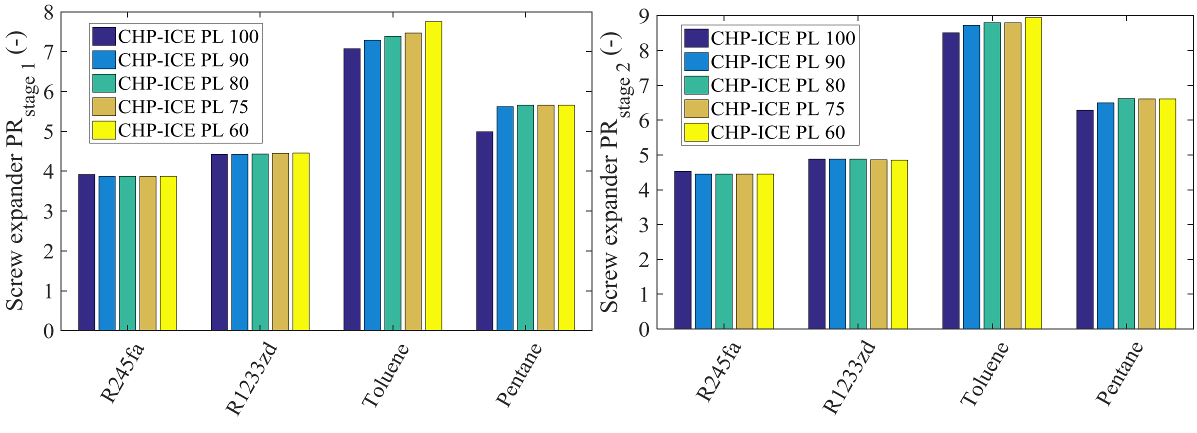

(a) (b)

Fig. 75: Optimum screw expander pressure ratios at CHP-ICE PL operation for: a) first stage expansion, and b) second stage expansion. The findings presented here refer to PHEX designs, but also reflect those recorded for DPHEX architectures.

Finally, although the best performing fluids between screw design and piston are similar, the relative magnitude of the power output generated with these fluids varies significantly between the two configurations. In ORC engines with piston designs, R1233zd seems to outperform all refrigerants generating 98 kW (at the design point), while having comparable power output to pentane (90 kW), followed by R1245fa (72 kW) and toluene (67 kW). In contrast, in screw designs toluene outperforms all fluids (115 kW), followed by pentane (100 kW), R1233zd (98 kW) and R245fa (88 kW). And this trend is consistent for the full spectrum of the CHP-ICE PL operating conditions.

5.6.3 Efficiency maps

The screw expander isotropic efficiency is presented in Fig. 76, for all fluids investigated and both HEX architectures. For all fluids investigated and at all PL operating conditions, the second stage expansion has higher isentropic efficiency than the first stage, due to the lower superheat, and thus VR and volume flow rate of the working fluid. The highest isentropic efficiency of the screw machine (at the second stage expansion) is recorded for R245fa (76%-77%), followed by R1233zd with (75-76%). In the case of DPHEX design, the screw expander efficiency of pentane is higher than that of toluene, corresponding to 74-75% and 73-74%, respectively. However, this trend reverses in the case of PHEX designs. The findings highlight, that the best performing fluids can tolerate lower isentropic efficiencies of the expander, and still generate more power output. Consequently, lower specification of the expander can be incorporated in the design of ORC engines without impacting negatively the engine performance. This is attributed to the different operating conditions of the cycle among the various fluids. In the case of hydrocarbons (toluene and pentane), which can operate at higher temperatures and pressures than the refrigerants, the increase in the heat-source temperature at PL is followed by an increase in the superheat of those fluids, resulting in higher VRs over the expander, reducing its efficiency. However, the increase of the enthalpy difference over the expander compensates for the reduction in the expander efficiency. Consequently, the optimiser selects the new operating points at higher pressures, although this may penalise the screw expander efficiency.

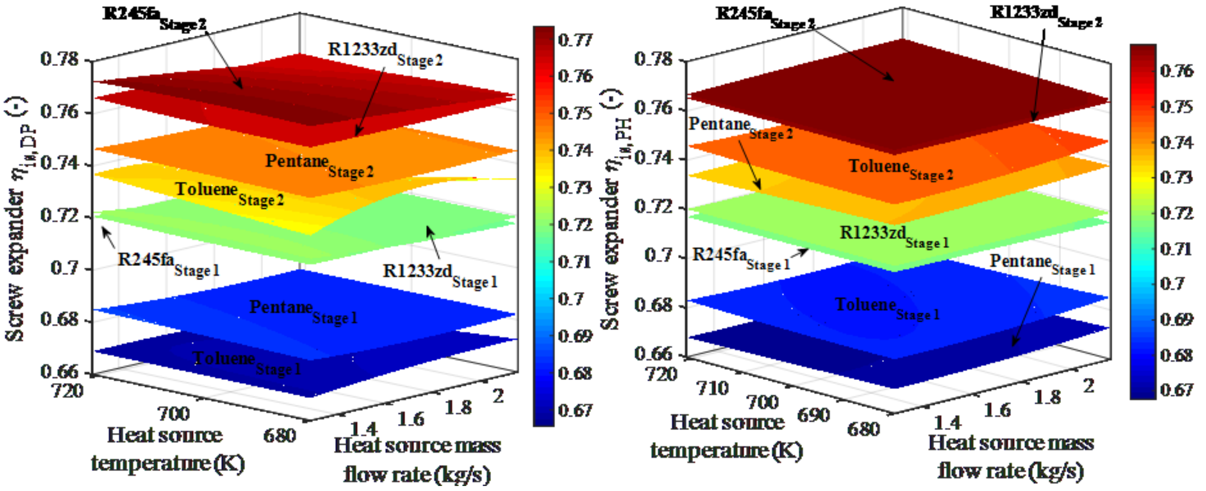

(a) (b)

Fig. 76: Screw expander isentropic efficiency maps with: a) DPHEX and b) PHEX, for R1233zd, R245fa, pentane, and toluene.

The ORC engine thermal efficiency with screw expanders is presented in Fig. 77. As expected, the best performing fluids in terms of power output are those achieving the highest thermal efficiencies. Toluene operates with 15-16% efficiency, followed by R1233zd and pentane with 14% and R245fa with 13%. Results highlight that by accounting for the interactions of the HEX and the expander, the ORC engine can maintain its efficiency at off-design operation, maximising its performance.

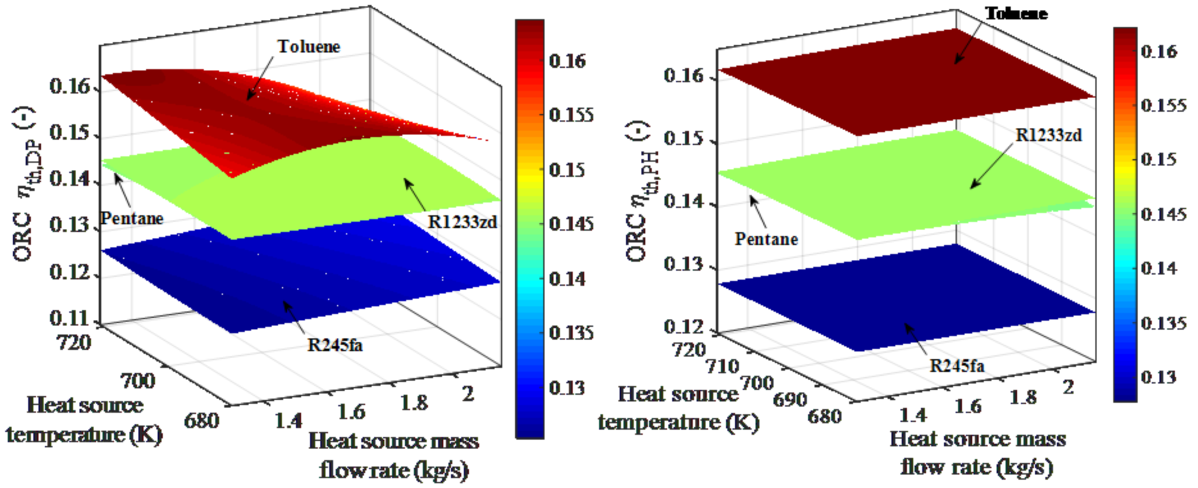

(a) (b)

Fig. 77: ORC thermal efficiency at off-design operation with variable screw expander efficiency with: a) DPHEX and b) PHEX, for R1233zd, R245fa, pentane, and toluene.

5.7 Summary and conclusions

ORC engines in real applications experience a variable heat-source profile, in terms of mass flow rate and temperature. To maximise their market penetration, and improve their economic proposition, optimising the engines performance at design and off-design conditions is of paramount importance. In this work, an optimisation tool has been developed, which captures the interactions of key ORC engine components, under varying heat-source conditions, aiming to identify the new optimum operating points of the engine that maximise its performance. This work goes beyond previous efforts in the literature by: i) accounting explicitly for the evaporator HEX and expander time-varying performance and interactions; and ii) investigating the integration of piston expanders in stationary power generation applications, at design and off-design operation. Two HEX architectures have been evaluated; DPHEX and PHEX designs, while the ORC engine examined is recovering high-grade heat from the exhaust-gas stream of a CHP-ICE. The framework is then also used to predict the optimum off-design performance of ORC engines with screw expanders, and the findings are compared to those obtained for piston machines.

First, findings reveal that when the interactions between the evaporator HEX and the piston expander are not considered, by assuming a fixed/constant performance of the system components at off-design operation, the ORC engine power output is underestimated by up to 17%. Additionally, the optimal operating points, when the components time-varying characteristics are not incorporated in the design are different to those obtained when the fully integrated system is considered. In the former case, the optimiser always aims to maximise the PR over the piston expander to increase the engine’s power output at off-design operation, while in the latter case the optimum PR decreases with PL, to increase the piston expander isentropic efficiency.

Results also reveal that different operating strategies should be adopted, when optimising the off-design operation of ORC engines with piston or screw expanders. Piston expanders at off-design conditions operate efficiently at lower mass flow rates and PRs, because this reduces the losses through the valves, thus improving the piston expander isotropic efficiency. Findings indicate piston expanders' isentropic efficiency improvement from nominal, to off-design operation, of up to 16%, while the PR reduces by 22%. In contrast, the optimum off-design operating points of ORC engines with screw expanders, have either similar or slightly higher PRs over the expanders in comparison to their design point, which slightly reduces their isentropic efficiency. However, the higher enthalpy difference over the screw expander for higher PRs, compensates for the expander isentropic efficiency reduction. Therefore, it is concluded that in the former case (piston expanders) the optimised ORCs at off-design conditions should operate at lower PRs and volume flow rates, to maximise the piston efficiency at off-design conditions, while in the latter case (screw expanders) the control strategy should aim to operate close to the nominal built-in VR/PR of the screws.

Looking at the evaporator HEX performance at off-design conditions, results highlight that ORC engines with PHEXs can generate more power than those with DPHEX at the design point, by up to 12%. However, PHEX designs have similar power output with that of engines with DPHEX designs at low PL, with the latter generating up to 4% more power output, depending on the fluid. It is also noted that the impact of the heat-source and working fluid mass flow rates reduction at off-design operation, on the HEX *U*-value is significant. While the CHP-ICE operates from 100% load down to 60% the *U*-value drops by up to 30%. In contrast, for fixed heat-source flow rate, as the temperature increases, the *U*-value stays fairly constant. These findings are recorded for both HEX architectures examined. Therefore, to select the most suitable HEX architecture, aspects such as that of the ORC engine operating profile over its lifespan should be considered, along with the cost of each design, since depending on the application, one configuration may be more suitable than the other.

By comparing the off-design performance of ORC engines with screw expanders to those with piston expanders, it is revealed that although the former generate more power at the design point, for all fluids investigated, piston expanders can operate more efficiently under variable load conditions than screw machines. The power output reduction of ORC engines with piston expanders does not exceed 25%, while the CHP-ICE PL reduces from 100% to 60%. In contrast, the power output of screw expanders under the same conditions reduces by more than 33%. This feature makes piston expanders a very robust and promising candidate for ORC applications, where the heat-source conditions are varying.

The best performing fluids in terms of power output differ between the screw and piston expander designs. Therefore, suitable components and fluid selection matching should be performed, to obtain the best performing ORC engine configuration, given the operating conditions of the application. It is highlighted that piston expanders can operate efficiently with new low GWP/ODP working fluids (such as R1233zd), making them a promising expander technology for the next generation of ORC engines, which would need to abide by the new regulations for the use of working fluids with low environmental impact. Finally, results highlight that by capturing the trade-offs between the evaporator and expander performance, the ORC engine thermal efficiency can remain constant and equal to the nominal (design) operation, or even increase at off-design conditions.

To conclude, the off-design optimisation tool developed here captures the interactions of key ORC engine components and provides off-design performance maps, for the complete system and for its constituent components. These maps can be used by ORC manufacturers to inform decisions on component or system design, and by ORC plant operators to inform decisions on optimum system operation, given their specific site conditions. Additionally, the potential of piston expanders in stationary power generation application has been revealed, and insights on the optimum operation of these expanders have been provided. Finally, some modern low-GWP ORC fluids have been considered that have not been the subject of previous ORC off-design studies, and which are very important in terms of their use in practical applications also from a regulatory perspective. In the next chapter the economic aspects of the various configurations examined here are evaluated.

Chapter 6

Organic Rankine cycle engine thermoeconomic evaluation

> *"To truly transform our economy, protect our security, and save our planet from the ravages of climate change, we need to ultimately make clean, renewable energy the profitable kind of energy."*
>
> – Barack Obama, former President of the United States

6.1 Introduction

Key for the wider adoption of organic Rankine cycle (ORC) systems, apart from their thermodynamic performance, is their financial proposition, which depends on the system's capital expenditure (CAPEX), operating and maintenance (O&M) costs and the overall project profitability against other competitive technologies. Currently, there is only limited data publicly available in the literature, related to ORC engine purchase or installations costs. Therefore, the lack of actual ORC engine cost data renders the development of credible cost correlations, capable of predicting the ORC system costs with a reasonable level of confidence very important.

In the efforts available in the literature aiming to evaluate ORC engine costs, the cost of each ORC engine component is first obtained, using relevant cost functions. Then some cost correction factors are applied, to capture variations in operating conditions (temperature/pressure) and materials, between different system configurations. Next, some cost multipliers are applied to the overall cost, to capture the ORC engine assembly costs. There is a variety of costing methods and correlations available in the ORC literature [117], with the module costing technique (as provided in Refs. [115,116]), being the most commonly used, although it originates from the chemical industry and was developed for costing major chemical plants and components. However, the validation of those cost predictions is an onerous task, since it requires available data from real ORC projects and installations.

As discussed in previous sections (Chapter 2), in the majority of thermoeconomic studies in the ORC field, such as those presented, among others, in Refs. [8,118,121], the type of each ORC component is preselected, and their geometric characteristics are predefined, before proceeding to the thermoeconomic evaluation of the ORC system, instead of forming the output of the optimisation exercise. There is very limited literature available on the simultaneous ORC thermoeconomic optimisation and components selection and sizing, with a couple of studies focusing on the heat exchanger (HEX) design optimisation only [51,53] and others focusing on the expander design [48]. Braimakis et al. [48] presented a thermoeconomic analysis of ORC engines using plate HEXs (PHEXs) only, and compared alternative expander machines, while Zhang et al. [53] investigated alternative HEXs configurations, while fixing the expander selection to turbine. It can also be concluded that not a single ORC system design can be identified as the optimal one. On the contrary, the most suitable HEXs and expander type vary with the application, and the heat-source conditions. Finally, it is revealed that there is not a consistent costing methodology used when assessing alternative ORC designs. These findings highlight the need for integrating the component selection, sizing and costing of ORC engines, to obtain the best performing designs for alternative applications.

In this chapter, a systematic ORC engine component selection, sizing and costing optimisation framework is presented, covering a range of HEXs and expander devices configurations. This work goes beyond other efforts in the literature in that the HEX typology, expansion stages, and components' sizing, are simultaneously optimised with the complete ORC system design for maximum power output or/and minimum SIC, instead of forming a designer predefined input. This allows the simultaneous selection of the best performing system configuration and size, given the application specific constraints, since the optimiser screens alternative components typologies, configurations and sizes to identify the best performing design.

In this chapter, we first compare alternative costing methods, while presenting new cost correlations, based on vendors' price lists and real ORC engine cost data, aiming to establish cost functions, which can provide realistic cost estimates for the CAPEX of ORC engines. In Section 6.2, the new correlations developed as part of this thesis are presented and compared to the cost predictions obtained, when using the module costing technique, a method widely used in the ORC literature. The details of the module costing technique have been previously presented in Section 3.8 (Chapter 3). To illustrate the framework developed, it is applied on a cogeneration system driven by an internal combustion engine (ICE-ORC CHP system), where the ORC engine recovers heat from the ICE exhaust-gas stream (Section 6.3). The cost correlations developed are used to obtain the specific investment cost (SIC) of optimised ORC systems, using the following objectives: i) ORC engines optimised for maximum power output; ii) ORC engines optimised for minimum SIC; and iii) multi-objective optimisation to obtain the Pareto front between the ORC engines power output and SIC (Section 6.4). The findings of the single-objective optimisation exercises are presented in Section 6.5, and of the multi-objective analysis in Section 6.6. The profitability of ORC engines in waste heat applications is assessed in Section 6.7, for a notional UK-based industrial user. Finally, a summary of the main findings and conclusions are discussed in Section 6.8.

6.2 Organic Rankine cycle engine overview

The ORC design considered here is for a subcritical non-recuperative engine, which recovers heat from the exhaust-gas stream of a CHP-ICE engine. The ICE-ORC system schematic considered has been previously presented in Chapter 5, in Fig. 29, while the thermodynamic equations that describe the system performance are listed in Section 3.3.

Two HEX architectures have been investigated, as suitable candidates for the small-medium power range scale ORC engines examined in this work; i) DPHEX; and ii) PHEX designs. The sizing of the HEXs is performed using the Nusselt number and pressure drop correlations presented in Chapter 3.

Two types of volumetric expander machines have been compared for their performance from thermoeconomic perspective, namely i) piston expander and ii) screw expander. It should be noted that in this chapter we consider the ORC engine design at nominal conditions only, and we compare alternative designs in terms of power output, equipment selection, sizing, and cost, at their design point.

To obtain reasonable estimates of the piston expander efficiency at nominal operating conditions and use these as input to the thermoeconomic optimisation, the piston expander efficiency findings presented in Chapter 5 have been used. The results of the piston expander analysis at nominal conditions indicate that it can achieve isentropic efficiencies of up to 0.9 depending on the working fluid investigated. In Fig. 78, example piston expander performance maps are presented for R1233zd and pentane, indicating that isentropic efficiencies of 0.6-0.9 are feasible for piston expanders

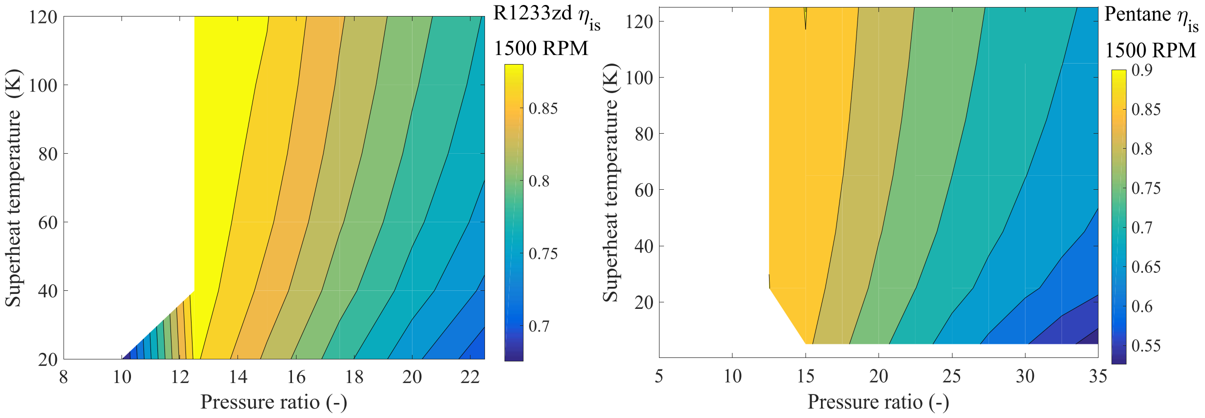

(a) (b)

Fig. 78: Piston expander performance maps for R1233zd and pentane, over a range of pressure ratios and working fluid superheat. Maps have been generated using the piston model presented in Refs. [138,151].

Based on these, in this work the piston expander efficiency at the design point is assumed to be equal to 0.7 (including mechanical losses), while further losses from the electric generator operating with an efficiency of 95% are allowed. Additionally, the expander operation is obtained for 1500 RPM, as the design point, which is the typical operating speed of electric generators [9]. The screw expander performance is predicted using the correlations developed by Astolfi [65], as previously presented in Chapters 3 and 5. Because in this chapter we only compare ORC engines at their design point, the off-design correction factor is not incorporated. Similarly to the piston expanders design, additional losses from the electric generator operating with an efficiency of 95% are allowed. Finally, the pump is assumed to be centrifugal variable-speed unit with an efficiency of 0.65 [40].

6.3 Organic Rankine cycle engine component costing

The aim of this section is to identify the cost correlations which can provide credible estimates of the ORC engines cost. The cost correlations developed in this thesis using available manufacturers' cost data are presented, and compared to the module costing technique results. The details of the module costing technique have been previously presented in Chapter 3.

6.3.1 Heat exchanger cost correlations comparison

Apart from the module costing technique cost correlations, as provided by Refs. [115,116] and previously presented in Section 3.8, the correlation of Lecompte et al. as provided in Ref. [8] has been used to estimate the cost of the various ORC system components. This correlation was based on prices of the various components in the Belgian market, in 2013. In this work, some new correlations are also developed for both DPHEX, and PHEX designs, by collating available material and manufacturers' prices for the various ORC engine HEXs. More precisely, data for the cost of stainless steel (SS) tubes/plates were obtained from Daccord et al. [52]. The authors had provided a cost breakdown of the different ORC engine components' cost for a vehicle waste heat recovery application. On top of the quoted materials' cost, an additional 60% of overhead for assembly was added, as proposed by the same authors. The correlation developed uses the SS mass of the DPHEX to obtain the cost of the unit. Another cost correlation has been also developed in this study, specifically for SS PHEX designed for high temperature and high pressure applications (fusion bonded type) based on cost data collated from Alfa Laval price catalogues [176]. This correlation also uses the mass of the plates to obtain the HEX cost. A summary of the cost correlations compared in this study is presented in Table 12.

To convert the costs to today's values the Chemical Engineering Cost Index (CEPCI) has been used. For Lecompte et al. [8] the base year is 2013 ($CEPCI_{2013}$ = 567), for Daccord et al. [52] is 2017 ($CEPCI_{2017}$ = 562.1), and for Alfa Laval [176] is 2016 ($CEPCI_{2016}$ = 541.71). All costs were converted to 2017 values, using $CEPCI_{2017}$ = 562.1. USD were converted to GBP using: for 2001, the conversion rate of 0.6944, and for 2013, the rate of 0.63955 [159]. Euros were converted to GBP using: for 2013, the rate of 1 euro = 0.849 GBP and 2017 rate of 1 euro = 0.85 GBP [159]. At the time of writing, the CEPCI for year 2018 was not available, therefore the CEPCI of 2017 has been used.

Table 12: Cost coefficients used for the economic analysis, based on Refs. [8,52,65,115,116,176–178].

Component	Z	F	$F_p/F_m/F_D$	K_1	K_2	K_3	K_4	K_5	Ref.
DPHEX Preheater/ Desuperheater	Area (ft^2)	1	1/2/-	7.2718	0.160	-	-	-	[116]
	Area (m^2)	1	1/1.8/-	3.3444	0.2745	-0.0472	-	-	[115]
	HEX Mass (kg)				$1.6\ (11.8\ Z)$				[52]
	Area (m^2)				$297\ Z$				[8]
DPHEX Evaporator/ Condenser (forced circulation)	Area (ft^2)	1	1/1/-	8.0369	0.6994	-0.00004	-	-	[116]
	Area (m^2)	1	F_p/3/-	5.0238	0.3475	0.0703	-	-	[115]
PHEX	Area (ft^2)				$10{,}070\ (Z)^{0.42}$				[116]
	Area (m^2)	1	1/2.4/-	4.6656	-0.1557	0.1547	-	-	[115]
	HEX Mass (kg)				$142\ Z + 733$				[176]
	Area (m^2)				$190 + 310\ Z$				[8]
Reciprocating compressor	Power (Hp)	1	-/1/1	4.6762	1.23	-	-	-	[116]
	Power (kW)	3.5	-/-/1	2.2897	1.3604	-0.1027	-	-	[115]
	Volume flow rate (m^3/s)				$32{,}769\ Z + 565.83$				[177,178]
Screw compressor	Power (HP)	1	-/1/1	8.2496	0.7243	-	-	-	[116]
	Power (kW)	2.5	-/-/1	5.0355	-1.8002	0.8253	-	-	[115]
	Volume flow rate (m^3/s)				$3{,}143.7 + 217{,}423\ Z$				[65]
Pump	S (gpm$\sqrt{ft_{\text{head}}}$)	1	2/1.35	12.1656	-1.1448	0.0862	-	-	[116]
Pump motor	Power (HP)	1	-/1.4	5.3992	0.16829	0.110056	0.071413	0.0063788	[116]

In Fig. 79, the DPHEX cost is presented, as calculated using the cost correlations discussed above. In line with the results, the single-phase DPHEX correlations provided by Seider [116] and Turton [115] significantly underestimate the HEX cost, when compared to the correlations developed using market data for HEXs as provided in Lecompte et al. [8] and Daccord et al. [52]. On the contrary, when using the forced convection cost correlations for estimating the two-phase zone cost, both Seider [116] and Turton [115] correlations result in cost figures which extremely overestimate the HEX cost, by being up to 4.5 times higher than those obtained for the DPHEX design, using vendors' costs. These findings highlight that the selection of the cost correlation can have major impact on the final ORC engine CAPEX estimates.

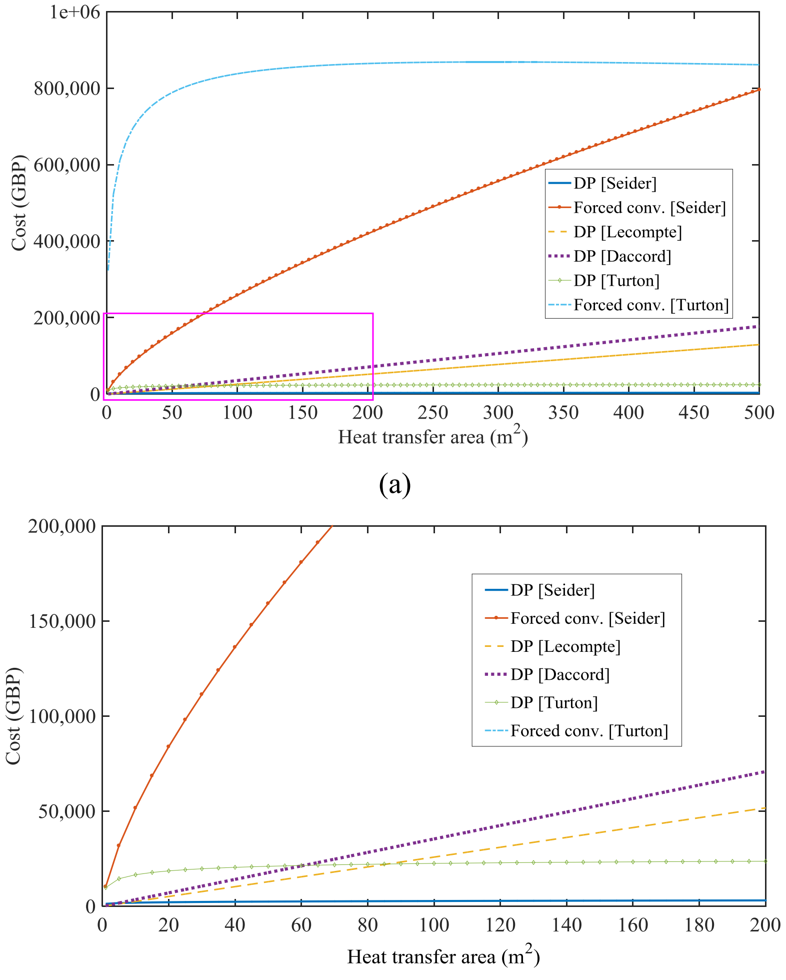

(a)

(b)

Fig. 79: DPHEX cost prediction comparison using: i) the module costing technique, ii) other cost correlations in the literature, and iii) the cost correlations developed in this work, using DHEX available cost data.

The PHEX costs are presented in Fig. 80. Similarly to the findings for DPHEX, Turton [115] overestimates the cost of the PHEX, by up to 400% when compared to the correlations obtained from the cost data provided by Alfa Laval [176]. Seider [116] seems to overestimate the cost for low area requirements but has similar cost to the vendors' data for high area requirements. The findings highlight that the validity of the various correlations may vary, depending on the range and size of the equipment under consideration.

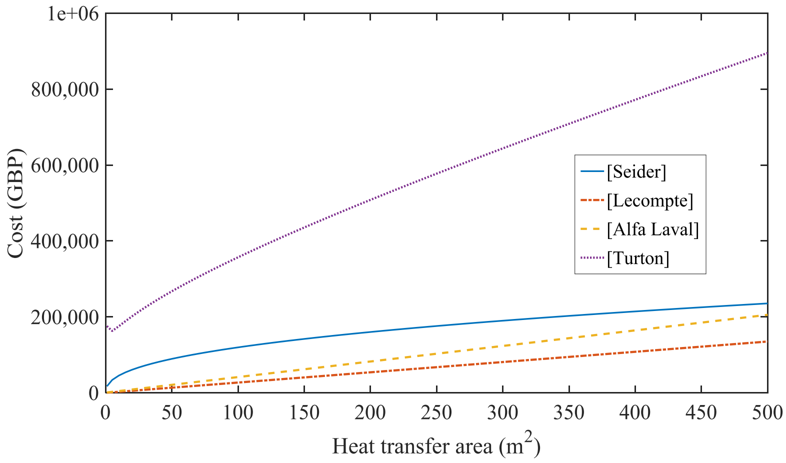

Fig. 80: PHEX cost prediction comparison using: i) the module costing technique, ii) other cost correlations in the literature, and iii) the cost correlations developed in this work using PHEX available cost data.

6.3.2 Expanders cost correlations comparison

Apart from the module costing technique correlations provided in Refs. [115,116], previously presented in Section 3.8, the correlation provided by Astolfi [65] has been used to estimate the cost of the screw expander devices. This correlation was generated collating data from manufacturers' price lists in Europe, for screw compressors available in the market, in 2013. An additional correlation for reciprocating piston expanders has been developed in this work, collating data from various types of reciprocating piston compressors available in the market, used in refrigeration systems. The price lists were provided by Refs. [177,178]. All values have been converted to today's values using the CEPCI. For Astolfi [65] the base year is 2013 ($CEPCI_{2013} = 567$), and for Refs. [177,178] is 2017 ($CEPCI_{2017} = 562.1$). A summary of the expander cost correlations compared in this study is also presented in Table 12.

In Fig. 81a, the compressor cost for medium-large scale machines is provided, using the module costing technique cost correlations. It is noted that there is a large deviation in the estimation of the screw compressor costs between the two well-established references for the module costing technique, especially for capacities exceeding 130 kW. For lower system sizes, the correlations predict costs between 20,000 GBP and 200,000 GBP. The costs for reciprocating expanders using Seider [116] are lower than the respective ones for screw, whilst when using the Turton [115] correlation the costs of the two machines deviate only slightly, for similar capacities.

In Fig. 82 the cost of piston and screw compressors for small-medium scale systems are presented, using the cost correlations obtained from manufacturers' price lists data. For very small machines, piston compressors are less expensive than screw, but while the working fluid volume flow rate increases, the former machines have almost double the cost of the latter.

These findings highlight the importance of choosing the correct cost correlation for each one of the ORC engine components. Therefore, to obtain the ORC engines total cost (TC), SIC, etc. in this thesis, the correlations developed using cost data available in the market (from Refs. [52,176]) have been used for the HEXs, and those developed using data from Refs. [65,177,178] for the expanders.

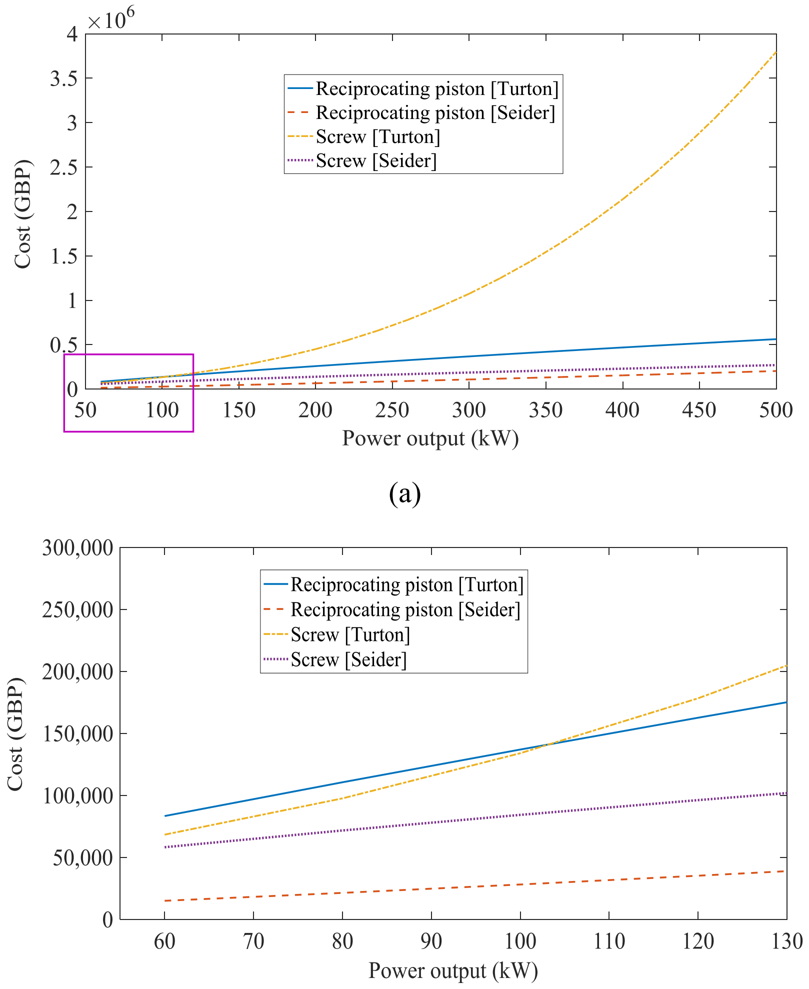

(a)

(b)

Fig. 81: Large scale volumetric compressor cost comparison, using the module costing technique correlations.

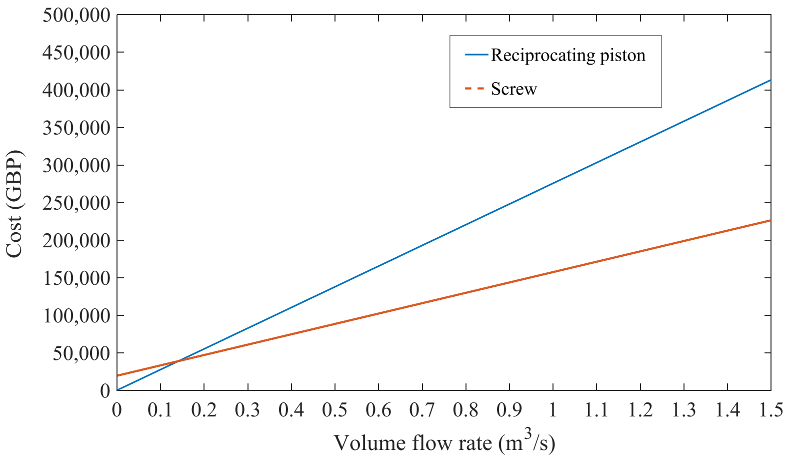

Fig. 82: Small-medium scale volumetric compressor cost comparison, using vendors' cost data.

6.3.3 System profitability analysis

The cost correlations presented in Section 6.3.2 will be used to obtain the TC, and SIC of the various optimised ORC engine configurations. For the optimised designs, a system profitability analysis is then performed, for a case study of an industrial commercial user based in the UK, where the ORC engines recover heat from the exhaust-gas stream of a stationary CHP-ICE.

To quantify the impact of the different ORC engine designs on the project whole life financial viability, two metrics have been evaluated: i) the discounted payback period (DPP); and ii) the net present value (NPV) of the ORCs, in an ICE-ORC CHP configuration. The methodology for calculating the aforementioned metrics is presented in Section 3.8.2 (Chapter 3). The cash-flows of any given design are estimated as the savings on the electricity bill of the user, on an annual basis, assuming that the additional electricity generated by the ORC is utilised by the user, displacing electricity purchase from the grid. No additional revenue streams are considered from potential sales to the grid or to other users in the proximity of the CHP facility. Half-hourly data for electricity prices, when purchasing from the grid, have been obtained for typical week days (WD) and weekend days (WE) of every month, for an industrial user, from Refs. [160,161], and have been previously presented in Section 3.8.2. Finally, annual operating and maintenance (O&M) costs of the ORC engine are considered. More details on the case study assumptions are presented in subsequent sections.

6.4 Optimisation

To quantify the impact of both the ORC thermodynamic operating points, and components selection and sizing, on the ORC engine power output and cost, three separate optimisation exercises have been performed: i) single-objective optimisation for maximum power output ($\dot{W}_{\mathrm{net}}$); ii) single-objective optimisation for minimum SIC; and iii) multi-objective optimisation for maximum power output and minimum SIC. Vector $\vec{X}$ contains all the decision variables, i.e. the set of variables the optimiser will alter, to minimise/maximise the objective function ($\vec{F}(\vec{X})$). For maximum power output optimisation, vector $\vec{X}$ contains six variables: i) the evaporating pressure P_{evap} [Pa]; ii) the condensing pressure P_{cond} [Pa]; iii) the working fluid mass flow rate $\dot{m}_{\mathrm{wf}}$ [kg/s]; iv) the superheating degree *SHD* [-], normalised over the maximum possible, given the heat-source inlet conditions to the cycle; v) the evaporator pinch point PP_{evap} [K]; and vi) the volume ratio of the expander r_{exp} [-]. When screw expander is used, the variable x_{exp} is defined instead of r_{exp}, which corresponds to the pressure ratio (PR) of the expander, normalised over the total PR in the ORC engine; it takes values between 0 and 1, and indicates the percentage of the expansion taking place in the first stage of the expansion, with the remaining being done in a second stage (if any). The decision variables vector for maximum power output is presented below:

$$\vec{X} = [P_{\mathrm{evap},}\, P_{\mathrm{cond},}\, \dot{m}_{\mathrm{wf},}\, SHD,\ PP_{\mathrm{evap},}\, r_{\mathrm{exp}}(\mathrm{or}\ x_{\mathrm{exp}})] \tag{177}$$

For the multi-objective and minimum SIC optimisation, the decision variables vector contains additional variables related to the specific system components design and geometry. The additional decision variables are as follows: i) $flag_1/flag_2$ to indicate the type of HEX, for the evaporator and the condenser, respectively; ii) velocity of the working fluid and the heat source in the DPHEX evaporator ($u_{\mathrm{wf,evap}}^{\mathrm{DP}}$ and $u_{\mathrm{hs,evap}}^{\mathrm{DP}}$ [m/s]); iii) velocity of the working fluid and the cooling water in the DPHEX condenser ($u_{\mathrm{wf,cond}}^{\mathrm{DP}}$ and $u_{\mathrm{cw,cond}}^{\mathrm{DP}}$ [m/s]); iv) velocity of the working fluid and the heat source in the PHEX evaporator ($u_{\mathrm{wf,h}}^{\mathrm{PH}}$, $u_{\mathrm{wf,ev}}^{\mathrm{PH}}$ $u_{\mathrm{wf,sh}}^{\mathrm{PH}}$and $u_{\mathrm{hs,h}}^{\mathrm{PH}}$, $u_{\mathrm{hs,ev}}^{\mathrm{PH}}$, $u_{\mathrm{hs,sh}}^{\mathrm{PH}}$ [m/s]); v) velocity of the working fluid and the cooling water in the PHEX condenser ($u_{\mathrm{wf,dsh}}^{\mathrm{PH}}$, $u_{\mathrm{wf,c}}^{\mathrm{PH}}$ and $u_{\mathrm{cw,dsh}}^{\mathrm{PH}}$, $u_{\mathrm{cw,c}}^{\mathrm{PH}}$ [m/s]); vi) plate width for the evaporator and the condenser ($W_{\mathrm{h}}^{\mathrm{PH}}, W_{\mathrm{ev}}^{\mathrm{PH}}, W_{\mathrm{sh}}^{\mathrm{PH}}, W_{\mathrm{dsh}}^{\mathrm{PH}}$and $W_{\mathrm{c}}^{\mathrm{PH}}$ [m]); vii) plate corrugation depth for the evaporator and the condenser ($z_{\mathrm{h}}^{\mathrm{PH}}, z_{\mathrm{ev}}^{\mathrm{PH}}, z_{\mathrm{sh}}^{\mathrm{PH}}, z_{\mathrm{dsh}}^{\mathrm{PH}}$and $z_{\mathrm{c}}^{\mathrm{PH}}$ [m]); viii) corrugation angle for the evaporator and the condenser ($\beta_{\mathrm{h}}^{\mathrm{PH}}, \beta_{\mathrm{ev}}^{\mathrm{PH}}, \beta_{\mathrm{sh}}^{\mathrm{PH}}, \beta_{\mathrm{dsh}}^{\mathrm{PH}}$and $\beta_{\mathrm{c}}^{\mathrm{PH}}$ [°]); The differentiation of the velocities in the different sections of the PHEX are capturing the potential of different corrugation patterns, or number of plates in the various PHEX sub-sections. The decision variable vector for minimum SIC and multi-objective optimisation is presented below:

$$\vec{X} = [P_{\mathrm{evap},}\, P_{\mathrm{cond},}\, \dot{m}_{\mathrm{wf},}\, SHD,\, PP_{\mathrm{evap},}\, x_{\mathrm{exp}}, flag_1, flag_2, u_{\mathrm{wf,evap}}^{\mathrm{DP}}, u_{\mathrm{hs,evap}}^{\mathrm{DP}}, u_{\mathrm{wf,cond}}^{\mathrm{DP}}, u_{\mathrm{cw,cond}}^{\mathrm{DP}}, u_{\mathrm{wf,h}}^{\mathrm{PH}}, u_{\mathrm{wf,ev}}^{\mathrm{PH}}, u_{\mathrm{wf,sh}}^{\mathrm{PH}}, u_{\mathrm{hs,h}}^{\mathrm{PH}}, u_{\mathrm{hs,ev}}^{\mathrm{PH}}, u_{\mathrm{hs,sh}}^{\mathrm{PH}}, u_{\mathrm{wf,dsh}}^{\mathrm{PH}}, u_{\mathrm{wf,c}}^{\mathrm{PH}}, u_{\mathrm{cw,dsh}}^{\mathrm{PH}}, u_{\mathrm{cw,c}}^{\mathrm{PH}}, W_{\mathrm{h}}^{\mathrm{PH}}, W_{\mathrm{ev}}^{\mathrm{PH}}, W_{\mathrm{sh}}^{\mathrm{PH}}, W_{\mathrm{dsh}}^{\mathrm{PH}}, W_{\mathrm{c}}^{\mathrm{PH}}, z_{\mathrm{h}}^{\mathrm{PH}}, z_{\mathrm{ev}}^{\mathrm{PH}}, z_{\mathrm{sh}}^{\mathrm{PH}}, z_{\mathrm{dsh}}^{\mathrm{PH}}, z_{\mathrm{c}}^{\mathrm{PH}}, \beta_{\mathrm{h}}^{\mathrm{PH}}, \beta_{\mathrm{ev}}^{\mathrm{PH}}, \beta_{\mathrm{sh}}^{\mathrm{PH}}, \beta_{\mathrm{dsh}}^{\mathrm{PH}}, \beta_{\mathrm{c}}^{\mathrm{PH}}] \tag{178}$$

The objective functions and the optimisation constraints are listed below:

Maximise: $\frac{\{\dot{W}_{\mathrm{net}}\}}{\vec{X}}$, (179)

Minimise: $\frac{\{SIC\}}{\vec{X}}$, (180)

Multi-objective optimisation: $\frac{\{\dot{W}_{\mathrm{net}}, SIC\}}{\vec{X}}$. (181)

Subject to:

$$P_{\mathrm{cond}} < P_{\mathrm{evap}} < P_{\mathrm{crit}} \, , \tag{182}$$

$$PP_{\mathrm{min}} \leq PP \, , \tag{183}$$

$$0 \leq SHD \leq 1 \, , \tag{184}$$

$$T_4 \leq T_{4\mathrm{v}} \, , \tag{185}$$

$$T_{\mathrm{lim}} \leq T_{\mathrm{hs,out}} \, , \tag{186}$$

$$P_{\mathrm{drp}} \leq P_{\mathrm{lim}} \, . \tag{187}$$

Eq. 182 describes the constraints related to the pressure levels of the cycle; the pressure at the condenser must be lower than the evaporating pressure, which should be lower than the working fluid critical pressure, for the subcritical ORC assumption to be valid. Eq. 183 ensures that the minimum pinch point (PP) of the HEXs is not violated. Eq. 184 is the normalised superheating degree restricted between 0 and 1; it is expressed as the ratio of the superheating degree the cycle actually operates at, over the maximum allowable, accounting for the PP in the evaporator. The next constraint (Eq. 185) ensures that the temperature after the expansion is higher than the saturation condensing temperature, while Eq. 186 has been added to limit the exhaust-gas leaving temperature from the evaporator, to minimise the risk of reaching the dew-point temperature. Studies in the literature report typical exhaust-gas dew point temperature of approximately 50-70 °C (323-343 K) [179,180]. Typical CHP units with natural gas ICE cool the exhaust gases down to approximately 100-120 °C (373-393 K) [9,30] to ensure that no condensation occurs. In this study for the design of the ORC engine, the heat carrier fluid temperature exiting the evaporator (T_{lim}) has been restricted to 80 °C (353 K), which is a temperature well above the reported dew point levels and close to the current state of the art figures reported in CHP systems design. In Eq. 187 the pressure drop in the evaporator HEX is restricted to a maximum of 60 kPa on the heat-source side, to avoid giving rise to backpressure antagonistic effects on the ICE, and to 100 kPa on the cooling water circuit, in line with typical values available in the literature.

The aforementioned optimisation framework is applied on an ICE-ORC CHP application, where the ORC engine recovers heat from the exhaust-gas stream of a CHP-ICE unit. The CHP-ICE is an 1500 $\mathrm{kW_{el}}$ engine provided by ENER-G [9]. Finally, a summary of the optimisation variables specification is presented in Table 9.

Table 13: Summary of the ORC engine specification for the thermoeconomic optimisation.

Parameter	Value	Parameter	Value
PP_{cond} (K)	10	$P_{\mathrm{evap,max}}$ (kPa)	0.95 P_{crit}
PP_{evap} (K)	5-30	$r_{\mathrm{exp}}/x_{\mathrm{exp}}$ (-)	8-18 / 0-1
$T_{\mathrm{cw,in}}$ (K)	288	T_{lim} (K) (for heat source)	353
$T_{\mathrm{cw,out}}$ (K)	298	W_{p} (m)	0.1-1
$\dot{m}_{\mathrm{hs}}$ (kg/s)	2.16	β *(rad)*	$\frac{\pi}{6}$ - $\frac{\pi}{3}$
$T_{\mathrm{hs,in}}$ (K)	682	z (m)	0.006-0.02
$P_{\mathrm{con,min}}$ (kPa)	30	u_{hs} (m/s)	3-25
u_{cw} (m/s)	0.4-5	u_{wf} (m/s)	0.2-6

The single-objective optimisation problem was solved using the *multistart* structure in MATLAB© [128], which calls the *fmincon* solver from multiple starting points, aiming to identify the local optima, which are closer to the global optima of the system. The multi-objective optimisation problem was solved using the *gamultiobj* structure, which uses the NSGA-II genetic algorithm. In Table 14, the settings of the genetic algorithm used are presented. More details on the optimisation methodology deployed in this thesis have been presented in the methodology chapter (Chapter 3).

Table 14: Summary of the genetic algorithm solver settings.

Parameter	**Value**	**Parameter**	**Value**
Population size	500	Generations	5000
Crossover Fraction	0.8	Mutation type	Gaussian (scale = 1 & shrink = 1)
Pareto Fraction	0.35	Crossover function	Crossover intermediate

6.5 Thermoeconomic optimisation results – I: Single-objective optimisation

6.5.1 Maximum power optimisation

The ORC engines power output, when the system is optimised for maximum power is presented in Fig. 83 a for piston expanders, and Fig. 83b for screw machines. The best performing working fluids operating with piston expanders, are pentane (110 kW), toluene and R1233zd (102 kW), hexane (93 kW), and butane (90 kW). On the same graph the estimated SIC values for different HEX configurations are presented. The SICs vary significantly even for ORC engines with similar power outputs. The SIC of R1233zd is approximately 2,000 GBP/kW, whilst the SIC of pentane is approximately 2,500 GBP/kW, while hexane and toluene present SICs of 6,000-7,500 GBP/kW. The reason for these variations are related to the optimum thermodynamic cycle for each one of those fluids, and its impact on the components design. Fluids with low LMDT, and PP at the evaporator (Fig. 84), require high heat transfer areas, increasing the HEX costs. This is the case for toluene, for which the optimised cycle has the lowest temperature difference between the heat source and the working fluid, among all candidate fluids investigated. Additionally, the operating temperature and pressure for pentane result in higher volume flow rates in the system than R1233zd (for similar power output), increasing the expander cost.

The temperature at the condenser also impacts the condenser HEX size and cost. In the maximum power output optimisation, the optimiser seeks to maximise the PR over the expander i.e. increase the evaporator pressure (without violating the subcritical ORC operation) and reduce the condenser pressure without violating the minimum PP at the condenser. The cooling circuit operates at 15-25℃, so working fluids with high condensation temperature at low condenser pressures, operate with small temperature difference across the condenser, increasing the HEX area requirements condensing pressure. A case in the point is comparing the heat transfer areas of toluene, and butane, which generate very similar power output.

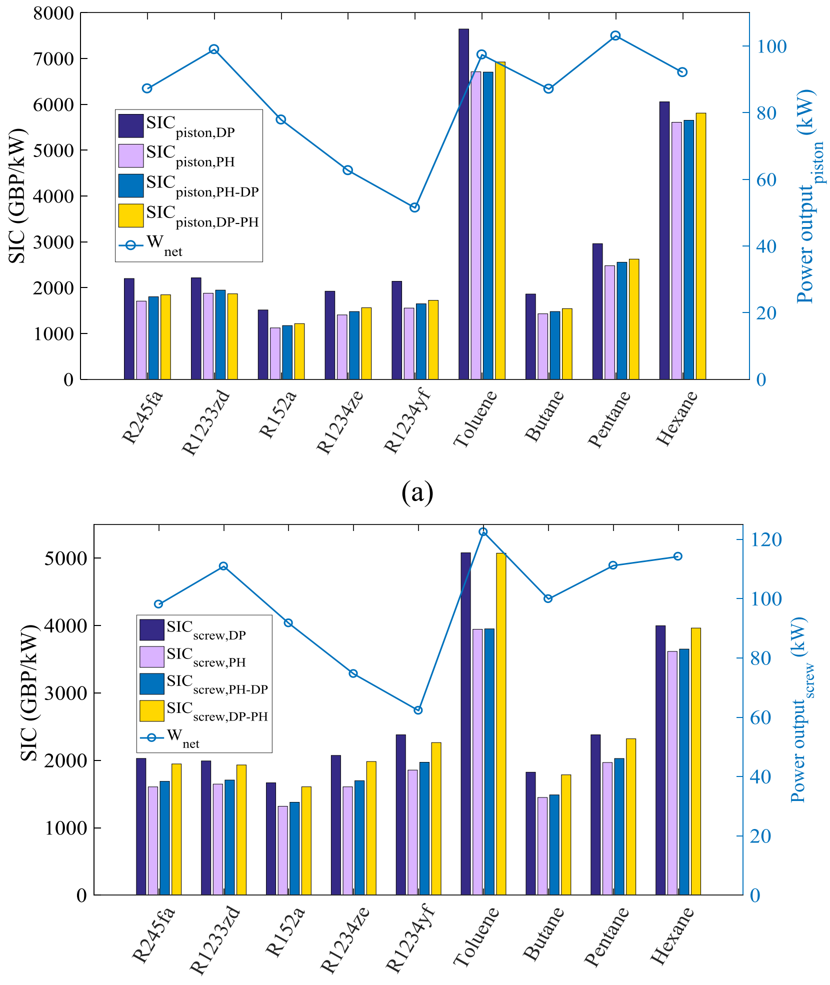

(a)

(b)

Fig. 83: SIC for ORC engines optimised for maximum power output with: a) piston expander, and b) screw expander. Subscript ‘DP’ corresponds to all HEXs in the system being DPHEX, ‘PH’ corresponds to all HEXs in the system being PHEX, ‘PH-DP’ to PHEX evaporator and DPHEX condenser, and ‘DP-PH’ to DPHEX evaporator and PHEX condenser.

For all fluids investigated, the highest SIC is recorded when DPHEXs are used for both the evaporator and the condenser HEXs, while the lowest SIC are reported when only PHEXs are deployed (Fig. 83). This is explained by looking at the HEX area requirements for the different HEX designs in Fig. 84. Findings illustrate that the PHEXs heat transfer area requirements are 40-60% lower than the respective ones with DPHEX design, for the majority of fluid investigated. The results are aligned with the data reported in the literature that PHEX design is more compact than DPHEX or shell-and-tube configurations. The SIC of ORC engines with PHEX evaporator and DPHEX condenser are slightly higher than the all PHEX designs, followed by ORC engines with DPHEX evaporators and PHEX condensers. The findings reveal the impact of the HEX configuration and size, on the overall system SIC, and thus its financial viability.

Similarly, the ORC engine power output and SIC for all working fluids for optimising for power with screw expanders, are presented in Fig. 83b. For all fluids investigated the optimiser selected two-stage expansion, aiming to maximise the screw expander isentropic efficiency. In contrast to the piston expander operation, the screw expanders' isentropic efficiency reduces significantly for volume ratios (VRs) higher than 7, therefore for the ORC engine to operate at high PRs the optimiser selects a two-stage expansion configuration. The best performing fluids are consistent in both designs, but ORC engines with screw expanders generate slightly higher power output than the designs with piston devices. ORC engines with screw expanders and toluene generate 123 kW, with hexane 118 kW, and with pentane and R1233zd, 115 kW. The increase in power output in this case ranges between 5-18%, when compared to ORC with pistons, but the respective SICs either stay constant or reduce slightly. The only exemption is toluene, for which the SIC reduces by 27%. As it will be discussed later this is attributed to the volume flow rate of toluene in the two-stage screw expanders.

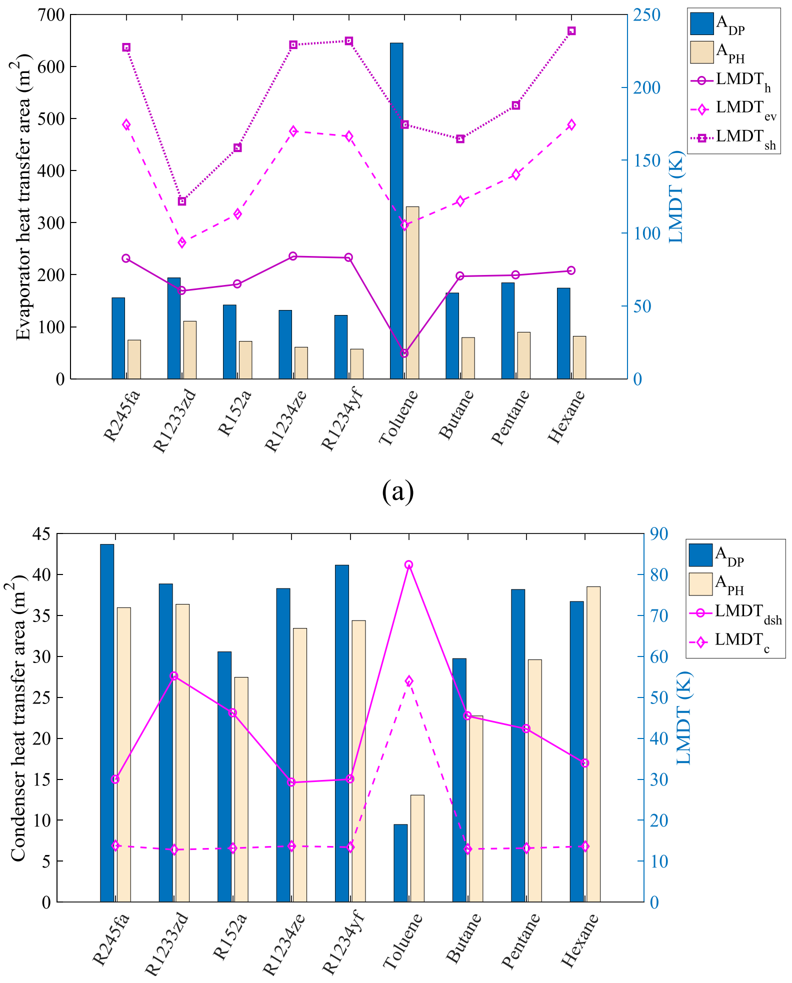

(a)

(b)

Fig. 84: HEX area breakdown comparison for ORC engines optimised for maximum power output: a) evaporator, and b) condenser, with piston expandes. Findings are representative of the HEX area breakdown in ORC engines with screw expanders.

The absolute costs of each component are illustrated in Fig. 85, for DPHEXs, and Fig. 86, for PHEXs, with piston and screw expanders. The expander costs dominate the total purchase costs at high temperatures (high PRs), amounting to approximately 50% of the ORC unit purchase cost (e.g. toluene and pentane TC). The evaporator is the second most expensive component (up to 30% of the total), followed by the condenser and the pump. These findings are in agreement with the cost data reported for a heat recovery ORC facility in Belgium of 375 kWe in Ref. [14]. When the oil circuit and installation costs are excluded, the expander and the pump are responsible for approximately 60% of the investment cost, followed by the HEXs [14]. For lower power outputs (low temperature and PRs) the expander costs are comparable to the cost of the condenser and the evaporator (for fluids such as R152a, R1234ze and butane), corresponding to 30-40%, 15-20%, and 30-50%, respectively.

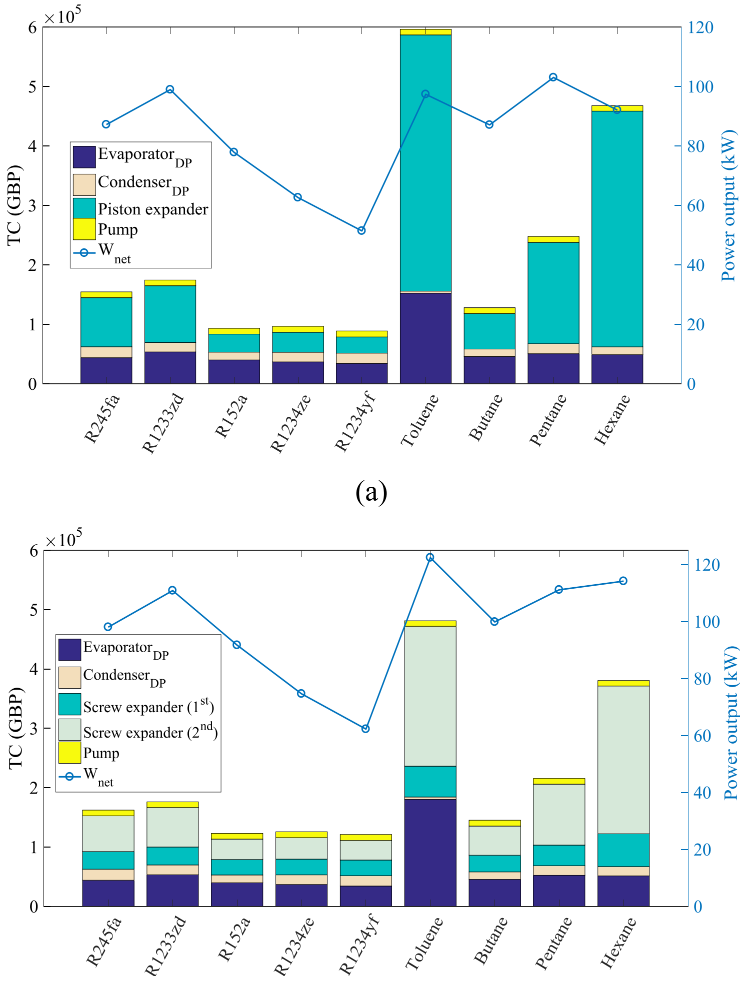

(a)

(b)

Fig. 85: ORC engine components TC breakdown for a system optimised for maximum power output with: a) piston expander, and b) screw expander. Results presented are for DPHEX design of the evaporator and the condenser.

Based on these findings, it is concluded that for low-medium temperatures, and low pressures, the cost of the HEXs is significant, therefore it is of high importance to design them to maximise the heat transfer. In this study, DPHEXs and PHEXs have been used for both the evaporator and the condenser, so the results might vary in case other types of HEXs are used. For higher power outputs, on the contrary, the selection and design of the expander and then of the evaporator is key factor for reducing the ORC costs. Finally, in should be noted that the percentage cost breakdown over the various components is very similar in the cases where a combination of DPHEX and PHEX is used.

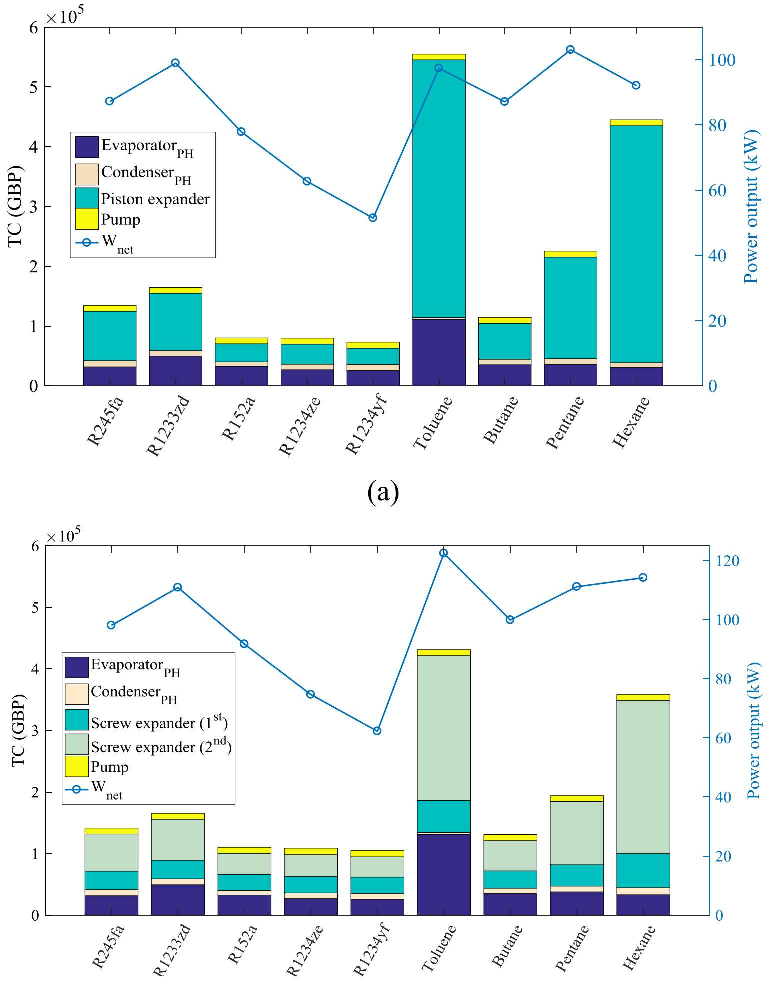

(a)

(b)

Fig. 86: ORC engine components TC breakdown for a system optimised for maximum power output with: a) piston expander, and b) screw expander. Results presented are for PHEX design of the evaporator and the condenser.

6.5.2 Minimum specific investment cost optimisation

The ORC engine power output and SIC for systems optimised for minimum SIC are presented in Fig. 87, for engines with piston and screw expanders. The trend in terms of the best performing fluids is similar to the results obtained in the maximum power output analysis, although the absolute values of power output and SIC vary significantly. In general, the designs for minimum SIC generate less power than the designs for maximum power output by 15-50%, depending on the fluid, considering how to reduce the components' size. Looking at the ORC with piston expander, the best performing fluid is butane with 65 kW of power output, and SIC equal to 1,200 GBP/kW. Pentane and R1233zd have similar

SICs of approximately 1,350 GBP/kW, generating 50-60 kW. These SICs are 30-35% lower than those obtained for maximum power output optimisation.

The power output of the ORC system with screw expanders is higher than the respective one with piston expander (Fig. 87b). The best performing ORC engine with piston expander generates 65 kW of power output with butane, while the same fluid operating with screw expander generates up to 90 kW. However, the higher power output results as expected in higher total CAPEX for the ORC with screw expander than in the case with piston expander. The SICs of the former (ORC with screw) range between 1,400 and 2,100 GBP/kW, whilst these correspond to 900-1,700 GBP/ kW for the latter (ORC with piston).

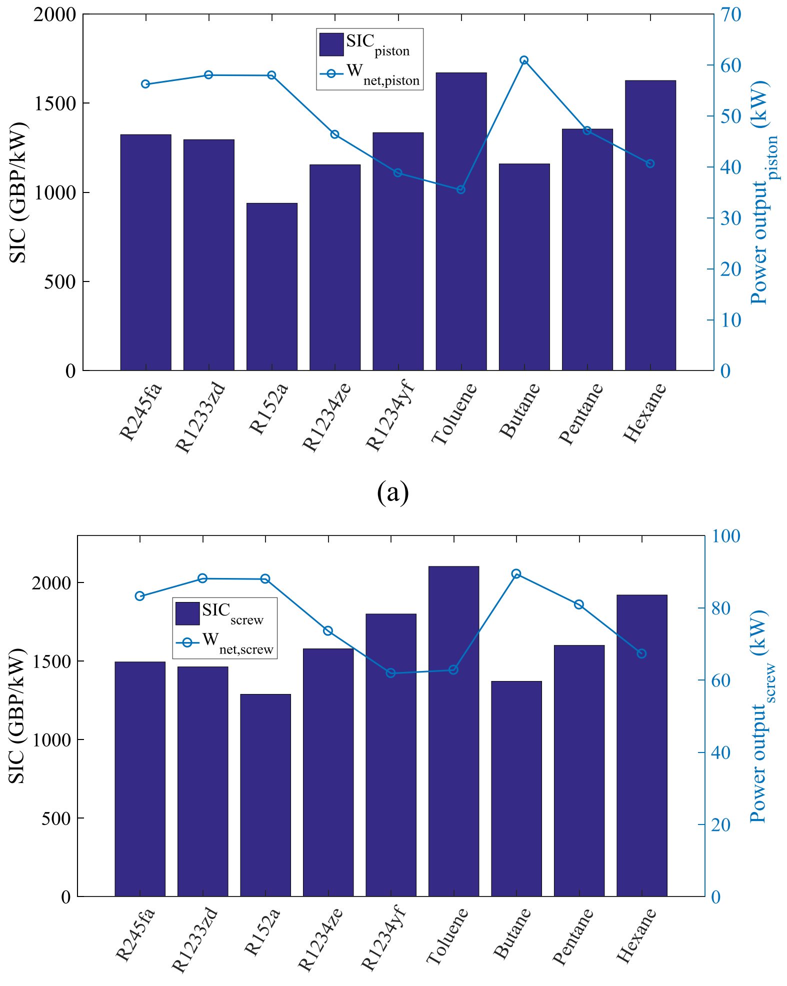

(a)

(b)

Fig. 87: SIC for ORC engines optimised for minimum SIC with: a) piston expander, and b) screw expander.

In all cases, the optimiser selected a PHEX design for the evaporator and a DPHEX for the condenser. In the case of the ORC engine with screw expander, the optimiser favours two-stage expansion, due to restrictions in the screw expander isentropic efficiency at high PR/VRs. The evaporator area requirements for the optimised ORC engines are presented in Fig. 88a. The evaporator area requirements for the optimum ORC with screw expander, is significantly higher than the respective one for piston expander for all fluids investigated. This is explained by the higher LMDT obtained in the ORC evaporator with piston, than with screw and to the fact that ORC engines with screw expanders generate more power (by 20-30%). Comparing these results to those obtained for maximum power output optimisation, the heat transfer areas are significantly lower. This is attributed to the fact that the optimiser aims to identify designs which satisfy low SIC, which result in HEX designs with higher PP. The condenser heat transfer requirements are also presented in Fig. 88b for both ORC engines. The requirements for the ORC engines with screw expander are higher than the respective ones for the ORC engine with piston, but the differences are smaller than those recorded for the evaporator HEX.

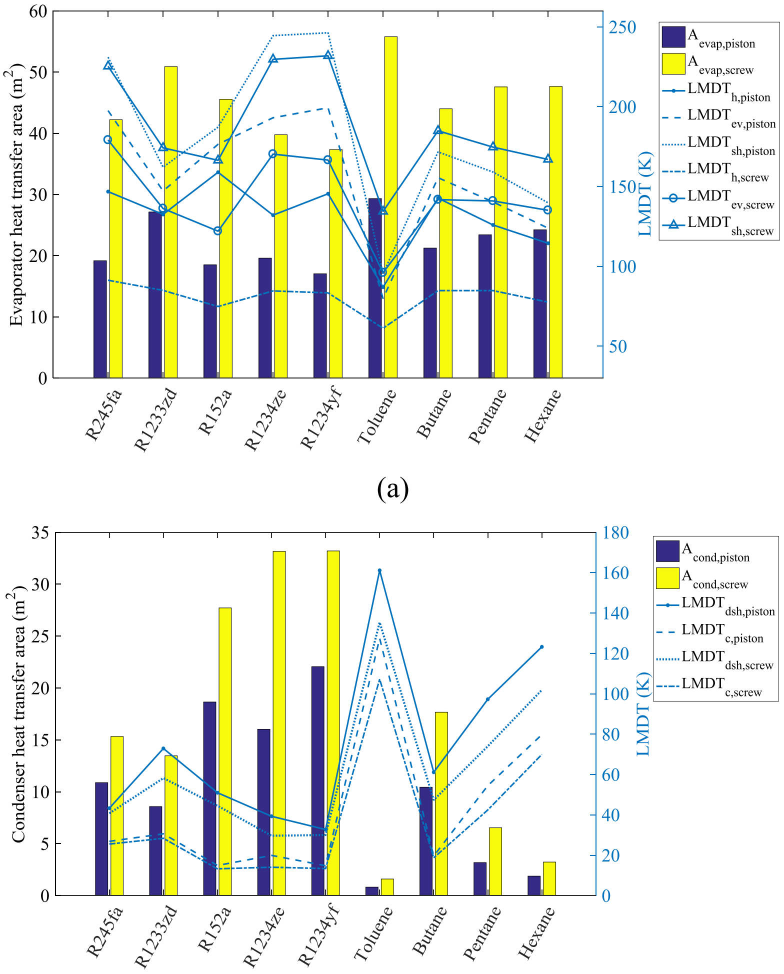

(a)

(b)

Fig. 88: HEX area breakdown comparison for ORC engines optimised for minimum SIC: a) evaporator, and b) condenser, with piston and screw expanders.

For the PHEX evaporator design, the heat-source maximum pressure drop constraint is active, while in the DPHEX condenser the pressure drop on the water side is close to the maximum allowable by the constraints. The PHEX evaporator corrugation pattern in this case, is the minimum to maximise heat transfer, while the corrugation angle (*β)* is around π/3. Additionally, the pressure at the condenser is higher than that recorded in the case of maximum power output design. This is in order to reduce the volume flow rate of the working fluid at the exit of the expander and subsequently reduce the expander cost. Higher exit temperature from the expander results in higher temperature difference between the cooling water and the working fluid, reducing the heat transfer area requirements.

The TC cost of ORC engines optimised for minimum SIC is presented in Fig. 89 , for piston and screw expander designs. The TC for ORC engines with pistons, optimised for minimum SIC are almost 50% of the TC obtained when optimising for maximum power output, while the SIC reduces on average by 35%, with some fluids such as toluene the SIC reduction reaching 73%. There is however a respective power output reduction by 15-30%, with the exemption of the power output of toluene and pentane that present a reduction of 45-50%. The TC of ORC engines with screw expanders are almost double the cost of the respective ones with piston (Fig. 89b), although the power output difference between the two configurations is in the range of 20-30%. Finally, the piston expander is responsible for 35-55% of the total ORC engine cost, depending on the fluid investigated, followed by the evaporator HEX and the condenser (with 20-50%). In the case of ORC engines with screw expander, due to the two-stage expansion two screw expanders are required, which increase their contribution to the total cost of the system up to 66% (for fluids such as toluene).

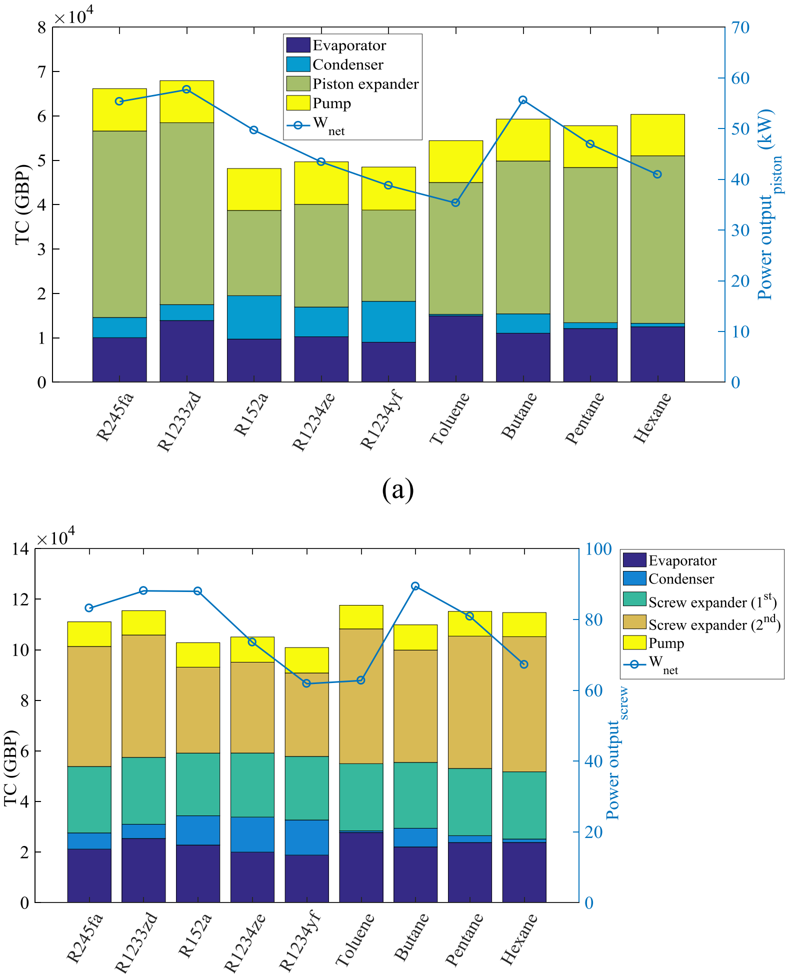

(a)

(b)

Fig. 89: ORC engine components CAPEX breakdown for a system optimised for minimum SIC with: a) piston expander, and b) screw expander.

6.6 Thermoeconomic optimisation results – II: Multi-objective optimisation

The Pareto front of the multi-objective optimisation for all fluids investigated, with piston expanders, is presented in Fig. 90, along with the single-objective optimisation results for: i) maximum power output and ii) minimum SIC. The SIC increases while moving towards low power outputs and low efficiency (reaching 3,000 GBP/kW), while it is minimised for power output in the range of 50-60 kW, reducing to 1,000 GBP/kW (depending on the working fluid selection). While the power output increases from 60 kW to 100 kW the SIC increases up to 2,500 GBP/kW, with some exemptions of extreme SIC values reaching 8,000 GBP/kW recorded for toluene, when the ORC design is optimised for maximum power output. This is attributed to the very low PP observed in the toluene ORC evaporator, as discussed in previous sections, which increases the heat transfer area requirements dramatically, and subsequently the HEXs cost. In general, at high power outputs the ORC engine cost increases, because of the higher pressure/temperature in the system, the larger heat transfer area requirements due to low PP, along with high volume flow rates. This cost increase cannot be offset by the increase in power output, thus the SIC increases. Results highlight that the best performing working fluids with regards to power output, such as R1233zd or Pentane (up to 100 kW), have higher SICs than fluids such as R152a (with up to 65 kW), when multi-objective optimisation is used. These findings highlight, that depending on the power output range and the project priorities the best performing fluids may vary.

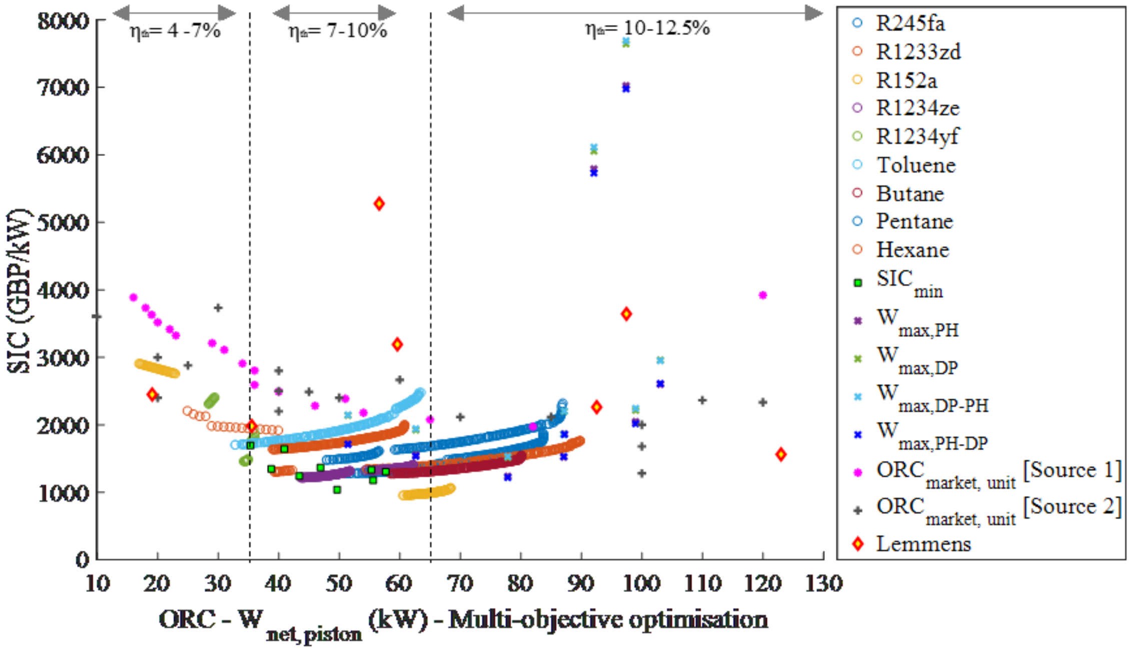

Fig. 90: ORC engines SIC and power output with piston expander: i) Pareto front of optimum ORC engine designs, using multi-objective optimisation; ii) ORC engines optimised for minimum SIC; iii) ORC engines optimised for maximum power output; and iv) ORC engines market prices. Source 1 refers to prices collected from ORC vendors quotations, Source 2 to the data provided in Ref. [120] and Lemmens' data are obtained from Ref. [117]. The thermal efficiency figures refer to the ORC engines designs obtained in this work.

On the same graph, ORC engine market prices are plotted using the data provided in Ref. [120] and from quotes collected from ORC vendors, along with the SIC cost data presented by Lemmens [117] for waste heat recovery applications, in similar power range. It should be noted that the latter data have been obtained from various studies in the literature, which also used cost correlations to predict the ORC engine SIC, rather than from actual cost data from real applications. These also include waste heat recovery from a range of applications, such as aerobic plant waste heat recovery or transracial CO_2 cycles. By comparing the optimisation results of this work, to the real engine cost data, it is noted that there is a very good agreement with the predicted values in the range of 50-90 kW power output, while for lower power output the model underestimates the cost of the ORC engine by 10-30% depending on the power output and the data source. On the contrary, for power output exceeding 100 kW the model overestimates the SIC of ORC engines by 8% approximately (excluding the extreme SIC figures noted for toluene), being on the conservative side of the cost estimates.

Some discrepancies recorded between the model cost estimates and the market prices are attributed to the following reasons: i) the costing model developed in this thesis is based on adding the individual components cost to obtain the ORC engine total cost, excluding potential profit margins added to the price of the unit from the ORC vendors; ii) the SICs appear to be lower than the market prices because also the modelling results are optimised designs, for the expander and HEX simultaneously; iii) the ORC engines for stationary power generation available in the market use different type of expanders (not piston expanders); and iv) the ORC unit market prices may refer to different ORC engine architectures, and system configurations, to the subcritical non-recuperative ORC engine, considered in this work. Therefore, some deviations in the cost predicted from the model were expected.

Looking at the ORC engine design when multi-objective optimisation is used, the system selects the evaporator pressure to be lower than the maximum power output results, in order to increase the LMDT of the heat-source and the working fluid, and accommodate smaller HEX heat transfer areas. Additionally, the pressure at the condenser is higher than in the designs for maximum power output. This is in order to reduce the volume flow rate at the exit of the expander and subsequently reduce the piston expander cost. It is also revealed that for most fluids investigated, the optimum evaporator architecture is PHEX while for the condenser is the DPHEX design.

Results also highlight that there is a region of ORC engine power output from 70 kW to 90 kW approximately, where the power output increases by almost 30% but the SIC increases by only 10%, indicating that the high potential of designing ORC engines with these capacities. On the contrary, for ORC engines with power output lower than 40 kW, the SIC increases by up to 40%.

The multi-objective optimisation results (Pareto front) for ORC engines with screw expanders, are presented in Fig. 91, for all fluids investigated. The single-objective optimisation results are also illustrated for maximum power output and minimum SIC analyses. The SIC trend is similar to that recorded for ORC engines with piston expanders, although the absolute values of SIC and power output vary. For power output between 30-45 kW the SIC increases to approximately 2,800 GBP/kW. While the power output increases from 45 to 90 kW, the SIC reduces down to 1,500 GBP/kW (for the best performing fluids). It is noted that moving to power output higher than 100 kW results in an increase of the SIC up to 2,000-5,000 GBP, depending on the fluid investigated. Looking at the minimum SIC results, the lowest SICs achieved are in the range of 1,400-1,500 GBP/kW for power outputs of approximately 88-92 kW. On the contrary, when the ORC engine design is optimised for power output, without considering the impact of the design on the engine cost, although the power output increases to 95-125 kW, the SIC varies from 1,700 up to 5,500 GBP/kW. The multi-objective optimisation results reveal that there is a range of power output between 75 to 100 kW, for which although power output increases by 33%, the SIC increases only by 9%, highlighting the potential of those ORC in terms of the project financial viability. In terms of the best performing fluids based on the multi-objective optimisation, these are pentane, and R1233zd, followed by R245fa, hexane and butane.

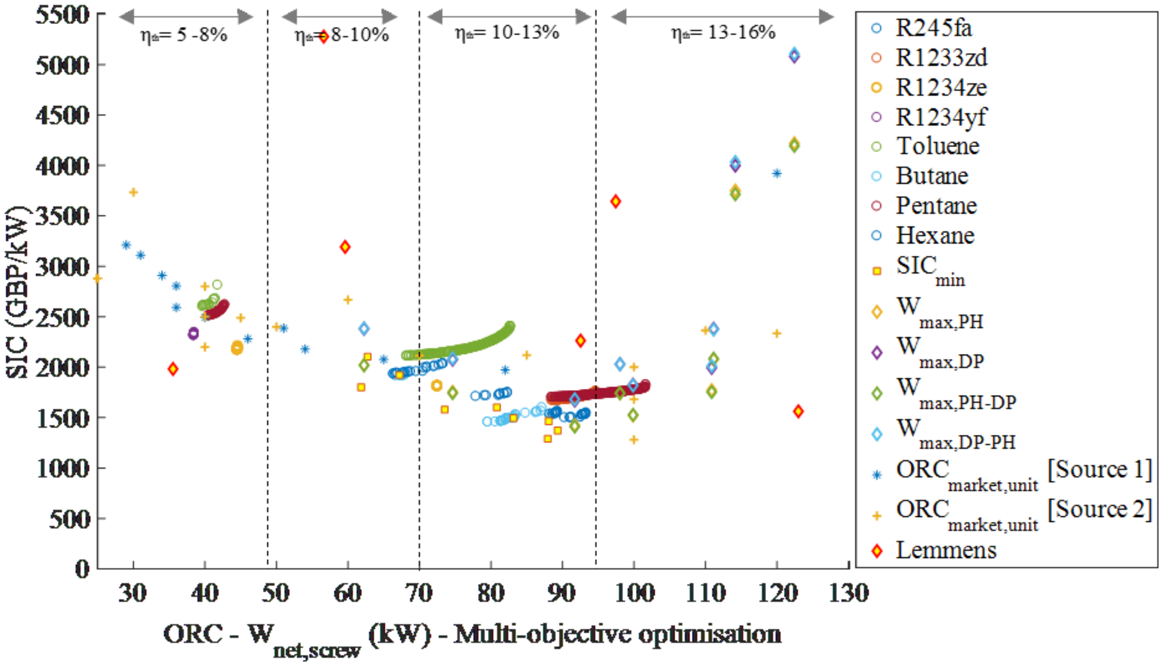

Fig. 91: ORC engines SIC and power output with screw expander: i) Pareto front of optimum ORC engine designs, using multi-objective optimisation; ii) ORC engines optimised for minimum SIC; iii) ORC engines optimised for maximum power output; and iv) ORC engines market prices. Source 1 refers to prices collected from ORC vendors' quotations, Source 2 to the data provided in Ref. [120], and Lemmens' data are obtained from Ref. [117]. The thermal efficiency figures refer to the ORC engines designs obtained in this work.

On the same figure, prices of ORC engines available on the market, along with other findings in the literature as reported by Lemmens [117] are also presented. The costing model for the ORC engines with screw expanders have a good match to the cost data available in the market, sitting on the medium range of the price-range. The SICs appear to be lower than the market prices in some cases because these results are optimised designs, for the expander and HEX simultaneously. The better match is attributed to the fact that there are ORC engines on the market that operate with screw expanders, whilst ORC engines for stationary applications with piston expanders are not commercially available.

6.7 Thermoeconomic optimisation results – III: Financial analysis

An economic analysis for all working fluids investigated has been performed aiming to evaluate how different ORC engine designs, impact the project profitability. The ORC engines optimised for maximum power output are compared to those optimised for minimum SIC, for a case study of energy intensive buildings in the UK, where an ICE-CHP 1500 is installed. The system is assumed to operate for 8,000 hours/year at its design capacity (100% loaded), with annual O&M costs equal to 1.5% of the ORC engine and installation costs, as per Ref. [53]. The ORC engine total installation cost is estimated by allowing an additional 20% margin to the engine costs estimated in the previous sections, in line with the figures reported in Ref. [120]. The ORC engines DPPs, and NPV are calculated assuming a range of interest rates from 5% to 10%, based on a range of interest rates provided in the literature [24,53,120,181]. The electricity prices used to estimate the annual savings are based on the forecasted 2019 electricity prices for industrial users in the UK [25]. The profile of the electricity prices has been previously presented in Section 3.8.2. Finally, no subsidies for the system CAPEX have been considered.

The DPP and NPV for ORC engine with piston and screw expander are presented in Fig. 92, when the systems are optimised for minimum SIC. Similarly, the DPP and NPV for ORC systems optimised for maximum power output are presented in Fig. 93. For all fluids and systems investigated, although the high power output engines have high NPVs, these designs come at the cost of high DPP. On the contrary, ORC engines optimised for minimum SIC present NPVs which are 25-35% lower than those obtained for maximum power output optimisation, but also have the lowest DPPs varying between 2.8-4 years. This highlights that depending on the interests of the project key holders, designs with higher upfront cost and high DPP, but high annual earnings may or may not be preferred, over ORC engine designs with low upfront cost and low DPP, but low earnings over the project lifetime.

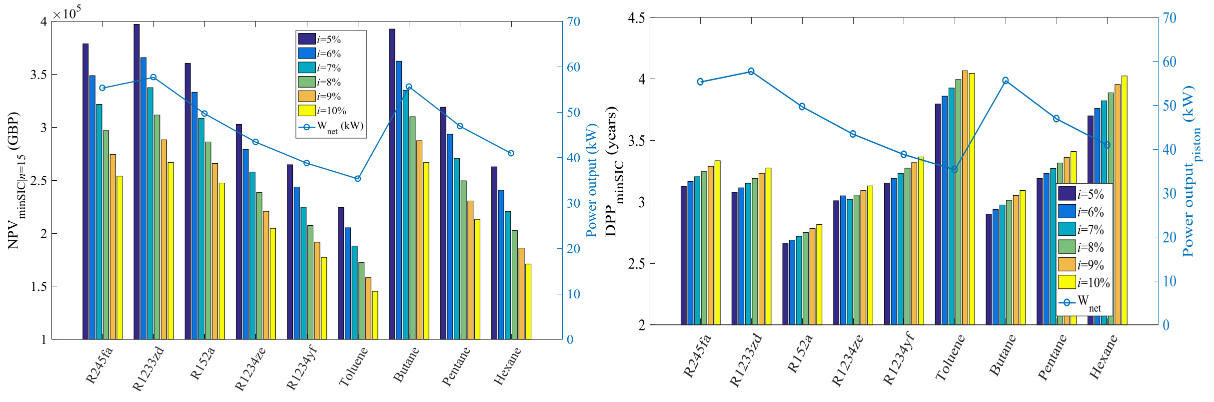

(a) (b)

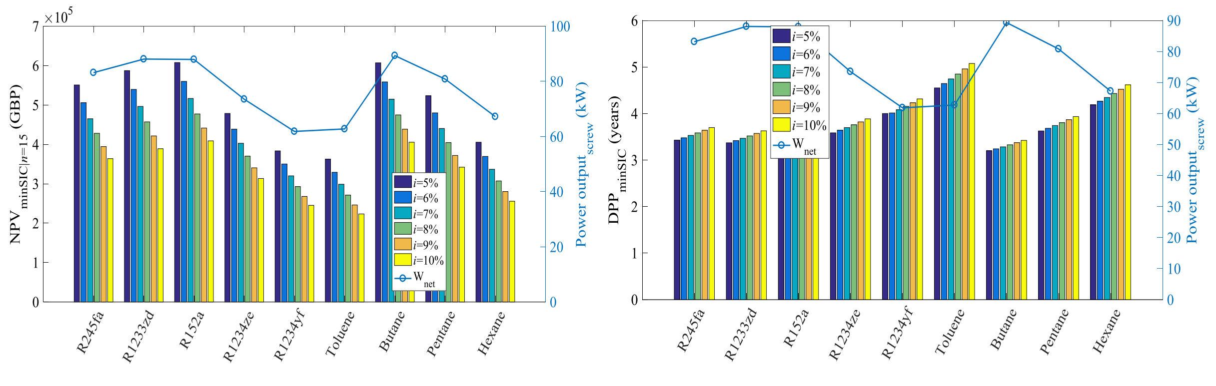

(c) (d)

Fig. 92: Profitability indicators for optimum ORC engines designed for minimum SIC: a) NPV and b) DPP with piston expanders; c) NPV and d) DPP with screw expanders.

The impact of the discount rate variation on the DPP is moderate; an increase of the discount rate from 5% to 10% (double) results in an increase of the DPP by only 5-7%. On the contrary, the increase of the discount rate has significant impact on the system NPV; while the interest rate increases from 5% to 10%, the NPV decreases by up to 30-40%. Overall the ORC engines with screw expanders optimised for maximum power, have slightly lower DPPs than those recorded for piston expanders (with the exemption of fluids such as toluene and hexane). On the contrary, when the objective of the optimisation is to minimise SIC, ORC engines with piston expanders perform better, achieving DPPs of 2.8-4 years.

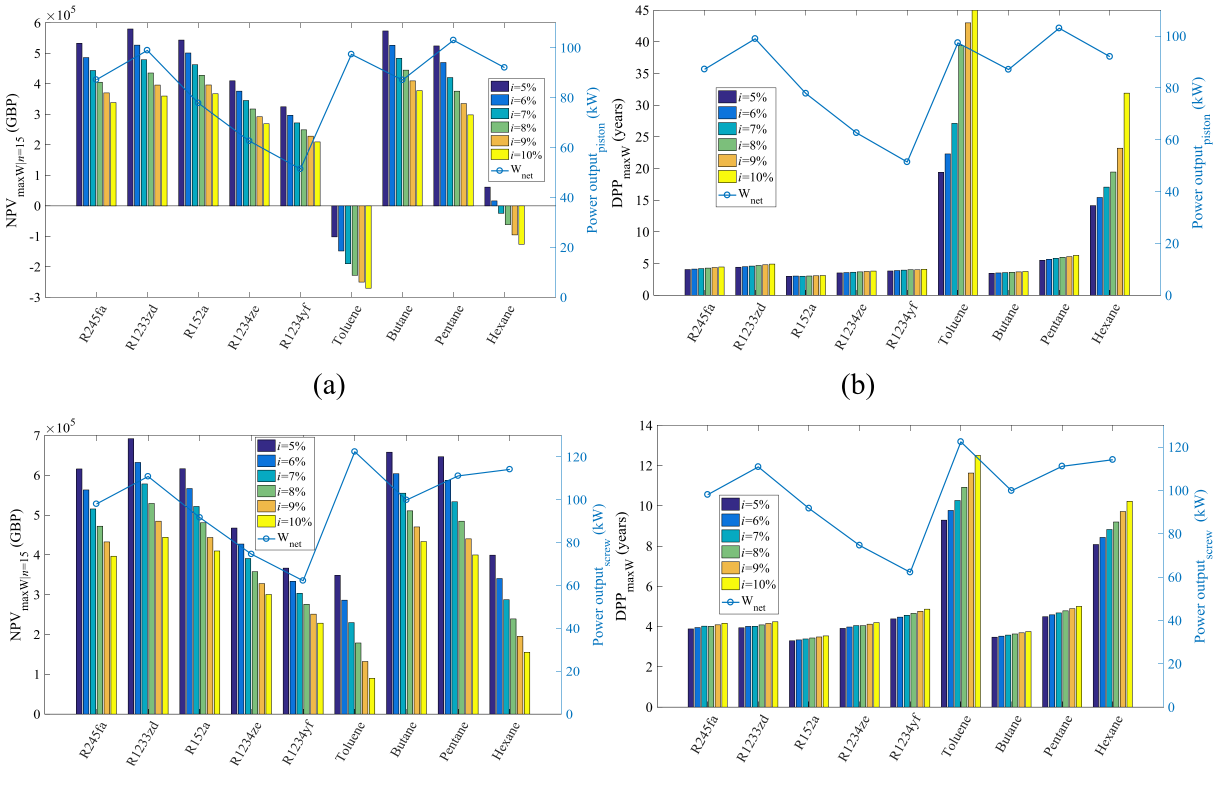

(a) (b)

(c) (d)

Fig. 93: Profitability indicators for optimum ORC engine designed for maximum SIC: a) NPV and b) DPP with piston expanders; c) NPV and d) DPP with screw expanders.

When evaluating the profitability of the ORC systems, fluids such as R152a and butane stand out as a good combination of resultant DPP and NPV, for ORC engines with both screw and piston expanders. These fluids although did not stand out for the highest power output or minimum SIC, present very good performance from a projects' profitability analysis perspective. This highlights that other optimisation objectives such as minimising DPP, or aiming for specific NPVs (over a specified project lifetime) may be also suitable indicators for the ORC engines design. However, those indicators can only be defined when specific case studies are available, whilst the optimisation for maximum power output/minimum SIC can be performed in complete isolation of the exact application. The tool developed in this work is versatile, since it can be used by: i) designers to obtain the best ORC system configuration, design and sizing, given the heat-source conditions; and ii) developers to compare the performance and costs of different ORC engines sizes/designs to assist them in selecting the system that meets their specific key performance indicators (KPIs).

Finally, in Fig. 94, financial performance maps for ORC engines with piston expanders (Fig. 94a) and screw (Fig. 94b) expanders are presented, for engines designed for minimum SIC. As discussed, ORC engines with piston expanders have lower DPPs, but also lower NPV than ORC engines with screw machines. The maps reveal that engines with similar power output, can have a range of DPPs, and NPVs, depending on the components design and working fluids. A case in the point is that an ORC engine generating 60 kW, can be designed to have DPP of 3.6 years, but annual earnings of 275,000 (n = 15) GBP, whilst the same power output can be generated by an ORC engine designed for higher annual earnings of 320,000 GBP (n = 15), but at the cost of higher DPP of almost 4.5 years. (All maps are generated assuming the same utilisation of the system, same electricity prices, and interest rates). Findings therefore highlight that ORC engines design can be very versatile and capable of meeting various KPIs, on a project-by-project basis.

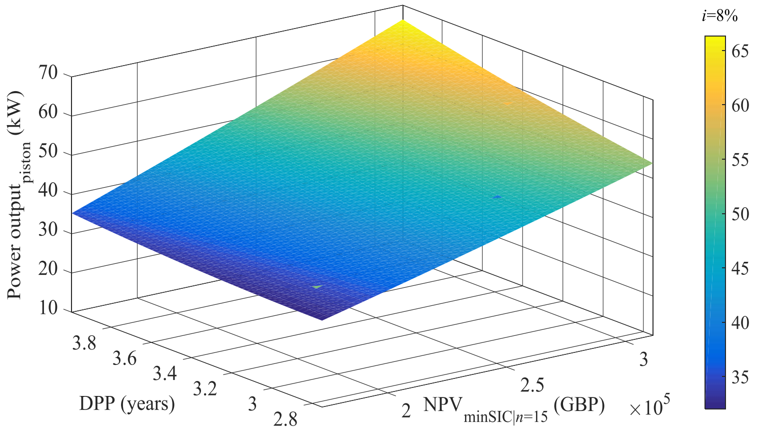

(a)

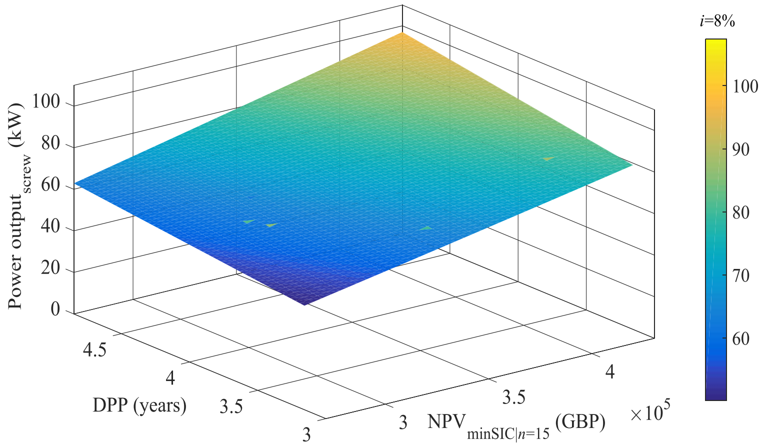

(b)

Fig. 94: Optimum ORC engine profitability maps for: a) piston expanders and b) screw expanders. Results presented here are based on ORC engines designed for minimum SIC.

6.8 Summary and conclusions

While thermodynamic optimisation and technical feasibility are at the core of ORC technology development, critical factors for their wider deployment is their CAPEX, and O&M costs. In this work, a holistic ORC system design, sizing and costing optimisation framework has been developed, covering a range of HEX and volumetric expander types and configurations. This work goes beyond other efforts in the literature in that the HEX and expander typology, expansion stages, and size are optimised simultaneously with the complete ORC system design for: i) maximum power output; ii) minimum SIC; and iii) multi-objective optimisation, instead of being predefined by the user. This feature allows the optimiser to scan alternative components' configuration and sizes simultaneously, to identify the best performing design, given the objective of interest.

First, new cost correlations have been developed to estimate the ORC engine CAPEX, using up-to-date manufacturer data-sheets. Findings highlight significant discrepancies between the HEX costs obtained using manufacturers' data sheets, and those obtained using the module costing technique cost functions (a commonly employed costing technique in the literature), with the latter overestimating the cost of DPHEX by up to 500%, and of PHEX by up to 400%. Similarly, the cost estimates for volumetric expanders are found to vary significantly, depending on the method used, with existing correlations being relevant mainly to high power output machines. Therefore, for the small-to-medium range ORC engines, the cost of volumetric expanders is obtained using the prices of volumetric compressors collated for units available in the market, in the absence of market prices for volumetric expanders.

Next, optimisation of an ORC engine design has been performed for maximum power output. The SIC varies between 1,000-7,500 GBP/kW (for piston expanders) and 1,500-5,500 GBP/kW (for screw expanders). These figures are the highest recorded among all the optimisation exercises performed. For all working fluids investigated, the optimised ORC engines with screw expanders operate with two expansion stages. This is attributed to the fact that the optimiser always aims to maximise the PR over the expansion machines, and the screw expander efficiency deteriorates significantly for PRs higher than 7. The best performing fluids - pentane, R1233zd, toluene and hexane- are consistent in both ORC engine designs with piston and screw expanders, although the absolute values of power output and SIC may vary significantly. The PHEX designs are also consistently those with the lowest area requirements (by up to 50% lower than DPHEX) and thus SIC, for all fluids investigated.

When comparing the minimum SIC optimisation results to those obtained for maximum power output, the SIC of the former varies between 900-1,700 GBP/kW (piston expander) and 1300-2,200 GBP/kW (screw expander), which is 30-35% lower than the latter, whereas the power output decreases by approximately 15-50% in comparison to the maximum power optimisation results. The optimiser favours again two-stage screw expander designs, while, for the majority of the working fluids investigated, the evaporator is selected to be PHEX (due to its compactness), and the condenser a DPHEX (due to its lower cost). The pressure at the condenser is higher than in the case for maximum power output design. This is in order to reduce the volumetric flow rate of the working fluid at the exit of the expander and subsequently reduce the expander cost. The screw expander results are associated with slightly higher power outputs than the ORC engines with piston expanders (by 20-30%). However, the former come at the cost of higher TC than the latter (by 20-50%).

By comparing the multi-objective optimisation results to those obtained from single-objective designs and to available ORC engine prices on the market, it is noted that while the ORC power output reduces below 30 kW, the SIC increases significantly up to 3,500-4,000 GBP/kW (depending on the fluid and design). Moving to higher power outputs of 100-125 kW can also result in an increase of the SIC up to 4,000-5,000 GBP/kW. However, findings have revealed a range of power outputs from 70 to 100 kW, over which increasing the engine capacity by 33% will result in only minor increase in costs by 9%. This highlights the great potential of ORC engines design at these capacities. When comparing the SIC results for ORC engines optimised for maximum power output to the available ORC market prices, the cost predictions are similar or slightly overestimate the cost of the engines (by 8%). On the contrary, the cost predictions for ORC engines designed for minimum SIC are underestimating the SIC by 10-30%, in comparison to the same price data set. The multi-objective optimisation results seem to have the best match to the market prices. Any discrepancies between the cost predictions and actual market prices are attributed to: i) the costing model developed does not account for profit margins added to the unit cost by the vendors; ii) the cost results are for optimal designs, indicating there is potential for reducing the engines cost, by deploying integrated optimisation tools, which simultaneously optimise the ORC thermodynamic cycle, and components sizing and configurations; iii) ORC engines for stationary applications in the market do not use piston expanders; and iv) the ORC market prices may refer to system configurations and architectures different to the subcritical non-recuperative ORC engine, considered in this work.

Results prove that optimised ORC engines in high temperature ICE-ORC waste heat recovery applications can achieve DPPs of less than 3 years, making them an appealing waste heat recovery technology and investment. Additionally, ORC engines with low upfront costs (medium power outputs) result in lower DPPs, but also have lower annual earnings (NPVs) over the project life. In contrast, ORC engines with high power outputs (high upfront costs) offer high annual earnings, but they have higher DPPs. DPPs for minimum SIC designs vary between 2.6-6 years, whilst DPPs for maximum power output result in DPPs of 3.8-15 years. Findings reveal that increasing interest rates from 5% to 10% have negligible impact on the DPP of the ORC engine investments, although the NPVs can be affected by up to 30-40% (assuming the same operating profile). Also, the financial performance maps generated in this work provide insights on how different ORC engine sizes (capacities) can be achieved with alternative designs, along with the corresponding DPPs/NPVs achieved. Finally, fluids such as R152a and butane stand out as a good combination of resultant DPP and NPV, for ORC engines with both screw and piston expanders. These fluids although did not stand out for the highest power output or minimum SIC, present very good performance from a projects' profitability analysis perspective. The findings illustrate that depending on the project KPIs and optimisation objectives different ORC design, size, and configurations will be suitable.

To conclude, the integrated systematic ORC components selection and sizing optimisation framework developed in this work can provide insights on the design of next-generation ORC engines. This framework allows us to answer questions on which components configuration and sizes are the best performing given the application constraints and alternative objectives. The tool can be used by: i) designers to obtain the best ORC system configuration, and size, given the heat-source conditions; and ii) project developers and planners to compare the performance and costs of different ORC engines designs, to assist them in selecting the system that meets their specific KPIs.

Chapter 7

Summary and conclusions

"We cannot solve our problems with the same thinking we used when we created them."

– Albert Einstein, Physicist

Decreasing our dependency on depleting resources, increasing the efficiency of energy conversion technologies, and averting the risks caused by excessive emissions are arguably some of the biggest economical, scientific and political challenges of our time. In this transition towards sustainable energy systems, there is little question that the power generation sector and the grid of the future, will operate differently than how they do today. Increasing the share of renewable sources of energy in the energy mix, and recovering medium-grade or waste heat will play a pivotal role in this transition, as societies move towards distributed energy systems. The research conducted within this PhD project aims to be a contribution to this human endeavour towards a sustainable energy future.

This work is concerned with the advancement of distributed combined heat and power (CHP) systems, via the deployment of technological solutions which can recover the, otherwise, wasted thermal surplus in the built environment and in industry. The aim of this research is to investigate the potential of organic Rankine cycle (ORC) engines as bottoming cycles to internal combustion engines (ICEs) within a CHP system, from technical, operating and economic perspectives. In considering these technologies, whole-system optimisation modelling tools have been developed, to identify the system design, size, components typologies, working fluids, and operating strategies, which maximise the performance of ICE-ORC CHP systems, while also improving their financial proposition. To achieve the main goal of this research, three main areas of interest have been identified:

- The performance optimisation of integrated ICE-ORC CHP systems, by capturing the interactions and performance trade-offs between the CHP-ICE and ORC engines, when operating as part of a single system;

- The prediction and optimisation of the off-design operation of ORC engines in real installations, considering the system components time-varying performance, under fluctuating boundary conditions;
- The thermoeconomic feasibility assessment of ICE-ORC CHP systems, providing suitable design tools, which can simultaneously optimise the ORC engine design, size and cost, given the specific project objectives.

7.1 Conclusions and main findings

First, a combined optimisation of an integrated CHP system that consists of interacting ICE and ORC components has been performed. Both engines are modelled in detail and validated (especially the ICE which is a dynamic model). The novelty of this research is that the ICE and ORC engines are optimised simultaneously within the combined system, and key interactions and trade-offs are captured between the operation of the two engines. This holistic approach gives new insights into appropriate designs and operating conditions for both engines, for which the optimum performance of the combined ICE-ORC CHP system can be expected. In particular, we are able to answer questions, such as: i) what is the difference in the system power output and fuel efficiency, when the integrated ICE-ORC CHP system is optimised simultaneously, in comparison to the conventional approach where the two engines are treated separately; ii) is the dominant driver for the integrated ICE-ORC system performance the ICE design or the ORC design, and how is this affected by the rated power of the ICE; iii) does the overall ICE-ORC CHP system performance improve equally for the case of small or larger ICEs coupled to ORCs; and iv) what is the effect of ICE aspiration on the ORC engine design and performance. The findings of this research reveal that:

- The whole-system optimisation of integrated ICE-ORC CHP systems can increase the combined system power output by up to 30%, the system electrical efficiency by up to 21% (in comparison to the stand-alone ICE), or reduce the fuel consumption by 17%;
- When only the ICE power output is maximised, the ICE optimum operating conditions result in lower exhaust-gas temperature exiting the ICE, which maximises the power delivered to the ICE shaft; in contrast, when the complete ICE-ORC CHP system is optimised for maximum power output the exhaust-gas stream leaving the ICE is at a higher temperature and pressure, so as to promote ORC generation, but at the cost of slightly reduced ICE power output;
- By analysing the waste heat recovery from different ICE capacities, results highlight that the improvement of the whole-system power output and fuel efficiency is higher in medium-size ICEs, making them very promising candidates for bottoming ORCs; this is partially attributed to the better fuel efficiency of the larger engines in the first place, but also to the fact that the ORC contribution to the total system power output is higher in smaller scale systems;

- ORC engines designed for naturally aspirated ICEs, can achieve thermal efficiencies of up to 25%, due to the high exhaust-gas temperature leaving the engine (up to 1,000 K), relative to the turbocharged ICEs, with exhaust-gas temperature of up to 700 K, achieving efficiencies up to 20%;
- The higher temperature difference observed in the ORC evaporator designed for naturally aspirated ICEs will result in lower heat transfer area requirements. In turn, the pressure drop experienced in this smaller heat exchanger (HEX) by both the exhaust gases and the working fluid will be lower, while the HEX will be less expensive, reducing the ORC engine capital cost;
- Different optimal pressure ratios (PR) are recorded for bottoming ORCs designed for natural and turbocharged engines. For the natural aspiration ICEs (higher temperature exhaust gases) the PR in the ORC ranges between 7 and 55, whilst in the case of turbocharged ICEs, this varies between 5 and 44. The latter case with its lower PRs will require a different expander technology and design, while multi-stage expansion may prove to be an efficient solution for the very high PR cases;
- Working fluids with low global warming potential (GWP) have been examined, and new hydrofluoroolefins such as R1233zd, are proved to be very promising candidates for high-temperature ORC applications, while being non-toxic, and having low flammability in comparison to hydrocarbons.

By employing such an integrated ICE-ORC system optimisation approach, insights are provided simultaneously for: i) the design of ICEs that are to be coupled with ORC engines, which can be used by the ICE manufacturers, interested in waste heat recovery projects with ORC technology; and ii) for ORC manufacturers on design/operational aspects of their engines for optimum coupling to ICEs. Finally, the tool can be used by decision makers to select between minimising operating costs (fuel consumption) or maximising power output, given their specific key performance indicators (KPIs) targets.

Next, the ORC engines off-design operation within an ICE-ORC CHP system was examined, given a real variable heat-source profile, in terms of temperature and mass flow rate. Various operating/control parameters can be adjusted to optimise the ORC power output/efficiency, at every new heat-source condition. Such optimisation can be computationally expensive (especially as the number of variables increases), so performing this exercise in real-time is a challenging task. In contrast, optimum ORC engine performance maps can be generated and used for predicting the new ORC engine operating points and performance. In this context, an ORC engine off-design operation optimisation framework has been developed. This work differs from previous studies in that the tool captures the time-varying characteristics and interactions between key system components, to maximise the ORC power output at off-design operation. In particular, the deployment of piston expanders in stationary power generation applications was evaluated, along with alternative HEXs architectures. The system performance was then compared to the off-design operation of ORC engines with screw expanders, another volumetric expander machine used in the industry.

This approach allows us to answer questions, such as: i) what is the impact on the optimum ORC engine operating points between assuming a simplified fixed expander efficiency approach and constant evaporating pressure, and accounting for the complete interactions of the evaporator and expander performance; ii) how piston expanders can be integrated in stationary ORC power generation, and how they perform in off-design conditions; iii) how piston expanders compare to other volumetric expander machines, such as screw machines, in high temperature waste heat recovery applications; and iv) do the best performing fluids in nominal design, perform also well in off-design operation. The findings reveal that:

- When the expander efficiency is assumed fixed, the system power output is underestimated by up to 17%, especially at low CHP-ICE part-load (PL) conditions;
- Piston expanders can operate with high isentropic efficiency, exceeding 85%, at PRs 15-35 (excluding mechanical and power generation losses), whilst all optimised ORC designs with screw expanders operate with two expansion stages, and PR of 4-8 per stage, achieving isentropic efficiencies up to 80%;
- When the evaporator HEX and piston expander interactions are considered, the optimal operating points for the ORC at off-design conditions result in lower pressure in the evaporator, for all working fluids investigated. This has the effect of: i) increasing the evaporator HEX effectiveness by increasing the percentage of heat transfer performed in the two-phase zone; and ii) maximising the piston expander isentropic efficiency by moving towards lower PRs and higher superheat. In contrast, screw expanders operate close to their design point pressure levels, aiming to reduce the deviation from their in-built volume ratios (VRs), since this has significant negative effect on the screw expander isentropic efficiency;
- The optimised piston expander isentropic efficiency improves by up to 10-16% at off-design operation (for a given size machine), depending on the fluid investigated. This highlights the potential of piston expanders in real applications with varying heat-source profile. In contrast, the optimised screw expander efficiency at off-design conditions slightly decreases, while VRs deviate only slightly, from the in-built VR of the machine;
- Although optimised ORC engines with two-stage screw expanders generate slightly higher power output than those with piston, the latter have better off-design performance; a case in the point is pentane, for which when the ORC engine operates with piston expander, while the CHP-ICE PL decreases from 100% to 60%, the power output of the ORC engines decreases from 100% to 76%, whilst with screw expander for the same fluid, the power output reduces down to 67%;
- By optimising the complete ORC engine operation at off-design conditions, we maintained or even increased the ORC engine thermal efficiency (with piston expanders) by up to 7%, while the heat-source mass flow rate reduces by 40% (CHP-ICE at 60% PL);

- In a similar vein, by optimising the complete ORC engine operation at off-design conditions, the power output of the ORC engine with piston expander reduces to 70-77% of the design capacity, while the CHP-ICE operates at 60% PL, or down to 63-71% of the design point, when screw expanders are used;
- The *U*-values of plate heat exchangers (PHEXs) are almost double that of the double-pipe designs (DPHEXs). The *U*-values of the evaporator for DPHEXs reduce by 28-30% compared to the design point values, and by 25% for PHEXs, while the mass flow rate of the heat source reduces to 50-60% of the design point. Additionally, the overall evaporator effectiveness either stays constant or even slightly increases at the new off-design operating points;
- ORC engines with PHEXs seem to generate 5-12% more power output than those with DPHEX designs, depending on the fluid and expander type investigated. This is attributed to the different mass flow rates and operating temperatures in the cycle with PHEXs, which increase its effectiveness in recovering heat from the heat-source stream;
- The best performing fluids at design point prove to also be the best performing at off-design operation, in terms of power output.

Based on this work, performance maps have been generated that cover not only the ORC engine overall performance, but also its constituent components, for the full spectrum of heat-source conditions (temperature and mass flow rate). These maps can be utilised by: i) ORC engine and component manufacturers to inform design decisions; and ii) by ORC plant operators to set up the control system of real ORC plants, and optimise the system operation, given the specific operating profile on their site.

A thermoeconomic analysis of ORC engines in ICE-ORC CHP systems was then performed. To improve the financial proposition of the next generation ORC systems, we need to answer questions such as: i) which components configuration and sizes are the best performing, given the application and project objectives; ii) can similar ORC engine capacities be achieved with different designs and components' selection, and what is the impact of each design on the specific investment cost (SIC), discounted payback period (DPP) and net present value (NPV) in every case; iii) how the various cost correlations available in the literature compare to real components' cost, and which correlations are more representative of the ORC engine costs; and iv) can we develop a tool where the optimiser scans the full spectrum of potential ORC designs to identify the best performing configuration given the project objectives, without requiring the users previous knowledge or input. The latter point will make the tool accessible to stakeholders, who may not have the technical knowledge to design ORC engines, but would like to assess alternative design options, but also to ORC vendors, who are interested in designing the next-generation ORC engines, to be a good fit to real applications.

In this context, a thermoeconomic optimisation framework was developed, which scans alternative components' configurations and sizes, simultaneously with the thermodynamic design, and identifies the best performing system, given the project objectives. The framework was applied on an ORC engine recovering heat from a CHP-ICE, optimising for maximum power output or/and minimum SIC. Results reveal that:

- There are significant discrepancies between the HEX costs obtained using manufacturers' data sheets, and those obtained using the module costing technique (a commonly used costing technique in the ORC literature), with the latter overestimating the cost of DPHEX by up to 500%, and of PHEX by up to 400%;
- ORC engines optimised for maximum power output have the highest SIC varying between 1,000-7,500 GBP/kW, for engines with piston expanders, and 1,500-5,500 GBP/kW for screw expanders;
- ORC engines optimised for minimum SIC have 15-50% lower power output than the engines optimised for the maximum power output, but also up to 35% lower SIC;
- The condenser pressure in ORC engines designed for minimum SIC increases, to reduce the working fluid volumetric flow rate, and thus the expander cost, but also the associated power output;
- Optimised ORC engines for minimum SIC, and those designs on the Pareto front of the multi-objective optimisation, have PHEXs as the evaporator (due to compactness) and DPHEXs as the condenser (due to lower cost);
- Optimised ORC engines with screw expanders always operate with two-stage expansion, even when the optimisation objective is minimising SIC, where the cost of two expanders is considered;
- Optimised ORC engines with two-stage screw expanders have higher power output than those with piston expanders (by up to 45%), but at higher total cost of the engine (by up to 85%);
- In ORC operating with low-medium temperatures, and low pressures, the cost of the HEXs is significant, therefore it is of high importance to design them to maximise the heat transfer. For higher power outputs, the selection and design of the expander machine and then of the evaporator are key factors, for reducing the ORC engine costs. (In this study, DPHEXs and PHEXs have been used for both the evaporator and the condenser, so the results might vary in case of other types of HEXs);
- A range of power output of 70 to 100 kW is revealed in the multi-objective optimisation, where increasing the power output of the ORC engine by 33% results in the SIC increasing by only 10%, indicating a promising range of capacities for the next-generation ORC engines;
- The SIC values recorded using the cost correlations developed in this work are well aligned with the SIC values of real ORC engines, giving confidence that the proposed cost functions can be utilised in ORC design studies for costing purposes;
- ORC engines with high power output and high upfront costs, have higher NPVs but also high DPP, whilst engines designed from minimum SIC have DPP of 2.8-6 years, but lower NPVs;

- The same ORC engine capacity can be achieved with different types of components, but this affects the system SIC and NPV;
- There are candidate ORC working fluids such as R152a and butane, which although did not stand out for their highest power output or minimum SIC, present a good performance from a project's profitability perspective (good resultant DPP and NPV).

These findings highlight the potential of ORC engines in CHP applications, and the need for a holistic approach when designing such systems, considering their thermodynamic, operational and cost aspects. Depending on the application, the most suitable working fluids, components typology and design, optimum ORC capacity and operating strategy can vary significantly. By optimising the ORC engines integration within CHP systems, and providing energy-efficient strategies to maximise their utilisation, the overall efficiency of the system will increase. In turn, this will lower their costs, and reduce payback period, thus, making these technologies an economically viable proposition.

7.2 Thesis main outcomes

- Integrated ICE-ORC CHP optimisation tool

An integrated optimisation tool has been developed for advanced CHP systems, comprised of ICEs and ORC engines. The interactions and performance trade-offs between the two engines are captured, aiming to optimise the combined ICE-ORC system performance, either for maximum power output or fuel efficiency. The tool developed can be used for the design of new installations of ICE-ORC systems, or in existing cogeneration facilities, where the designers can optimise the existing CHP-ICE operation, while selecting the ORC engine. Relevant publications on this tool are listed in the beginning of this thesis.

- Off-design ORC operation optimisation tool

A whole-system computational platform has been developed, comprised of detailed sub-component models, capable of predicting the ORC engine performance, under varying boundary conditions. ORC engine off-design performance maps can be generated, for alternative system configurations, to predict the system performance over an operating profile. The tool can be used: i) to inform decisions about new systems' sizing and schematic; and ii) to identify the optimum off-design control strategy of an installed ORC plant, given the engine specification and the variable heat-source conditions onsite. Relevant publications on this tool are listed in the beginning of this thesis.

- ORC thermoeconomic optimisation tool

A systematic ORC engine component selection, sizing and costing optimisation tool was developed, covering a range of HEXs and expander machines configurations. The HEX typology, and components' sizing, can be simultaneously optimised with the complete ORC design, for maximum power output or/and minimum SIC, instead of forming a designers' predefined input. This allows the simultaneous selection of the best performing system configuration and size, given the application specific constraints, since the optimiser screens the whole solution space of components typologies, configurations and sizes to identify the best performing design. The tool can be used by ORC engines' manufacturers, and integrators to compare alternative design options from both technical and financial perspective. Relevant publications on this tool are listed in the beginning of this thesis.

- ORC components sizing and costing models

The components' model developed in this work, such as the PHEX and DPHEX sizing models, are versatile, and can be used to study ORC engines in various applications, apart from the ICE-ORC CHP systems that have been the focus of this thesis. To-date, the components sizing models have been used for predicting the performance of solar-driven ORC CHP systems, and also in computer-aided molecular design (CAMD) ORC optimisation studies, in collaboration with other researchers. Finally, the costing models developed in this thesis have been also applied to solar-driven ORC systems, and to other low-to-high heat recovery applications. Relevant publications on these areas of research are listed in the beginning of this thesis.

7.3 Recommendations for future work

Several areas of future work have been highlighted as a result of this research.

The off-design ORC modelling tool developed has been applied to a waste heat recovery application from CHP-ICEs with ORC engines. However, the input vector with the heat-source boundary conditions can be adjusted, to replicate other applications, such as solar driven ORCs or ORC engines in geothermal plants, where the heat-source stream also varies. The library of components can be extended, by adding more types of HEXs and expander machines, to compare various system configurations, under time-varying heat-source conditions. A further research area identified is the integration of the working fluid charge of the ORC engine, in the ORC modelling, when optimising at design and off-design conditions. Some work in this area has been performed in Refs. [109,182]. Another interesting approach is to optimise the ORC engine design, considering the potential operating profile of the engine, once installed (multi-period design). This can be added to the capabilities of the existing tool, while some work on this aspect has been presented in Refs. [106,183], focusing on turbine expanders, and large scale ORC systems.

Another important area of research identified is the design of real-time controllers, which will be capable of monitoring the heat-source variations, and send signals to the ORC engine, to adjust its operation accordingly. Overcoming this challenge will fully unlock the potential of ORC engines performance optimisation, under off-design conditions. Some work on the controls aspects and controller design of ORC engines can be found in Ref. [39] for engines with turbines, in Refs. [113,184] for ORC engines with scroll expanders, and in Ref. [79] for engines with single-stage single screw machines.

In this study, the potential of piston expanders in stationary high-efficiency power generation has been highlighted. Further work on the design of piston expanders and optimisation of their performance should be performed. In this research, to obtain the piston or screw expander efficiency within the ORC engine, we used performance maps of these devices. The next step would be to incorporate the detail expander sizing model in the ORC design and off-design modelling tool.

The direct heat recovery from the exhaust-gas stream of an ICE, in the ORC evaporator has been evaluated from technical, operating and economic perspectives. Alternative configurations could be examined in the future using the same optimisation tools, and compared to this system, in terms of off-design performance and costs. These configurations include designs with an intermediate oil loop between the ORC engine evaporator and the exhaust-gas stream, or the use of the ICE jacket water, as a preheater of the ORC. Although studies that compare such configurations from a thermodynamic perspective exist, literature lacks efforts that account for their off-design performance, and costs. This will allow identifying the best configuration for stationary power generation applications. A relevant study can be found in Ref. [174] comparing heat recovery from ICEs with different ORC configurations at PL operation. Nevertheless, only the HEXs time-varying performance was modelled in detail, and the system costs were not considered.

The library of components of the thermoeconomic tool developed in this work can be populated with more types of HEXs and expander technologies, enabling the optimiser to search a wider solutions space. More options can be added in the tool for the optimiser to be able to choose, not only among various component types, but also between different ORC architectures, such as subcritical non-recuperative or recuperative cycles, to evaluate the most well-suited system design. In the present work, the profitability appraisal of the ORC system was performed assuming a flat all-year round operation of the system. The next step will be to evaluate the ORC project profitability, by accounting for specific case-studies annual operating profile. Some work on this aspect can be found in Ref. [24]. In the ORC thermoeconomic optimisation the objectives were the maximum power output and minimum SIC. An alternative approach would be to use the project NPV, DPP or other relevant KPIs as the optimisation objectives, to evaluate the impact on the optimum ORC engine design. Finally, a broader range of ORC engines and components cost data can be used in the future, to establish further the validity of the costing methodology presented in this thesis, as these become available.

References

[1] Mahmoudi A, Fazli M, Morad MR. A recent review of waste heat recovery by Organic Rankine Cycle. Appl Therm Eng 2018;143:660–75. doi:10.1016/j.applthermaleng.2018.07.136.

[2] International Energy Agency (IEA). World Energy Outlook 2018. 2018.

[3] DECC. Central England and global surface temperature. 2013.

[4] UNFCCC. The Paris Agreement. 2015.

[5] UNFCCC. Paris Agreement - Status of ratification 2018. https://unfccc.int/process/the-paris-agreement/status-of-ratification (accessed November 27, 2018).

[6] International Energy Agency (IEA). World Energy Outlook 2017. 2017.

[7] Dutil Y, Rousse D, Lassue S, Zalewski L, Joulin A, Virgone J, et al. Modeling phase change materials behavior in building applications: Comments on material characterization and model validation. Renew Energy 2012;61:132–5. doi:10.1016/j.renene.2012.10.027.

[8] Lecompte S, Huisseune H, van den Broek M, De Schampheleire S, De Paepe M. Part load based thermo-economic optimization of the organic Rankine cycle (ORC) applied to a combined heat and power (CHP) system. Appl Energy 2013;111:871–81. doi:10.1016/j.apenergy.2013.06.043.

[9] EnerG. ENER-G CHP Units 2017. http://www.energ-group.com/media/808715/ener-g-natural-gas-chp-range-guide-2017-uk-ireland-small-scale-≤530kwe-.pdf.

[10] Bianchi M, Branchini L, De Pascale A, Peretto A. Application of environmental performance assessment of CHP systems with local and global approaches. Appl Energy 2014;130:774–82. doi:10.1016/j.apenergy.2014.04.017.

[11] Lecompte S, Huisseune H, van den Broek M, Vanslambrouck B, De Paepe M. Review of organic Rankine cycle (ORC) architectures for waste heat recovery. Renew Sustain Energy Rev 2015;47:448–61. doi:10.1016/j.rser.2015.03.089.

[12] Oyewunmi OA, Pantaleo AM, Markides CN. ORC cogeneration systems in waste-heat recovery applications. Energy Procedia 2017;142:1736–42. doi:10.1016/j.egypro.2017.12.557.

[13] Backhaus S, Swift GW. A thermoacoustic stirling heat engine. Nature 1999;399:335–8. doi:10.1038/20624.

[14] Markides CN, Solanki R, Galindo A. Working fluid selection for a two-phase thermofluidic oscillator: Effect of thermodynamic properties. Appl Energy 2014;124:167–85. doi:10.1016/j.apenergy.2014.02.042.

[15] Markides CN. Low-concentration solar-power systems based on organic Rankine cycles for distributed-scale applications: Overview and further developments. Front Energy Res 2015;3:1–16. doi:10.3389/fenrg.2015.00047.

[16] Tchanche BF, Lambrinos G, Frangoudakis A, Papadakis G. Low-grade heat conversion into power using organic Rankine cycles – A review of various applications. Renew Sustain Energy Rev 2011;15:3963–79. doi:10.1016/j.rser.2011.07.024.

[17] Quoilin S, Declaye S, Tchanche BF, Lemort V. Thermo-economic optimization of waste heat recovery organic Rankine cycles. Appl Therm Eng 2011;31:2885–93. doi:10.1016/j.applthermaleng.2011.05.014.

[18] Bronicki LY. History of organic Rankine cycle systems. Org Rank Cycle Power Syst 2017:25–66. doi:10.1016/B978-0-08-100510-1.00002-8.

[19] Tartière T, Astolfi M. A World Overview of the Organic Rankine Cycle Market. Energy Procedia, vol. 129, 2017. doi:10.1016/j.egypro.2017.09.159.

[20] Ormat. ORMAT Technologies Inc 2018.

[21] Turboden. Turboden Organic Rankine cycle units 2018. https://www.turboden.com/turboden-orc-technology/1065/innovation.

[22] The European Commision. Communication from the Commission to the European Parliament, the Council, the Economic and Social Committee and the Committee of the Regions, Energy Roadmap 2050, SEC(2011) 1565 Part 2/2. Brussels: 2011.

[23] The European Commission. Communication from the Commission to the European Parliament, the Council, the Economic and Social Committee and the Committee of the Regions Energy Efficiency Plan 2011, 2011, Brussels, 8.3.2011 COM(2011) 109. Brussels: 2011.

[24] Acha S, Mariaud A, Shah N, Markides CN. Optimal design and operation of distributed low-carbon energy technologies in commercial buildings. Energy 2018;142:578–91. doi:10.1016/j.energy.2017.10.066.

[25] Chatzopoulou MA, Acha S, Oyewunmi OA, Markides CN. Thermodynamic and economic evaluation of trigeneration systems in energy-intensive buildings. Proc. 13th Int. Conf. Heat Transf. Fluid Mech. Thermodyn., Portoroz, Slovenia: 2017.

[26] Chatzopoulou MA, Markides CN. Thermodynamic optimisation of a high-electrical efficiency integrated internal combustion engine – Organic Rankine cycle combined heat and power system. Appl Energy 2018;226:1229–51. doi:10.1016/j.apenergy.2018.06.022.

[27] Chintala V, Kumar S, Pandey JK. A technical review on waste heat recovery from compression ignition engines using organic Rankine cycle. Renew Sustain Energy Rev 2018;81:493–509. doi:10.1016/J.RSER.2017.08.016.

[28] Vélez F, Segovia JJ, Martín MC, Antolín G, Chejne F, Quijano A. A technical, economical and market review of organic Rankine cycles for the conversion of low-grade heat for power generation. Renew Sustain Energy Rev 2012;16:4175–89. doi:10.1016/j.rser.2012.03.022.

[29] Quoilin S, Broek M Van Den, Declaye S, Dewallef P, Lemort V. Techno-economic survey of organic Rankine cycle (ORC) systems. Renew Sustain Energy Rev 2013;22:168–86. doi:10.1016/j.rser.2013.01.028.

[30] Maraver D, Royo J, Lemort V, Quoilin S. Systematic optimization of subcritical and transcritical organic Rankine cycles (ORCs) constrained by technical parameters in multiple applications. Appl Energy 2014;117:11–29. doi:10.1016/j.apenergy.2013.11.076.

[31] Yu G, Shu G, Tian H, Wei H, Liang X. Multi-approach evaluations of a cascade-Organic Rankine Cycle (C-ORC) system driven by diesel engine waste heat: Part B-techno-economic evaluations. Energy Convers Manag 2016;108:596–608. doi:10.1016/j.enconman.2015.10.085.

[32] Yağlı H, Koç Y, Koç A, Görgülü A, Tandiroğlu A. Parametric optimization and exergetic analysis comparison of subcritical and supercritical organic Rankine cycle (ORC) for biogas fuelled combined heat and power (CHP) engine exhaust gas waste heat. Energy 2016;111:923–32. doi:10.1016/j.energy.2016.05.119.

[33] Wang E, Yu Z, Zhang H, Yang F. A regenerative supercritical-subcritical dual-loop organic Rankine cycle system for energy recovery from the waste heat of internal combustion engines. Appl Energy 2017;190:574–90. doi:10.1016/j.apenergy.2016.12.122.

[34] Song S, Zhang H, Lou Z, Yang F, Yang K, Wang H, et al. Performance analysis of exhaust waste heat recovery system for stationary CNG engine based on organic Rankine cycle. Appl Therm Eng 2015;76:301–9. doi:10.1016/j.applthermaleng.2014.11.058.

[35] Zhang T, Zhu T, An W, Song X, Liu L, Liu H. Unsteady analysis of a bottoming organic Rankine cycle for exhaust heat recovery from an internal combustion engine using Monte Carlo simulation. Energy Convers Manag 2016;124:357–68. doi:10.1016/j.enconman.2016.07.039.

[36] Yu G, Shu G, Tian H, Wei H, Liu L. Simulation and thermodynamic analysis of a bottoming

organic Rankine cycle (ORC) of diesel engine (DE). Energy 2013;51:281–90. doi:10.1016/j.energy.2012.10.054.

[37] Zhao R, Zhang H, Song S, Tian Y, Yang Y, Liu Y. Integrated simulation and control strategy of the diesel engine–organic Rankine cycle (ORC) combined system. Energy Convers Manag 2018;156:639–54. doi:10.1016/j.enconman.2017.11.078.

[38] Yue C, Han D, Pu W. Analysis of the integrated characteristics of the CPS (combined power system) of a bottoming organic Rankine cycle and a diesel engine. Energy 2014;72:739–51. doi:10.1016/j.energy.2014.05.103.

[39] Xu B, Rathod D, Kulkarni S, Yebi A, Filipi Z, Onori S, et al. Transient dynamic modeling and validation of an organic Rankine cycle waste heat recovery system for heavy duty diesel engine applications. Appl Energy 2017;205:260–79. doi:10.1016/j.apenergy.2017.07.038.

[40] Freeman J, Hellgardt K, Markides CN. An assessment of solar-powered organic Rankine cycle systems for combined heating and power in UK domestic applications. Appl Energy 2015;138:605–20. doi:10.1016/j.apenergy.2014.10.035.

[41] Shah RK, Sekulic DP. Fundamentals of heat exchanger design. John Wiley & Sons, Inc., Hoboken, New Jersey; 2003.

[42] Astolfi M. Technical options for organic Rankine cycle systems. Org. Rank. Cycle Power Syst., Elsevier; 2017, p. 67–89. doi:10.1016/B978-0-08-100510-1.00003-X.

[43] Hewitt GF, Shires GL, Bott TR. Process heat transfer. CRC Press; 1994.

[44] Verein Deutscher Ingenieure V. VDA Heat Atlas. VDI Heat Atlas. Second, Springer; 2010. doi:10.1017/cbo9781107415324.004.

[45] Oyewunmi OA, Markides CN. Thermo-economic and heat transfer optimization of working-fluid mixtures in a low-temperature organic Rankine cycle system. Energies 2016;9:1–21. doi:10.3390/en9060448.

[46] White MT, Oyewunmi OA, Chatzopoulou MA, Pantaleo AM, Haslam AJ, Markides CN. Computer-aided working-fluid design, thermodynamic optimisation and thermoeconomic assessment of ORC systems for waste-heat recovery. Energy 2018;161:1181–98. doi:10.1016/J.ENERGY.2018.07.098.

[47] Ramos A, Chatzopoulou MA, Freeman J, Markides CN. Optimisation of a high-efficiency solar-driven organic Rankine cycle for applications in the built environment. Appl Energy 2018;228:755–65. doi:10.1016/j.apenergy.2018.06.059.

[48] Braimakis K, Karellas S. Integrated thermoeconomic optimization of standard and regenerative ORC for different heat source types and capacities. Energy 2017;121:570–98. doi:10.1016/j.energy.2017.01.042.

[49] Feng Y, Hung T, Greg K, Zhang Y, Li B, Yang J. Thermoeconomic comparison between pure and mixture working fluids of organic Rankine cycles (ORCs) for low temperature waste heat recovery. Energy Convers Manag 2015;106:859–72. doi:10.1016/j.enconman.2015.09.042.

[50] Tian H, Shu G, Wei H, Liang X, Liu L. Fluids and parameters optimization for the organic Rankine cycles (ORCs) used in exhaust heat recovery of internal combustion engine (ICE). Energy 2012;47:125–36. doi:10.1016/j.energy.2012.09.021.

[51] Walraven D, Laenen B, D'haeseleer W. Comparison of shell-and-tube with plate heat exchangers for the use in low-temperature organic Rankine cycles. Energy Convers Manag 2014;87:227–37. doi:10.1016/j.enconman.2014.07.019.

[52] Daccord R. Cost to benefit ratio of an exhaust heat recovery system on a long haul truck. Energy Procedia 2017;129:740–5. doi:10.1016/j.egypro.2017.09.108.

[53] Zhang C, Liu C, Wang S, Xu X, Li Q. Thermo-economic comparison of subcritical organic

Rankine cycle based on different heat exchanger configurations. Energy 2017;123:728–41. doi:10.1016/j.energy.2017.01.132.

[54] García-Cascales JR, Vera-García F, Corberán-Salvador JM, Gonzálvez-Maciá J, Fuentes-Díaz D. Assessment of boiling heat transfer correlations in the modelling of fin and tube heat exchangers. Int J Refrig 2007;30:1004–17. doi:10.1016/j.ijrefrig.2007.01.006.

[55] García-Cascales JR, Vera-García F, Corberán-Salvador JM, Gonzálvez-Maciá J. Assessment of boiling and condensation heat transfer correlations in the modelling of plate heat exchangers. Int J Refrig 2007;30:1029–41. doi:10.1016/j.ijrefrig.2007.01.004.

[56] Zhang J, Desideri A, Kærn MR, Ommen TS, Wronski J, Haglind F. Flow boiling heat transfer and pressure drop characteristics of R134a, R1234yf and R1234ze in a plate heat exchanger for organic Rankine cycle units. Int J Heat Mass Transf 2017. doi:10.1016/j.ijheatmasstransfer.2017.01.026.

[57] Zywica G, Kaczmarczyk TZ, Ihnatowicz E. A review of expanders for power generation in small-scale organic Rankine cycle systems: Performance and operational aspects. Proc. Inst. Mech. Eng. Part A J. Power Energy, vol. 230, 2016, p. 669–84. doi:10.1177/0957650916661465.

[58] Landelle A, Tauveron N, Haberschill P, Revellin R, Colasson S. Organic Rankine cycle design and performance comparison based on experimental database. Appl Energy 2017;204:1172–87. doi:10.1016/j.apenergy.2017.04.012.

[59] Triogen. Triogen E-Box engine application 2018. http://www.triogen.nl/upload/files/Triogen Productflyer e-box Gas Engine WEB.pdf.

[60] Cryostar. Heat to Power. 2018.

[61] Electratherm. Electratherm CHP 2018. https://electratherm-electratherm.netdna-ssl.com/wp-content/uploads/2015/02/ET-0030-Master-Configuration-Brochure_issu.pdf.

[62] BEP Europe. E-Rational ORC. 2018.

[63] Bao J, Zhao L. A review of working fluid and expander selections for organic Rankine cycle. Renew Sustain Energy Rev 2013;24:325–42. doi:10.1016/jrser.2013.03.040.

[64] Song P, Wei M, Shi L, Danish SN, Ma C. A review of scroll expanders for organic rankine cycle systems. Appl Therm Eng 2015;75:54–64. doi:10.1016/j.applthermaleng.2014.05.094.

[65] Astolfi M. Techno-economic optimization of low temperature CSP systems based on ORC with screw expanders. Energy Procedia 2015;69:1100–12. doi:10.1016/j.egypro.2015.03.220.

[66] Hu D, Zheng Y, Wu Y, Li S, Dai Y. Off-design performance comparison of an organic Rankine cycle under different control strategies. Appl Energy 2015;156:268–79. doi:10.1016/j/apenergy.2015.07.029.

[67] Atlas Corpo Gas and Process solutions. Atlas Copco ORC. 2018.

[68] Calnetix. Calnetix 2018. https://www.calnetix.com/calnetix-hydrocurrent-marine-orc-shipboard-heat-recovery.

[69] Lemort V, Legros A. Positive displacement expanders for organic Rankine cycle systems. Org. Rank. Cycle Power Syst., Elsevier; 2017, p. 361–96. doi:10.1016/B978-0-08-100510-1.00012-0.

[70] Air Scuared Inc. Air Scuared 2018. https://airsquared.com/products/scroll-expanders/.

[71] Oudkerk JF, Dickes R, Dumont O, Lemort V. Experimental performance of a piston expander in a small- scale organic Rankine cycle. IOP Conf. Ser. Mater. Sci. Eng., vol. 90, 2015. doi:10.1088/1757-899X/90/1/012066.

[72] Shonda O, Descombes G, Glavatskaya Y, Lemort V, Podevin P. Reciprocating expander for an exhaust heat recovery Rankine cycle for a passenger car application. Energies 2012;5:1751–65.

[73] Clemente S, Micheli D, Reini M, Taccani R. Performance analysis and modeling of different volumetric expanders for small-scale organic Rankine cycles. ASME 2011 5th Int. Conf. Energy Sustain. Parts A, B, C, 2011, p. 375–84. doi:10.1115/ES2011-54302.

[74] Dumont O, Dickes R, Lemort V. Experimental investigation of four volumetric expanders. Energy Procedia 2017;129:859–66. doi:10.1016/j.egypro.2017.09.206.

[75] Bloch HP, Hoboken N. Compressors and modern process applications. John Wiley & Sons, Inc; 2006.

[76] Heliex Power. Heliex Power Screw Expanders 2018. https://www.heliexpower.com/technology-products-services/the-technology/core-technology/.

[77] Yang K, Zhang H, Song S, Zhang J, Wu Y, Zhang Y, et al. Performance analysis of the vehicle diesel engine-ORC combined system based on a screw expander. Energies 2014;7:3400–19. doi:10.3390/en7053400.

[78] Lei B, Wang W, Wu Y-T, Ma C-F, Wang J-F, Zhang L, et al. Development and experimental study on a single screw expander integrated into an Organic Rankine Cycle. Energy 2016;116:43–52. doi:10.1016/J.ENERGY.2016.09.089.

[79] Ziviani D, Gusev S, Lecompte S, Groll EA, Braun JE, Horton WT, et al. Optimizing the performance of small-scale organic Rankine cycle that utilizes a single-screw expander. Appl Energy 2017;189:416–32. doi:10.1016/j.apenergy.2016.12.070.

[80] UNEP: United Nations Enviroment Protection. The Montreal Protocol on substances that deplete the ozone layer. 2000. doi:10.1163/15718069620847781.

[81] Michos CN, Lion S, Vlaskos I, Taccani R. Analysis of the backpressure effect of an organic Rankine cycle (ORC) evaporator on the exhaust line of a turbocharged heavy duty diesel power generator for marine applications. Energy Convers Manag 2017;132:347–60. doi:10.1016/j.enconman.2016.11.025.

[82] UN: United Nations. Kyoto Protocol to the United Nations framework convention on climate change. 1998. doi:10.1111/1467-9388.00150.

[83] The European Parliament and the Council of the European Union. Regulation (EU) No 517/2014 of the European Parliament and of the Council on fluorinated greenhouse gases and repealing Regulation (EC) No 842/2006. 2014. doi:https://doi.org/10.4271/1999-01-0874.

[84] The European Commision. EU legislation to control F-gases 2018. https://ec.europa.eu/clima/policies/f-gas/legislation_en.

[85] Ramos A, Chatzopoulou MA, Freeman J, Markides CN. Optimisation of a high-efficiency solar-driven organic Rankine cycle for applications in the built environment. Proc. 30th Int. Conf. Effic. Cost, Optimisation, Simul. Environ. Impact Energy Syst., San Diego: 2017.

[86] Freeman J, Hellgardt K, Markides CN. Working fluid selection and electrical performance optimisation of a domestic solar-ORC combined heat and power system for year-round operation in the UK. Appl Energy 2017;186:291–303. doi:10.1016/j.apenergy.2016.04.041.

[87] Aljundi IH. Effect of dry hydrocarbons and critical point temperature on the efficiencies of organic Rankine cycle. Renew Energy 2011;36:1196–202. doi:10.1016/j.renene.2010.09.022.

[88] Feng Y, Hung T, Zhang Y, Li B, Yang J, Shi Y. Performance comparison of low-grade ORCs (organic Rankine cycles) using R245fa, pentane and their mixtures based on the thermoeconomic multi-objective optimization and decision makings. Energy 2015;93:2018–29. doi:10.1016/j.energy.2015.10.065.

[89] Yang K, Zhang H, Wang Z, Zhang J, Yang F, Wang E, et al. Study of zeotropic mixtures of ORC (organic Rankine cycle) under engine various operating conditions. Energy 2013;58:494–510. doi:10.1016/j.energy.2013.04.074.

[90] Noriega Sanchez CJ, Gosselin L, K. da Silva A. Designed binary mixtures for subcritical organic Rankine cycles based on multiobjective optimization. Energy Convers Manag 2018;156:585–96. doi:10.1016/j.enconman.2017.11.050.

[91] Yang K, Zhang H, Wang Z, Zhang J, Yang F, Wang E, et al. Study of zeotropic mixtures of ORC (organic Rankine cycle) under engine various operating conditions. Energy 2013;58:494–510. doi:10.1016/j.energy.2013.04.074.

[92] Li G. Organic Rankine cycle performance evaluation and thermoeconomic assessment with various applications part I: Energy and exergy performance evaluation. Renew Sustain Energy Rev 2016;53:477–99. doi:10.1016/j.rser.2015.08.066.

[93] Vescovo R, Spagnoli E. High temperature ORC systems. Proc. IV Semin. ORC Power Syst., Milan: 2017.

[94] Brignoli R, Brown JS. Organic Rankine cycle model for well-described and not-so-well-described working fluids. Energy 2015;86:93–104. doi:10.1016/J.ENERGY.2015.03.119.

[95] Papadopoulos AI, Stijepovic M, Linke P, Seferlis P, Vouterakis S. Toward optimum working fluid mixtures for organic Rankine cycles using molecular design and sensitivity analysis. Ind Eng Chem Res 2013;52:12116−12133. doi:dx.doi.org/10.1021/ie400968j.

[96] Freeman J, Hellgardt K, Markides CN. Working fluid selection and electrical performance optimisation of a domestic solar-ORC combined heat and power system for year-round operation in the UK. Appl Energy 2017;186:291–303. doi:10.1016/j.apenergy.2016.04.041.

[97] Song J, Gu C, Ren X. Parametric design and off-design analysis of organic Rankine cycle (ORC) system. Energy Convers Manag 2016;112:157–65. doi:10.1016/j.enconman.2015.12.085.

[98] Cao Y, Dai Y. Comparative analysis on off-design performance of a gas turbine and ORC combined cycle under different operation approaches. Energy Convers Manag 2017;135:84–100. doi:10.1016/j.enconman.2016.12.072.

[99] Punov P, Milkov N, Danel Q, Perilhon C, Podevin P, Evtimov T. Optimization of automotive Rankine cycle waste heat recovery under various engine operating condition. AIP Conf. Proc., vol. 1814, American Institute of Physics; 2017. doi:https://doi.org/10.1063/1.4976293.

[100] Yang F, Zhang H, Bei C, Song S, Wang E. Parametric optimization and performance analysis of ORC (organic Rankine cycle) for diesel engine waste heat recovery with a fin-and-tube evaporator. Energy 2015;91:128–41. doi:10.1016/j.energy.2015.08.034.

[101] Badescu V, Aboaltabooq MHK, Pop H, Apostol V, Prisecaru M, Prisecaru T. Design and operational procedures for ORC-based systems coupled with internal combustion engines driving electrical generators at full and partial load. Energy Convers Manag 2017;139:206–21. doi:10.1016/j.enconman.2017.02.046.

[102] Jiménez-Arreola M, Wieland C, Romagnoli A. Response time characterization of organic Rankine cycle evaporators for dynamic regime analysis with fluctuating load. Energy Procedia 2017;129:427–34. doi:10.1016/j.egypro.2017.09.131.

[103] Liu L, Pan Y, Zhu T, Gao N. Numerical predicting the dynamic behavior of heat exchangers for a small-scale organic Rankine cycle. Energy Procedia 2017;129:419–26. doi:10.1016/j.egypro.2017.09.127.

[104] Di Battista D, Mauriello M, Cipollone R. Waste heat recovery of an ORC-based power unit in a turbocharged diesel engine propelling a light duty vehicle. Appl Energy 2015;152:109–20. doi:10.1016/j.apenergy.2015.04.088.

[105] Mazzi N, Rech S, Lazzaretto A. Off-design dynamic model of a real organic Rankine cycle system fuelled by exhaust gases from industrial processes. Energy 2015;90:537–51. doi:10.1016/j.energy.2015.07.083.

[106] Pili R, Romagnoli A, Jimenez-Arreola M, Spliethoff H, Wieland C. Simulation of Organic

Rankine Cycle – Quasi-steady state vs dynamic approach for optimal economic performance. Energy 2018. doi:10.1016/j.energy.2018.10.166.

[107] Koppauer H, Kemmetmüller W, Kugi A. Modeling and optimal steady-state operating points of an ORC waste heat recovery system for diesel engines. Appl Energy 2017;206:329–45. doi:10.1016/j.apenergy.2017.08.151.

[108] Kosmadakis G, Manolakos D, Papadakis G. Experimental investigation of a low-temperature organic Rankine cycle (ORC) engine under variable heat input operating at both subcritical and supercritical conditions. Appl Therm Eng 2016;92:1–7. doi:10.1016/j.applthermaleng.2015.09.082.

[109] Dickes R, Dumont O, Daccord R, Quoilin S, Lemort V. Modelling of organic Rankine cycle power systems in off-design conditions: An experimentally-validated comparative study. Energy 2017;123:710–27. doi:10.1016/j. energy.2017.01.130.

[110] Lecompte S, Gusev S, Vanslambrouck B, De Paepe M. Experimental results of a small-scale organic Rankine cycle: Steady state identification and application to off-design model validation. Appl Energy 2018;226:82–106. doi:10.1016/j.apenergy.2018.05.103.

[111] Read M, Smith I, Stosic N, Kovacevic A. Comparison of organic Rankine cycle systems under varying conditions using turbine and twin-screw expanders. Energies 2016;9. doi:10.3390/en9080614.

[112] Xu B, Yebi A, Onori S, Filipi Z, Liu X, Shutty J, et al. Transient power optimization of an organic Rankine cycle waste heat recovery system for heavy-duty Diesel engine applications. SAE Int J Altern Powertrains 2017;6:2017-01–0133. doi:10.4271/2017-01-0133.

[113] Usman M, Imran M, Lee DH, Park B-S. Experimental investigation of off-grid organic Rankine cycle control system adapting sliding pressure strategy under proportional integral with feed-forward and compensator. Appl Therm Eng 2017;110:1153–63. doi:10.1016/j.applthermaleng.2016.09.021.

[114] Feru E, Willems F, de Jager B, Steinbuch M. Modeling and control of a parallel waste heat recovery system for Euro-VI heavy-duty diesel engines. Energies 2014;7:6571–92. doi:10.3390/en7106571.

[115] Turton R, Bailie RC, Whiting WB, Shaelwitz JA. Analysis, synthesis and design of chemical processes. vol. 53. 3rd Editio. Pearson Education, Inc.Rights and Contracts Department 501 Boylston Street, Suite 900 Boston, MA 02116; 2009. doi:10.1017/CBO9781107415324.004.

[116] Seider WD, Lewin DR, Seader JD, Widagdo S, Gani R, Ming NG K. Product and process design principles: Synthesis, analysis and evaluation. Fourth. Wiley; 2017.

[117] Lemmens S. Cost engineering techniques and their applicability for cost estimation of organic rankine cycle systems. Energies 2016;9:485–503. doi:10.3390/en9070485.

[118] Yang F, Zhang H, Song S, Bei C, Wang H, Wang E. Thermoeconomic multi-objective optimization of an organic Rankine cycle for exhaust waste heat recovery of a diesel engine. Energy 2015;93:2208–28. doi:10.1016/j.energy.2015.10.117.

[119] Kazemi N, Samadi F. Thermodynamic, economic and thermo-economic optimization of a new proposed organic Rankine cycle for energy production from geothermal resources. Energy Convers Manag 2016;121:391–401. doi:10.1016/j.enconman.2016.05.046.

[120] Le Brun N, Simpson M, Acha S, Chatzopoulou MA, Oyewunmi O, Lambert R, et al. Prospects for commercial small-scale stationary ORC-ICE CHP (200-500 kWe ICE): the case of the UK food retail sector. Energy n.d.;In prepara.

[121] Neto R de O, Sotomonte CAR, Coronado CJR, Nascimento MAR. Technical and economic analyses of waste heat energy recovery from internal combustion engines by the organic Rankine cycle. Energy Convers Manag 2016;129:168–79. doi:10.1016/j.enconman.2016.10.012.

[122] Walraven D, Laenen B, D'haeseleer W. Optimum configuration of shell-and-tube heat exchangers for the use in low-temperature organic Rankine cycles. Energy Convers Manag 2014;83:177–87. doi:10.1016/j.enconman.2014.03.066.

[123] Ferguson CR, Kirkpatrick AT. Internal Combustion Engines: Applied Thermosciences. Third Edit. John Wiley & Sons; 2015.

[124] Karamangil MI, Kaynakli O, Surmen A. Parametric investigation of cylinder and jacket side convective heat transfer coefficients of gasoline engines. Energy Convers Manag 2006;47:800–16. doi:10.1016/j.enconman.2005.05.018.

[125] Heywood JB. Internal Combustion Engines Fundamentals. McGraw-Hill; 1989.

[126] Salau NPG, Fagundez JLS, Martins MES, Lanzanova T. Heat transfer evaluation of an internal combustion engine operating using wet ethanol fuel - Part A. 23rd SAR Brazil Int. Conf. Disp., Sao Paulo: 2014. doi:10.4271/2014-36-0361.

[127] Rakopoulos CD, Kosmadakis GM, Dimaratos AM, Pariotis EG. Investigating the effect of crevice flow on internal combustion engines using a new simple crevice model implemented in a CFD code. Appl Energy 2011;88:111–26. doi:10.1016/j.apenergy.2010.07.012.

[128] Mathworks. MATLAB 2015.

[129] Kotas T. The exergy method of thermal plant analysis. 1st ed. Butterworths; 1985.

[130] Al-Sulaiman FA, Hamdullahpur F, Dincer I. Greenhouse gas emission and exergy assessments of an integrated organic Rankine cycle with a biomass combustor for combined cooling, heating and power production. Appl Therm Eng 2011;31:439–46. doi:10.1016/j.applthermaleng.2010.09.019.

[131] Cengel YA, Boles M. Thermodynamics An Engineering Approach. 8th ed. New York ; McGraw-Hill Education; 2015.

[132] Mansoury M, Jafarmadar S, Khalilarya S. Energetic and exergetic assessment of a two-stage Organic Rankine Cycle with reactivity controlled compression ignition engine as a low temperature heat source. Energy Convers Manag 2018;166:215–32. doi:10.1016/j.enconman.2018.04.019.

[133] Al-Sulaiman FA, Dincer I, Hamdullahpur F. Thermoeconomic optimization of three trigeneration systems using organic Rankine cycles: Part I – Formulations. Energy Convers Manag 2013;69:199–208. doi:10.1016/j.enconman.2012.12.030.

[134] Abusoglu A, Kanoglu M. Exergetic and thermoeconomic analyses of diesel engine powered cogeneration: Part 1 – Formulations. Appl Therm Eng 2009;29:234–41. doi:10.1016/j.applthermaleng.2008.02.025.

[135] Nemati A, Fathi V, Barzegar R, Khalilarya S. Numerical investigation of the effect of injection timing under various equivalence ratios on energy and exergy terms in a direct injection SI hydrogen fueled engine. Int J Hydrogen Energy 2013;38:1189–99. doi:10.1016/j.ijhydene.2012.10.083.

[136] Sapin P, Taleb A, Barfuss C, White AJ, Fabris D, Markides CN. Thermodynamic losses in a gas spring: Comparison of experimental and numerical results. 12th Int. Conf. Heat Transf. Fluid Mech. Thermodyn., 2016, p. 172–7.

[137] Uusitalo A, Honkatukia J, Turunen-Saaresti T. Evaluation of a small-scale waste heat recovery organic Rankine cycle. Appl Energy 2017;192:146–58. doi:10.1016/j.apenergy.2017.01.088.

[138] Chatzopoulou MA, Simpson M, Sapin P, Markides CN. Off-design optimisation of organic Rankine cycle with piston expander for medium-scale combined heat and power applications. Appl Energy 2018;Under revi.

[139] ASHRAE. 2013 ASHRAE Handbook: Fundamentals. ASHRAE, 1791 Tullie Circle, N.E.,

Atlanta, GA 30329; 2013.

[140] Bergman TL, Lavine AS, Incropera FP, DeWitt DP. Fundamentals of heat and mass transfer. John Wiley & Sons; 2011.

[141] Chatzopoulou MA, Markides CN. Advancements in organic Rankine cycle system optimisation for combined heat and power applications: Components sizing and thermoeconomic considerations. Proc. 30th Int. Conf. Effic. Cost, Optimisation, Simul. Environ. Impact Energy Syst., San Diego: 2017.

[142] Dobson MK, Wattelet JP, Chato JC. Optimal sizing of two-phase heat exchangers. 1993.

[143] Chen JC. Correlation for boiling heat transfer to saturated fluids in convective flow. Ind Eng Chem Process Des Dev 1966;5:322–9. doi:10.1021/i260019a023.

[144] Shah MM. A general correlation for heat transfer during film condensation inside pipes. Int J Heat Mass Transf 1979;22:547–56. doi:10.1016/0017-9310(79)90058-9.

[145] Muley A, Manglic RM. Experimental study of turbulent flow heat transfer and pressure drop in a plate heat exchanger with chevron plates. J Heat Transfer 1999;121:110–7.

[146] Focke WW, Zachariades J, Olivier I. The effect of the corrugation inclination angle on the thermohydraulic performance of plate heat exchangers. Int J Heat Mass Transf 1985;28:1469–79. doi:10.1016/0017-9310(85)90249-2.

[147] Han D-H, Lee K-J, Kim Y-H. Experiments on the characteristics of evaporation of R410A in brazed plate heat exchangers with different geometric configurations. Appl Therm Eng 2003;23:1209–25. doi:10.1016/S1359-4311(03)00061-9.

[148] Hsieh YY, Lin TF. Saturated flow boiling heat transfer and pressure drop of refrigerant R-410A in a vertical plate heat exchanger. Int J Heat Mass Transf 2002;45:1033–44. doi:10.1016/S0017-9310(01)00219-8.

[149] Yan Y-Y, Lin T-F. Evaporation heat transfer and pressure drop of refrigerant R-134a in a plate heat exchanger. J Heat Transfer 1999;121:118–27. doi:10.1115/1.2825924.

[150] Han DH, Lee KJ, Kim YH. The characteristics of condensation in brazed plate heat exchangers with different chevron angles. J Korean Phys Soc 2003;43:66–73. doi:10.1016/S1359-4311(03)00061-9.

[151] Sapin P, Simpson M, White AJ, Markides CN. Lumped dynamic analysis and design of a high-performance reciprocating-piston expander. Proc. 30th Int. Conf. Effic. Cost, Optimisation, Simul. Environ. Impact Energy Syst., San Diego: 2017.

[152] Moss RW, Roskilly AP, Nanda SK. Reciprocating Joule-cycle engine for domestic CHP systems. Appl Energy 2005;80:169–85. doi:10.1016/j.apenergy.2004.03.007.

[153] Serrano JR, Olmeda P, Arnau FJ, Dombrovsky A, Smith L. Turbocharger heat transfer and mechanical losses influence in predicting engines performance by using one-dimensional simulation codes. Energy 2015;86:204–18. doi:10.1016/j.energy.2015.03.130.

[154] Winandy E, Saavedra O C, Lebrun J. Simplified modelling of an open-type reciprocating compressor. Int J Therm Sci 2002;41:183–92. doi:10.1016/S1290-0729(01)01296-0.

[155] Shapiro A. The dynamics and thermodynamics of compressible fluid flow. New York: John Wiley & Sons; 1953.

[156] Lekić UB. Fluid flow and heat transfer in a helium gas spring-computational fluid dynamics and experiments. University of Twente, Enschede, the Netherlands, 2011.

[157] Simpson M, Rotolo G, Sapin P, P DP, White AJ, Markides CN. Thermodynamic performance maps of reciprocating-piston expanders for operation at off-design and part-load conditions. Proc. 13th Int. Conf. Heat Transf. Fluid Mech. Thermodyn., Portorož: 2017.

[158] Imran M, Usman M, Park B-S, Lee D-H. Volumetric expanders for low grade heat and waste heat recovery applications. Renew Sustain Energy Rev 2016;57:1090–109. doi:10.1016/j.rser.2015.12.139.

[159] Ofx. OFX Rates 2018. https://www.ofx.com/en-gb/forex-news/historical-exchange-rates/yearly-average-rates/.

[160] Acha S, Bustos-Turu G, Shah N. Modelling real-time pricing of electricity for energy conservation measures in the UK commercial sector. ENERGYCON 2016, IEEE Intrernational Energy Conference; 2016. doi:10.1109/energycon.2016.7514090.

[161] Soler A. Half-hourly regional electricity price modelling for commercial end users in the UK. Imperial College London, 2016.

[162] Evins R. A review of computational optimisation methods applied to sustainable building design. Renew Sustain Energy Rev 2013;22:230–45. doi:10.1016/j.rser.2013.02.004.

[163] NIST. Reference Fluid Thermodynamic and Transport Properties Database (REFPROP) 2016.

[164] Byrd RH, Gilbert JC, Nocedal J, Byrd RH, Gilbert JC, Nocedal J, et al. A trust region method based on interior point techniques for nonlinear programming. Math Program 2006;185:149–85.

[165] Deb K. Multi-objective optimisation using evolutionary algorithms. Chichester : Wiley; 2001.

[166] Keirstead J, Shah N. Urban energy systems an integrated approach. Abingdon, Oxford, UK: Routledge; 2013.

[167] Zhang HG, Wang EH, Fan BY. A performance analysis of a novel system of a dual loop bottoming organic Rankine cycle (ORC) with a light-duty diesel engine. Appl Energy 2013;102:1504–13. doi:10.1016/j.apenergy.2012.09.018.

[168] Da Silveira M, Gertz L, Cervieri A, Rodrigues A. Analysis of the friction losses in an internal combustion engine. 21st SAE Bras. Int. Congr. Exhib., SAE; 2012. doi:10.4271/2012-36-0303.

[169] Jiménez-Arreola M, Pili R, Wieland C, Romagnoli A. Analysis and comparison of dynamic behavior of heat exchangers for direct evaporation in ORC waste heat recovery applications from fluctuating sources. Appl Energy 2018;216:724–40. doi:10.1016/j.apenergy.2018.01.085.

[170] Yun KT, Cho H, Luck R, Mago PJ. Modeling of reciprocating internal combustion engines for power generation and heat recovery. Appl Energy 2013;102:327–35. doi:10.1016/j.apenergy.2012.07.020.

[171] Wang EH, Zhang HG, Zhao Y, Fan BY, Wu YT, Mu QH. Performance analysis of a novel system combining a dual loop organic Rankine cycle (ORC) with a gasoline engine. Energy 2012;43:385–95. doi:10.1016/j.energy.2012.04.006.

[172] Ziviani D, Woodland BJ, Georges E, Groll EA, Braun JE, Horton WT, et al. Development and a validation of a charge sensitive organic Rankine cycle (ORC) simulation tool. Energies 2016. doi:10.3390/en9060389.

[173] Peña F, Blanco JM. Evaluation of the physical dew point in the economizer of a combined cycle burning natural gas. vol. 27. 2007. doi:10.1016/j.applthermaleng.2006.12.021.

[174] Wang X, Shu G, Tian H, Feng W, Liu P, Li X. Effect factors of part-load performance for various Organic Rankine cycles using in engine waste heat recovery. Energy Convers Manag 2018;174:504–15. doi:10.1016/j.enconman.2018.08.024.

[175] Alshammari F, Karvountzis-Kontakiotis A, Pesyridis A, Usman M. Expander technologies for automotive engine organic rankine cycle applications. Energies 2018;11:1–37. doi:10.3390/en11071905.

[176] Alfa Laval. Pricelist refrigeration equipment – 2016 2016. http://www.aotech.cz/UploadFiles/Doc/Refrigeration PPL-EN 2016-01-01.pdf.

[177] Bitzer. Bitzer semi-hermetic reciprocating compressors 2017. https://www.bitzer.de/shared_media/documentation/kp-104-4.pdf.

[178] Bitzer. Price list 2017 2017. http://ref-com.ru/files/BITZER_Price_2017.pdf (accessed February 18, 2018).

[179] Lee C-E, Yu B, Lee S. An analysis of the thermodynamic efficiency for exhaust gas recirculation-condensed water recirculation-waste heat recovery condensing boilers (EGR-CWR-WHR CB). Energy 2015;86:267–75. doi:10.1016/j.energy.2015.04.042.

[180] Shi Y, Zhang X, Li F, Ma L. Engineering acid dew temperature: the limitation for flue gas heat recovery. Chinese Sci Bull 2014;59:4418–25. doi:10.1007/s11434-014-0577-y.

[181] Shu G, Yu G, Tian H, Wei H, Liang X, Huang Z. Multi-approach evaluations of a cascade-organic Rankine cycle (C-ORC) system driven by diesel engine waste heat: Part A – Thermodynamic evaluations. Energy Convers Manag 2016;108:579–95. doi:10.1016/j.enconman.2015.10.084.

[182] Rech S, Zandarin S, Lazzaretto A, Frangopoulos CA. Design and off-design models of single and two-stage ORC systems on board a LNG carrier for the search of the optimal performance and control strategy. Appl Energy 2017;204:221–41. doi:10.1016/j.apenergy.2017.06.103.

[183] Capra F, Martelli E. Numerical optimization of combined heat and power organic Rankine cycles – Part B: Simultaneous design & part-load optimization. Energy 2015;90:329–43. doi:10.1016/j.energy.2015.06.113.

[184] Quoilin S, Aumann R, Grill A, Schuster A, Lemort V, Spliethoff H. Dynamic modeling and optimal control strategy of waste heat recovery organic Rankine cycles. Appl Energy 2011;88:2183–90. doi:10.1016/j.apenergy.2011.01.015.

Appendix A.

Organic Rankine cycle off-design optimisation: Additional results

A.1. ORC engine with screw expander: Evaporator heat transfer coefficient

The overall heat transfer coefficient (*U*-values) achieved in the evaporator heat exchanger (HEX) with screw expander are presented in Fig. A. 1 (for double-pipe designs - DPHEX) and Fig. A. 2 (for plate-frame designs - PHEX). The overall heat transfer coefficient for DPHEX ranges between 30-52 W/m^2 K, depending on the fluid and the HEX section. As expected the evaporator two-phase section has always the highest *U*-value, followed very closely by the superheating section. The preheating sections presents the lowest *U*-values, mainly due to the higher fluid density, that leads to smaller volume flow rates, and thus velocities in the tubes, decreasing the Reynolds number, while also the temperatures are lower for both the heat source and the working fluid. PHEXs have significantly higher *U*-values than those achieved in the DPHEX architecture. This is in line with the findings in Chapter 5, where the PHEX heat transfer area requirements are significantly, lower than those of DPHEXs. Finally, the influence of the heat source and working fluids' mass flow rate reduction at off-design operation on the *U*-values is significant; while the heat source mass flow rate reduces from 2.1 kg/s to 1.3 kg/s (CHP-ICE PL 100% to 60%), the *U*-value reduces by up to 30%. On the contrary for fixed heat source mass flow rate the temperature increase has on only marginal impact on the HTC achieved.

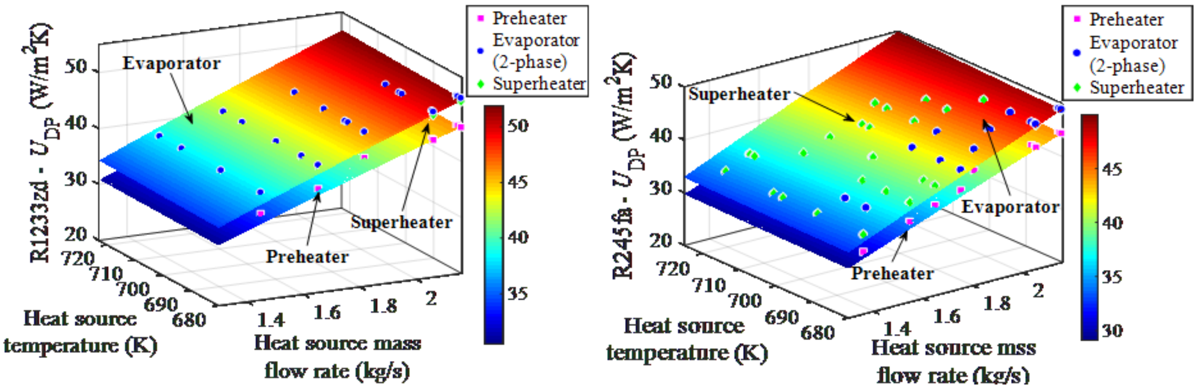

(a) (b)

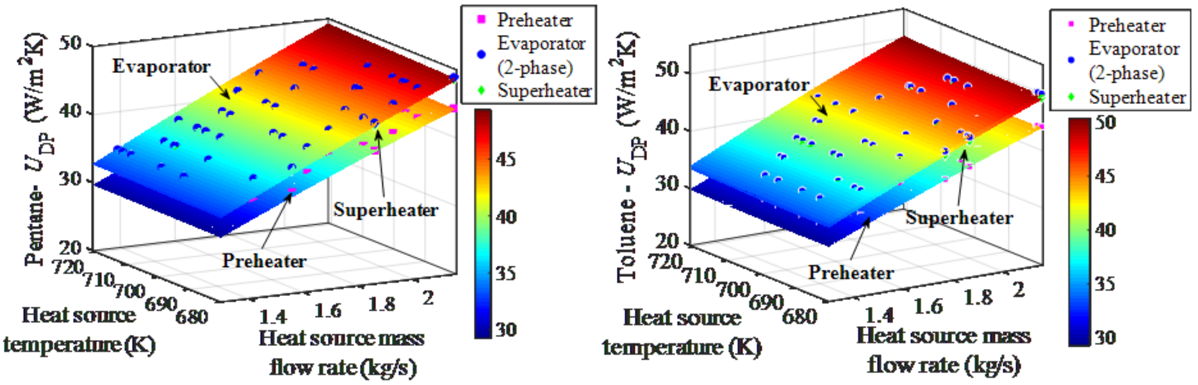

(c) (d)

Fig. A. 1: DPHEX evaporator overall heat transfer coefficient map at off-design operation, with variable screw expander efficiency for: a) R1233zd, b) R245fa, c) pentane, and d) toluene.

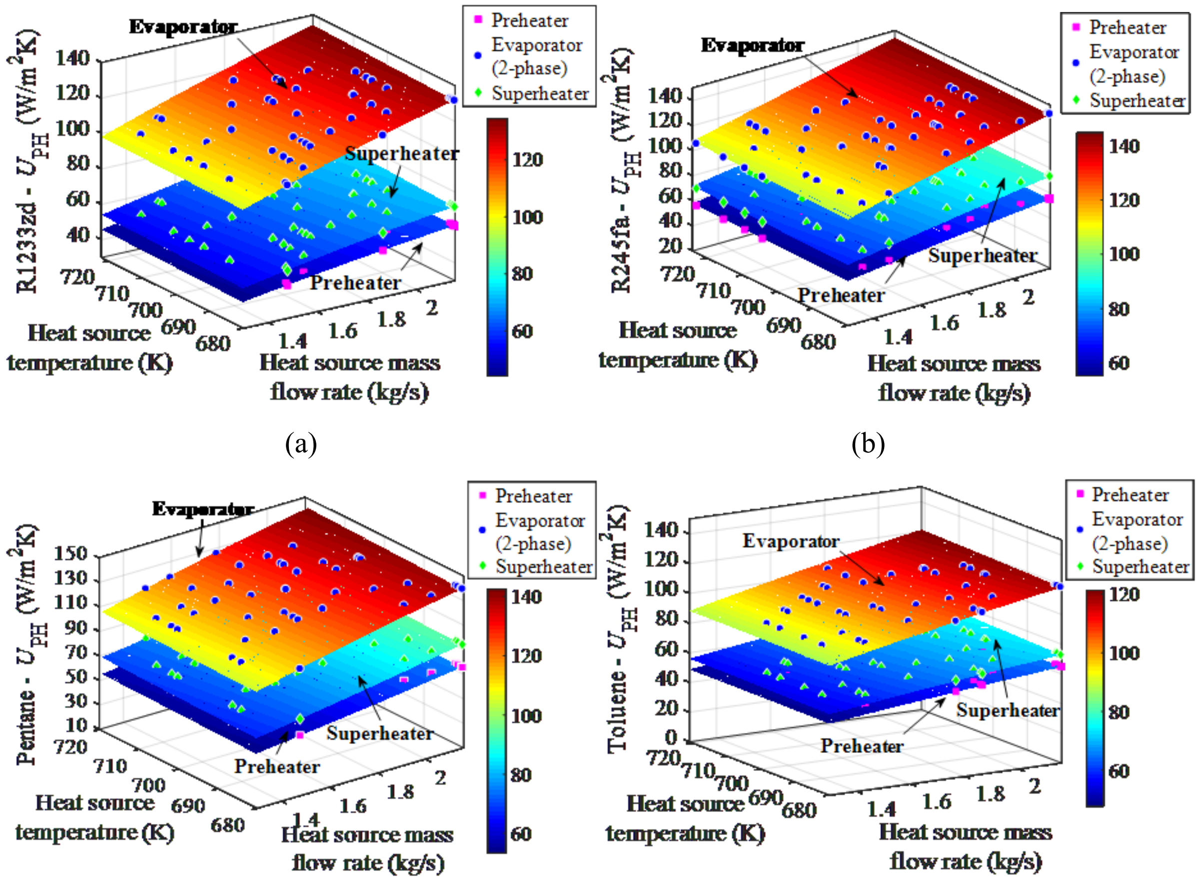

(c) (d)

Fig. A. 2: PHEX evaporator overall heat transfer coefficient map at off-design operation, with variable screw expander efficiency for: a) R1233zd, b) R245fa, c) pentane, and d) toluene.

A.2. ORC engine with screw expander: Evaporator effectiveness

The effectiveness maps of the evaporator HEX are presented in Fig. A. 3 for DPHEXs, and in Fig. A. 4 for PHEXs. The findings are similar to those presented for ORC engines with piston expanders, in Section 5.5.2. The preheater section has the highest effectiveness, followed by the evaporator and the superheater sections. This is attributed to the pinch point location inside the evaporator HEX, which is located in the preheating section. It is noted that the toluene has the highest effectiveness in the evaporator section among all fluids investigated and in both HEX architectures. This is explained by the high evaporating temperature of this fluid, at a relatively low pressure, which allows a good temperature match to that of the heat source. Additionally, toluene evaporation pressure is relatively lower than that achieved by the other fluids, resulting in high latent heat of evaporation being available to the working fluid. Finally, in contrast with the U-value reduction at off-design operation, the effectiveness of the HEXs either increases or stays constant. This is attributed to the changes in the LMDT of the HEX at off-design operation. As illustrated in Fig. A. 5-Fig. A. 6, the LMDT increases at PL, making the heat transfer over the same area more effective.

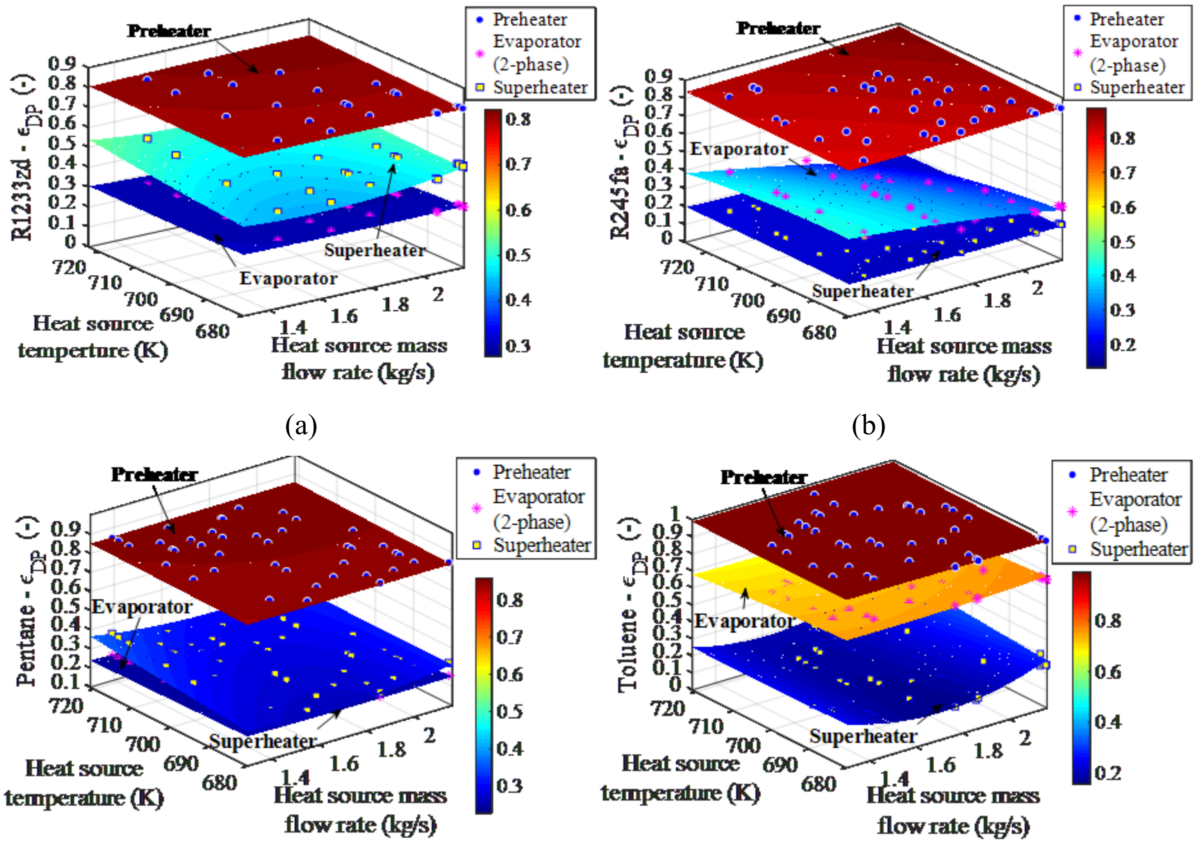

(a) (b)

(c) (d)

Fig. A. 3: DPHEX evaporator effectiveness map at off-design operation with variable screw expander efficiency for: a) R1233zd, b) R245fa, c) pentane, and d) toluene.

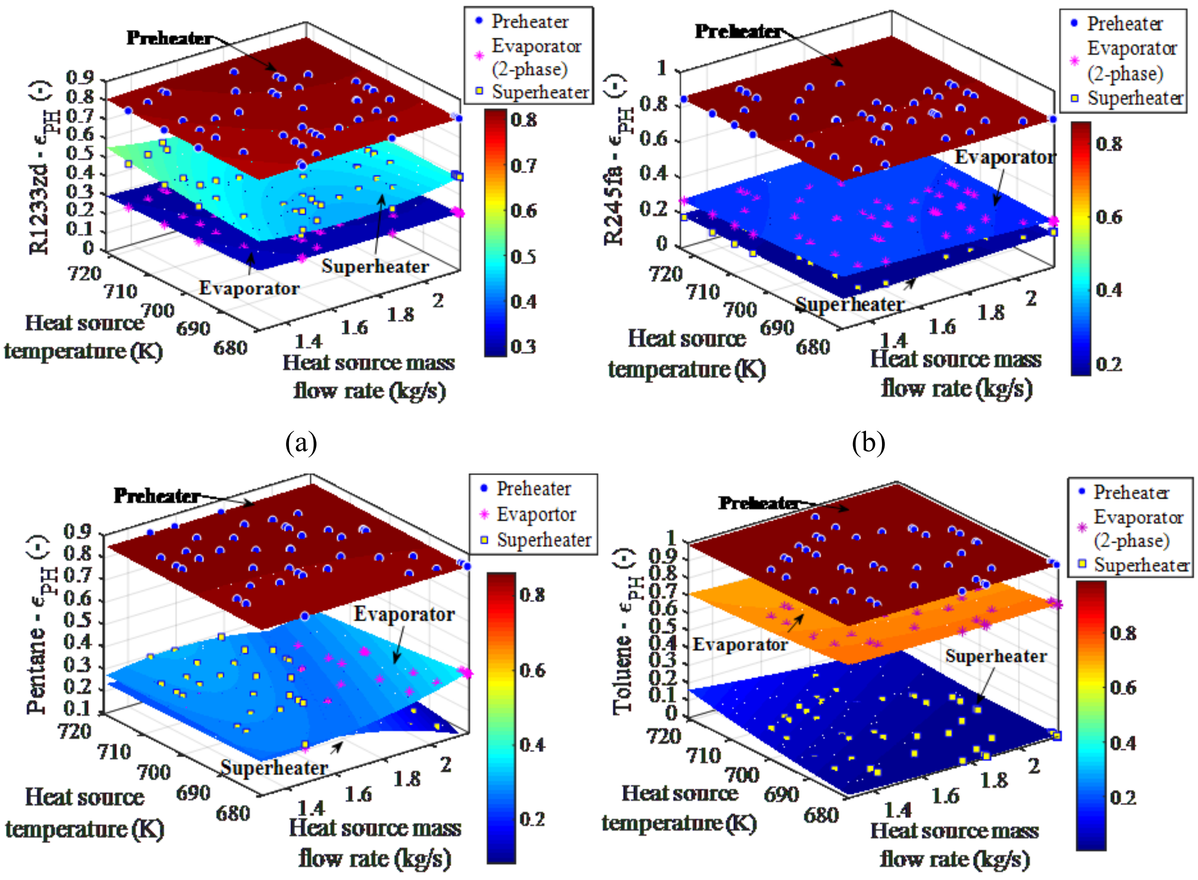

(a) (b)

(c) (d)

Fig. A. 4: PHEX evaporator effectiveness map at off-design operation with variable screw expander efficiency for: a) R1233zd, b) R245fa, c) pentane, and d) toluene.

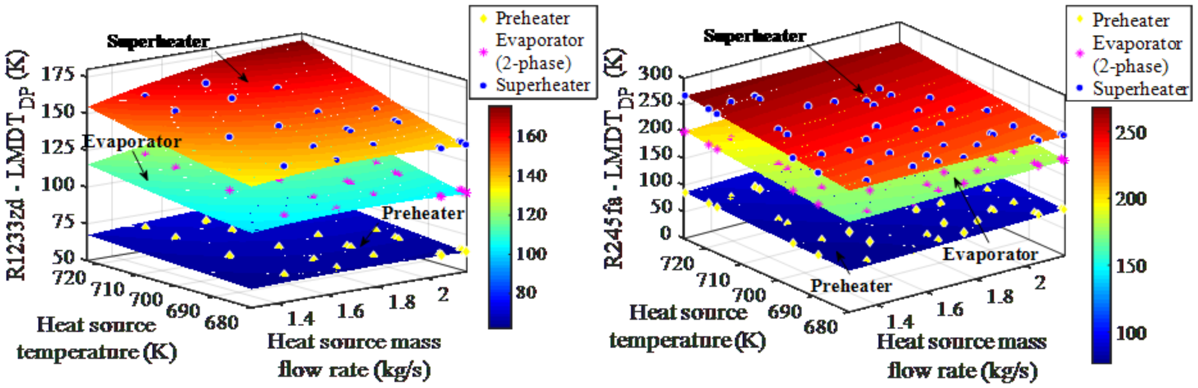

(a) (b)

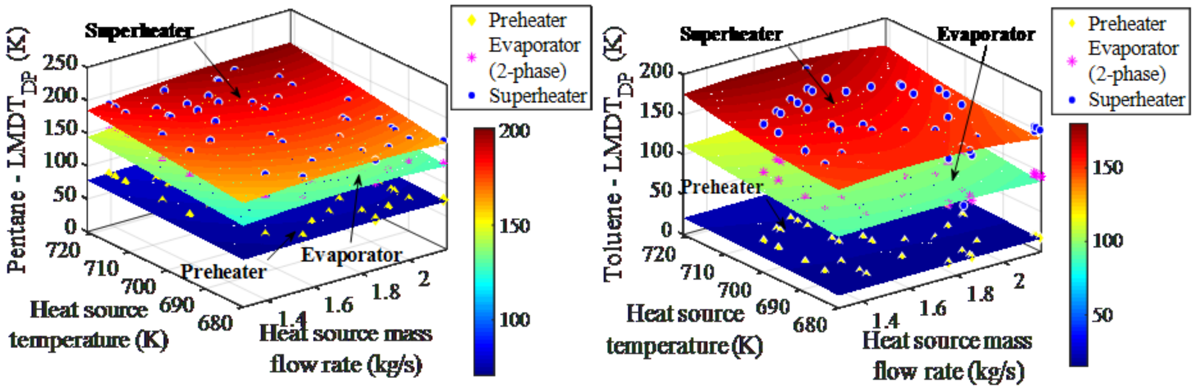

(c) (d)

Fig. A. 5: DPHEX evaporator temperature gradient map at off-design operation with screw expander for: a) R1233zd, b) R245fa, c) pentane, and d) toluene.

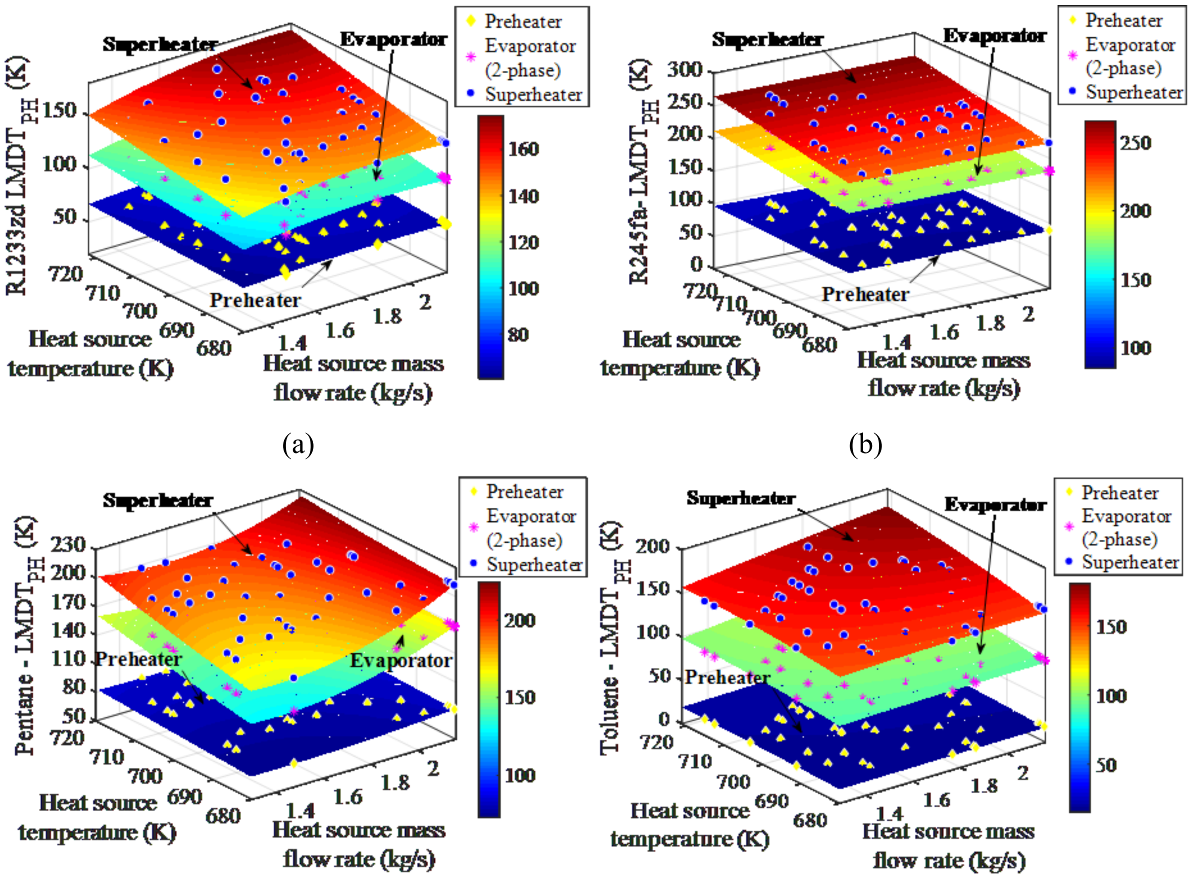

(a) (b)

(c) (d)

Fig. A. 6: PHEX evaporator temperature gradient map at off-design operation with screw expander for: a) R1233zd, b) R245fa, c) pentane, and d) toluene.